



HAL
open science

MEMS-based High-Frequency(100-300MHz) Ultrasonic Linear Phased Arrays

Jin-Ying Zhang

► **To cite this version:**

Jin-Ying Zhang. MEMS-based High-Frequency(100-300MHz) Ultrasonic Linear Phased Arrays. Engineering Sciences [physics]. Université de Valenciennes et du Hainaut-Cambrésis, 2011. English. NNT : 2011VALE0024 . tel-03350518

HAL Id: tel-03350518

<https://hal.science/tel-03350518>

Submitted on 21 Sep 2021

HAL is a multi-disciplinary open access archive for the deposit and dissemination of scientific research documents, whether they are published or not. The documents may come from teaching and research institutions in France or abroad, or from public or private research centers.

L'archive ouverte pluridisciplinaire **HAL**, est destinée au dépôt et à la diffusion de documents scientifiques de niveau recherche, publiés ou non, émanant des établissements d'enseignement et de recherche français ou étrangers, des laboratoires publics ou privés.

瓦朗谢讷大学（联合培养）博士学位论文

专业：电子学

基于 MEMS 技术的高频（100-300 MHz）

超声线性相控阵换能器

张金英

答辩委员会成员：

Gilles DESPAUX	蒙彼利埃第二大学 教授（评审人）
Sylvain BALLANDRAS	贝桑松 FEMTO-ST 实验室 主任研究员（评审人）
Bertrand NONGAILLARD	瓦朗谢讷大学 教授（论文导师）
Wei-Jiang XU (徐卫疆)	瓦朗谢讷大学 副教授（合作导师）
Julien CARLIER	瓦朗谢讷大学 副教授（合作导师）
张碧星	中国科学院声学研究所 教授
张健	华东师范大学电子工程系 教授
黄宜平	复旦大学微电子学系 教授（论文导师）
纪新明	复旦大学微电子学系 助理教授（合作导师）
周嘉	复旦大学微电子学系 教授
鲍敏杭	复旦大学微电子学系 教授

Ph. D. Thesis

MEMS-based High-Frequency (100-300 MHz)

Ultrasonic Linear Phased Arrays

Department	Department of Opto Acoustic Electronics
Specialty	Microelectronics
Name	Jinying Zhang
Supervisors	Prof. Bertrand Nongaillard Prof. Yiping Huang
Co-supervisors	Dr. Weijiang Xu Dr. Julien Carlier Dr. Xinming Ji
Date	Oct. 10, 2011

Content

Abstract.....	1
Résumé.....	2
摘 要.....	3
Acknowledgments.....	7
General introduction of the thesis	8
Chapter 1: Introduction	11
1.1 Ultrasonic imaging and its development	11
1.1.1 Development of ultrasonic phased arrays	11
1.1.2 Ultrasonic imaging.....	12
1.2 High-frequency ultrasonic imaging.....	15
1.2.1 Imaging resolution	15
1.2.2 Acoustic microscopy	16
1.2.3 Development of high-frequency ultrasonic phased arrays	18
1.3 Theory of ultrasonic phased array	19
1.3.1 Principle of ultrasonic phased array	19
1.3.2 Some particularities of high frequency arrays.....	23
1.4 Different techniques for the fabrication of ultrasonic arrays.....	27
1.4.1 Conventional arrays fabrication technologies	28
1.4.2 High-frequency arrays based on MEMS technologies	30
1.4.3 cMUT pMUT and mMUT.....	35
1.4.4 Laser technique	40
1.5 Summary and outline of the thesis	41
Chapter 2: Acoustic Waves in Elastic Media and Fundamentals of Piezoelectric Ultrasonic Transducers.....	44
2.1 Waves propagation in fluid, solid and piezoelectric materials	44
2.1.1 Waves equation in fluids	44
2.1.2 Waves equation in solid materials	45
2.1.3 Waves equation in piezoelectric materials.....	47
2.1.4 Numerical solution of Christoffel equation for analysis of material elasticity and piezoelectricity	52
2.2 Modelling and characteristics of piezoelectric transducers.....	59
2.2.1 KLM model.....	59
2.2.2 Structure and characteristics of high frequency piezoelectric transducers	61
2.2.3 Electrical impedance and electrical matching	67
2.2.4 Acoustic impedance and mechanical matching.....	70
2.3 Summary	75
Chapter 3: Finite Element Modeling of Piezoelectric Ultrasonic Array Transducers .77	
3.1 Finite element formalism using COMSOL	78
3.1.1 PDE and COMSOL formalism.....	79
3.1.2 Sources of excitation	80
3.1.3 Boundary conditions	81
3.1.4 Simulation examples	87
3.2 Simulation of buffered transducer arrays	96
3.2.1 2-D simulation in x-y plane (simulation of array transducer with a buffer layer)..	97
3.2.2 2-D simulation in z-y plane (simulation of single element transducer with a focal lens).....	105
3.3 Summary	108
Chapter 4: LiNbO ₃ -based array fabrication and characterization.....	110
4.1 Simulation of backing transducer arrays	111

4.1.1 Model design.....	111
4.1.2 Beam behaviour	113
4.2 Investigation of etching LiNbO ₃ 36°/Y-cut arrays	120
4.2.1 Focusing Ion Beam (FIB).....	121
4.2.2 Inductively Coupled Plasma (ICP) Reactive Ion Etching (RIE)	123
4.3 Fabrication of LiNbO ₃ 36°/Y-cut transducer array on silicon.....	127
4.3.1 Process flow	127
4.3.2 Fabricated array transducers.....	129
4.3.3 Discussion of fabricated patterns	131
4.4 Characterization of LiNbO ₃ 36°/Y-cut transducer array	131
4.4.1 Measurement method	131
4.4.2 Measured results.....	133
4.5 Summary	134
Chapter 5: ZnO-based array fabrication and characterization	136
5.1 Fabrication of ZnO-based transducer array using wet etching method.....	137
5.1.1 Geometry design	138
5.1.2 Fabrication of thick-film ZnO transducer arrays.....	138
5.1.3 Discussion of fabricated patterns	144
5.1.4 Characterization of thick-film ZnO transducer arrays.....	144
5.1.5 Summary	147
5.2 A novel method for fabrication of piezoelectric transducer arrays on Si substrate	148
5.2.1 Fabrication of thick-film ZnO transducer arrays.....	148
5.2.2 Discussion of fabricated patterns	152
5.2.3 Characterization of thick-film ZnO transducer arrays.....	152
5.2.4 Improvement of sputtering process with rotation 90°	154
5.2.5 Discussion of fabricated patterns using rotation method	156
5.2.6 Summary	157
Conclusions and prospects	158
Annex 1: Calculation of phase delay	160
Annex 2.1: Parameters of the used materials.....	164
Annex 2.2: Material tensor transformations	167
Annex 2.3: Multiple quarter wavelength mechanical matching	172
References.....	175

Abstract

High-frequency ultrasonic phased array transducer is a desired candidate in real-time and high resolution imaging. Many difficulties will arise in the development of array imaging systems with an operating frequency of above 100 MHz. These difficulties include high-frequency phase-delay system, electrical matching problem, mechanical matching problem, and especially the fabrication of high-frequency array transducers which play a critical role in ultrasonic phased array imaging systems. This dissertation focuses on the array transducers with a central frequency of above 100 MHz, which mainly investigates two aspects. The first one is the finite element numerical simulations in the optimized design. The second one is the fabrication using different experimental processes based on micro electromechanical system (MEMS) technologies.

In the section of numerical studies, a commercial finite element tool, COMSOL3.5a, is employed which benefits from well-performed coupling capabilities in combining fluidic model, solid model and electrical model. In piezoelectric backing array transducers, the effects of pitch size, kerf filler and kerf depth on the acoustic field, electrical impedance and crosstalk are investigated. Systematic simulations are carried out for a designed buffered transducer array.

In the section of experimental fabrication and characterization, MEMS based technologies are applied to obtain high-frequency array elements, such as radio frequency (RF) sputtering and etching thin film, etc. Single crystal LiNbO₃ arrays are made using ICP RIE technique. Two kinds of ZnO arrays are kerfed using wet chemical etching technique and micromachining silicon substrate, respectively. All of these arrays are characterized by Network Analyzer. The measured electrical impedance and crosstalk are consistent with the theoretical predictions obtained from finite element calculations.

Key words: Ultrasonic phased array; High-frequency; MEMS; FEM simulation; Piezoelectric

Résumé

Les réseaux de transducteurs ultrasonores haute fréquence à déphasage sont des candidats intéressants pour l'imagerie haute résolution en temps réel. De nombreuses difficultés interviennent lors du développement de réseaux avec une fréquence d'émission supérieure à 100 MHz: déphasage en haute fréquence, adaptation électrique, adaptation mécanique et fabrication des réseaux de transducteurs haute fréquence qui joue un rôle critique pour le développement de ces systèmes. Cette thèse porte notamment sur deux aspects spécifiques: la modélisation numérique par élément fini et la fabrication basée sur les microtechnologies et les MEMS.

Dans la partie consacrée aux simulations numériques, un modèle commercial basé sur les éléments finis, COMSOL 3.5a, est utilisé. Pour les réseaux de transducteurs piézoélectriques sur absorbeur en face arrière, l'influence du pas spatial, de la profondeur de séparation des transducteurs, de l'isolation mécanique de ces transducteurs sur le champ acoustique ont été étudiés ainsi que l'impédance électrique et le couplage. Ces simulations ont également été réalisées pour des réseaux de transducteur sur ligne à retard de propagation

Dans la partie consacrée aux réalisations expérimentales et à leur caractérisation, des réseaux ont été obtenus grâce aux technologies dédiées aux MEMS à partir de monocristaux de LiNbO_3 gravés par les technologies plasma et de ZnO déposé en couche mince. Ces réseaux de transducteur ont ensuite été caractérisés à l'analyseur de réseaux et les mesures électriques des impédances et des couplages ont permis de montrer la cohérence avec les prédictions théoriques.

Mots clés: Réseaux de transducteurs ultrasonores à déphasage, MEMS, simulation Eléments finis, Transducteur piézoélectrique haute fréquence

摘 要

超声相控传感器由多个独立的压电换能器组成的几何阵列，用电子控制系统按一定的时序延迟规则激发各个阵列单元，来控制超声束的位置聚焦和方向扫描。在超声成像应用中，相控阵相比于传统的单探头换能器，极大地提高了检测效率、精确性和可靠性。

超声相控阵技术已有 40 多年的发展历史。最初主要应用于医疗领域，如器官的超声成像检测、大功率超声利用其可控聚焦特性局部升温热疗治癌等。最初由于系统的复杂性、超声波在固体中传播的复杂性及成本费用高等原因使其在工业无损检测中的应用受限。随着电子技术和计算机技术的快速发展，使得超声相控阵技术逐渐应用于工业无损检测，特别是在石油钻井、核电站、航空航天等领域，如焊接缝隙、材料缺陷如疲劳裂纹等等的检测。由于数字电路和 DSP 技术的发展，使得精确延时越来越方便，超声相控阵技术发展和应用的也越来越迅速和广泛。

近几年，随着微电子技术、微机电系统（MEMS）技术和压电材料研究的不断发展，高频超声相控阵传感器在高精度成像领域越来越受到关注。尤其是要实现对微小的生物组织乃至细胞的成像，就要求传感器的工作频率高于 100 兆赫兹。然而，要开发工作频率大于 100 兆赫兹的阵列成像系统，目前还存在很多困难。这些困难包括高频相位延迟系统、传感器电阻抗和机械阻抗的匹配，尤其是高频阵列换能器本身的制备工艺。

高频超声相控阵换能器的研制面临二方面的挑战。一方面迄今为止对 100 兆赫兹以上的阵列换能器设计方面尚没有系统研究，也没有见到全面而系统的仿真结果的相关报道，因此如何对器件进行仿真和优化设计显得十分重要。另一方面高频阵列换能器的加工难度很大。比如，加工中心工作频率为 100 兆赫兹的阵列，通常压电薄膜的厚度在 30 微米左右，而阵元中心间距理论上要被限制在半波长约 7.5 微米以内。要制备出一系列各自独立的阵元，就需要采用刻蚀等微加工技术在压电薄膜上刻蚀出深宽比大约为 15:1 的缝隙，这个要求对于现阶段的技术是个极大的挑战。目前，一些研究人员已经制备出 100 兆赫兹以上的高频超声换能器阵列，但是因为尚没有解决高深宽比刻蚀技术难点，该高频超声换能器阵列的结构是无刻蚀缝隙的。这种无刻蚀缝隙，即无隔离的换能器阵元会产生严重的串扰，从而降低成像质量。

本论文针对上述二个问题，重点研究了中心频率为 100-300 兆赫兹的有缝隙隔离的阵列换能器，采用有限元数值仿真优化了器件设计并全面系统地模拟了器件性能，同时结合微机电系统（MEMS）技术成功研制了基于铌酸锂单晶和氧化

锌薄膜二种材料的高频超声相控阵传感器。

论文的工作及其贡献和创新点主要在两个方面：

一是用有限元计算方法（使用 COMSOL 软件），全面系统研究了基于铌酸锂单晶和氧化锌薄膜二种不同材料阵元中心间距、阵元间缝隙填充物和刻蚀缝隙深度对声场、电阻抗和串扰的影响，尤其是系统地模拟了自行设计的缓冲层阵列传感器和背衬层阵列传感器。

二是采用基于 MEMS 的加工工艺研制了基于铌酸锂单晶和氧化锌薄膜不同材料的高频超声相控阵传感器。本文研究了采用电感耦合等离子体反应离子刻蚀铌酸锂单晶、化学湿法刻蚀氧化锌薄膜和先刻蚀硅衬底再淀积氧化锌薄膜等三种不同的方法，制备了 100-300 兆赫兹的有缝隙隔离的阵列传感器。

在有限元数值仿真优化设计方面：

1. 为了减小衬底材料平坦背面反射声波引起的混响噪声，本文提出了一种在衬底背面刻蚀出粗糙沟槽结构以散射声波来降低混响噪声的方法。模拟结果表明这种沟槽结构的深度和宽度须大于一倍波长（声波在衬底中的波长），才能有效散射大多数入射波。

2. 传感器阵元中心间距会直接影响栅瓣的位置，仿真结果显示当阵元中心间距大于 1.5 倍波长（声波在传播媒介中的波长，传播媒介通常指水）时，栅瓣的影响将导致阵列换能器几乎无法使用。因此，在设计高频阵列换能器时，阵元中心间距不应超过 1.5 倍波长。另外，若阵元中心间距保持不变，当缝隙宽度增加时，传感器的分辨率将减小而方向性指数基本保持不变。

3. 本文分别采用一维 KLM 模型和二维有限元模型对压电阵列换能器阵元的电阻抗进行了模拟计算，发现阵列换能器中阵元的宽度和厚度相比拟时，不再符合一维等效模型。有必要使用二维有限元模型计算压电阵列换能器阵元的电阻抗。

4. 大部分报道的缝隙阵列传感器都对缝隙进行了填充，本文模拟发现无填充物的缝隙阵列比有填充物的缝隙阵列具有更好的声束性能。

5. 刻蚀缝隙深度对声场特性和阵列传感器的串扰有重要影响。本文模拟对比了不同刻蚀深度的缝隙阵列传感器，结果证明，全刻蚀的阵列传感器性能最优，但从实际加工的可行性方面考虑，研究表明半刻的阵列是一种比较理想的技术路线，因为它对制备要求低（其要求刻蚀缝隙的深宽比要比全刻蚀缝隙要求的比值低很多），同时表现出的传感器性能能够达到实际应用的要求。

6. 系统仿真和对比了缓冲层阵列传感器和背衬层阵列传感器的特性。总体来说，背衬层阵列传感器的分辨率更高。然而，它对阵元中心间距的限制很苛刻，须小于 0.5 倍波长才能抑制栅瓣的产生。即便采用目前最先进的工艺技术也无法

成功制备出满足这种要求的背衬层阵列。而缓冲层阵列传感器对阵元中心间距的要求则要低得多，这就使得阵列传感器的制备成为了可能。

在用 MEMS 技术研制铌酸锂单晶和氧化锌薄膜高频超声相控阵方面

1. 研究和制备了基于铌酸锂单晶材料的 230 兆赫兹的有刻蚀缝隙的阵列换能器。对 Y 切向 36° 的铌酸锂单晶压电材料的刻蚀是研制高频超声相控阵传感器的关键技术，本文比较了电感耦合等离子体反应离子刻蚀、聚焦离子束刻蚀和激光刻蚀等刻蚀铌酸锂单晶的技术，并总结和对比了这些技术在该单晶材料上刻蚀深宽比的极限，以确定是否可以用于制备高频阵列。最终，采用电感耦合等离子体反应离子刻蚀技术制备了单晶铌酸锂阵列。该阵列阵元中心间距为 42 微米，阵元厚度为 16 微米。采用网络分析仪测试了该阵列的电阻抗和串扰。测试结果显示，在谐振频率 230 兆赫兹处，各阵元的电阻抗模约为 1000 欧姆，最近邻阵元的串扰为 -46 dB。这些测试结果都和有限元理论计算值相一致。根据刻蚀结果可推理得到，对一个工作于 200 兆赫兹的半刻蚀缝隙的铌酸锂单晶阵列，采用电感耦合等离子体反应离子刻蚀技术有望达到的阵元中心间距最小为 10 微米。

2. 研究了采用化学湿刻技术刻蚀氧化锌薄膜来制备高频超声相控阵传感器的方法。采用射频 (RF) 磁控溅射的方法制备出沿 c 轴晶向生长的多晶氧化锌薄膜。化学湿法刻蚀的结果显示不同种类的腐蚀液以及不同浓度的腐蚀液对腐蚀结果影响很大。首先试验了用质量百分比为 0.5 % 的盐酸湿法刻蚀氧化锌薄膜。但通过扫描电子显微镜得到的剖面图显示，此溶液刻蚀氧化锌薄膜呈现各向同性，产生严重的横向钻蚀，从而使得此方法无法加工出期望的氧化锌阵列。然后试验了质量百分比为 10 % 的氯化铵水溶液来湿法刻蚀氧化锌薄膜。结果显示，在室温 (20 °C) 下，该溶液刻蚀氧化锌薄膜呈现各项异性，纵向刻蚀速率约为 60 纳米/分钟。刻蚀时间必须精确控制，以免刻蚀不充分或者过刻蚀引起更多的横向钻蚀。研究发现，利用该技术制备工作于 300 兆赫兹的阵列的阵元中心间距最小可达一倍波长。试验中，我们成功制备了阵元中心间距为 13 微米的氧化锌薄膜阵列，横纵刻蚀比仅为 0.25。本文首次研究和讨论了采用质量百分比为 10 % 的氯化铵水溶液来刻蚀氧化锌薄膜的横向钻蚀问题。对照利用有限元方法计算得到的阵列传感器的电阻抗和串扰，利用网络分析仪测试的传感器特性参数与其基本一致。在谐振频率 300 兆赫兹处，电阻抗的实部约为 200 欧姆，最近邻阵元的串扰约为 -53 dB。

3. 研究和制备了基于新概念加工技术的高频且完全隔离的氧化锌薄膜阵列。

由于湿法刻蚀氧化锌薄膜工艺中存在着明显的横向钻蚀问题且刻蚀速率较慢,我们另外提出了一种全新的加工步骤。该方法采取先刻蚀硅衬底再淀积氧化锌的步骤,这样就避免了直接刻蚀氧化锌薄膜。刻蚀硅衬底技术已经非常成熟,不但刻蚀尺寸能有效控制而且刻蚀速率较快,可达4微米/分钟。该方法无需金属掩膜、步骤简单、加工效率高。基于这种新加工工艺可制备得到一种新型的阵列传感器结构。利用有限元方法仿真得到的声场结果显示,该新结构的传感器具有良好的性能。本文成功加工了工作于300兆赫兹的、氧化锌薄膜厚度为8微米的三明治阵列,阵元中心间距为13微米。利用网络分析仪得到的测试结果与有限元仿真得到的理论预测值进行了对比,结果显示电阻抗和串扰这两个参数的实测值和仿真值都基本一致。

4. 基于新概念加工技术的氧化锌薄膜阵列,研究和探索了减小氧化锌薄膜横向生长的解决途径。由于在硅衬底上氧化锌薄膜在纵向生长的同时还会横向生长,这种方法将会达到的最小阵元间距为两倍的波长,这就使要获得更小的阵元间距受到限制。为此,本文系统探讨了氧化锌薄膜的横向生长,并研究了减小该横向生长的镀膜工艺。我们提出了将溅射淀积12小时氧化锌薄膜的工艺分为4步完成,每一步只溅射淀积3个小时,且每进行一步,就将待溅射样片旋转90°放置。结果显示,氧化锌的横向生长可减少21%。

最后,本文提出了未来研究工作的方向,主要内容包括:消除氧化锌横向生长以达到更小的阵元中心间距;减小阵列传感器阵元的电阻抗以实现电学匹配。由于阵元的等效电阻抗很大,使用传统的微同轴电缆匹配方法已经无法满足宽带电学匹配的要求,比较有发展潜力的匹配方法是将微阵列与集成电路直接集成到一起。此外,未来的研究工作还需考虑电互联以测试和表征尺寸很小的阵列。制备声学匹配层和测试传感器的脉冲-回波信号也需要进一步研究。

关键词: 超声相控阵; 高频; 微机电系统; 有限元法仿真; 压电材料

中图分类号: TN 384

Acknowledgments

I would like to express my deep gratitude to all those who gave me the possibility to complete this thesis.

I wish to thank my supervisors, Prof. Bertrand Nongaillard and Prof. Yiping Huang, for their invaluable guidance and assistance in making this research possible. I am greatly indebted to them for helping me to overcome obstacles in the process of conducting the research.

I would like to thank my co-supervisor, Dr. Weijiang Xu, for the patient guidance, encouragement and advice he has provided throughout my time as his student. I have been extremely lucky to have a supervisor who cared so much about my life and study and created me the opportunity to study abroad.

I would like to thank my co-supervisors, Dr. Julien Carlier, who gave me a lot of professional suggestions on experiments, and Dr. Xinming Ji for his scientific instruction and constant support. I would also like to thank all my colleagues who helped me and were always very kind to me, Jiaming Gao, Xianmei Wu, Frédéric Faese, Assane NDiaguene and Nadine Saad. Thanks also to Prof. Jia Zhou, Prof. Zongming Bao, Prof. Minhang Bao, Prof. Quan Liu, for their professional advices.

Great thanks are given to the reviewers, Gilles DESPAUX, Professor from University of Montpellier 2 and Sylvain BALLANDRAS, Director of research from Femto-St Lab, for their great contributions to review this dissertation.

I would also like to express special appreciations to my parents. Their deep love and full support are always the power of my success.

Regarding the study of high-frequency ultrasonic transducer arrays, the authors are grateful to Mr. Samuel QUESTE from Femto-St Lab, Mr. Christophe BOYAVAL and Prof. Denis REMIENS, for the technical supports and also to Fudan University, for its financial support. Finally, I would like to thank French Embassy, not only for providing the funding which allowed me to undertake this research, but also for giving me the opportunity to meet so many interesting people.

At last, I dedicate this dissertation to my husband, Mr. Gang Han. His complete understanding, strongest support, continuous encouragement and endless love gave me the courage and confidence to conquer the difficulties in my life and research career.

General introduction of the thesis

With the rapid development of microelectronics, micromechanics and piezoelectric material technologies, high-frequency ultrasonic phased array transducers are highlighted again and again in real-time and high resolution imaging. However, many difficulties will arise in the development of array imaging systems with an operating frequency of above 100 MHz. These difficulties include high-frequency phase-delay system, electrical matching problem, mechanical matching problem, and especially the fabrication of high-frequency array transducers which play a critical role in ultrasonic phased array imaging systems. Several researchers have fabricated kerfless arrays above 100 MHz. These arrays suffer from a severe crosstalk which would degrade imaging quality.

The objective of this thesis focuses on the development of kerfed array transducers with a central frequency of above 100 MHz. Two aspects are mainly investigated. The first one is the finite element numerical simulations for the optimized design. The second one is the fabrication using different experimental processes based on micro electromechanical system (MEMS) technologies.

In the section of numerical studies, a commercial finite element tool, COMSOL3.5a, is employed which benefits from well-performed coupling capabilities in combining fluidic model, solid model and electrical model. In piezoelectric backing array transducers, the effects of pitch size, kerf filler and kerf depth on the acoustic field, electrical impedance and crosstalk are investigated. And systematic simulations are carried out for a designed buffered transducer array. Several conclusions arrive based on these simulations.

Firstly, in order to decrease the noise from reflectance waves in backing, a rough surface whose dimension is around 1.0λ should be considered to scatter a majority of incident waves.

Secondly, when the pitch is more than 1.5λ , the grating lobes get close to the main lobe, which will lead the array transducer hardly useful. Thus, the pitch size

should be limited to smaller than 1.5λ . In addition, when kerf width increases while pitch size keeps the same, sensitivity will decrease while directivity pattern keeps almost the same.

Thirdly, 2-D FEM model is more accurate to calculate the electrical impedance for piezoelectric array elements than KLM model which is usually used in 1-D models.

Fourthly, the no filled array has better beam performances than the filled array. Moreover, kerf depth plays an important role in acoustic field and crosstalk of array transducers. Half-cut array is demonstrated to be a promising candidate for micromachining due to much smaller depth/width aspect ratio and acceptable transducer performances.

Finally, comprehensive studies are made for the backing-layer and buffered-layer arrays. Generally, the backing one serves a higher sensitivity. Nevertheless, the buffered one has a less constraint on pitch size, and it brings possibilities in the fabrication.

In the section of experimental fabrication and characterization, MEMS based technologies are applied to obtain high-frequency array elements. In conclusion, three approaches are investigated.

Firstly, different etching methods, such as ICP RIE, FIB, and laser, are studied to obtain the limit in the feasible fabrication of 36° /Y-cut single crystal LiNbO_3 arrays. 36° /Y-cut single crystal LiNbO_3 have been patterned by means of ICP RIE micromachining to create ultrasonic arrays resonating in the frequency range of 100-200 MHz. For a realized LiNbO_3 kerfed array with a pitch of $42 \mu\text{m}$ and thickness of $16 \mu\text{m}$, the electrical impedance and crosstalk are evaluated using a network analyzer. The impedance magnitude is around $1 \text{ k}\Omega$ at the resonant frequency of 230 MHz. The crosstalk of the adjacent element is -46 dB. They agree well with the theoretical predictions.

Secondly, a novel wet etching method with very small lateral undercut is presented to fabricate thick-film ZnO-based ultrasound transducer arrays. The wet-chemical etchant is NH_4Cl aqueous solution with a concentration of 10 wt% and the etching rate is 60 nm/min at 20°C . The duration should be controlled precisely to

avoid over etching as well as non-sufficient etching. This technique results in a possibility to obtain a pitch of a λ at 300 MHz. A 13- μm -pitch ZnO array is achieved due to a small ratio (0.25) of lateral etching to vertical etching. This ratio of small lateral etching from NH_4Cl aqueous solution is studied and discussed. Finite element method is employed to calculate electrical impedance, crosstalk and focusing/steering acoustic field performances of the transducer. The characteristics of the transducer are measured and compared to the theoretical predictions. The real part of the electrical impedance is around 200 Ω at the resonant frequency of 300 MHz. The adjacent crosstalk is about -53 dB.

Thirdly, we propose a novel method using silicon micromachining integrated with deposition of piezoelectric thick films to fabricate high-frequency ZnO-based linear array transducers. Piezoelectric elements are formed by sputtering thick-film ZnO onto etched features of a silicon substrate so that the difficult etching process for ZnO films is avoided by etching silicon. This integration makes it simple and efficient to define the features in an array instead of etching ZnO films. Finite element method is employed to simulate the wave propagation in water based on this new transducer configuration. The acoustic field results indicate this configuration has an acceptable performance. A 13- μm -pitch ZnO sandwich array is achieved with a thickness of 8 μm for 300 MHz. The characteristics of the transducer are measured and compared to the theoretical predictions (finite element results) including electrical impedance and crosstalk. On the other hand, the lateral growth of ZnO films is studied. A 4-step method with rotation 90° between each step of sputtering is investigated. The lateral growth of ZnO has been decreased by 21% by using the improved approach.

Chapter 1: Introduction

1.1 Ultrasonic imaging and its development

1.1.1 Development of ultrasonic phased arrays

Beginning in the late 1940's, ultrasound was first used in medical diagnostic applications ^[1]. When commercial equipment became available in the 1960s, radiologists and obstetricians began to fully use diagnostic ultrasounds ^[2]. Since the 1960s, diagnostic ultrasound technology has continued to develop and become more available to doctors with the creation of specialized transducers and real-time imaging. At first, the ultrasonic transducer had single element and the detected range was limited along the axial direction. The scanner required a mechanical system. This resulted in low efficiency.

In the 1960s, researchers began developing ultrasonic phased array systems that utilized multiple point source transducers that were pulsed so as to direct sound beams by means of these controlled interference patterns. In the early 1970s, commercial phased array systems for medical diagnostic use first appeared, using steered beams to create cross-sectional images of the human body. Initially, the use of ultrasonic phased array systems was largely confined to the medical field (for example, for acoustic imaging of the human body and guidance of needles ^[3,4]), aided by the fact that the predictable composition and structure of the human body make instrument design and image interpretation relatively straightforward. Industrial applications, on the other hand, represent a much greater challenge because of the widely varying acoustic properties of metals, composites, ceramics, plastics, and fiberglass, as well as the enormous variety of thicknesses and geometries encountered across the scope of industrial testing. The early industrial phased array system, introduced in the 1980s, was extremely large, and required data transfer to a computer in order to do the processing and image presentation. These systems were most typically used for

in-service power generation inspections. In large part, this technology was pushed heavily in the nuclear market, where critical assessment more greatly allows use of cutting edge technology for improving probability of detection. Other early applications involved large forged shafts and low pressure turbine components. The industrial applications of phased arrays for non-destructive testing (NDT) have been widely reported ^[5,6] since the 1980s.

Portable, battery-powered phased array instruments for industrial use appeared in the 1990s. To create the multi-channel configurations necessary for beam steering, analogous circuit designs require higher power and more space than digital circuit. With the rapid development of inexpensive embedded microprocessors, the digital circuit designs replaced analogous circuit gradually and enabled more rapid development of the next generation phased array equipment. In addition, the availability of low power electronic components, better power-saving architectures, and industrial widely used surface mount board design led to miniaturization of this advanced technology. This resulted in phased array tools which allowed electronic setup, data processing, display and analysis all within a portable device, and so the doors were opened to more widespread use across the industrial sector. This in turn drove the ability to specify standard phased array probes for common applications. Generally, with dramatic progress of piezoelectric material technologies, micromechanics, microelectronics, and advanced computers (including calculation ability and simulation softwares), ultrasonic phased array technologies have been developed rapidly in the past 20 years.

1.1.2 Ultrasonic imaging

Ultrasound refers to mechanical waves whose vibrations are above the upper limit of the human audible range (above 20 kHz). Ultrasound is used in many different fields, typically to penetrate a medium and measure the reflection signature or supply focused energy. The reflection signature can reveal details about the inner structure of the medium, a property also used by animals such as bats for hunting. The most well-known application of ultrasound is its use in sonography to produce pictures of

fetuses in the human womb. There are a vast number of other applications as well [7]. Ultrasonic imaging is known as a safe and portable modality. It has many benefits as follows.

- (1) Most ultrasound scanning is noninvasive (no needles or injections) and is usually painless.
- (2) Ultrasound is widely available, easy-to-use and less expensive than other imaging methods.
- (3) Ultrasound imaging does not use any ionizing radiation.
- (4) Ultrasound scanning gives a clear picture of soft tissues that do not show up well on x-ray images.
- (5) Ultrasound is the preferred imaging modality for the diagnosis and monitoring of pregnant women and their unborn babies.
- (6) Ultrasound provides real-time imaging, making it a good tool for guiding minimally invasive procedures such as needle biopsies and needle aspiration.
- (7) For standard diagnostic pulsed ultrasound there are no known harmful effects on humans.
- (8) Ultrasound is a desired method to image the subsurface of the materials.
- (9) Ultrasonic imaging affords a way to obtain the elastic constant and viscoelastic coefficient.
- (10) Ultrasonic pulses have a relatively slow velocity of propagation (1500 m/s) in the body compared to x-rays (3×10^8 m/s). This means that electronic circuitry can distinguish reflections, in pulse mode operation, at different depths in the body by the time taken for the round trip for an echo, which is not possible with x-rays.

On the other hand, it has limitations including:

- (1) Ultrasound waves are disrupted by air or gas; therefore ultrasound is not an ideal imaging technique for the bowel or organs obscured by the bowel. In most cases, barium exams, computed tomography (CT) scanning, and magnetic resonance imaging (MRI) are the methods of choice in this setting.
- (2) Ultrasound has difficulty penetrating bone and therefore can only see the outer surface of bony structures and not what lies within. For visualizing internal

structure of bones or certain joints, other imaging modalities such as MRI are typically used.

- (3) The penetration ability limits the application of ultrasound. Although high frequency ultrasound supplies high resolution, attenuation in medium arises greatly with the increase of working frequency. Most ultrasonic transducers require coupling materials to enhance transmission efficiency. It is difficult to use ultrasound in non-destructive evaluation (NDE) in some particular conditions. For example, in high temperature circumstances, many coupling materials would be evaporated.

Based on the above discussion, ultrasonic imaging is a desired modality for medical diagnosis and industrial NDE.

In recent years, 3-Dimensional (3-D) ultrasonic imaging gains more and more attention. As far as 3-D ultrasonic imaging is concerned, 3-D resolution is required. Some ultrasonic transducer developers have implemented 3-D imaging using 2-D arrays ^[8,9,10,11]. 3-D ultrasonic imaging provides important clinical benefits compared to traditional 2-D ultrasonic imaging. For example, 3-D ultrasound imaging is able to acquire and display volumetric data; 2-D cross-sectional scans can be obtained at arbitrary orientations relative to the transducer arrays. However, 3-D ultrasonic imaging is substantially more complex than 2-D imaging. 2-D arrays are needed normally for volumetric imaging. Spatial sampling of a 2-D transducer aperture requires that the element pitch in both dimensions be less than about one-half the wavelength of ultrasound in tissue ^[12]. This requirement results in that 2-D arrays can have a very large number of elements. For comparison, 1-D arrays in current commercial systems commonly have 128 elements. A 128×128-element 2-D array has 16,384 elements, which poses significant data processing and packaging challenges. On the other hand, because 2-D array elements have limited sizes in both dimensions, they are usually much smaller than comparable 1-D array elements. Their smaller size means they have higher electrical impedance ^[13]. Conventional 1-D arrays can be connected to an external imaging system by matching to 50-Ω micro-coaxial cables. However, because of the high equivalent impedance of the 2-D array elements,

broadband electrical matching is difficult. In summary, these difficulties, including the complex system, the great mismatch in electrical impedance, and the fabrication processes^[14], have limited the development of 2-D arrays.

1.2 High-frequency ultrasonic imaging

1.2.1 Imaging resolution

As the spatial resolution is anti-proportional to the frequency of ultrasound, higher frequency ultrasound enables higher resolution imaging. Fig.1.2.1 shows the relationship between ultrasound frequency and resolution in clinical settings. Several MHz ultrasound is used in conventional echography and echocardiography; approximately 10 MHz ultrasound is used in carotid scan and some surface organs such as thyroid scan, breast scan and muscle scans. 20-45 MHz ultrasound is used for intravascular ultrasound (IVUS). Ultrasound microscope uses ultrasonic frequency higher than 100 MHz and it has achieved 15 micron resolution (equivalent to 40 times magnification in optical microscopy). Higher frequency such as GHz range ultrasound enables imaging of a single cell.

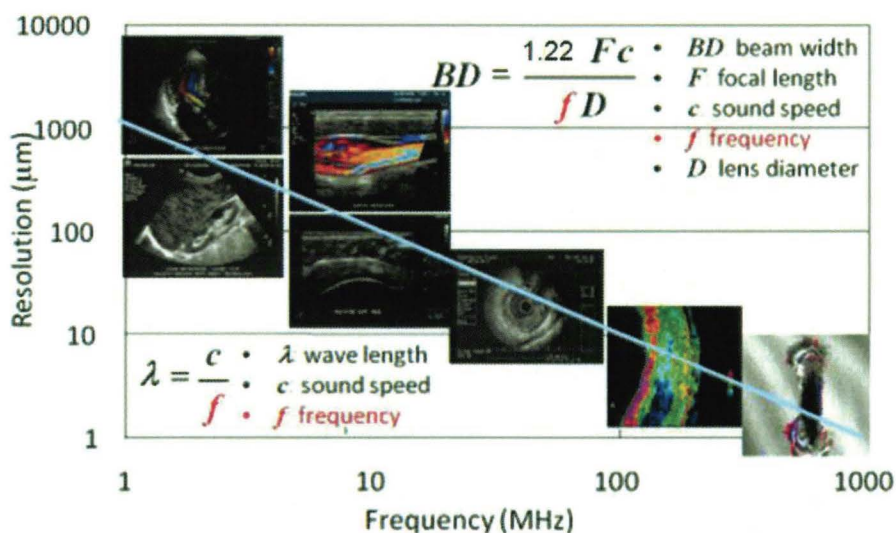


Figure 1.2.1: Relationship between ultrasound frequency and resolution in clinical settings^[15]

1.2.2 Acoustic microscopy

Acoustic imaging is mainly applied in three domains—underwater exploration (sonar system), biomedical diagnostics and therapy, and material non-destructive evaluation (NDE). The imaging resolution depends on the working frequency of the transducer. The working frequency is conditioned by the penetrating capacity of the acoustic wave in the exploited medium. Thus, we can choose a specialized operating frequency according to the application objective and correspondingly choose the acoustic transducers and the imaging systems.

A sonar system has usually an operating frequency of several tens of Hz to a few hundred of kHz. An ultrasonic system in NDE covers a frequency range from several MHz to tens of MHz permitting to obtain an imaging resolution of mm or even sub-mm. A traditional ultrasonic medical scanner works in the similar frequency range.

For biomedical applications, ultrasonic scanners are often referred as “Ultrasonic Backscatter Microscope” (UBM) which uses a transducer with resonant frequency between 30 and 100 MHz ^[16]. Their utilities include: the eye imaging in diagnostic such as glaucoma, ocular tumors, assisting refractive surgery ^[17]; skin imaging ^[18]; catheter-based intravascular imaging to characterize atherosclerotic plaque and to guide stent placement and angioplastic procedures ^[19]; intra-articular imaging; Doppler blood flow mapping; and small animal imaging such as *in-vivo* imaging of mouse embryonic development for evaluating the efficacy of drugs and gene therapy ^[20].

Another well-developed acoustic imaging system, working in very high frequency ranging from 100 MHz to GHz, is the Scanning Acoustic Microscope (SAM) ^[21]. It provides acoustic imaging with a spatial resolution in the order of μm or sub- μm , comparable to that of the optical instrument. Based on the fundamental difference between a SAM (based on acoustic waves reflection) and an optical microscope (based on optical waves scattering), the SAM is a unique tool to exploit quantitatively, on a microscopic scale, elasticity properties of materials ^[22] such as

biological tissues and cells. It has the capacity of observing into the subsurface, to measure local values of acoustic wave velocity, attenuation, and other mechanical properties such as anisotropic, viscoelastic, inhomogeneous, heterogeneous properties.

In material characterization, SAM is mainly used in three fields. The first is to determine cracks and patterns of mechanical stress fields, the piezoelectric, photoelectric, and superconducting properties. The second is to detect defects like adhesion failure, exfoliation, alien inclusions, layer thickness changes in coatings and multi-layer structures. The third is to study dynamic phenomena associated with reconstruction of the material properties induced by varying physical factors (pressure, temperature, radiation) and by chemical and pharmacological impacts, etc.

In the biomedical application, SAM is employed not only for tissue characterization ^[23], but also used for molecular imaging and cell visualization ^[24] to investigate cellular elastic properties ^[25], motility ^[26], tumor type classification ^[27], biological phenomenon such as apoptosis ^[28], etc.

Generally, in acoustic imaging, there are three types of acoustic transducers. Each operates with their associated imaging system.

Single element transducers are the most often used acoustic transducers. Either UBM or SAM uses a single element transducer. They operate in transmission or reflection mode. Their excitation and reception electronics is very simple. The imaging is performed by mechanically scanning the transducer. To obtain high imaging resolution, the acoustic beam is often focused and a transducer with a working frequency up to several GHz is adopted. But single element transducers have two great drawbacks. The first one is that the single element transducer has fixed focal distance where the spatial resolution is best only within the depth of focus and degrades rapidly beyond the focal point. The second is that the mechanical motion of the transducer limits the imaging frame rate and degrades the imaging quality.

An ultrasonic phased array transducer is composed of a number of individual piezoelectric elements, arranged in a linear or 2-Dimensional (2-D) array, working in the same way as is operated in a radar system. Each element is driven by an electric

pulse with a relative delay to steer and focus a transmitting ultrasonic beam in an inspection medium. An image of the object located in the scanned plane can be build up by displaying the reflected pulse waves (returning echoes received by the elements). The phased array system permits to obtain fast image frame rate and perform *in-vivo* real-time imaging. But it needs sophisticated electronics which is often cumbersome and expensive. Because of the difficulties in transducer technology and electronics, actually, there is no array system working at a frequency more than 80 MHz.

The third type of the acoustic imaging system is the scanning near field acoustic microscope ^[29]. It combines the ultrasonic detection technology with scanning near-field microscopy (such as scanning electron microscopes-SEM, scanning tunneling microscopes-STM, and atomic force microscopes-AFM) and obtains an image resolution superior to the diffraction limit, or the so-called "super resolution", by using an aperture or tip that is far smaller than the wavelength. Such kind of microscope often needs sample preparation and electrical conduction that is not convenient for penetrating and non-invasive imaging of living cells.

1.2.3 Development of high-frequency ultrasonic phased arrays

For real time and high resolution acoustic imaging, it is very desirable that the high frequency acoustic transducer can also adopt phased array technology as is used in traditional "low frequency" array scanner. Theoretically, the development of high-frequency arrays means the proportional miniaturization in geometrical sizes of transducer elements. But many technical difficulties will arise in their manufacture using conventional materials and fabrication procedures. There are several technological lock-in preventing from developing transducer arrays with frequency range above 50 MHz. Firstly, there exists no fabrication technique permitting to cut the piezoelectric material into so small elements (usually with a pitch of a half wavelength in propagation medium, with thickness of a half wavelength in transducer material, and with very small kerfs). Secondly, with high frequency excitation, the step of phase delay must be controlled in high resolution and a high sampling rate is

also necessary for reception signals. At present, these are very difficult (if not impossible) to be realized with high speed electronic devices. Thirdly, the small transducer elements will cause electrical impedance mismatch. This will degrade the electroacoustic coupling efficiency and sensibility.

The current progress in microelectronics and micro electromechanical system (MEMS) technology brings new possibilities in the development of high-frequency array transducer. For examples, the MEMS based capacitive micro-machined ultrasound transducers (cMUTs) ^[30] and piezoelectric micro-machined ultrasound transducers (pMUTs) ^[31] have been realized at frequency in the order of MHz and tens MHz. These devices have the advantage of being fabricated with integrated electronics, which will reduce the bulky and complex instrumentation and is economically inexpensive. There is a tendency that cMUTs would replace the traditional piezoelectric array transducer technique. But the working frequency of cMUTs hasn't reached to 100 MHz. Other new theories have been proposed such as "limited-diffraction beams" ^[32], "image segmentation" ^[33], permitting new concepts for acoustic imaging system.

In summary, high-frequency ultrasonic phased array transducers is a desired and novel candidate in real time and high resolution imaging despite of many difficulties in its development. This dissertation focuses on the development of MEMS based high frequency ultrasonic linear arrays and will present our efforts and investigations.

1.3 Theory of ultrasonic phased array

1.3.1 Principle of ultrasonic phased array

As stated previously, ultrasonic phased arrays (UPA) benefit from fast electronic scanning. The UPA probe consists of many small elements, each of which can be pulsed separately. By varying the timing, a pattern of constructive interference is set up. That results in a beam at a set angle. In other words, the beam can be steered electronically. The beam is swept like a search-light through the tissue or object being

examined, and the data from multiple beams are put together to make a visual image showing a slice through the object. For example, in Fig.1.3.1, the element on the right is pulsed first, and emits a pressure wave that spreads out like a ripple on a pond (largest semicircle). The second to right element is pulsed next, and emits a ripple that is slightly smaller than the first because it was started later. The process continues down the line until all the elements have been pulsed. The multiple waves add up to one single wave front travelling at a set angle. In other words, the beam angle can be set just by programming the time delays.

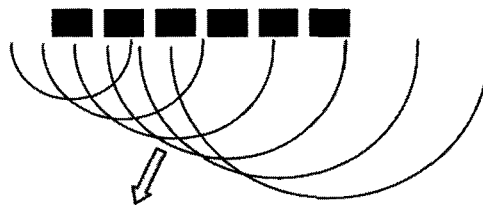


Figure 1.3.1: Principle of ultrasonic phased array

The small elements may be arranged in a strip (linear array), a ring (annular array), a circular matrix (circular array), or a more complex shape (2-D array or 3-D array). Because phasing technology permits acoustic beam shaping and steering through dynamically programmed control, it is possible for a linear array to generate a vast number of different ultrasonic beam profiles from a single probe assembly as shown in Fig.1.3.2. The detailed calculation method is attached in Annex 1.

Compared with conventional single element ultrasonic transducer, the benefits of phased array technology come from its ability to use multiple elements to steer and focus beams.

Beam steering, commonly referred to as sectorial scanning, can be used for mapping components at appropriate angles, which can greatly simplify the inspection of components with complex geometry. The ability of the transducer array to sweep the beam without moving the probe also aids inspection of such components in situations where there is limited access for mechanical scanning. Sectorial scanning is also typically used for weld inspection. The ability to test welds with multiple angles

from a single probe greatly increases the probability of detection of anomalies.

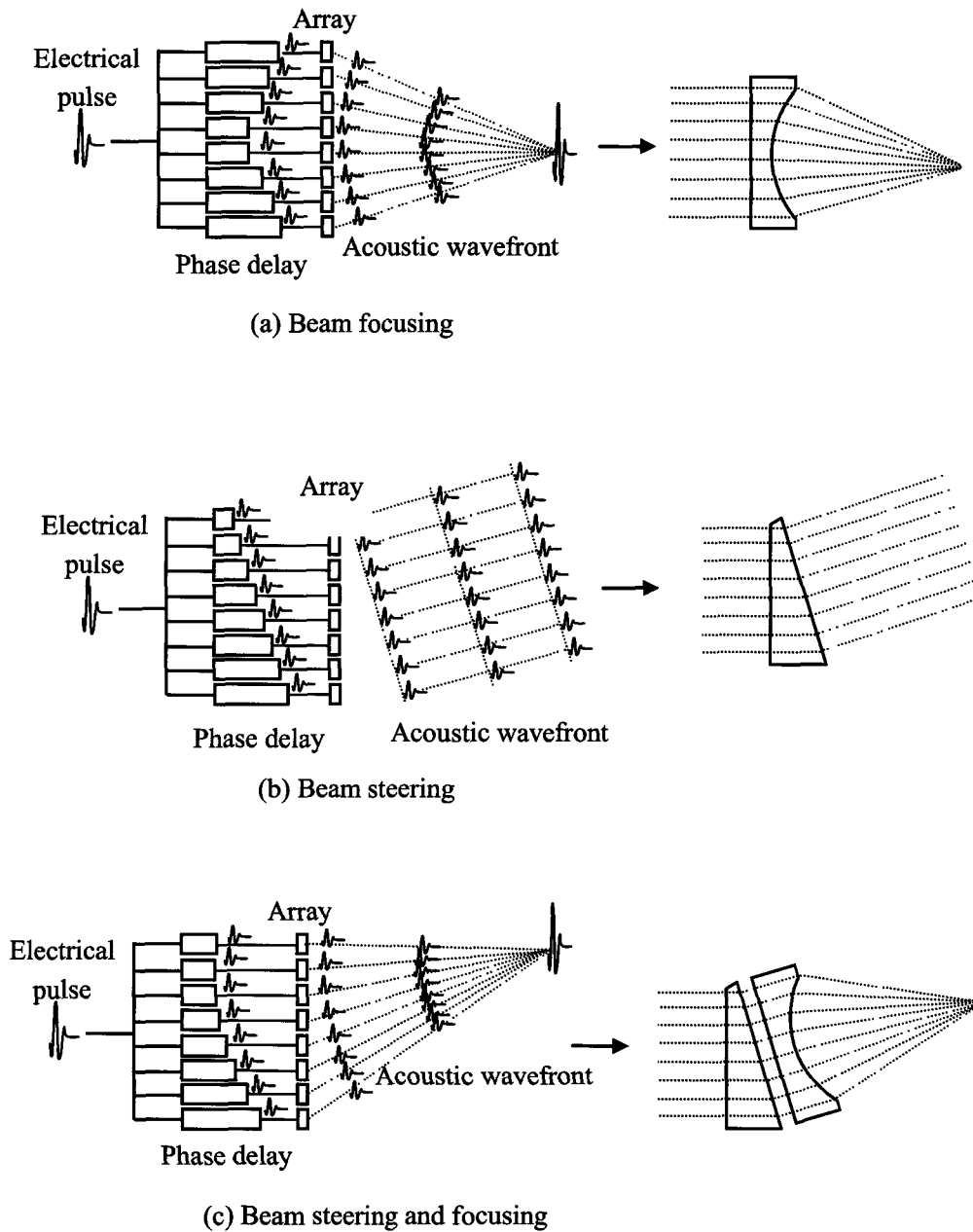


Figure 1.3.2: Different beam profiles in a linear ultrasonic phased array: (a) Focusing beam is like a focal lens (b) Steering beam is like a prism (c) Steering and focusing beam is like a group of a prism and a focal lens

Electronic focusing optimizes the beam shape and size at the expected defect location, which further optimizes the probability of detection. The ability to focus at multiple depths supports sizing critical defects for volumetric inspections. Focusing

can significantly improve signal-to-noise ratio in challenging applications. Moreover, electronic focusing and scanning across many groups of elements allows for C-Scan images to be produced very rapidly.

In general, UPA technology offers the following benefits. It enables the generation of an ultrasonic beam whose parameters such as angle, focal distance, and focal point size can be controlled through software. It also enables scanning inspection by an electronic system instead of a mechanical system. The electronic scanning speed is much faster than a conventional mechanical system. A phased focusing beam improves signal-to-noise ratio, and also expands the detection range regardless of the defect location.

As shown in Fig.1.3.3, the principle of UPA imaging is similar to that of radar. A group of elements are switched and excited by different phased electronic pulses. The generated acoustic pulses propagate through an object and reflect at various discontinuities throughout the path of the beam. The echo signals are received by the transducers and superposed by the phased array unit. After superposition these echo signals are transferred into one signal. At last, this signal is acquired by the acquisition unit.

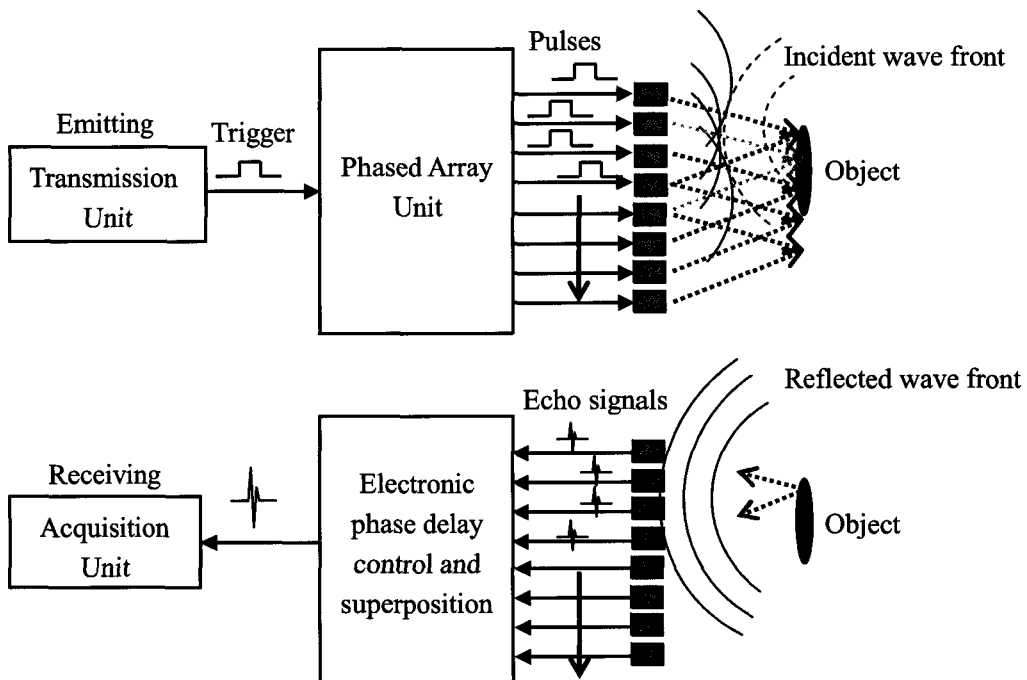


Figure 1.3.3: Overall principle of ultrasonic phased array (UPA) imaging system

A more detailed description about the imaging principle is illustrated in Fig.1.3.4. When the transmitted pulses arrive at the boundaries of the inspected object, they will be reflected by each interface. The first reflected pulse (such as A) arrives at the array elements firstly. The acoustic pulse is converted into electronic pulses by the transducer elements. After delayed and superposed into one signal (such as A') by the electronic phase delay control and superposition unit, the electronic pulse can be used to reconstruct images through signal processing system. Similarly, the latter pulse B' can be obtained from reflected pulse B. Because the delay time of each element and steering angle are set by the phased array unit, the image reconstruction can be realized using a symmetrical system. However, if there is a grating lobe, the undesired echoes will be acquired by the receiving unit from unexpected direction, resulting in false signals or superimposed images and degrading imaging resolution.

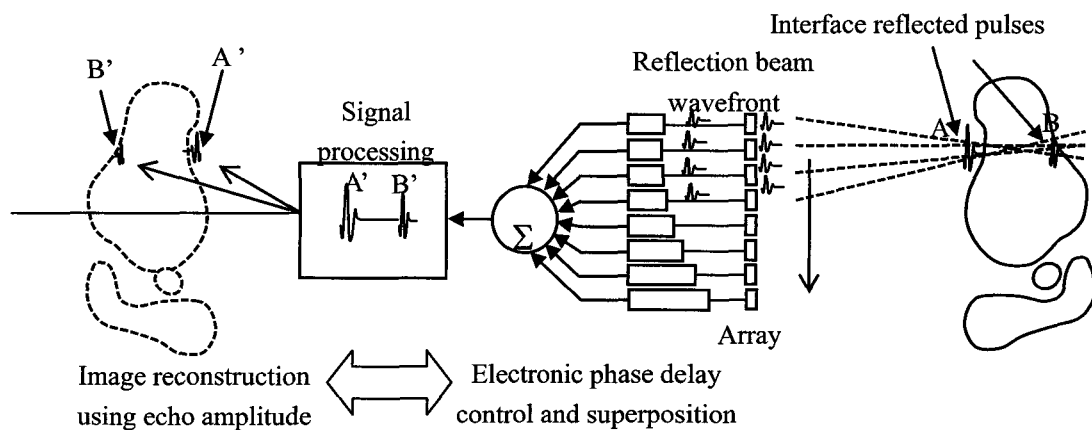


Figure 1.3.4: Schematic of acoustic imaging principle with ultrasonic phased array

1.3.2 Some particularities of high frequency arrays

1.3.2.1 Transducer material and manufacture

Piezoelectric composites (such as polyvinylidene difluoride (PVDF)) or piezoelectric ceramics (such as lead zirconate titanate (PZT)) are always chosen as the active materials in conventional low frequency arrays due to their wide bandwidths. The bonding, lapping and dicing techniques are applied when these composites are

used. However, these techniques are not suitable to fabricate high frequency arrays. The small scale patterning in the piezoelectric arrays is required for high frequency devices, while these techniques cannot be used to obtain such small scales. The maximum central frequency of transducer elements is actually limited to 20~30 MHz.

For high frequency transducer, piezoelectric crystals are chosen as the active materials using micro electromechanical system (MEMS) techniques to fabricate piezoelectric arrays. Two ideal candidate materials are ZnO and LiNbO₃ which has, respectively, electromechanical coupling coefficient about $k_t = 0.27$ and $k_t = 0.49$. ZnO thin film can be obtained using sputtering technique and the sputtering technique is relatively simple for thin film realization ^[34,35], so we choose ZnO thin film technology to fabricate high frequency array transducers. LiNbO₃ single crystal (36°/Y-cut) has the best electromechanical coupling coefficient $k_t = 0.49$ for generating compression waves, but, hitherto, it can only be manufactured by bonding and thinning techniques. In our lab, the thickness of LiNbO₃ single crystal can be obtained to as small as tens of micrometers over a 6 mm×6 mm area. For its best electromechanical coupling efficiency and the manufacturing techniques we have proposed, LiNbO₃ single crystal is also considered for the development of our high frequency array transducer. Another important characteristic should be mentioned about ZnO and LiNbO₃. It is about their electrical impedance which is critical for electrical matching. For the electrical impedance of ZnO, the imaginary part is about 7 times of the real part. For the electrical impedance of LiNbO₃, the imaginary part is almost the same as the real part.

1.3.2.2 Mechanical matching problem

To transmit a maximum of energy into the transmission medium (water in general), a mechanical matching layer should be deposited onto the surface of the transducer elements. This layer serves as, at the same time, the protection layer of the active elements. The existence of such a layer will produce the so-called “crosstalk” between neighboring elements which will degrade the spatial resolution ^[36]. Theoretically, insertion of a mechanically “very soft” or “very hard” medium between

elements could be a solution to the problem. The material choice for mechanical matching and the insertion procedure by MEMS technology have to be studied.

High frequency piezoelectric elements are very thin in thickness (in micro scale) and have to be adhered to a solid buffer. When excited, the wave in the buffer should be suppressed to eliminate parasitic echoes. Two techniques can be considered. One is the use of a backing material to absorb this wave. This technique is usually employed for low frequency transducers. Another is the use of an active charge with a second piezoelectric layer inserted between the buffer and the source layer. This second layer is excited in such a way that its own excitation will compensate or cancel the energy transmitted from the source layer to the buffer. This method is much interesting when the active electronic circuits can be integrated with the transducer as there will be less electrical perturbation caused by using transmission line in high frequency circuitry.

1.3.2.3 Electrical matching problem

In the design of ultrasonic transducers, in order to transfer as much energy as possible from the signal source to the active element, electrical matching is necessary.

The term impedance is used for the resistance of a system to an energy source. For constant signals, this resistance can also be constant. For varying signals, it usually changes with frequency. Electrical impedance, like electrical resistance, is measured in ohms. In general, impedance has a complex value, which means that loads generally have a resistance to the source that is in phase with a sinusoidal source signal and reactance that is out of phase with a sinusoidal source signal. The total impedance (symbol: Z) is the vector sum of the resistance (symbol: R ; a real number) and the reactance (symbol: X ; an imaginary number). In simple cases, such as low-frequency or direct-current power transmission, the reactance is negligible or zero and the impedance can be considered a pure resistance, expressed as a real number. In our transducer design, we will consider the general case because the resistance and reactance are both significant.

In electronic systems, electrical matching (also called as impedance matching) is the practice of designing the input impedance of an electrical load or the output

impedance of its corresponding signal source in order to maximize the power transfer and minimize reflections from the load. In the case of a complex source impedance Z_S and load impedance Z_L , matching is obtained when:

$$Z_S = *Z_L,$$

where * indicates the complex conjugate.

In high frequency, the radiation resistance of the piezoelectric transducer at the resonant frequency is usually much higher than the 50 Ω output impedance of RF signal generators, making impedance matching very difficult. Some researchers designed the input impedance of transducers to close to 50 Ω by using proper transducer size [37]. C. Lee's group developed an off-resonant frequency method to match the input impedance of acoustic transducers [38]. Instead of matching transducer to standard impedance, our idea is to design the drive electronics unit to have internal impedance matched to that of array elements.

1.3.2.4 Numerical Simulation

Simulation has played an important role in all engineering disciplines [39]. In electrical engineering SPICE has been used for accurate simulation of linear and non-linear electrical circuits. In mechanical engineering finite element and finite difference programs are standard tools for evaluating the performance and reliability of mechanical structures, materials, and buildings. Often very accurate results can be obtained, which can save many iterations in prototype development.

Designing better array transducers is the critical issue for further improving quality of ultrasonic imaging. To obtain the optimized design of high frequency arrays, numerical modeling and simulation are necessary, because conducting the experiments over a wide range of geometries and dimensions is quite time consuming. The high cost of phased array transducer is also a factor that motivates the use of models for simulation of the experimental procedures. For this purpose, it is necessary to gain better fundamental understanding on the transducer operations. Many issues in array design—such as crosstalk, electrical impedance, and directivity pattern—cannot be accurately studied using analytical method due to the complexity of the Partial

Differential Equations (PDE) involved. In such cases, numerical methods such as Finite Difference Time Domain (FDTD) method can be suitably used to solve for the displacement and stress values in the solid domain of interest ^[40]. Finite Element Method (FEM) is also a very appropriate way to gain more detailed information ^[41,42].

In this thesis, the FEM modeling is applied and takes into account the following factors: piezoelectric material performance, electromechanical conversion, crosstalk, acoustic matching, electrical matching network, pulse-echo signal and bandwidth. All parameters will be optimized in a global system modeling.

1.4 Different techniques for the fabrication of ultrasonic arrays

Conventional ultrasonic imaging systems typically use frequencies from 2 to 15 MHz. To improve spatial resolution, one obvious strategy would be to increase the frequency. High and ultrahigh frequency (several hundred MHz to GHz) ultrasonic microscope has been developed. However, it uses single element transducer and for the scanning it needs movements provided by a mechanical system. This results in a low efficiency. Multiple probe elements can produce a steerable, tightly focused, high-resolution beam. Thus, array technology is widely used in ultrasonic applications due to its capability for electronically focusing and steering an ultrasound beam at different depths and angles without moving the transducer mechanically. In developing high frequency ultrasonic transducer arrays, however, the patterning of small-scale features within the array is a great challenge. For example, with thickness resonance mode, a transducer operating at 100 MHz frequency has a thickness of about 30 μm ($\lambda_{\text{piezo}}/2$), while the pitch of array elements should be inferior to 10 μm to avoid the beam grating lobes when wave propagates in biological media (typically the pitch is 7.5 μm equaling to half wavelength in water). This needs the realization of a very high depth/width aspect ratio (about 15) kerf in a piezo-active material, which is actually a great challenge. A number of techniques are summarized as follows for the fabrication of ultrasonic arrays. Generally, they are divided into four types.

1.4.1 Conventional arrays fabrication technologies

Low frequency arrays typically use the “dice-and-fill” technique to separate array elements, whereby elements are mechanically cut from a plate of piezoelectric material and backfilled with polymer filler. Two research/industrial collaborative studies in France have applied this technique to build 20 MHz arrays [43,44]. Their results were very promising. K. K. Shung’s group has extended this method to develop a 35 MHz linear array using 2-2 composite elements [45]. The composite was fabricated using a 13 μm Asahi blade. The composite dicing pitch was 25 μm . After dicing, the composite was lapped to a final thickness of 50 μm . A scanning electron microscope (SEM) image of a composite cross-section is shown in Fig.1.4.1. 64 elements were spaced at a 50 μm pitch and the kerf width was 14 μm on average.

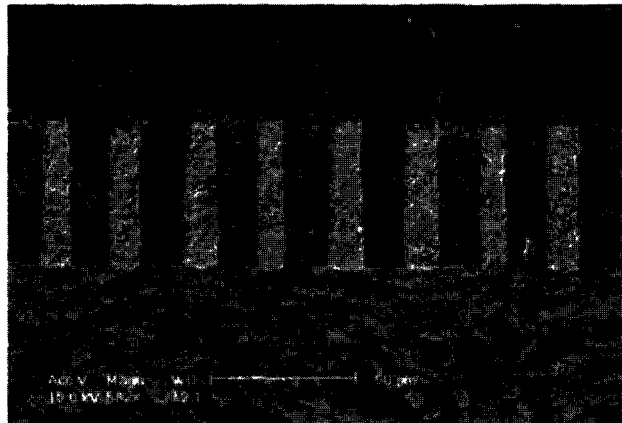


Figure 1.4.1: SEM image of a finished 2-2 composite [45]. The lighter portions of this image are the piezoceramic posts whereas the darker portions are the kerf filler. The marbled section under the composite is a silver epoxy backing layer.

Interdigital pair bonding (IPB) is a modification of the “dice-and-fill” process that allows one to use wider and more robust dicing saw blades [46]. It has the capacity to increase the ceramic volume fraction and decrease the kerf width of the epoxy phase for high-frequency composites. This idea firstly appeared in 1993 [47]. S. Foster’s group prepared high-frequency 1-3 composites according to the IPB procedure of Fig.1.4.2 [47]. The first step [Fig. 1.4.2a] involves dicing identical parallel

grooves with $W_c < W_p$ (W_c and W_p are defined in Fig. 1.4.2b). Two pieces of ceramic sheets processed in Fig. 1.4.2a are then impregnated with epoxy and interdigitally inserted [Fig. 1.4.2b]. The top surface of this sandwich is lapped away to reveal the 2-2 composite as shown in Fig. 1.4.2c. At this point, the ceramic volume fraction has been doubled, and the kerf width of the epoxy is equal to $(W_p - W_c)/2$. The 2-2 composite shown in Fig. 1.4.2c is subsequently processed into 1-3 composite by repeating the processes of Fig. 1.4.2a–c at right angles to the original 2-2 cutting direction. These steps are illustrated in Fig. 1.4.2d–f. A dicing saw blade with a thickness of 40 μm was used for the fabrication. The index distance perpendicular to the cutting grooves was set at 80 μm . The resultant width of cutting grooves was 44 μm , and the width of the ceramic strips was 36 μm . Therefore, the average epoxy kerf width was 4 μm . The ceramic volume fraction for the composite was 81%.

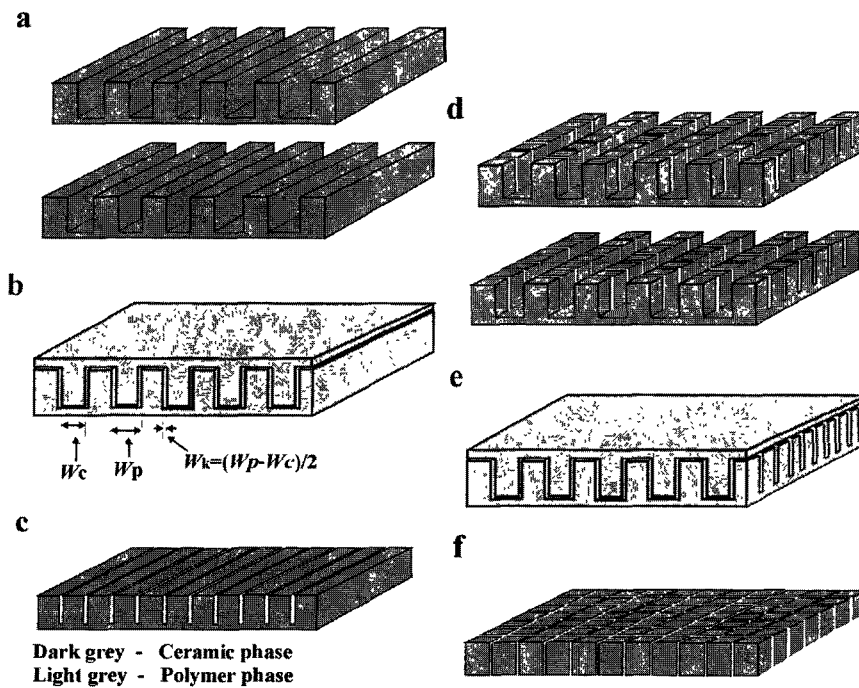


Figure 1.4.2: Processing procedure for 1-3 composite by interdigital pair bonding ^[47]

To further reduce the size of composite structures, the interdigital phase bonding technique (IPhB) can be applied ^[48]. The IPhB is a 2-step IPB technique and involves the dicing of two original IPB composites. Published results ^[49] suggest that

composite structures fabricated by IPhB have the potential of being a candidate material for linear-array designs with center frequencies of up to 85 MHz.

1.4.2 High-frequency arrays based on MEMS technologies

To achieve increased spatial resolution in diagnostic ultrasonic imaging, transducers that generate high frequency ultrasound are required. Since attenuation within tissue increases with frequency, the transducer must be placed very close to the tissue of interest. High frequency ultrasonic imaging (30-100 MHz) has been studied extensively because of its improved image resolution. It is gaining acceptance as a clinical tool for the eye, skin and intravascular imaging ^[50,51]. As the critical frequency of the designed array increases, the dimension of the array elements decreases. While, with traditional technologies of transducer fabrication, lapping and dicing bulk materials will become more difficult in the fabrication of high frequency devices. Currently, PZT ultrasonic arrays up to 35 MHz have been reported using a precise dicing method ^[52]; however, fabrication of even higher frequency transducers (> 50 MHz) is still a bottleneck due to dicing mechanical limitation ^[53]. Recent research shows that micro electromechanical systems (MEMS) technology is a possible solution to such high-frequency applications although much improvement still needs to be made ^[54,55,56,57].

K. K. Shung's group has described the development and characterization of a high frequency (65 MHz) ultrasonic transducer array ^[58]. They used the fabrication procedure illustrated in Fig. 1.4.3 to build all of the transducer arrays. A bulk PZT-5H (CTS, Bloomington, IL) wafer having a thickness of 500 μm was double-sided lapped and then polished on one side. A thin layer of nickel (Ni) was sputtered onto the polished side as a seed layer for subsequent electroplating. A photolithography-based method was then applied to transfer design patterns onto the PZT surface. First, a thick positive photoresist layer was spin-coated on the PZT. After baking on a hot plate, the photoresist was exposed directly by a laser writer. The wafer was dipped in photoresist developer for developing. The patterned photoresist structures were then formed. Next, the Ni electroplating process was run to form a

6- μm -thick Ni hard mask through the openings of the photoresist pattern. After electroplating, the photoresist was stripped off using Acetone. Finally, the PZT wafer with Ni hard mask was etched using an inductively coupled plasma (ICP) reactive ion etching (RIE) system employing Cl_2/Ar based chemistry, and the transducer array elements were formed as designed. The etching rate of bulk PZT was 8 μm /hr. Fig. 1.4.4 shows an array pattern with an etching depth of 40 μm . The sidewall angle is about 83°. The array consists of 32 elements with an element width of 24 μm and a kerf width of 12 μm . The element length is 4 mm, and the thickness is in the range of 25 μm to 36 μm . After the transducer was bonded using two flexible circuits, it was characterized.

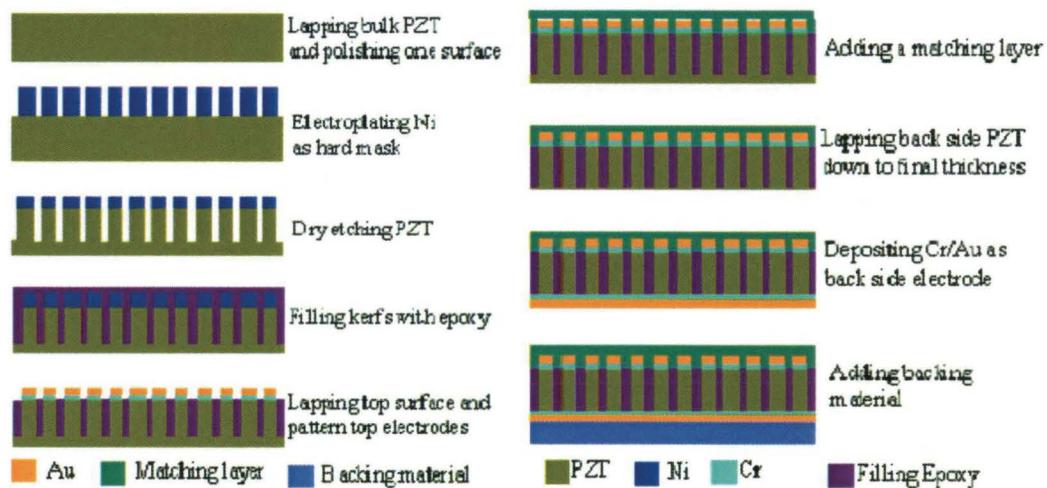


Figure 1.4.3: Process flow for micromachining bulk PZT ultrasound transducer arrays [58]

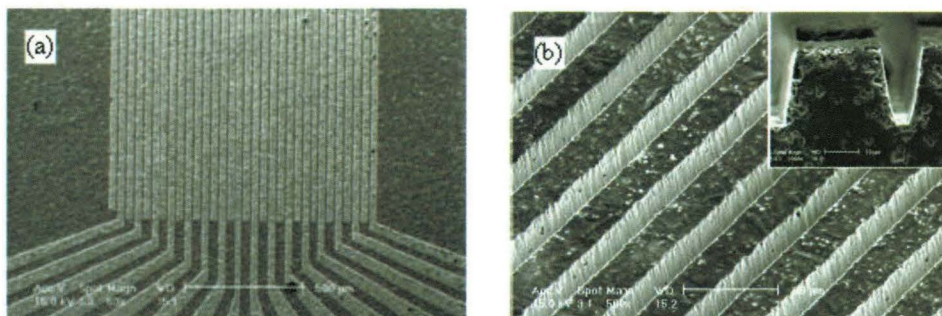


Figure 1.4.4: SEM pictures of etched bulk PZT array transducers (a) top view (b) 45° view with a cross-section view embedded [58]

The task is still a challenge to build arrays working at frequency higher than 100 MHz, which has the potential to provide more detailed skin texture for early diagnosis of melanoma, to image small objects such as stem cells, to control the movement of biological cells, and for real-time tissue differentiation. The objective of our work is to develop an ultrasonic phased array of above 100 MHz. Some researchers have focused their efforts on the development of very-high-frequency (beyond 100 MHz) ultrasonic transducer arrays to obtain high-resolution ultrasonic imaging. For comparison, all of the reported ultrasonic arrays beyond 100 MHz are concluded as follows.

Yukio Ito's group has reported 100 MHz arrays using zinc oxide (ZnO) thin films [59,60,61,62]. They fabricated a 32-element array on a sapphire focal lens. The ZnO array was constructed by photolithography with an appropriate etch. V-shaped grooves between adjacent elements were formed by using an anisotropic etchant (HCl and HNO₃-based). Typical array elements were 90 μm wide, 3.2 mm long, 10 μm thick and the pitch of the array is 100 μm . The structure of their device is illustrated in Fig. 1.4.5. Nevertheless, the pitch of 100 μm results in a low resolution.

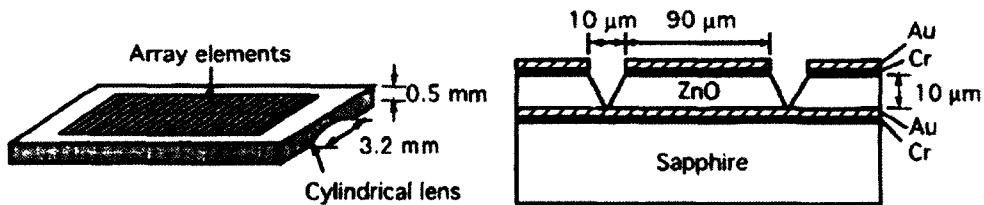


Figure 1.4.5: Schematic drawing of thin-film ZnO transducer array and a cross-sectional view of individual array elements [62].

Some research groups around the world have developed kerfless high-frequency linear arrays as an alternative to kerfed arrays. Because dicing fine kerfs at present is still a very expensive endeavor. This issue has been addressed by C. Morton et al. [63] and C. E. M. Démoré et al. [64].

Xu Zhu and Eun Sok Kim presented a novel approach for producing microfluidic motion by loosely focused acoustic waves (generated by piezoelectric zinc oxide thin film) [65]. They fabricated an annular array of aluminum (Al) electrodes on

10- μm -thick ZnO the resonant frequency of which is above 100 MHz. Their self-focusing acoustic transducer is shown in Fig. 1.4.6. The ZnO array was kerfless. The results showed that the acoustic waves generated by radio frequency (RF) sources with frequencies corresponding to the thickness-mode resonances of the piezoelectric film were very effective in moving liquid around when the waves were loosely focused. The device operated without any significant temperature increase in the liquid, and would be very attractive for mixing or transporting temperature-sensitive fluids.

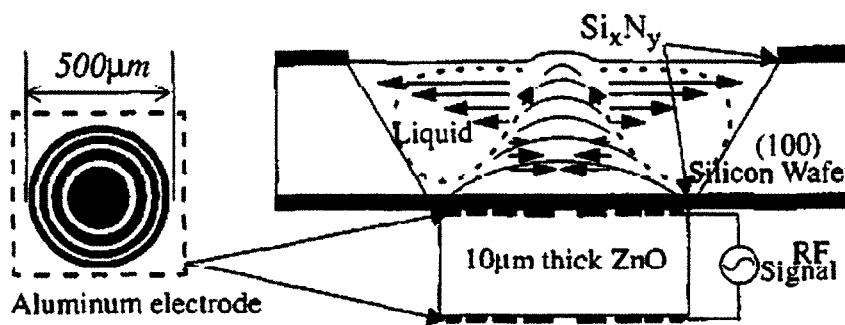


Figure 1.4.6: Cross-sectional view (along with typical liquid-flow directions) of the liquid mixer microfabricated on a silicon wafer. Also shown on the left is the electrode pattern of the transducer to form the acoustic-wave sources for a constructive wave interference in the liquid ^[65].

T. Takayasu reported a 100 MHz 32-element array transducer using lithographically-made electrodes and vapour-deposited polyurea film ^[66]. They used two methods to fabricate kerfless array transducers as shown in Fig. 1.4.7. Typical values of the Al array electrodes on polyimide substrates were 10- μm -width, 20- μm -pitch, 3-mm-length, and 0.5- μm -thickness. In their measurements, a resonant frequency of about 100 MHz was observed in the electrical admittance. Beam steering experiments and pulse/echo test were carried out using the prototyped transducers.

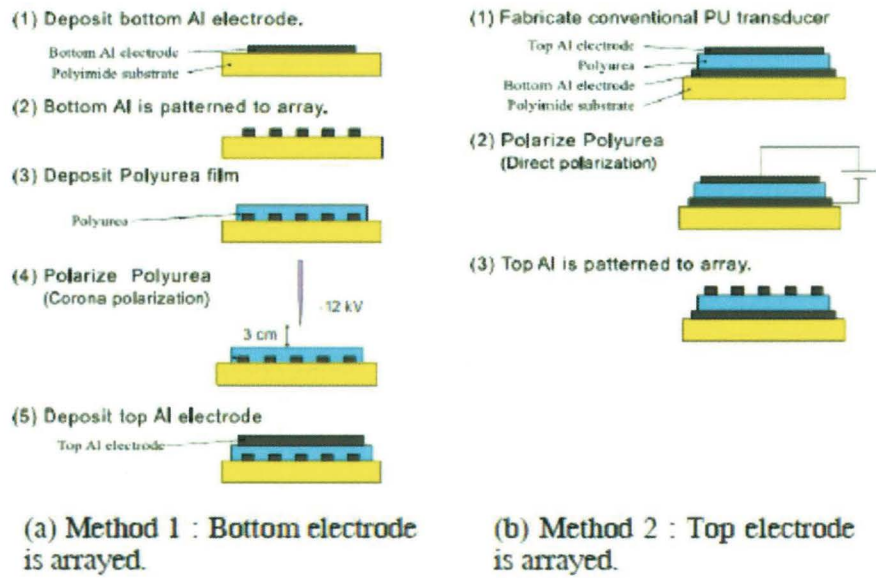


Figure 1.4.7: Fabrication methods of polyurea array transducer [65]

K. K. Shung's group has developed two 120 MHz kerfless arrays prepared from a 12- μm PZT thick film [67,68] and a piece of 15- μm PZT-5H bulk material [68], respectively. The two transducers had an identical electrode pattern of 32-element linear array. Typical dimensions were 24- μm -width, 36- μm -pitch, and 4-mm-length. The PZT thick film was prepared by spin-coating of PZT-5H ceramic powder/sol-gel composite solution as described in [69,70]. Fig. 1.4.8 shows SEM images of their prepared PZT thick films. Fig. 1.4.9 shows fabrication flow of PZT thick film kerfless linear arrays. The thin PZT-5H sheet sample was prepared by lapping a PZT-5H ceramic with a precision lapping machine. The measured results of the two linear arrays were compared.

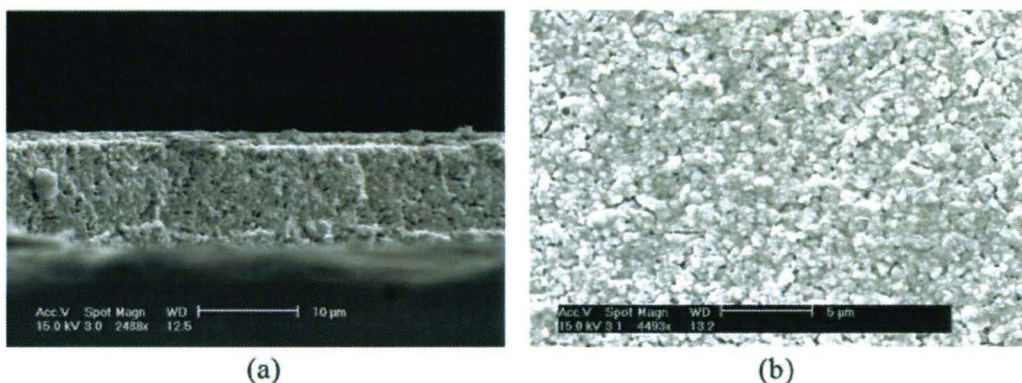


Figure 1.4.8: SEM pictures (a) cross-section and (b) top view of 12- μm PZT thick film [68]

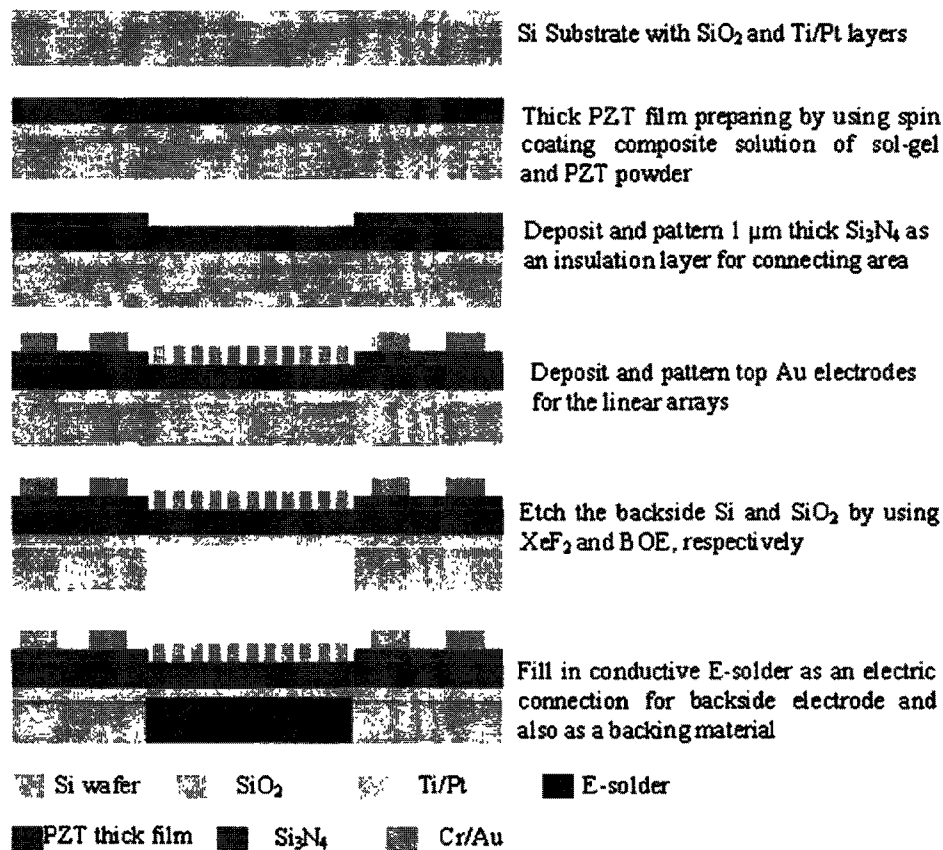


Figure 1.4.9: Fabrication flow of PZT thick film kerfless linear arrays ^[68]

However, the crosstalk in the kerfless array is very severe (in the order of 10 dB) resulting in significant ringing. As a result, these arrays have not had a significant amount of research effort and applications have been limited.

1.4.3 cMUT pMUT and mMUT

A summary of array fabrication would not be complete without mentioning the expanding field of micromachined ultrasonic transducers (MUTs). In recent years, MUTs have gained more and more attention in the development of ultrasonic phased arrays. It represents a new approach to ultrasound detection and generation. Two dimensional MUT arrays can be easily made with excellent reproducibility by using micromachining techniques. MUT offers advantages of improved bandwidth, easy fabrication of large arrays with compact designs, and integration with support electronics ^[71,72]. These advantages inherent in MUT enable revolutionary advances in

ultrasonic imaging, acoustic devices ^[73], low cost phase arrays in distance measurement and simple object recognition in air ^[74,75]. According to the working principle, MUT can be divided into three categories: piezoelectric micromachined ultrasonic transducer (pMUT), capacitive micromachined ultrasonic transducer (cMUT) and magnetic micromachined ultrasonic transducer (mMUT).

Conventional ultrasonic transducers, as shown in Fig. 1.4.10, consist of PZT strips electroded and poled in the thickness direction to operate as extensional mode resonators. In this mode of operation, the frequency of the transducer is governed by the thickness of the strip, with the fundamental resonant frequency occurring when the strip thickness is equal to half the wavelength at the speed of sound in PZT ^[76]. This direct dependence of the device operating frequency (resonant frequency) on the PZT thickness can be a limiting factor as geometrical and/or constructional restrictions on the thickness can conflict with the thickness requirement for a certain frequency. Furthermore, by nature of their operation as extensional resonators, conventional ultrasonic transducers are limited in their performance, particularly their bandwidth when operating in fluid media, due to the large acoustic impedance mismatch between the ceramic (34 MRayls for PZT) and a fluid such as water or air (1.5 MRayls and 340 Rayls, respectively) ^[77]. Although quarter wavelength ($\lambda/4$) matching layers have been successfully used to overcome the impedance mismatch problem and to improve the bandwidth, nevertheless, this solution has its limitations. The right matching layer materials with the required properties are not readily available and the layers become too thin to mechanically handle as the application frequency of the transducer increases ^[78].

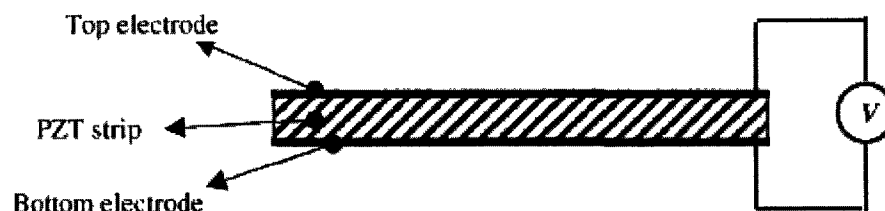


Figure 1.4.10: Schematic of the basic design of conventional extensional ultrasonic transducers ^[78]

PMUT represent a new approach to ultrasound detection and generation that can overcome the shortcomings of conventional ultrasonic transducers. A pMUT uses a piezoelectric layer adhered to an inert membrane and operation in flexural mode (in other words, bending mode), exploiting the piezoelectric d_{31} coefficient to drive it. Fig. 1.4.11 is the schematic structure of an individual element in the pMUT arrays with PZT thick film ^[79]. The sound-radiating element is a micromachined multi-layered membrane actuated by a thin piezoactive layer. Typical membrane dimensions are on the order of micrometers in thickness and tens of micrometers in the lateral direction. In this bending mode device, the PZT is poled in the thickness direction. By applying an electric field across the thickness, the lateral strain induces membrane bending; thus causing a pressure sound wave to propagate in the medium in contact. Upon the impinging of the back scattered sound waves on the membrane, the induced flexural motion causes a charge displacement in the electroded PZT, which can be detected by the receiving circuitry and further processed to extract useful information about features in the tested medium. In this scheme, the thickness of the PZT layer does not dictate the operating frequency (the membrane resonant frequency), as it is the case in conventional transducers. Instead, frequency is governed by the dimensions and the layering materials of the membrane ^[80] and can thus be controlled independent of the PZT layer thickness, offering more design flexibility and control over the frequency. Other performance parameters, such as the device acoustic impedance and coupling coefficient, can also be controlled through the proper manipulation of the device geometry. Due to the low acoustic impedance of the membrane, the acoustic impedance of a pMUT can be made to match that of a fluid, which implies that pMUTs inherently have higher bandwidth ^[81]. Although the electromechanical coupling in a flexural mode pMUT is significantly compromised by the presence of the inert membrane, pMUT can obtain large vibration amplitude, thus higher output acoustic power. Therefore, pMUT offers an advantage when it is used as a transmitter.

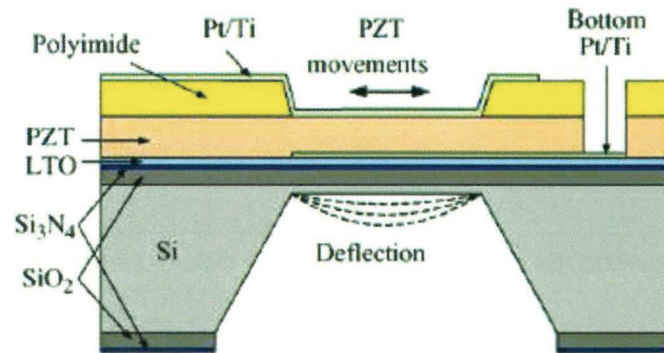


Figure 1.4.11: Schematic structure of a membrane-type pMUT fabricated on a silicon wafer ^[79]

CMUT devices operate on a capacitive principle of ultrasonic transducers via a large electric force applied to a thin membrane covering a very small cavity of microns in diameter. It is basically a miniaturized parallel plate capacitor with a back plate fixed while the other one is flexing membrane. Fig. 1.4.12 shows a schematic structure of a single element cMUT ^[82]. The flexing membrane can be set into vibration under the effect of electrostatic attraction between the oppositely charged plates and the opposing restoring force provided by the stiffness of the flexing membrane. The cMUT devices possess high coupling coefficient and can operate with bandwidths in excess of 100%, and cMUT working at frequencies as high as 60 MHz have been reported ^[83]. These devices have the potential of extending the frequency range of transducers, as they will not be limited by the integrity of a ceramic grain structure. This technology, based on traditional and mature semiconductor microfabrication, offers the advantages of batch fabrication at the expense of setting up, or gaining access to, a full microfabrication facility ^[84]. Although cMUT generally provides a wider bandwidth than current piezoelectric transducers ^[85], the device reliability is still a practical issue ^[86]. As shown in Fig. 1.4.12, a DC voltage bias is required in a cMUT. In order to achieve the theoretical coupling, this voltage bias needs to be near the collapse voltage of the cMUT ^[87]. With the current level of manufacturing control over the device dimensions and residual stresses, it seems difficult to secure an intended safety margin on the bias voltage, to avoid collapse, on

all the array elements. L. Ginzton lab has investigated cMUT with isolation posts (Post-cMUT) to tackle this problem ^[88].

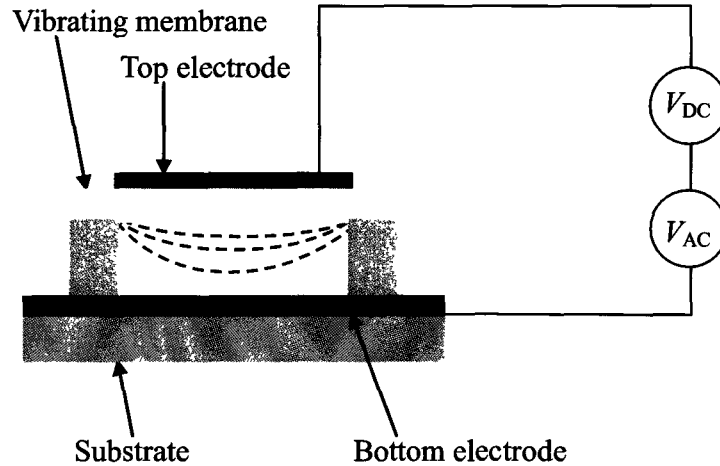


Figure 1.4.12: Schematic structure of a single element cMUT

CMUT is based on electrostatic effect, and pMUT is based on piezoelectric effect. Unlike cMUT and pMUT, mMUT is based on magnetostrictive effect. Magnetostriction is a property of ferromagnetic materials that causes them to change their shape or dimensions during the process of magnetization. The variation of material's magnetization due to the applied magnetic field changes the magnetostrictive strain until reaching its saturation value. The effect was first identified in 1842 by James Joule when observing a sample of nickel ^[89]. Acoustic transducers featuring magnetostriction as the active means for transduction have been used since before the First World War. The principle of magnetostrictive transducer is to place a magnetically oriented material within a coil, bias the material with a direct-current field (either through a direct current or through placement in a magnetic field), and drive the coil with an alternating-current field directed into the coil. In the 1970s, the finding of rare-earth-iron compounds with strains approaching 1% resulted in the design of magnetostrictive projectors for high-power, low-frequency underwater applications. Research continues into improving manufacturing methods and material quality. A mMUT has a similar structure to the cMUT cell except that the capacitor (the top and the bottom electrodes) are replaced by a magnetic layer on the

membrane as shown in Fig. 1.4.12. Unlike cMUT, the mMUT structure does not have electrodes to form a capacitor. Magnetic layers function as a transducing member or energy exchanger activating the top plate in response to the substantially vertical motion of the top plate layer. Despite the similarities in the overall structure, the material selection may be different for mMUT because the electric connections in the mMUT are different due to a different energy transformation method. Currently, the literatures on mMUT is not as many as those on cMUT and pMUT. Y. L. Huang et al. ^[90] have developed some novel structures of mMUT.

1.4.4 Laser technique

Laser micromachining offers many advantages over other material removal and structuring methods. It is a fast, non-contact and abrasionless technique that eliminates tool wear, cutting forces and mechanical vibrations. Aspect ratio (depth: width) of 4: 1 can be obtained in ceramic materials. Laser micromachining also minimizes the restrictions on the array geometry. Not only can laser ablate through ceramics, but they can pattern through quarter wave matching layers, backing materials and more. Mechanical techniques such as dicing saws cannot turn corners and ion etching is very slow. A chemical etch 20-50 μm deep into PZT cannot achieve high aspect ratio due to undercutting. S. Foster's group demonstrated the ability of lasers to micromachine desirable patterns for annular and linear arrays for frequencies in excess of 30 MHz ^[91]. A 5-element annular array was fabricated using pre-poled 125 μm thick Motorola PZT-5H substrate that was manually polished to 40 μm for a thickness mode resonance of 45 MHz. They also fabricated a 16-element linear array using single crystal Y-cut lithium niobate (LiNbO_3) substrate from Valpey Fisher. The elements were 23 μm wide, 90 μm thick and 1 mm long. The pitches were one wavelength wide at 40 MHz. Both arrays were totally kerfed based on laser micromachining.

In fabrication of 1-3 composite transducers, the current process involves the use of either a wire saw or a semiconductor dicing saw to cut a pattern of rectangular pillars in a monolithic piezoceramic plate. However, this technique has obvious

limitations in terms of pillar shape and size. Some researchers have devoted to investigate the feasibility of using laser technique to overcome this problem. In collaboration with Oxford Laser, R. Farlow et al. ^[92] used copper vapour laser (CVL) to dice a small region of a 30 mm diameter, 0.5 mm thick PZT5A plate to produce a 2-D array of pillars with 65 μm pitch. The kerf width was 13 μm and the material was cut to a depth of 250 μm . Fig. 1.4.13 shows the SEM images of laser cut ceramic plate. This method could be extended to the fabrication of ultrasonic phased arrays.

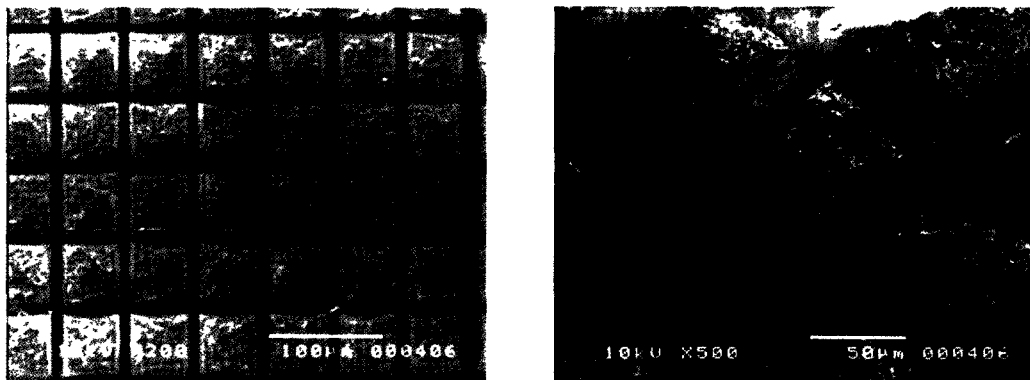


Figure 1.4.13: SEM images of laser cut ceramic plate ^[92]

1.5 Summary and outline of the thesis

Ultrasonic arrays, benefiting from fast electronic scanning, are used in different domains including medical imaging, sonar and material non-destructive evaluation. Traditional phased array transducer has usually a working frequency of several MHz which is convenient for human organs imaging. In recent years, high-frequency (30-100 MHz) ultrasonic array transducers are being developed for high-resolution ultrasonic imaging, for applications to skin, eye and vessel imaging ^[93]. Higher-frequency array (> 100 MHz) has been found potential applications in microfluidics for biological cell control ^[94] and in real-time tissue differentiation ^[95].

In ultrasonic phased array imaging systems, ultrasonic transducers play a critical role. Our research project aims at the development of linear phased array transducers of 100 MHz and upwards. Two main applications are expected for biological cell testing and layered material non-destructive evaluation. The first application is to

integrate ultrasonic sensor in micro-fluidics for single cell elasticity testing. The second is to use phased array system to replace the mechanical scanning in acoustic microscopes for high resolution real-time ultrasonic imaging of material subsurface and for characterization of layered media (thin film, coating and bonding) using acoustic material signature.

As stated previously, the MEMS technology has offered opportunities to fabricate miniaturized devices. In order to design devices as well-performed as possible, we need to optimize the geometrical parameters within the limit of the MEMS processes and the properties of the piezoelectric materials. This dissertation reports the finite element simulations for optimization and experimental fabrications of high-frequency ultrasonic transducer arrays. According to the special requirements of high frequency transducer arrays, three different types of transducers are investigated based on MEMS technology and the latest developments of piezoelectric materials.

In Chapter 1, the background and principle of ultrasound imaging have been reviewed, especially the fabrication techniques in ultrasonic array transducers. Then the objective and outline of this thesis are introduced.

Chapter 2 introduces the theoretical study of high-frequency ultrasonic linear phased arrays. I demonstrate the formalisms of wave motion in fluidic materials and in solid (including non-piezoelectric and piezoelectric) materials. Mason model, KLM model and some key parameters are introduced, such as longitudinal wave, shear wave, phase velocity, slowness, group velocity, electromechanical coupling coefficient, piezoelectric coupling coefficient, crosstalk, electrical impedance, electrical matching, acoustic impedance, acoustic matching, and transducer bandwidth, etc.

Chapter 3 emphasizes on the numerical simulation and optimization by finite element method. It includes three parts. In the first part, the formulism and theoretical settings in COMSOL is summarized, including partial differential equation (PDE) and COMSOL formulism, sources of excitation, and boundary conditions. Several simulation cases are presented based on COMSOL numerical method, including wave

propagation in solids and in fluids, wave steering of a linear phased array and wave scattering of a rough boundary. In the second part, a buffered transducer array with a focal lens is designed and simulated in 2-D models. The simulation includes calculation of acoustic field, electrical impedance, and crosstalk. In the third part, a short summary is presented.

Chapter 4 presents the simulation, fabrication and characterisation of a LiNbO₃-based array. Chapter 5 presents the fabrication and characterisation of two ZnO-based arrays. Based on LiNbO₃ arrays, several important characteristics for a piezoelectric backing transducer are investigated, including effect of pitch size on grating lobes, effect of kerf filler, and effect of kerf depth. Etching technique is studied and the LiNbO₃-based array is made by dry etching single crystal LiNbO₃. The ZnO-based arrays are fabricated using two different methods. One is wet etching ZnO films, and the other is dry etching Si and then depositing ZnO films. All of the fabricated arrays are characterised by Network Analyzer. The measured results, including electrical impedance and crosstalk, are consistent to the theoretical predictions. This proves the validity of 2-D simulation of COMSOL and the possibility of fabrication of high-frequency ultrasonic transducer arrays.

Finally, a conclusion of this thesis is presented including main contributions and problems, as well as suggested future work.

Chapter 2: Acoustic Waves in Elastic Media and Fundamentals of Piezoelectric Ultrasonic Transducers

The first objective of this chapter is to present the mathematics of acoustic wave propagation in different media (including fluids, solids and piezoelectric materials). Numerical solution of Christoffel equation is obtained for analysis of material elasticity and piezoelectricity. The theoretical fundamental is necessary either for the understanding of wave phenomena and behaviours relating to ultrasonic transducers or for the establishment of theoretical models for simulation and optimization of the piezoelectric ultrasonic transducers. It will be also helpful for further employment of numerical approaches such as the finite element method (FEM). Particular attention will be paid to the material anisotropy, piezoelectricity, and the electromechanical coupling coefficient.

The second part of this chapter concerns the development of modelling techniques for ultrasonic transducers in order to study their characteristics and performances. One dimensional KLM model is introduced and used in the simulation of the single element transducers. Numerical examples are given for different piezo-active materials such as ZnO, LiNbO₃ and PZT-4, each of which has their particular piezoelectric characteristic. Transducer performances in terms of the sensitivity (insertion loss), the bandwidth (return transfer function) and the impulsion response will be calculated and compared. The performance improvement by electrical matching and acoustical matching are discussed in details.

2.1 Waves propagation in fluid, solid and piezoelectric materials

2.1.1 Waves equation in fluids

According to Newton's Law, the equation of motion in a fluid is given by

$$-\nabla p + \mathbf{f} = \rho \frac{\partial^2 \mathbf{u}}{\partial t^2} \quad (2.1.1)$$

where p is the pressure and ∇ is the gradient operator, \mathbf{u} the displacement vector, \mathbf{f} the body force vector, ρ the fluid mass density that is assumed undisturbed with very small displacements and velocities of motion.

Another part, in an ideal compressible fluid, the pressure is proportional to the divergence of the displacement vector, known as the dilatation of the fluid

$$p = -\lambda \nabla \cdot \mathbf{u} \quad (2.1.2)$$

where $\nabla \cdot$ is the divergence operator and the proportionality constant λ is the bulk modulus of the fluid.

To turn the differential equation of motion Eq. (2.1.1) into an equation only with a single variable, such as pressure, taking the divergence of both sides of Eq. (2.1.1) and using Eq. (2.1.2), it can be obtained

$$\nabla^2 p + f = \frac{\rho}{\lambda} \frac{\partial^2 p}{\partial t^2} \quad (2.1.3)$$

where $\nabla^2 = \nabla \cdot \nabla$ is the Laplacian operator and $f = -\nabla \cdot \mathbf{f}$ is a scalar body force term. Eq. (2.1.3) can also be written as

$$\nabla^2 p - \frac{1}{v_f^2} \frac{\partial^2 p}{\partial t^2} + f = 0 \quad (2.1.4)$$

where the quantity $v_f = (\lambda / \rho)^{1/2}$ is the speed of sound in the fluid.

2.1.2 Waves equation in solid materials

In a continuous linear elastic body, the Newton's motion equation is

$$\frac{\partial}{\partial x_j} T_{ij} + f_i = \rho \frac{\partial^2 u_i}{\partial t^2} \quad (2.1.5)$$

where T_{ij} is the second order stress tensor, f_i the applied body force, ρ the mass density, u_i the displacement vector and x_j the position vector and $i, j = 1, 2, 3$ representing the direction components of x, y, z under Cartesian coordinates.

The Hooke's Law states that the stress is linearly proportional to the strain

$$T_{ij} = c_{ijkl} S_{kl} \quad (2.1.6)$$

where c_{ijkl} is the elasticity or the stiffness tensor and S_{kl} is the strain tensor which is expressed in the deformation by

$$S_{kl} = \frac{1}{2} \left(\frac{\partial u_k}{\partial x_l} + \frac{\partial u_l}{\partial x_k} \right) \quad (2.1.7)$$

The strain and the stress tensor being symmetric, Eq. (2.1.6) can be is written as

$$T_{ij} = c_{ijkl} \frac{\partial u_k}{\partial x_l} \quad (2.1.8)$$

Replacing Eq. (2.1.8) into Eq. (2.1.5), the general form of the elasto-dynamic equation in free body force elastic solids is

$$\frac{\partial}{\partial x_j} \left(c_{ijkl} \frac{\partial u_l}{\partial x_k} \right) = \rho \frac{\partial^2 u_i}{\partial t^2} \quad (2.1.9)$$

For homogeneous materials in which elastic constants c_{ijkl} and density are constant, Eq. (2.1.9) becomes

$$c_{ijkl} \frac{\partial^2 u_l}{\partial x_j \partial x_k} = \rho \frac{\partial^2 u_i}{\partial t^2} \quad (2.1.10)$$

Now, consider harmonic plane waves moving through a homogeneous and anisotropic (including isotropic) medium, the solution can be supposed in the form

$$u_i = U_i e^{j(k_j x_j - \omega t)} = U_i e^{j(k \cdot n_j x_j - \omega t)} \quad (2.1.11)$$

where U_i is the displacement amplitude vector component, k_j is the wave number vector component and k is its modulus, n_j is the unit vector (or director cosines) in the wave number direction.

Replacing Eq. (2.1.11) into the elasto-dynamic equation of Eq. (2.1.10), we get

$$c_{ijkl} n_j n_k U_l = \rho v_p^2 U_i \quad (2.1.12)$$

where $v_p = \frac{\omega}{k}$ corresponds to the phase velocity of the plane waves.

Let $\Gamma_{il} = c_{ijkl} n_j n_k$, known as the Christoffel matrix, Eq. (2.1.12) can be written

in a matrix form

$$\left[\Gamma_{il} - \delta_{il} \rho v_p^2 \right] U_k = 0 \quad (2.1.13)$$

In the derivation of Eq. (2.1.13), the tensor subscripts of c_{ijkl} need to be expressed in terms of the equivalent matrix subscripts c_{IJ} by $I \rightarrow ij, J \rightarrow kl$ using Voigt notation

$$1 \rightarrow 11, 2 \rightarrow 22, 3 \rightarrow 33, 4 \rightarrow 23, 32, 5 \rightarrow 31, 13, 6 \rightarrow 12, 21$$

and the Christoffel matrix components Γ_{il} are obtained as

$$\begin{aligned} \Gamma_{11} &= c_{11}n_1^2 + c_{66}n_2^2 + c_{55}n_3^2 + 2c_{56}n_2n_3 + 2c_{15}n_3n_1 + 2c_{16}n_1n_2 \\ \Gamma_{22} &= c_{66}n_1^2 + c_{22}n_2^2 + c_{44}n_3^2 + 2c_{24}n_2n_3 + 2c_{46}n_3n_1 + 2c_{26}n_1n_2 \\ \Gamma_{33} &= c_{55}n_1^2 + c_{44}n_2^2 + c_{33}n_3^2 + 2c_{34}n_2n_3 + 2c_{35}n_3n_1 + 2c_{45}n_1n_2 \\ \Gamma_{23} = \Gamma_{21} &= c_{56}n_1^2 + c_{24}n_2^2 + c_{34}n_3^2 + (c_{23} + c_{44})n_2n_3 + (c_{36} + c_{45})n_3n_1 + (c_{25} + c_{46})n_1n_2 \\ \Gamma_{13} = \Gamma_{31} &= c_{15}n_1^2 + c_{46}n_2^2 + c_{35}n_3^2 + (c_{36} + c_{45})n_2n_3 + (c_{13} + c_{55})n_3n_1 + (c_{14} + c_{56})n_1n_2 \\ \Gamma_{12} = \Gamma_{32} &= c_{16}n_1^2 + c_{26}n_2^2 + c_{45}n_3^2 + (c_{25} + c_{46})n_2n_3 + (c_{14} + c_{56})n_3n_1 + (c_{12} + c_{66})n_1n_2 \end{aligned} \quad (2.1.14)$$

Eq. (2.1.13) signifies that the eigenvalues and the associated eigenvectors of the Christoffel matrix Γ_{il} are ρv_p^2 and U_k , which correspond to respectively the solutions for the phase velocity v_p and the polarization of the plane waves. As the Christoffel equation has an order of 3, three solutions of plane wave are admitted. Their polarization vectors are mutually orthogonal. If the wave propagation direction is parallel to the polarization direction, such type of waves is called compression waves or longitudinal waves. If the wave propagation direction is perpendicular to the polarization direction, they are called shear waves or transversal waves. In a general anisotropic solid, the waves are not purely longitudinal or transversal. There are usually one quasi-longitudinal wave and two quasi-transversal waves. Varying all the direction of n_j in the Cartesian space coordinates, three phase velocity surfaces v_p or slowness surfaces $1/v_p$ can be constituted.

2.1.3 Waves equation in piezoelectric materials

In a piezoelectric solid, when strained, the material will be electrically polarized and manifests itself by the appearance of bound electrical charges at the surfaces. This direct piezoelectric effect is always accompanied by its converse effect: the solid

becomes strained when placed in an electric field. The piezoelectricity is a linear phenomenon and the polarization changes sign when the sign of the strain is reversed.

In the case of piezoelectric solid, the Hooke's Law relation for non-piezoelectric solid $T_{ij} = c_{ijkl} S_{kl}$ will be coupled with a stress term induced by electric field (converse piezoelectric effect) such that

$$T_{ij} = c_{ijkl}^E S_{kl} - e_{kij} E_k \quad (2.1.15)$$

where c_{ijkl}^E is the elastic constant tensor superscripted with E which means that these constants describe elastic properties measured under conditions of constant electric field, E_k is the electric field and e_{kij} is the proportionality piezoelectric constant tensor.

Conversely, the constitutive relation of the electric displacement of $D_j = \varepsilon_{jk} E_k$ will be added by in a strain induced term (direct piezoelectric effect)

$$D_j = \varepsilon_{jk}^S E_k + e_{jkl} S_{kl} \quad (2.1.16)$$

where ε_{jk}^S are the permittivity constants superscripted with S corresponding to those describe dielectric properties obtained under conditions of constant stress.

As derived for wave propagation in non-piezoelectric media, the motion equation in piezoelectric solid can be obtained using Eqs. (2.1.5), (2.1.7) and (2.1.15)

$$c_{ijkl}^E \frac{\partial^2 u_l}{\partial x_j \partial x_k} - e_{ijk} \frac{\partial E_k}{\partial x_j} = \rho \frac{\partial^2 u_i}{\partial t^2} \quad (2.1.17)$$

The resolution of this motion equation should be undertaken by coupling it with the Maxwell's electromagnetic wave equation, permitting to get either the acoustic waves or electromagnetic waves. But it's assumed that for plane wave solutions in unbounded media, the associated electromagnetic wave propagations can be negligible compared to the influence of the quasi-static electric field [96]. So in the following, the wave motion resolution will be based on quasi-static approximation.

The quasi-static electric field E_k is related to the scalar electric potential ϕ by

$$E_k = -\frac{\partial \phi}{\partial x_k} \quad (2.1.18)$$

The electric displacement satisfies the Poisson equation in a free electrically charged isolate medium

$$\frac{\partial D_j}{\partial x_j} = 0 \quad (2.1.19)$$

Substituting respectively Eq. (2.1.18) into Eq. (2.1.16) and Eq. (2.1.16) into Eq. (2.1.19), one can get the following equation group

$$\begin{cases} c_{ijkl}^E \frac{\partial^2 u_l}{\partial x_j \partial x_k} + e_{kij} \frac{\partial^2 \phi}{\partial x_j \partial x_k} = \rho \frac{\partial^2 u_i}{\partial t^2} \\ e_{jkl} \frac{\partial^2 u_l}{\partial x_j \partial x_k} - \varepsilon_{jks}^S \frac{\partial^2 \phi}{\partial x_j \partial x_k} = 0 \end{cases} \quad (2.1.20)$$

from which the acoustic wave displacement u_i and the electric potential ϕ may be obtained.

Again supposing the plane wave propagation along a given direction such that

$$u_i = U_i e^{j(k \cdot n_j x_j - \omega t)}, \quad \phi = \Phi e^{j(k \cdot n_j x_j - \omega t)} \quad (2.1.21)$$

Replacing these plane wave solutions into Eq. (2.1.20), there are

$$\begin{cases} c_{ijkl}^E k^2 n_j n_k U_l + e_{kij} k^2 n_j n_k \Phi = \rho \omega^2 U_i \\ e_{jkl} k^2 n_j n_k U_l + \varepsilon_{jks}^S k^2 n_j n_k \Phi = 0 \end{cases} \quad (2.1.22)$$

Then, eliminating Φ in Eq. (2.1.20), and let $\bar{v}_p = \frac{\omega}{k}$, the equation giving the wave amplitude U_i is

$$\left(c_{ijkl}^E n_j n_k + \frac{(e_{kij} n_j n_k)(e_{jkl} n_j n_k)}{\varepsilon_{jks}^S n_j n_k} \right) U_l = \rho \bar{v}_p^2 U_i \quad (2.1.23)$$

Let $\Gamma_{il} = c_{ijkl}^E n_j n_k$, $\gamma_i = e_{kij} n_j n_k$, $\gamma_l = e_{jkl} n_j n_k$ and $\varepsilon^S = \varepsilon_{jks}^S n_j n_k$, one has

$$\left[\left(\Gamma_{il} + \frac{\gamma_i \gamma_l}{\varepsilon^S} \right) - \delta_{il} \rho \bar{v}_p^2 \right] U_k = 0 \quad (2.1.24)$$

This has exactly the same form as the Christoffel equation (2.1.13) for non-piezoelectric media but with Γ_{il} replaced by $\Gamma_{il} + \frac{\gamma_i \gamma_l}{\varepsilon^S}$ which is called a

piezoelectrically stiffened elastic constant. In the matrix coefficient subscripts, the equivalent Christoffel matrix components Γ_{il} and $\frac{\gamma_i \gamma_l}{\varepsilon^S}$ can be calculated respectively by Eqs. (2.1.14) and by

$$\begin{aligned}\gamma_1 &= e_{11}n_1^2 + e_{26}n_2^2 + e_{35}n_3^2 + (e_{25} + e_{36})n_2n_3 + (e_{15} + e_{31})n_3n_1 + (e_{16} + e_{21})n_1n_2 \\ \gamma_2 &= e_{16}n_1^2 + e_{22}n_2^2 + e_{34}n_3^2 + (e_{24} + e_{32})n_2n_3 + (e_{14} + e_{36})n_3n_1 + (e_{12} + e_{26})n_1n_2 \\ \gamma_3 &= e_{15}n_1^2 + e_{24}n_2^2 + e_{33}n_3^2 + (e_{23} + e_{24})n_2n_3 + (e_{13} + e_{35})n_3n_1 + (e_{14} + e_{25})n_1n_2 \\ \varepsilon^S &= \varepsilon_{11}^S n_1^2 + \varepsilon_{22}^S n_2^2 + \varepsilon_{33}^S n_3^2 + 2\varepsilon_{23}^S n_2n_3 + 2\varepsilon_{13}^S n_3n_1 + 2\varepsilon_{12}^S n_1n_2\end{aligned}\quad (2.1.25)$$

Eq. (2.1.24) shows that the influence of the piezoelectricity on the phase velocity may be attributed to a modification of the stiffness of the medium. The equivalent Christoffel tensor may be written as

$$\left[\bar{\Gamma}_{il} - \delta_{il} \rho \bar{v}_p^2 \right] U_k = 0 \quad (2.1.26)$$

with $\bar{\Gamma}_{il} = c_{ijkl}^D n_j n_k$ and $c_{ijkl}^D = c_{ijkl}^E + \frac{(e_{kij} n_k)(e_{jkl} n_j)}{\varepsilon_{jk}^S n_j n_k}$ is the ‘‘stiffened’’ elastic constants.

The change of the stiffness due to the piezoelectric effect can also be expressed in a relative variation form

$$c_{ijkl}^D = c_{ijkl}^E \left(1 + \frac{e_{kij} n_k e_{jkl} n_j}{c_{ijkl}^E \varepsilon_{jk}^S n_j n_k} \right) = c_{ijkl}^E \left(1 + \frac{\Delta c_{ijkl}^E}{c_{ijkl}^E} \right) = c_{ijkl}^E (1 + K^2) \quad (2.1.27)$$

where $K = \left(\frac{\Delta c_{ijkl}^E}{c_{ijkl}^E} \right)^{1/2} = \left(\frac{e_{kij} n_k e_{jkl} n_j}{c_{ijkl}^E \varepsilon_{jk}^S n_j n_k} \right)^{1/2}$ is a parameter describing the piezoelectricity

effect and is dependent on the wave propagation direction n_i . Thus, for a given direction, the wave phase velocity of a piezoelectric material (the stiffened phase velocity \bar{v}_p) is solved from the Christoffel equation of (2.1.24) in the form

$$\bar{v}_p = \sqrt{\frac{c^D}{\rho}} = \sqrt{\frac{c^E + e^2 / \varepsilon^S}{\rho}} = \sqrt{\frac{c^E}{\rho}} (1 + K^2) \quad (2.1.28)$$

where $K^2 = \frac{e^2}{c^E \varepsilon^S}$ (2.1.29)

and the constants c^E , e and ε^S without subscript signify the equivalent constants in the given direction resulting from the algebraic combination of their respective tensor elements. A virtual phase velocity v_p without accounting for the piezoelectricity effect (the non-stiffened or piezoelectricity inactive phase velocity) in the form

$$v_p = \sqrt{\frac{c^E}{\rho}} \quad (2.1.30)$$

With the above equations, we obtain an important relation

$$\bar{v}_p = v_p \sqrt{1 + K^2} \quad (2.1.31)$$

from which

$$K^2 = (\bar{v}_p / v_p)^2 - 1 \quad (2.1.32)$$

K is called the **piezoelectric coupling constant**^[97]. Like the piezoelectric constant e_{kj} , this parameter characterizes also the piezoelectricity of a material in a different manner. But it should not be confused with the **electromechanical coupling constant (or coefficient, or factor)** k_t which is defined by

$$k_t^2 = \frac{K^2}{1 + K^2} \quad (2.1.33)$$

By the relation of Eq. (2.1.32), k_t can be calculated by using the formula

$$k_t = \sqrt{1 - (v_p / \bar{v}_p)^2} \quad (2.1.34)$$

With small difference between v_p and \bar{v}_p or small K^2 value, k_t can be estimated approximately by

$$k_t^2 = \frac{\bar{v}_p^2 - v_p^2}{\bar{v}_p^2} = \frac{(\bar{v}_p - v_p)(1 + v_p / \bar{v}_p)}{\bar{v}_p} \cong \frac{2(\bar{v}_p - v_p)}{\bar{v}_p} = \frac{2|\Delta v|}{\bar{v}_p} \quad (2.1.35)$$

Another part
$$K^2 = \frac{k_t^2}{1 - k_t^2} = \frac{\bar{v}_p^2 - v_p^2}{v_p^2} = \frac{(\bar{v}_p - v_p)(1 + \bar{v}_p / v_p)}{v_p} \cong \frac{2|\Delta v|}{v_p} \quad (2.1.36)$$

This shows that numerically there will be no significant difference between K and

k_i in condition that the material piezoelectric effect is small (for most piezoelectric materials $K^2 < 0.3$).

2.1.4 Numerical solution of Christoffel equation for analysis of material elasticity and piezoelectricity

To calculate the plane wave phase velocity or slowness, the wave polarization, the group velocity and the electromechanical coupling coefficient using the formalism given in the above sections, a computer software developed in Matlab codes with GUI interface^[98] by the laboratory is available (Fig.2.1.1). The materials constants data (ρ , c_{IJ}^E , e_{kij} , ε_{jk}^S) can be stored in a Matlab data file document or be input directly by the graphic interface window as shown in Fig. 2.1.1.

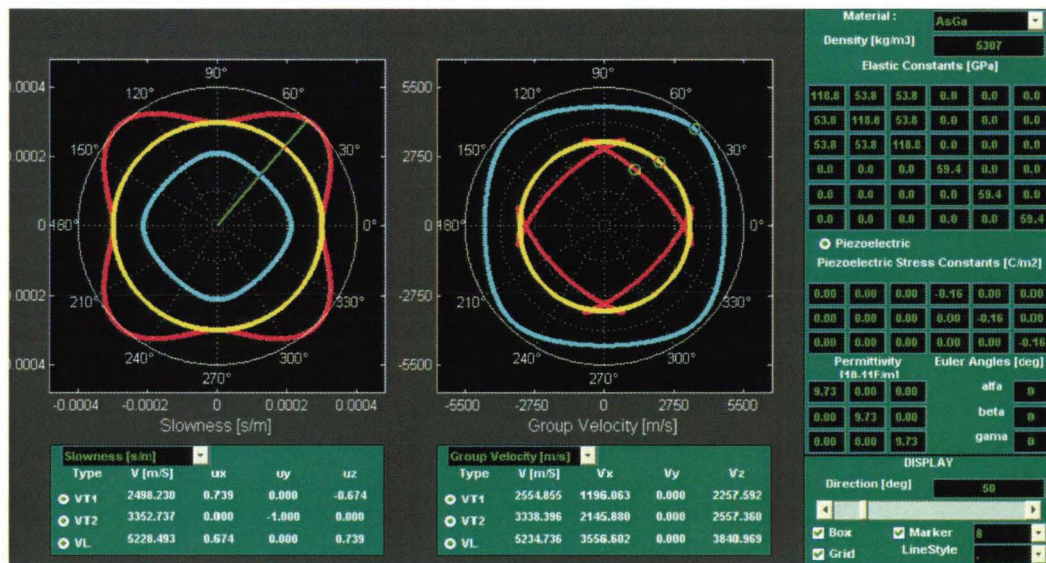


Figure 2.1.1: Software in Matlab codes with GUI interface for the calculation and displaying of plane wave phase velocity or slowness, wave polarization, group velocity and electromechanical coupling coefficient.

Table A.2.1.1 in Annex 2.1 cites the elastic constants c_{IJ} and the mass density ρ of some solid materials that may eventually be concerned in this works. Table A.2.1.2 in Annex 2.1 gives the stiffness piezoelectric constants and the permittivity for some typical piezoelectric materials.

In the calculation the velocity or the slowness surfaces can be cut in any plane

section by rotating three Euler angles of [Alpha, Beta and Gamma]. The displaying is always carried out in a reference plane of xOz [010]. The material constants data $(c_{IJ}^E, e_{kij}, \epsilon_{jk}^S)$ needs also to be transformed in the displaying coordinates. The method and procedure of axis transformations are explained in Annex 2.2.

Fig. 2.1.2 illustrates an example of the velocity surfaces for a non piezoelectric material as silicon that may be used as the backing material of the array transducer to be developed. Silicon single crystal has a cubic (m3m) symmetry that has the same velocity sections in the planes xOy [001], xOz [010] and yOz [100].

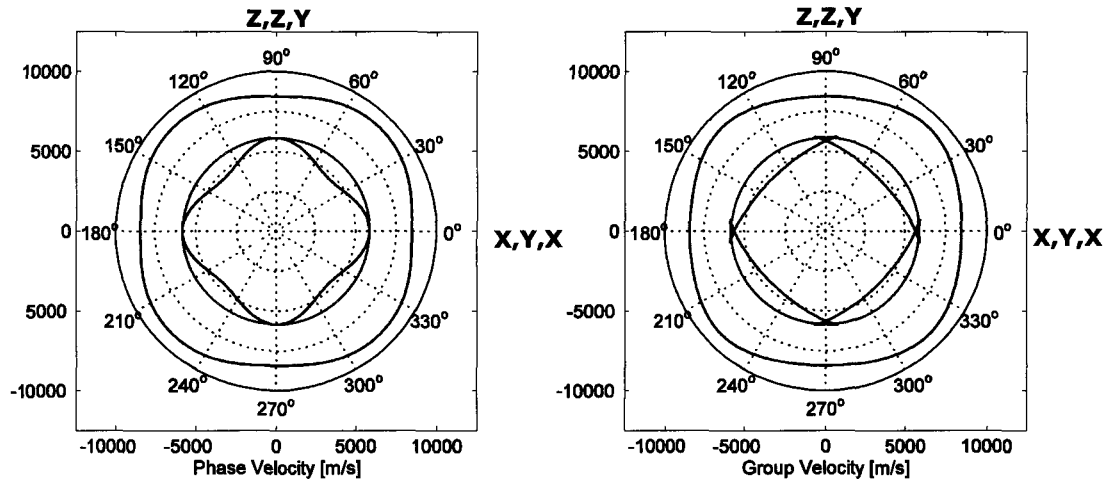


Figure 2.1.2: Sections of the phase velocity and the group velocity surfaces for silicon (class: cubic m3m) in [010], [100] and [001] planes (line in red for quasi-longitudinal wave; lines in blue and green for two quasi-transversal waves).

For the development of piezoelectric transducers, the choice of the piezo-active materials depends essentially on their piezoelectric property (the electromechanical coupling coefficient k_t), the acoustical (impedance) and the electrical (dielectric) properties and the complexity of the technologies to fabricate the transducers. To get better understanding and have a global view on k_t value evolution as a function of wave direction, it's necessary to observe the surfaces of k_t in 3-D coordinate system, as is usually processed for the phase or the group velocity of the materials. Among a variety of disposal piezoelectric materials, the traditionally most common used ones

for high frequency applications, include α -quartz (crystal-SiO₂), lithium niobate (LiNbO₃, LN), lithium tantalite (LiTaO₃, LT), zinc oxide (ZnO) and lead zirconate titanate ceramics (PZT-4, for example).

LiNbO₃ [99] and LiTaO₃ are two important and extensively used piezoelectric materials for applications of surface acoustic wave (SAW) and bulk acoustic wave (BAW) devices, piezoelectric transducers and sensors, optical waveguides, electro-optical modulators and various other optical applications. These two crystal materials belong to the same space class (3m) and have very similar piezoelectric property. Fig. 2.1.3 illustrates the three sections (planes [010], [100] and [001]) of slowness ($1/\bar{v}_p$) surfaces for LiNbO₃.

Here, the dashed lines correspond to the inactive piezoelectric-effect slowness curves, line in red for quasi-longitudinal wave, and lines in blue and green for two quasi-transversal waves. The wave modes in LiNbO₃ having piezoelectric effect are the quasi-longitudinal wave (in red) and the fast quasi-transversal waves (in blue). The slow quasi-transversal mode (in green) presents no piezoelectricity as its piezoelectric stiffened velocities are equal or inferior to the un-stiffened ones.

For longitudinal mode, it can be found that its electromechanical coupling coefficient k_r^L attains the maximum value of 0.494 in the [100] plane at an angle of $\theta = 30^\circ$ with respect to the y axis, while the transversal mode electromechanical coupling coefficient k_r^T is about 0.122. To avoid coupling between the longitudinal and transversal modes, this angle must be shifted to 36° with the k_r^L value slightly reduced to 0.485, where $k_r^T = 0$. This is the so called Y-cut/ 36° rotation for obtaining pure longitudinal thickness mode generation.

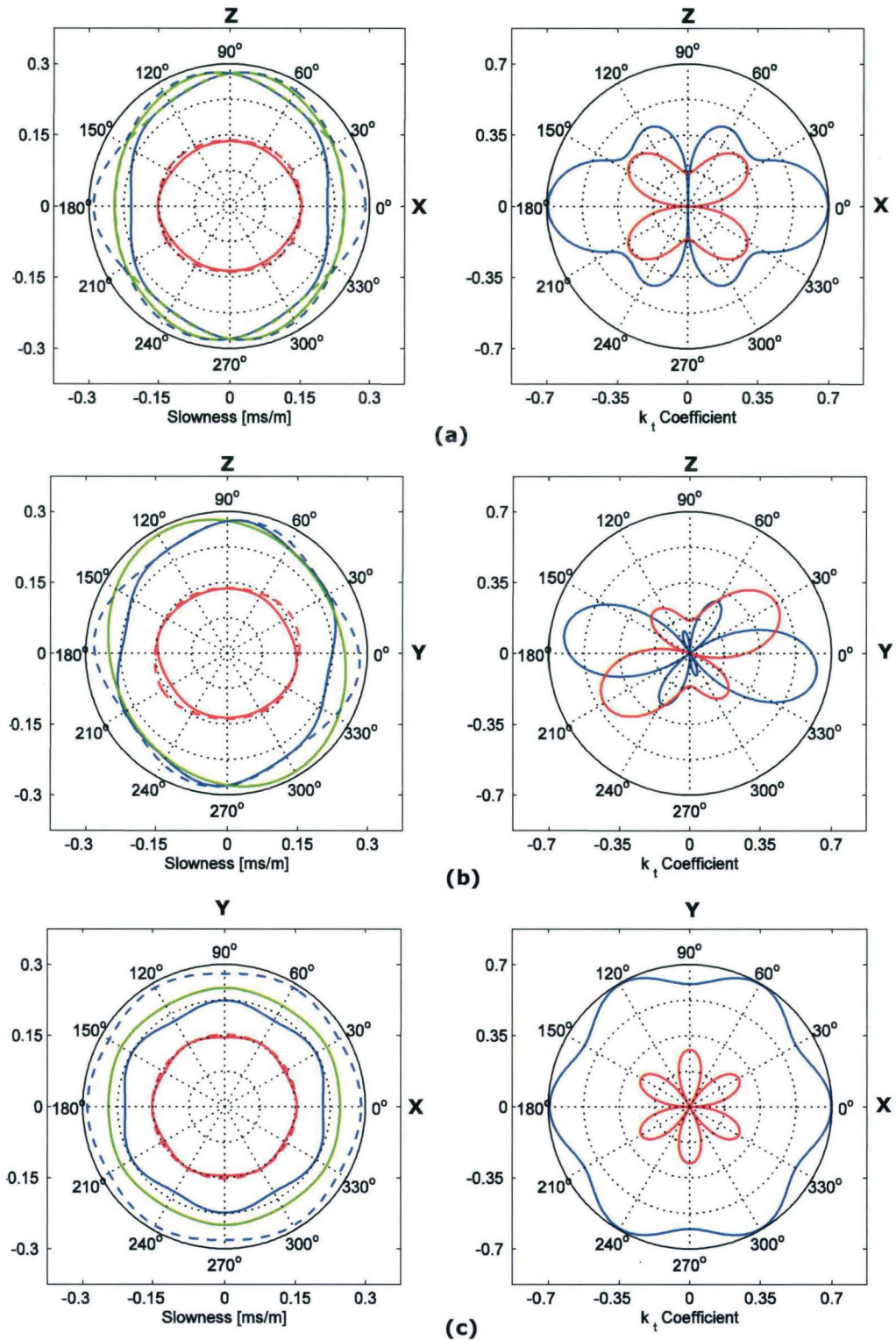


Figure 2.1.3: Sections of the slowness and the electromechanical coupling coefficient k_t surfaces for LiNbO₃ (class: trigonal 3m) in: (a) [010] plane (b) [100] plane (c) [001] plane.

In this same plane, the transversal mode has the maximum value of $k_i^T = 0.633$ at the angle of $\theta = 171^\circ$ with a $k_i^L = 0.131$. Similarly, to vanish k_i^L for efficient transversal mode generation, the angle θ will be orientated to 163° where $k_i^T = 0.610$ and $k_i^L = 0$. In the plane [010], only in one direction (along the z axis) single longitudinal mode exists ($k_i^T = 0$ and $k_i^L = 0.162$) and in another one direction (along the x axis) single transversal mode occurs ($k_i^L = 0$ and $k_i^T = 0.696$). In the [001] plane, there is no direction in which only one piezoactive mode exists.

For high frequency ultrasonic transducer development, zinc oxide (ZnO - an inorganic compound or crystal) is also a popular piezoelectric material. It has been widely used in different traditional industries and a lot of new and attractive properties are being found in advanced technologies for applications from thin-film and semiconductor devices, to photovoltaics, gas and nano-rod sensor^[100].

Figure 2.1.4 presents the elasticity and piezoelectricity of ZnO crystal that has space symmetry of hexagonal (class 6mm). It has a rotation invariance property around the z axis and is transversal isotropic in [001] plane. The maximum k_i^L value of 0.27 for longitudinal mode without mode coupling takes place in the direction of z axis. The maximum value of $k_i^T = 0.373$ for transversal mode is found in a direction of $\theta = 30.5^\circ$ with respect to the z axis with $k_i^L = 0.08$. The pure transversal mode ($k_i^L = 0$) locates at $\theta = 39^\circ$ with $k_i^T = 0.348$.

Another famous piezoelectric material for ultrasonic transducer use is the lead zirconate titanate (PZT in abbreviation), a ceramic composed of the elements lead (Pb), zirconium (Zr) and the compound titanate ($\text{Pb}[\text{Zr}_x\text{Ti}_{1-x}]\text{O}_3$ $0 \leq x \leq 1$)^[101,102]. The material symmetry is classified as hexagonal group of 6mm-transversal isotropy. The elasticity and piezoelectricity represented by slowness and electromechanical coupling coefficient k_i may be consulted in Fig. 2.1.5. The particular features of PZT are its high electromechanical coupling coefficient and extremely large dielectric

constant.

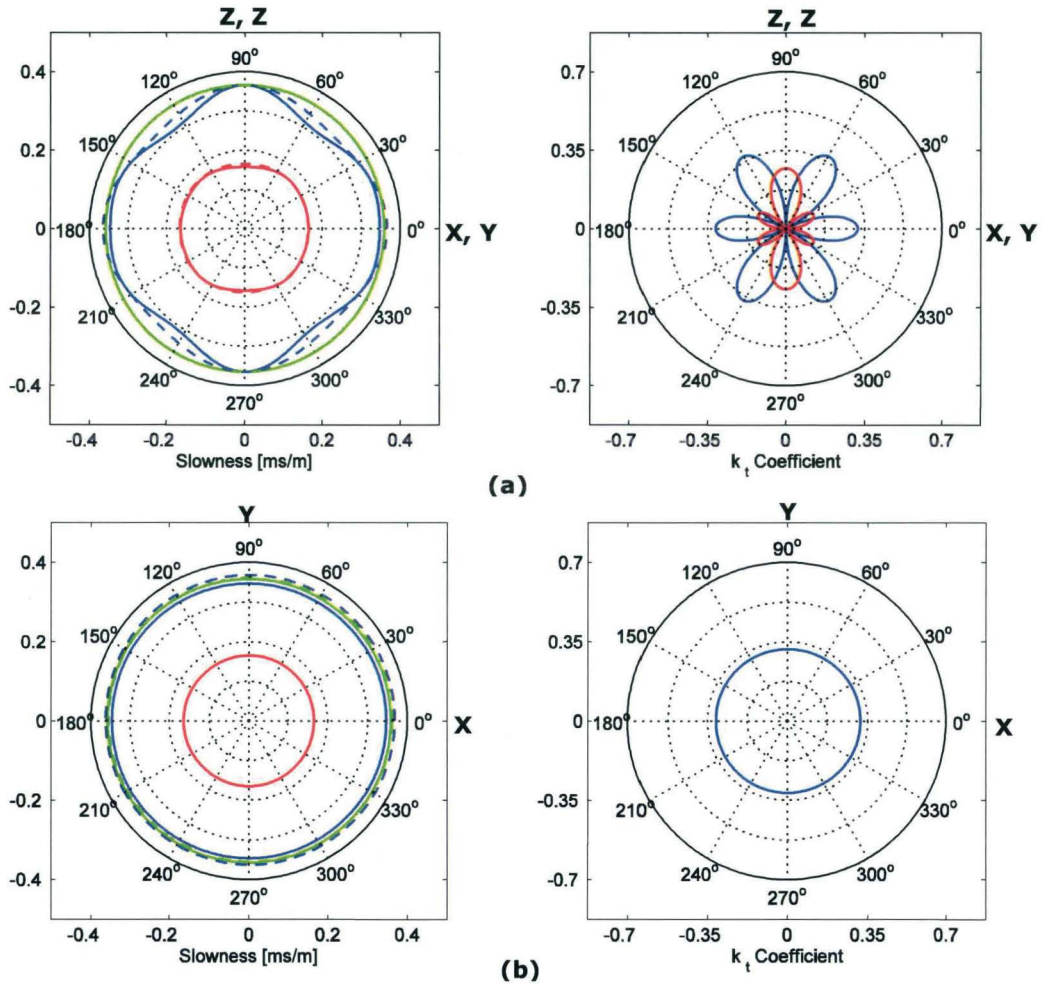


Figure 2.1.4: Sections of the slowness and the electromechanical coupling coefficient k_t surfaces for ZnO (class: hexagonal 6mm) in: (a) [010] and [100] planes (c) [001] plane. (dashed lines correspond to the inactive piezoelectric-effect slowness curves; line in red for quasi-longitudinal wave; lines in blue and green for two fast and slow quasi-transversal waves).

In conclusion, three piezoelectric materials as LiNbO_3 , ZnO and PZT may be the suitable candidates for high frequency (> 100 MHz) ultrasonic transducer with their own advantages and shortcomings. Generally speaking, a high performance ultrasonic transducer has a high transmission and receiving sensibility that requires the use of a high electromechanical coupling coefficient piezoelectric material. Both LiNbO_3 crystal ($k_t = 0.49$) and PZT ($k_t = 0.51$ for PZT-4) has a coupling coefficient superior to that of ZnO ($k_t = 0.27$). Secondly, to get efficient energy transmission ability and

large frequency bandwidth, the acoustic impedance of the transducer needs to be matched to that of ultrasonic wave radiating medium (usually a liquid of small impedance) and the electrical impedance be matched to that of the electronic pulser source.

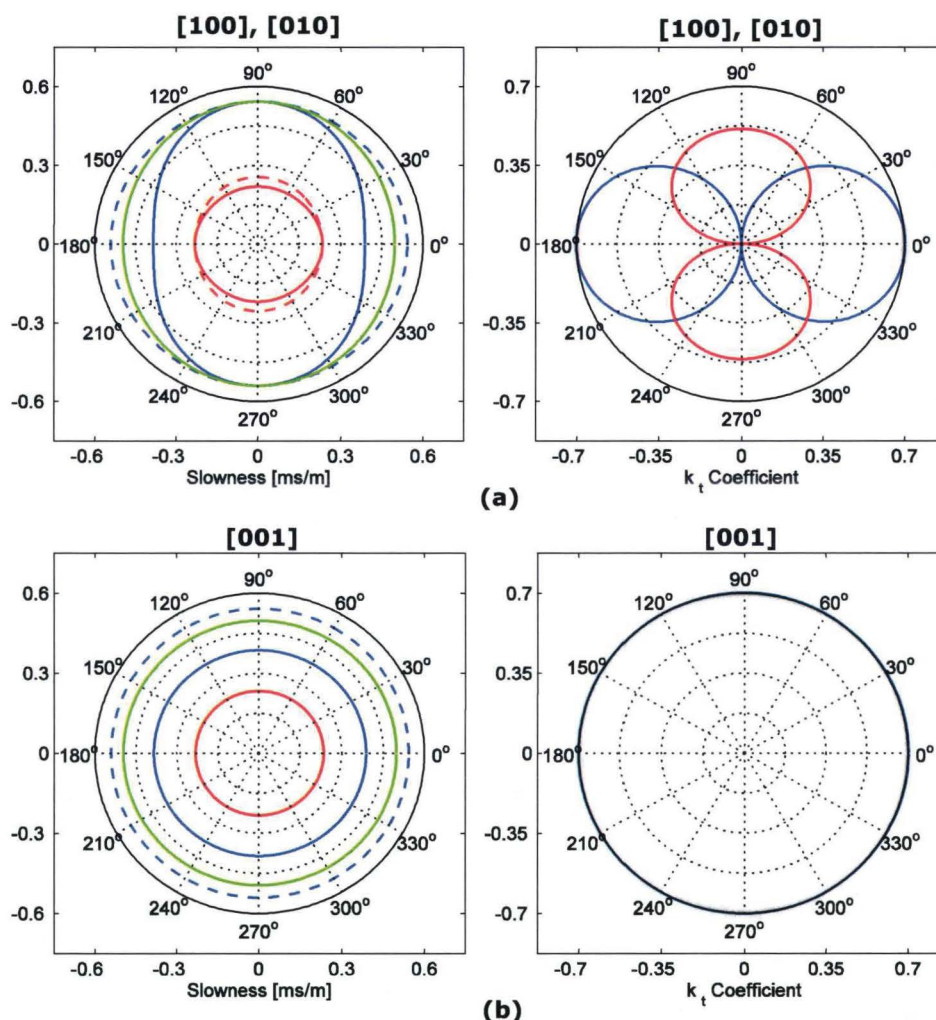


Figure 2.1.5: Sections of the slowness surfaces and the electromechanical coupling coefficient k_t for lead zirconate titanate (PZT-4) (class: hexagonal 6mm-trans.isotropic) in: (a) [010] and [100] planes (b) [001] plane. (dashed lines correspond to the inactive piezoelectric-effect slowness curves; line in red for quasi-longitudinal wave; lines in blue and green for two quasi-transversal waves)

The three materials have almost the same characteristic in term of the acoustic impedance (between 34 and 36 MRayls). For electrical properties, the electroded transducer will have a clamped capacitance whose value is proportional to the transducer surface area and the dielectric constant. At high frequency, the transducer

size is reduced (especially for array transducer) and the capacitive impedance will become very high. The PZT ceramic that has a large dielectric constant can compensate this high capacitive impedance and makes the electrical impedance matching easier. Thirdly, the cost and the technology complexity for the transducer fabrication will be the other important factors to be considered in the material choice. This will be the main topics in the following chapters.

2.2 Modelling and characteristics of piezoelectric transducers

A piezoelectric ultrasonic transducer exploits the piezoelectricity of materials to convert electrical energy to acoustical one and vice versa. To obtain a high energy conversion rate, one needs to choose a piezoelectric material of high electromechanical coupling coefficient k_t and cuts it into a layer at a suitable direction where only one particular wave mode (polarization) with a maximum k_t can be effectively excited. The cut layer is then electroded in its thickness d to form a “resonator”. When the resonator is excited, the fundamental resonance takes place near the frequency where the layer thickness is a half wave-length $f_0 = \frac{v_P}{\lambda} = \frac{v_P}{2d}$ with v_P the wave phase velocity. If the resonator is mechanically charged with a radiation medium, it transforms the electrical energy into the acoustic one and emits an acoustic wave into the medium. Such resonator becomes a transducer.

The optimum design of transducers in terms of their energy conversion efficiency, sensitivity, transmitting bandwidth, and matching, necessitates efficient modelling approaches. The electric network or transmission line theory, proposed by Mason ^[103,104,105], KLM (Krimholtz, Leedom and Matthae) ^[106,107] and other researchers ^[108], were developed, among which the KLM models ^[109,110,111,112] is the most commonly used.

2.2.1 KLM model

In KLM model, the three port equivalent network for piezo-active layer is described in Fig. 2.2.1. To represent electromechanical coupling, the transducer layer

is divided into two equal half thickness non piezo-active layers (left and right acoustical ports), and an electromechanical transformer is connected in the middle by injecting an “acoustic current” of Δv . The electromechanical transformer has a turn ratio of ϕ with an electrical impedance element Z'_e in the electrical port. Based on the network theory, it can be written

$$\begin{bmatrix} F_2 \\ v_2 \end{bmatrix} = \mathbf{A}_2 \begin{bmatrix} \Delta F \\ v'_2 \end{bmatrix} \quad \text{and} \quad \begin{bmatrix} \Delta F \\ v'_1 \end{bmatrix} = \mathbf{A}_1 \begin{bmatrix} F_1 \\ v_1 \end{bmatrix} \quad (2.2.1)$$

Wher $v'_2 = v'_1 + \Delta v$

$$\mathbf{A}_1 = \mathbf{A}_2 = \begin{bmatrix} \cos k_p d/2 & -jZ_p \sin k_p d/2 \\ -j \sin k_p d/2 / Z_p & \cos k_p d/2 \end{bmatrix} \quad (2.2.2)$$

are the A parameter matrices for the two half thickness layers, v'_2 and v'_1 are respectively the output current of the left acoustical port and the input current of the right acoustical port.

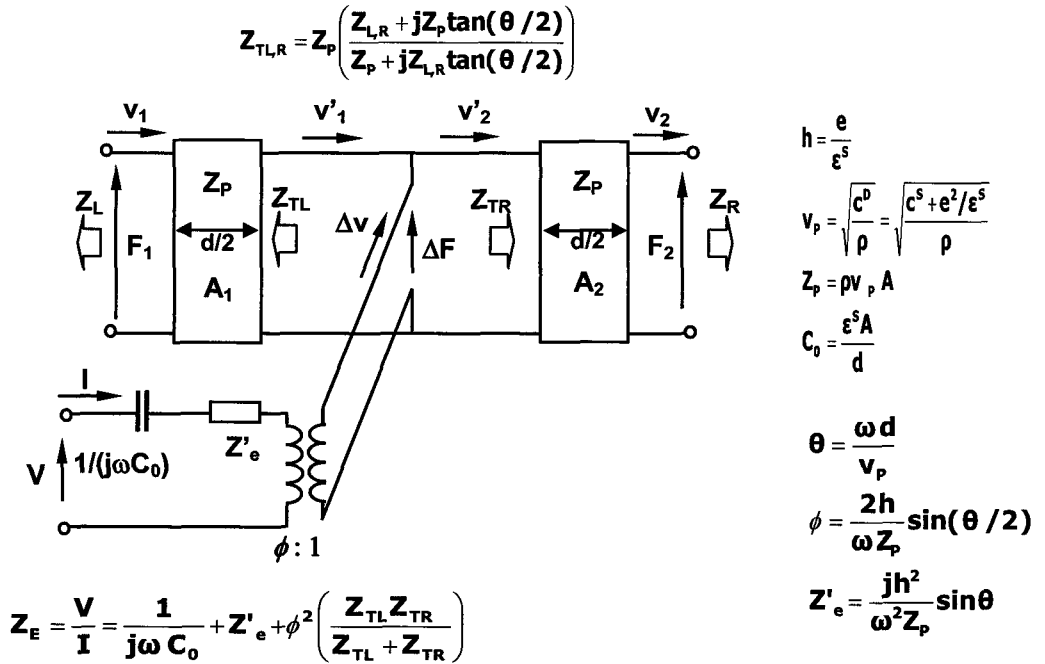


Figure 2.2.1: Schema of KLM equivalent circuit model of a piezoelectric layer working in thickness mode (here, $\theta = k_p d = \omega d / v_p$).

Using KLM model (1-D model), we can calculate the transmitting bandwidth and electrical impedance of the single element transducer (which can be seen as one-dimensional model). In the following part, the electrical impedance and acoustic impedance will be introduced and the importance of electrical matching and acoustic matching will be demonstrated by KLM calculation.

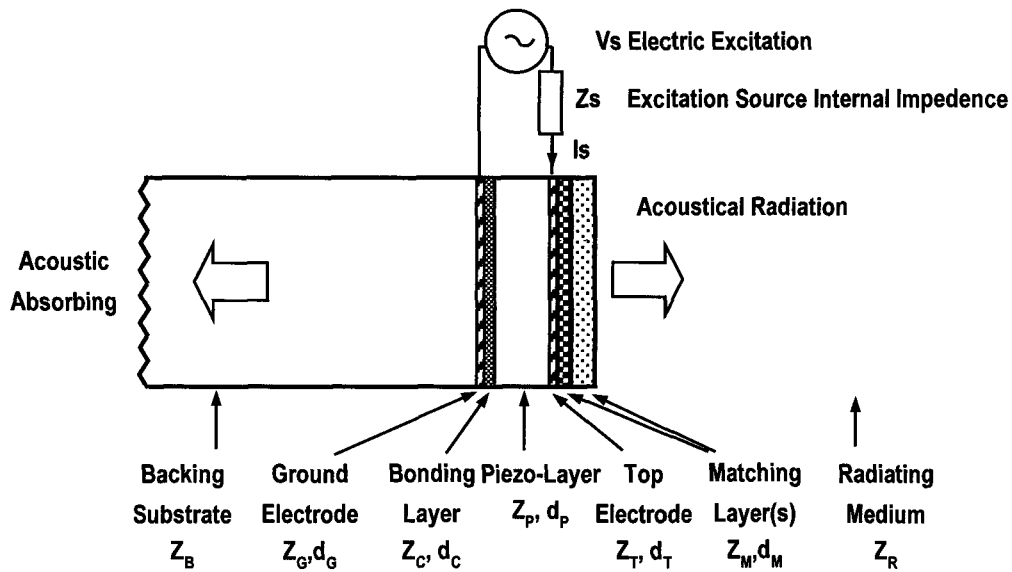
2.2.2 Structure and characteristics of high frequency piezoelectric transducers

There are essentially two kinds of structure configuration (Figure 2.2.2) to be studied for piezoelectric transducers of frequency superior to 100MHz (half wavelength layer thickness in the order of several to several tenths of micrometers). One is the backing structure (Figure 2.2.2 (a)) and the other is the buffered structure (Figure 2.2.2 (b)). Both have a multi-layered structure. Their characteristics and performances in terms of the electrical impedance, frequency transfer function and impulse response, insertion loss, can be simulated by Mason or KLM modelling. Transducers made of commonly used piezoelectric materials such as ZnO, LiNbO₃ and PZT-4 are considered here and their performances will be compared and analyzed. The material constants employed in simulation are resumed in Table A.2.1.3 in Annex 2.1.

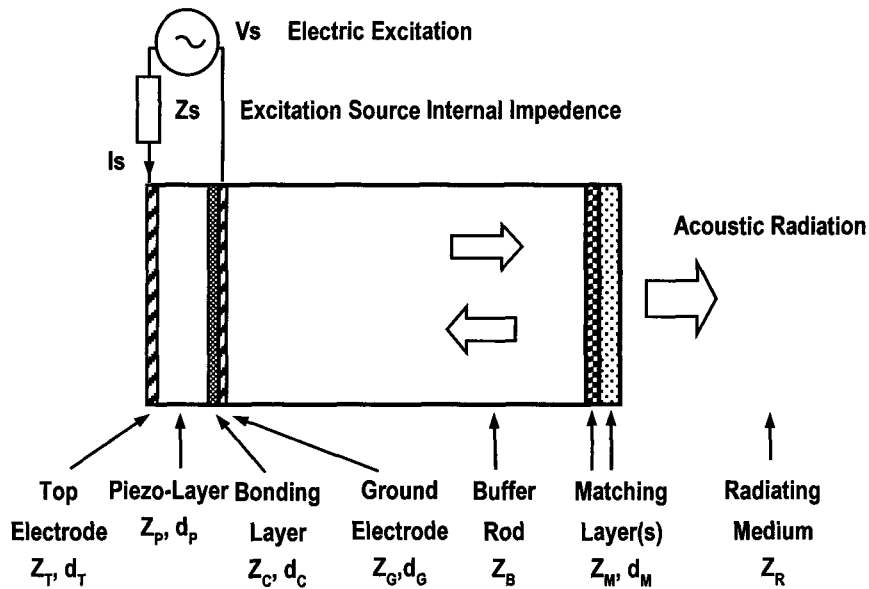
Before simulation, some well-known criteria and basic phenomena in the design of piezoelectric transducers need to be recalled. An optimized transducer is desired to have a large bandwidth and consequently short impulsion duration in transmission ultrasonic beam because it determines the axial resolution of imaging; a high sensibility (small insertion loss) to have high signal-to-noise ratio in ultrasonic testing and imaging; matched input electrical impedance and matched transmission mechanical impedance that condition the electromechanical conversion efficiency of the transducer. Simultaneous improvement of all these characteristics is usually difficult to be fulfilled and trade-offs must be taken, among which an optimization procedure is necessarily employed.

In all the following simulation, if not specifically indicated, the internal

impedance of the excitation source is considered to be 50Ω and the input impedance of the reception circuit is supposed to be a real resistance of $1 M\Omega$. The frequency functions are calculated in a range of frequency from zero to two times of resonant frequency and their impulsion response corresponds to that with limited band source excitation. All the transducers have a section area of $A = \text{wide} * \text{length} = 40 \mu\text{m} * 2 \text{ mm}$ and the normalized frequency f_0 is referred to as 100 MHz.



(a)



(b)

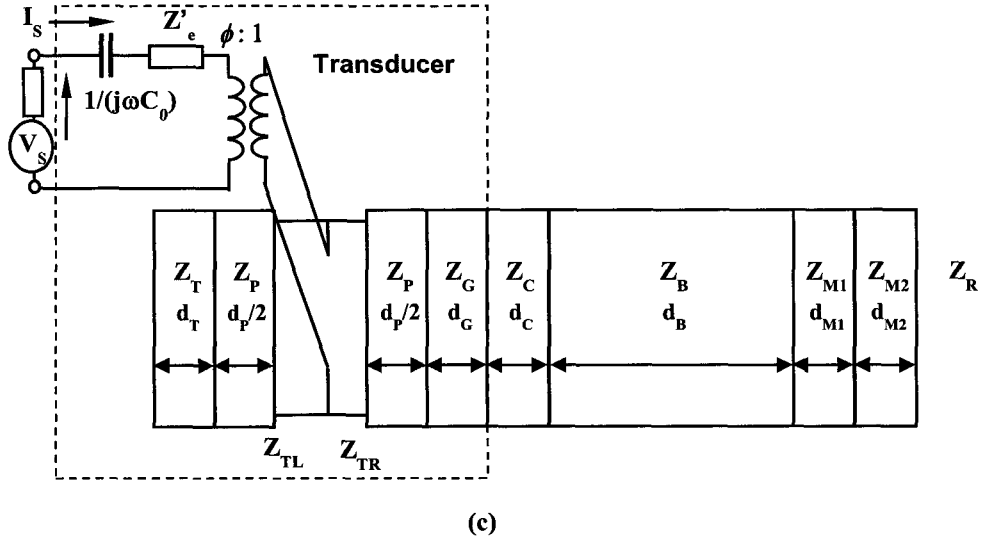


Figure 2.2.2: Piezoelectric transducer description: (a) Backing structure configuration; (b) Buffered structure configuration; (c) KLM model description of the transducer (b).

Figure 2.2.3 presents an example of the simulation results for three transducers of ZnO, LiNbO₃ and PZT-4, each with silicon baking and water front loading. The electrode, bonding and matching layers are not taken into consideration here. In Figure 2.2.3, are plotted the input electrical impedance Z_e in its magnitude, real and imaginary parts; the return (called also two ways or round trip) frequency transfer function $H_r(f/f_0)$ in its normalized magnitude $\frac{|H_r(f/f_0)|}{\max\{|H_r(f/f_0)|\}}$; and the corresponding insertion loss $-20\log|H_r(f/f_0)|$. The frequency axis is normalized in its half wavelength thickness resonant frequency f_0 . As the transfer function is given in its normalized form, the transducer sensibility can be deduced and compared by the insertion loss function. The time impulsion response is obtained by the inverse Fourier transform of $H_r(f/f_0)$, supposing that the frequency band of $H_r(f/f_0)$ or the exciting source signal frequency band is limited in a fixed range to avoid high order harmonic component excitation.

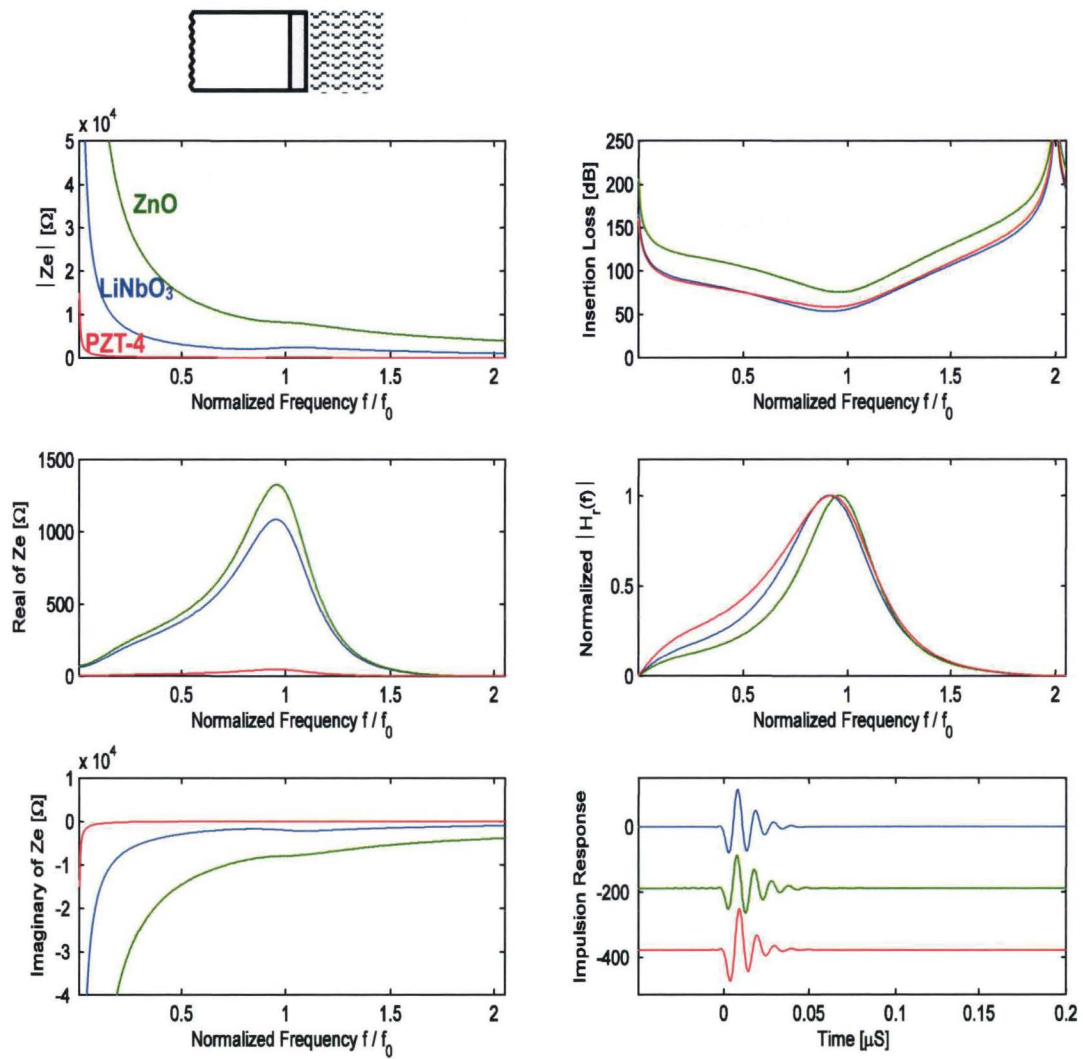


Figure 2.2.3: Electrical impedance, return transfer function and its impulse response for silicon backing and water front charged piezoelectric transducers of ZnO, LiNbO₃ and PZT-4.

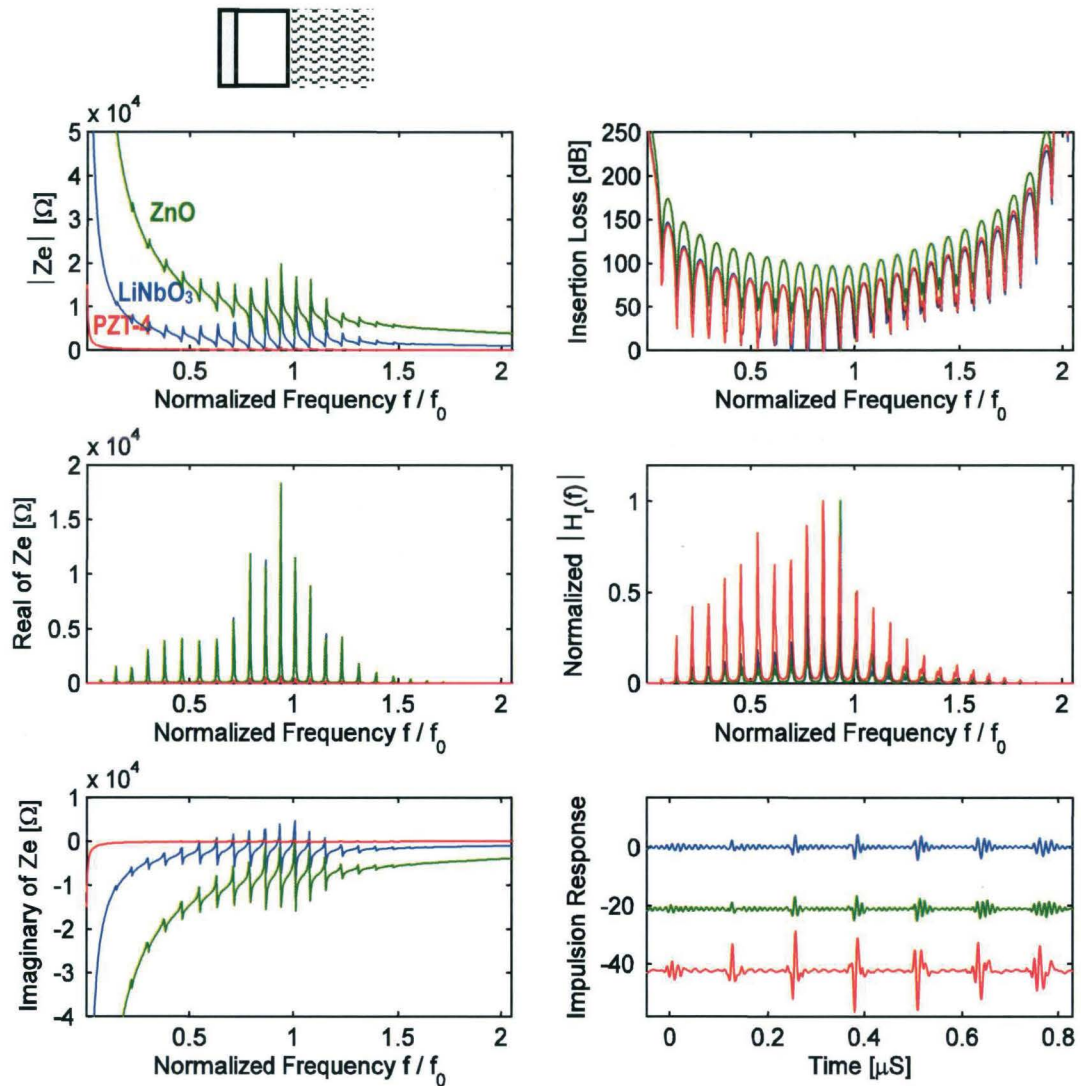


Figure 2.2.4: Electrical impedance, transfer function and impulse response for silicon buffered (0.5mm length) and water front charged piezoelectric transducers of ZnO, LiNbO₃ and PZT-4 at $f_0 = 100$ MHz.

It can be stated that the baking or front charge of a piezo-transducer as resonator will enlarge its bandwidth and reduce its resonant frequency (this can be characterized by the Q factor that is defined as the ratio of resonant frequency to the bandwidth). If the material dissipation is not considered, the real part of the electrical impedance corresponds to the energy radiation in the backing and transmission media. Concerning the material's piezoelectric characteristics, the PZT-4 has the most high

electromechanical coupling coefficient and dielectric constant. This permits the PZT-4 transducer to have an electrical impedance near 50Ω (about 43Ω) at its resonant frequency (100 MHz) with the given transducer dimension. The insertion loss (sensitivity) at the resonant frequency is about 55 dB for LiNbO_3 , 60 dB for PZT-4 and 75 dB for ZnO respectively.

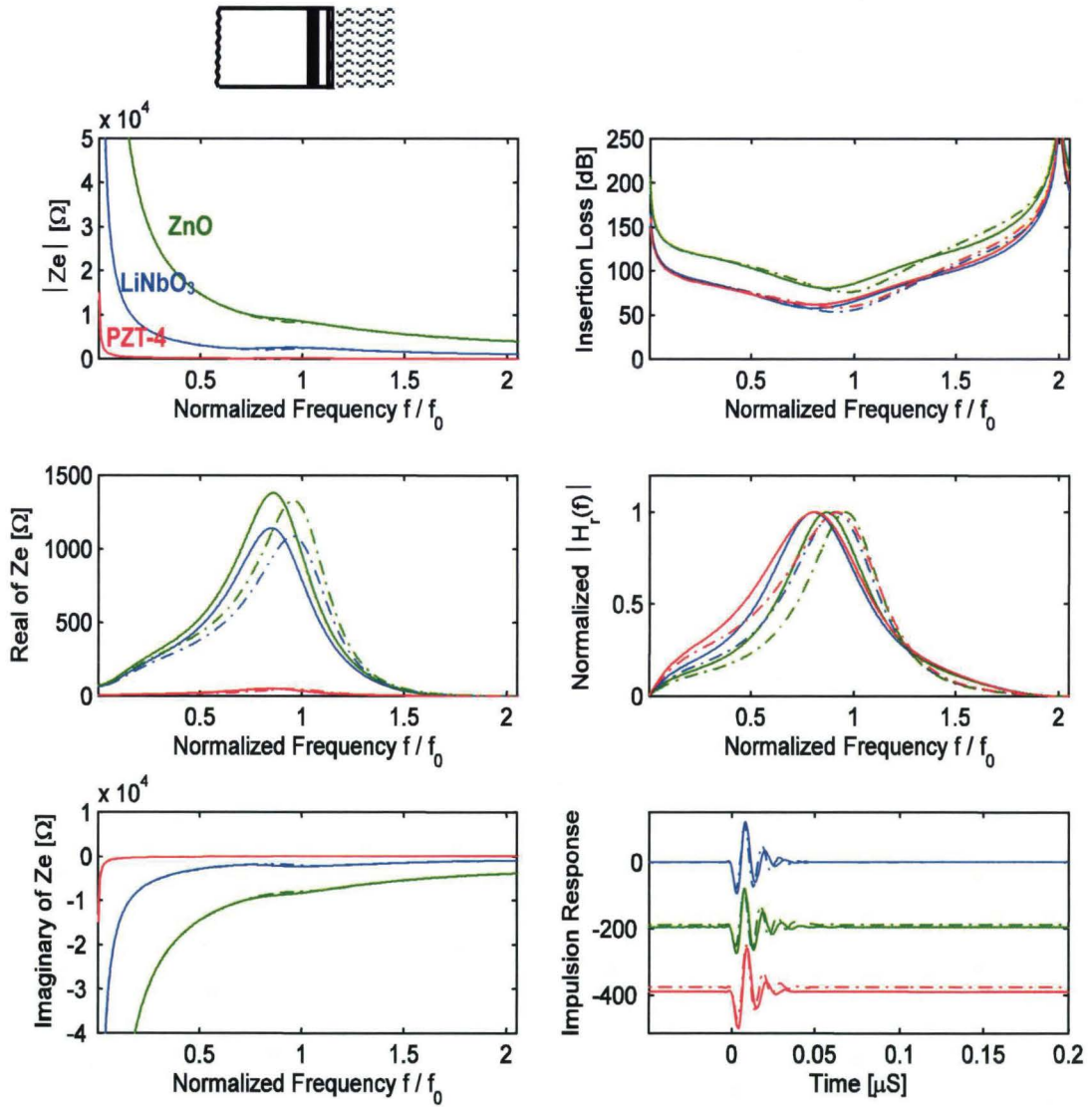


Figure 2.2.5: Comparison in electrical impedance, frequency transfer function and impulse response for silicon baked and water front charged piezoelectric transducers of ZnO, LiNbO_3 and PZT-4 at $f_0 = 100$ MHz with (solid line) and without (dash-point line) the presence of two electrodes (in gold of $0.5 \mu\text{m}$ thickness) and one bonding layer (in indium of $1.5 \mu\text{m}$ thickness).

Figure 2.2.4 is the simulation results for silicon buffered (0.5 mm in length) and water front charged piezoelectric transducers (without backing) of ZnO, LiNbO₃ and PZT-4. In such transducer configuration, comb like frequency functions are observed due to the high thickness of the silicon buffer forming the standing waves in the buffer. In the time impulsion response, multiple reflections between the transducer and the silicon-water interface occur. As can be observed, in the high order reflections, there is the dispersion of impulsions that is originated from the double-reflections by the two faces of the transducer layer at the one side of the buffer.

The influence of other parameters such as electrode, bonding layer, on the transducer performances, usually neglected with low frequency transducer, become important at high frequencies. Figure 2.2.5 gives the simulation by taking into account these layers with a silicon baking transducer of the structure: silicon (substrate) /gold-electrode (0.5 μm) /indium-bonding (1.5 μm) /piezo-layer/gold-electrode (0.5 μm) /water. Compared the results (solid lines) to those obtained without (dash-point lines) the integration of these layers: the main difference is a reduction in their resonant frequency and a slight increment in their electrical impedance. It should be noted that for high frequency transducers (> 100 MHz), the material dissipation factor needs usually to be taken into consideration.

2.2.3 Electrical impedance and electrical matching

For a piezoelectric transducer, its sensibility or the capacity to transform electrical energy to acoustic one (or inversely) depends one part on the electromechanical coupling coefficient of the piezoelectric material used, and another part on how the electrical impedance is matched between the transducer and the external driving source (generator or pulser).

The electrical impedance of an ultrasonic transducer consists of a capacitance $\frac{1}{j\omega C_0}$ due to the two metallic electrode layers (clamped capacity) in series (KLM) or in parallel (Mason) with another equivalent complex impedance coupled from the acoustic load. The energy dissipation on the real part of this latter impedance

corresponds to the acoustic energy transmission into the radiation medium and the heat dissipation in the material itself if it is considered. For an ideal electrical matching, the internal impedance of the generator should equal to the transducer input impedance. But in practice this is not feasible for a source generator to have its internal impedance adapted identically to a complex impedance of charged transducer. Usually a standard source generator possesses an internal impedance of 50Ω . In this case, one approach for the electrical matching is to neutralize the capacitance $\frac{1}{j\omega C_0}$

by adjusting in series an inductance $L_0 = \frac{1}{(2\pi f_0)^2 C_0}$ (called shunt inductance), where

f_0 is the transducer fundamental free resonant frequency.

Fig. 2.2.6 and Fig. 2.2.7 are respectively the simulation results obtained for three transducers of ZnO, LiNbO₃ and PZT-4 at $f_0 = 100$ MHz with and without such inductance impedance compensation. Compared Figures 2.2.6 with 2.2.7, it can be observed that the real part of the electrical impedance remains strictly unchanged. The transducer electrical impedance becomes real near the resonance. For ZnO transducer, the return insertion loss is significantly reduced near the resonant frequency which means an increment in the sensitivity, but with also a reduction in its bandwidth leading the impulsion response less damped. For LiNbO₃ transducer, the return insertion loss is improved and the bandwidth also enlarged, but few changes in damping. For PZT-4 one, there is no gain in the insertion loss with slight improvement in the bandwidth, keeping the best impulsion response damping. So the conclusion is that for sensitivity improvement the inductance compensation has the most significant effect on the ZnO transducer which has worst performance in term of the sensitivity.

Another advantage of inductance compensation is the suppression of high order harmonic generations.

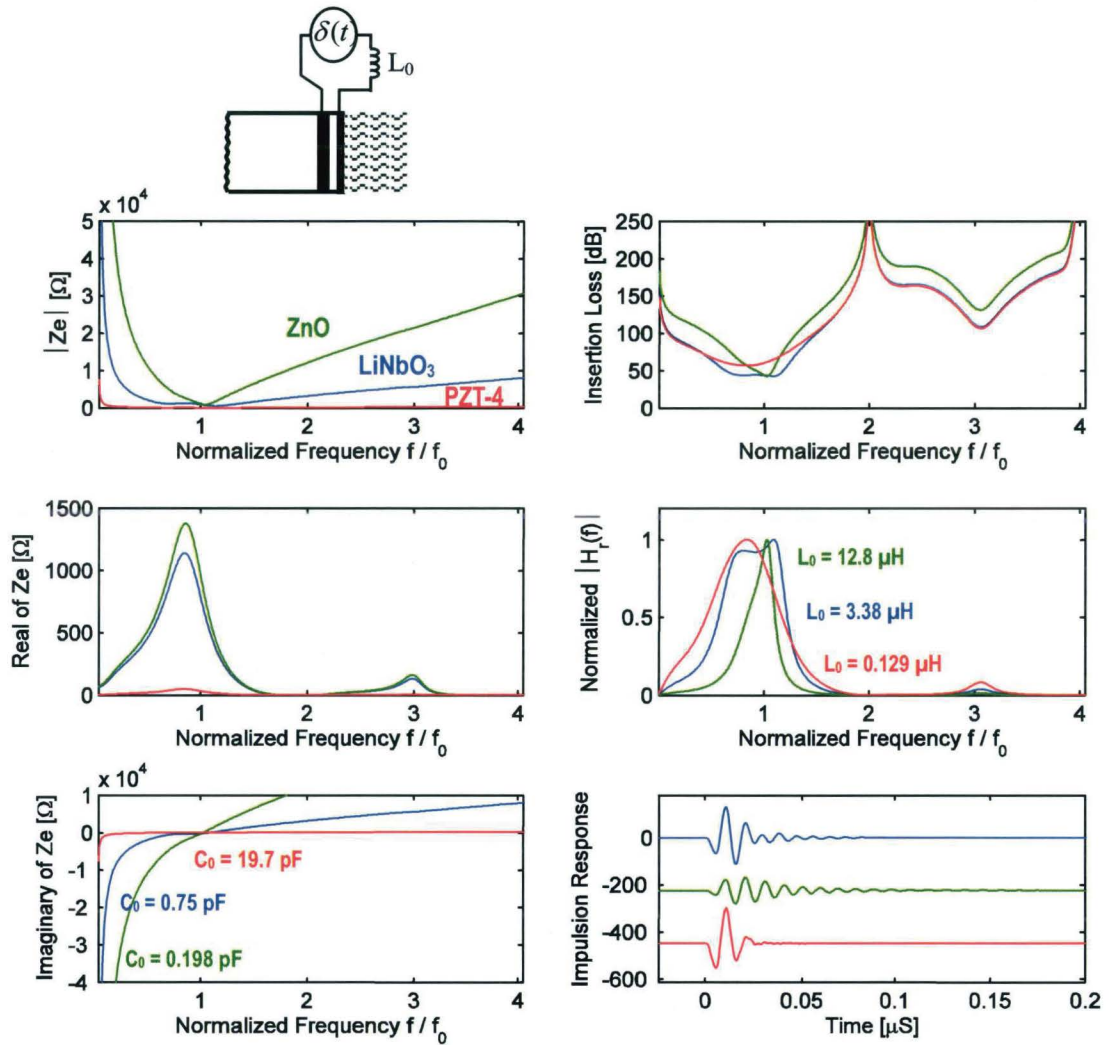


Figure 2.2.6: Electrical impedance, frequency transfer function and impulsion response for silicon backing and water front charged piezoelectric transducers of ZnO, LiNbO₃ and PZT-4 at $f_0 = 100$ MHz with the presence of electrodes ($0.5 \mu\text{m}$ gold layers) and bonding layer ($1.5 \mu\text{m}$ indium layer) and with the inductance compensation in series of $L_0 = 1/(2\pi f_0)^2 C_0$.

In the simulation results given in Figs. 2.2.6 and 2.2.7, the frequency functions are calculated up to four times of the free resonant frequency $4f_0$ instead of $2f_0$. It shows that there is an important third order harmonic resonance (Fig. 2.2.7) in the frequency responses, (much higher order resonances exist if we extend the frequency rang), and these peaks almost disappear for the compensated transducers (Fig. 2.2.6). In the Fourier inverse impulsion time responses, corresponding to those obtained with

an exciting source of at least $4f_0$ bandwidth, high frequency component will be superposed in the case without the inductance insertion (Fig. 2.2.7).

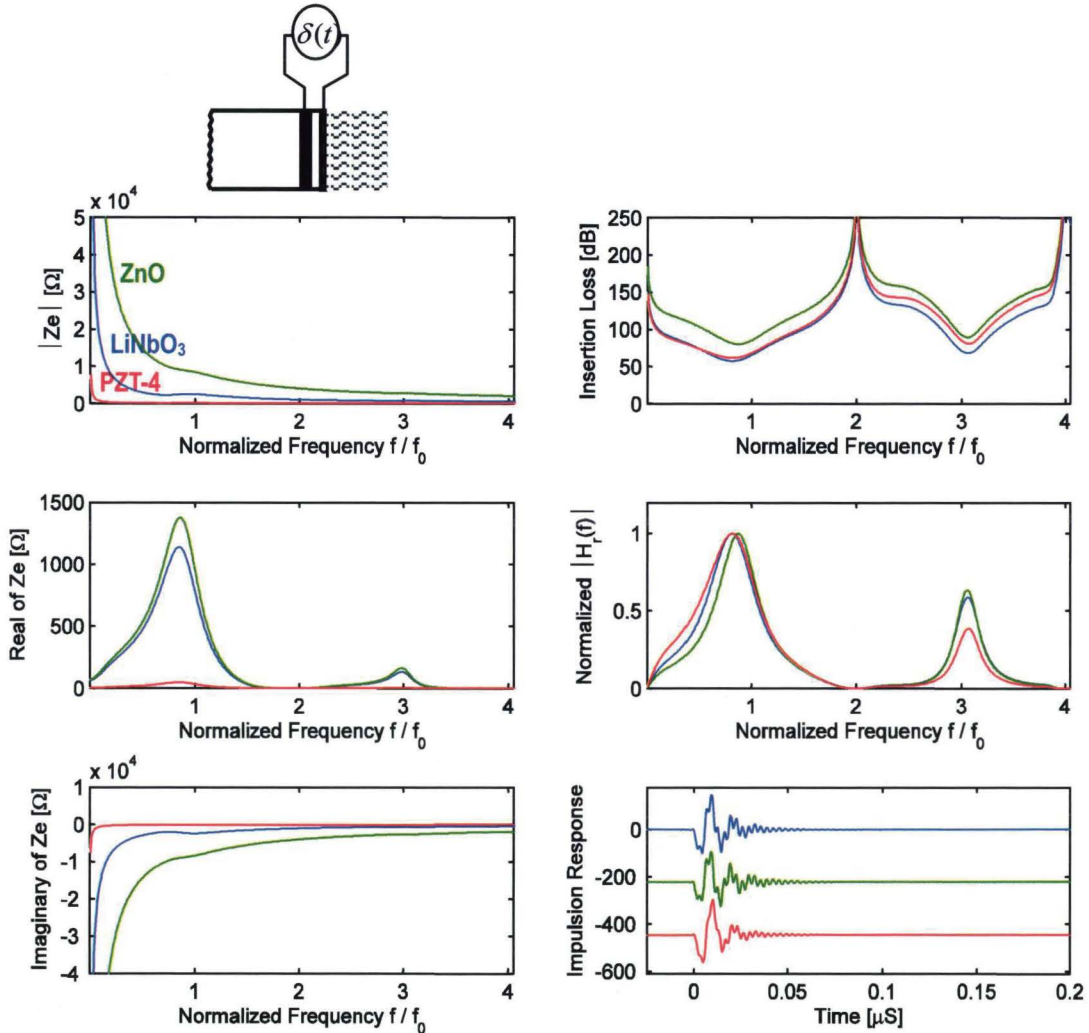


Figure 2.2.7: Electrical impedance, frequency transfer function and impulsion response for silicon backing and water front charged piezoelectric transducers of ZnO, LiNbO₃ and PZT-4 at $f_0 = 100$ MHz with the presence of electrodes (0.5 μm gold layers) and bonding layer (1.5 μm indium layer) with large band excitation.

2.2.4 Acoustic impedance and mechanical matching

Similar to electromagnetic waves in transmission line ^[113], a propagating acoustic wave will be partly reflected at the interface of two media having different acoustic impedance ^[114]. The reflectivity depends on the level of the impedance

rupture. Insertion of a quarter-wavelength layer between the two media permits a maximum energy transmission of the wave, conducting an “acoustic impedance matching”. For a piezoelectric ultrasonic transducer, to increase the energy transmission ability and enlarge the frequency bandwidth, it’s necessary to carry out the acoustic impedance matching between the transducer made of piezo-active material (such as crystal, ceramics, polymer or composite) having high acoustic impedance (34~36 MRayls for ZnO, LiNbO₃, PZT) and the transmission or load medium (usually a liquid or viscous-elastic tissue) of low impedance (1.5 MRayls for water).

A free piezo-layer resonator with no energy radiation has very sharp resonant peak. However, a mechanically charged piezo-transducer, either by backing or by buffer, expands significantly its frequency bandwidth ^[115]. For buffered structure transducers, all the excited wave energy is first transmitted into the buffer. The matching is hence performed between the buffer and its front load (both non active media) to favourite the through transmission of the wave from the buffer to the load or vice versa. While for backing structure transducers, one part of energy is absorbed in the backing side of the transducer and the matching needs to be realized between the transducer layer and the front load in the aim to transmit more useful energy towards the loading side. In this latter case, the matching layer is either mechanically or electrically coupled to the source layer, modifying the transducer’s vibration behavior when it’s excited.

Consider a matching layer of impedance Z_M and thickness d , inserted between two media having different acoustic impedance: Z_I for the incident medium and Z_T for the transmission one. From KLM model, the acoustic impedance as seen by the incident medium and looking into the matching layer is

$$Z_{in} = Z_M \frac{Z_T + jZ_M \tan(k_M d)}{Z_M + jZ_T \tan(k_M d)} \quad (2.2.3)$$

The pressure reflection and transmission coefficients by and through the layer can be calculated from

$$R(f) = \frac{Z_{in} - Z_I}{Z_{in} + Z_I}, \quad T(f) = \frac{2Z_{in}}{Z_{in} + Z_I} \quad (2.2.4)$$

and the transmission coefficient in power density

$$T^e(f) = 1 - R(f)R^*(f) = T(f)T^*(f)Z_I / Z_T \quad (2.2.5)$$

where $R(f) = \frac{(Z_T / Z_I - 1) + j(Z_M / Z_I - Z_T / Z_M) \tan(2\pi f d / v_M)}{(Z_T / Z_I + 1) + j(Z_M / Z_I - Z_T / Z_M) \tan(2\pi f d / v_M)}$ with v_M the wave

phase velocity in the matching layer.

When $d = (2n + 1) \frac{\lambda_M}{4}$, there is $Z_{in} = Z_M^2 / Z_T$. So the matching condition is

$$Z_I = Z_M^2 / Z_T$$

or $Z_M = \sqrt{Z_I Z_T} \quad (2.2.6)$

with $R(f) = 0$ and $T^e(f) = 1$.

To better understand the improvement in the transducer sensibility and the bandwidth by acoustic matching, the above developed KLM model can be used to simulate the transducer's behavior. For the transducers of the three piezo-materials such as ZnO, LiNbO₃ and PZT-4 considered, their acoustic impedance is respectively 35.93MPa, 34.50MPa and 34.18MPa (Table A.2.1.3 in Annex 2.1). To get these materials matched to water ($Z_T = 1.5MPa$), the impedance of quarter-wavelength matching layer has to be 7.431MPa, 7.194MPa and 7.160MPa respectively. As these impedance values are very close, only the results for silicon backing LiNbO₃ transducer will be presented.

Fig. 2.2.8 and Fig. 2.2.9 display the simulation results for the LiNbO₃ transducer on the transfer functions by varying respectively the matching layer impedance and its thickness. A fictive matching material of phase velocity 2886 m/s, giving $\lambda_M / 4 = 7.215\mu m$ at 100 MHz, was used in calculation. Fig. 2.2.8a and Fig. 2.2.9a represent respectively the wave energy transmission coefficient through the matching layer from the LiNbO₃ to the water for different values of the impedance Z_M and the thickness d of the matching layer. The transmission coefficients behave just like the

wave transmission on a segment of transmission line: having a maximum unity coefficient at the matching condition ($Z_M = \sqrt{Z_I Z_T}$ and $d = \lambda_M / 4$) and the mismatch by the impedance will reduce the peak amplitude while the variation in the thickness shifts the peak's frequency position (decreased for $d > \lambda_M / 4$ and increased for $d < \lambda_M / 4$).

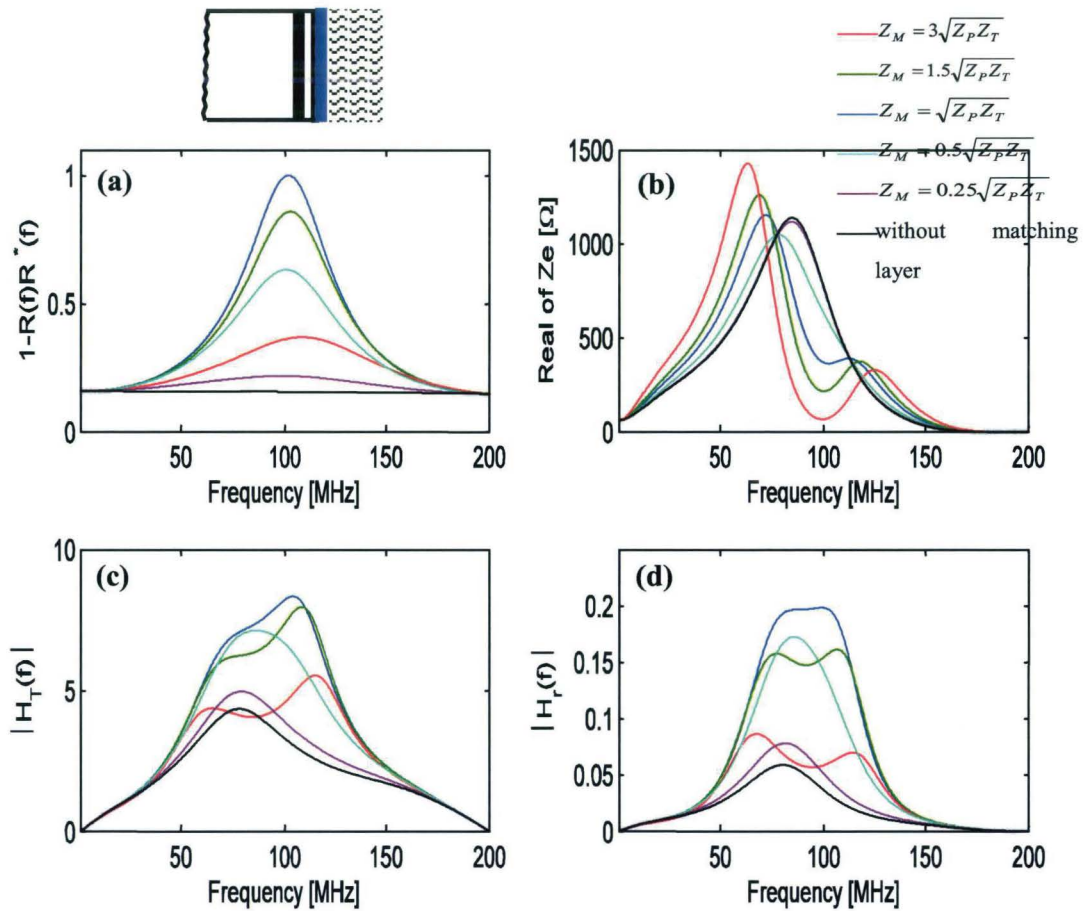


Figure 2.2.8: Insertion of single quarter-wavelength matching layer $d = \lambda_M / 4 = 7.2 \mu m$ in different acoustic impedance Z_M for LiNbO_3 transducer ($Z_p = 34.5 \text{ MPa}$) of 100 MHz free resonant frequency with water front load ($Z_T = 1.5 \text{ MPa}$), (a) Energy transmission coefficient $1 - R(f)R^*(f)$ from piezo-material to water load; (b) Real part of the transducer electrical impedance $\text{Re}(Z_e)$; (c) Forward transfer function $H_T(f)$ (d) Return transfer function $H_r(f)$.

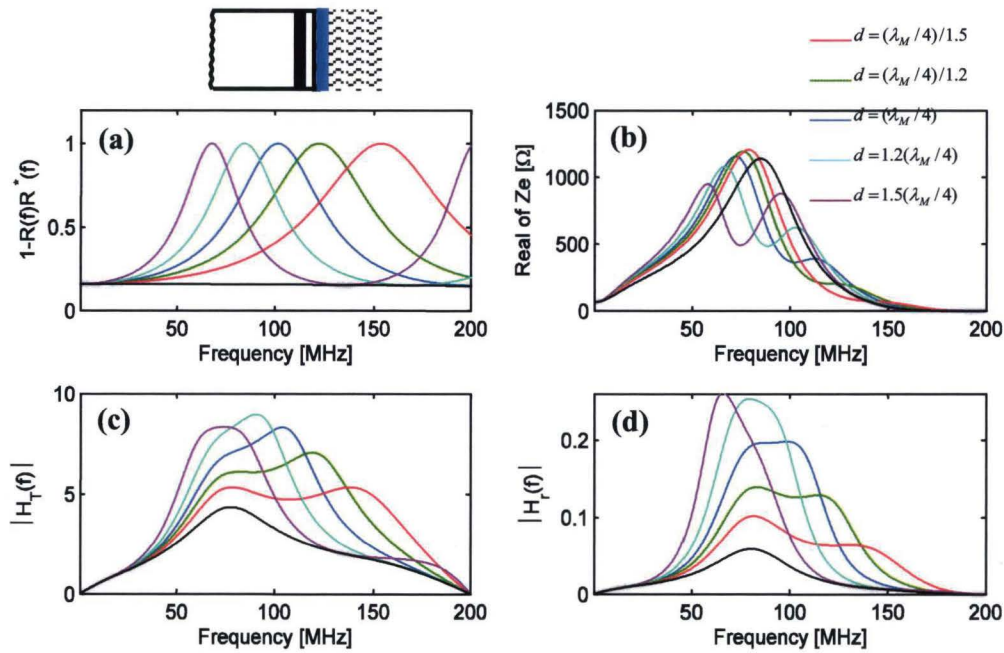


Figure 2.2.9: Insertion of single matching layer $Z_M = \sqrt{Z_P Z_T} = 7.194 \text{ MPa}$ in different thickness for LiNbO_3 transducer ($Z_P = 34.5 \text{ MPa}$) of 100 MHz free resonant frequency with water front load ($Z_T = 1.5 \text{ MPa}$), (a) Energy transmission coefficient $1 - R(f)R^*(f)$ from piezo-material to water load; (b) Real part of the transducer electrical impedance $\text{Re}(Z_e)$; (c) Forward transfer function $H_T(f)$ (d) Return transfer function $H_r(f)$.

Fig. 2.2.8b and Fig. 2.2.9b show the influences of the matching layer on the transducer equivalent electrical impedance. Figures (c) and (d) of (2.2.8) and (2.2.9) are respectively the frequency forward transfer function $H_T(f)$ and return transfer function $H_r(f)$ from which the gain H_{\max} (sensitivity) and the bandwidth BW of the transducer can be determined. It can be concluded that at $d = \lambda_M/4$ the mismatch in impedance will reduce the transducer sensitivity H_{\max} and BW decreases for $Z_M < \sqrt{Z_I Z_T}$ and increase for $Z_M > \sqrt{Z_I Z_T}$; at $Z_M = \sqrt{Z_I Z_T}$ the

reduction (increase) in matching layer thickness $d < \lambda_M / 4$ ($d > \lambda_M / 4$) will enlarge (reduce) BW and reduce (increase) H_{\max} . Compared to the results obtained for no matching case (the curves plotted in black), the gain in H_{\max} and BW is significant, which confirms the importance and the necessity of the acoustical matching in the transducer performance improvement.

As shown above, the ideal matching takes place only at a single frequency for $f = v_M / \lambda_M$, or in other words, the transducer sensibility reaches its maximum at its matching frequency. There is usually a trade-off between the transducer sensitivity and the frequency bandwidth. To break such limitation, the possible solution is the utilization of multiple quarter wavelength matching layers with progressive impedance variation, which permits to keep the maximum through transmission and to further widen the bandwidth. In the literatures, many studies in this domain have been reported and different formalism based on different optimization criteria have been established [116,117,118,119]. The widely used is the double quarter matching layer [120,121,122]. The multilayer (number > 2) or graded matching scheme [123,124,125,126], though much interesting, will increase significantly the cost and the complexity in its fabrication process. More information of multiple quarter wavelength matching could be found in Annex 2.3.

Technically, there is a large choice of materials available for use of acoustic matching layers [127]. Epoxy resin, parylene, and composite have been the commonly used materials for traditional matching layers in the transducers development [128]. Advanced material technologies permit to elaborate the material whose acoustic impedance could be arbitrarily adjusted to meet the required value. However for transducers working at the frequencies up to or more than 100 MHz, realizing such layers requires specific material fabrication technology with high precision [129,130,131,132].

2.3 Summary

This chapter presents the theoretical fundamentals of piezoelectric ultrasonic

transducers. Waves equations in fluids, solid materials and piezoelectric materials are given and phase velocity, slowness, group velocity and electromechanical coupling coefficient are presented by numerical solution of Christoffel equation.

KLM model is introduced and used to simulate the properties of different transducers based on three commonly used piezoelectric materials – ZnO, LiNbO₃ and PZT-4. The three materials have almost the same characteristic in term of the acoustic impedance which results in little difference in mechanical matching. LiNbO₃ and PZT-4 possess higher electromechanical coupling coefficient than ZnO. Although the PZT ceramic that has a large dielectric constant can compensate high capacitive impedance at high frequency and makes the electrical impedance matching easier, ZnO thin films have more flexibility in the fabrication due to the integration with microfabrication technology such as sputtering. In this thesis, ZnO and LiNbO₃ are chosen to be active materials considering the technology complexity and the foundation of our lab in LiNbO₃ high frequency transducers. The realized arrays will be presented in Chapter 4 and Chapter 5 in detail.

KLM model is also used to calculate the transmitting bandwidth and the electrical impedance in a single element transducer. The electrical matching and mechanical matching is demonstrated to be critical in improvement of the transducer's performances. In the following chapters, the one-layer acoustic matching will be included in the array transducer design and FEM simulation.

Chapter 3: Finite Element Modeling of Piezoelectric Ultrasonic Array Transducers

Designing array transducers is a critical issue for further improving the quality of ultrasonic imaging. For this purpose, it is necessary to gain fundamental understanding on the transducer operations in order to design new and novel arrays. Many issues in array design-such as acoustic field, crosstalk, and electrical impedance-cannot be accurately studied using analytic method^[133] due to mainly the complexity of geometric structure. Finite element method (FEM) is an efficient appropriate way to obtain the exact solution^[134].

The establishment of the modelling procedure is very important for improving transducer designs and exploring new designs. Using FEM simulation, we can optimize the element geometry, pitch size, kerf width, kerf depth, kerf filler and all the active and passive materials used in the transducer. In other words, it can help us find the best combination to produce a desired transducer.

COMSOL, a finite element software, becomes more and more popular in numerical simulations because of its perfect performances in coupling of multiphysics modules and the simplicity in postprocessing. In this chapter, the appropriate model is established in COMSOL and compared to the results from the analytic model (such as KLM model). The wave propagations in solid (including isotropic and anisotropic solids) and in fluid (with Partial Differential Equation (PDE) module) are studied at first. Then piezoelectric transducer is coupled with non piezoelectric materials. Some special simulations are carried out in piston mode, including wave steering excited by linear phased array sources and wave scattering of coarse boundary (rough surface). Most of the results were obtained using the COMSOL finite element models, and the general meshing scheme is to maintain at least 8 elements per wavelength. Optimized meshing size was obtained by continuously reducing the element size until the relative error for a calculated target quantity between consecutive runs is less than 1%.

Based on these models, we propose a buffered array structure and some

important characteristics are investigated for this piezoelectric array, such as acoustic field, crosstalk, electrical impedance, and etc.

3.1 Finite element formalism using COMSOL

A flow diagram is illustrated in Figure 3.1 for modelling and simulation using COMSOL3.5a. Attention needs to be paid on three points: governing equations, boundary conditions and source of excitation. The following parts will emphasize on these points.

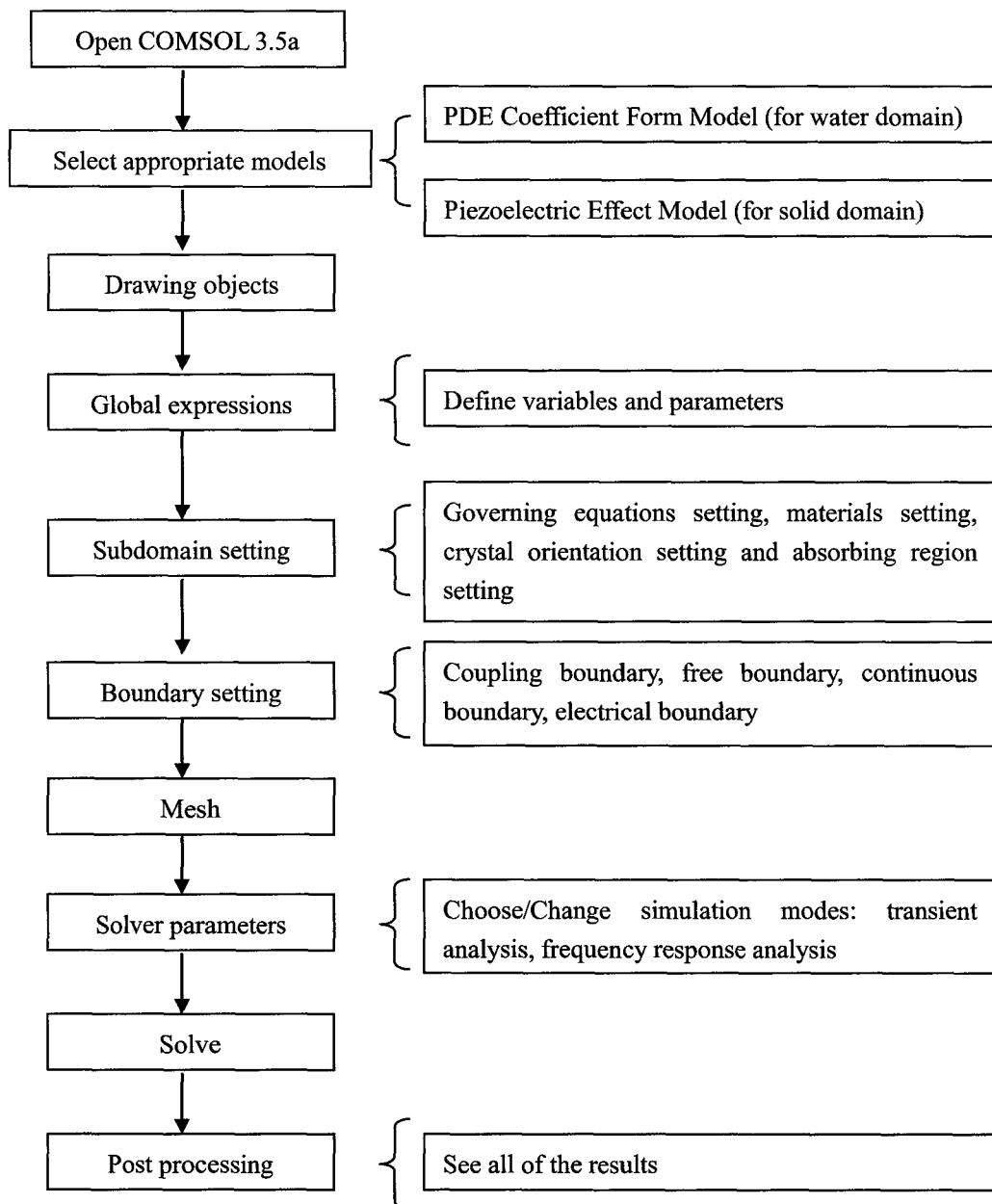


Figure 3.1: Flow diagram of modelling and simulation using COMSOL 3.5a

3.1.1 PDE and COMSOL formalism

For solid medium: in time domain and in frequency domain

The general form of force-free ($f = 0$) dynamic equilibrium equation for a solid medium with density ρ and elastic stiffness tensor c_{ijkl} is given as:

$$c_{ijkl} \frac{\partial^2 u_l}{\partial x_j \partial x_k} = \rho \frac{\partial^2 u_i}{\partial t^2}, \quad i, j, k, l=1, 2, 3 \quad (3.1.1)$$

Simulation of wave propagation in time domain is hard to be realized due to the limit from number of degrees of freedom and numerous time steps. Normally, modeling needs to be carried out in frequency domain (using a resonant frequency) to avoid these shortages and give some information such as directivity patterns. Since the wave motion concerned here is harmonic, Eq. (3.1.1) should be converted to that in frequency domain by using the Fourier transform as below:

$$c_{ijkl} \frac{\partial^2 u_l}{\partial x_j \partial x_k} + \rho \omega^2 u_i = 0, \quad i, j, k, l=1, 2, 3 \quad (3.1.2)$$

where, $\omega = 2\pi f$ is the angular frequency.

The “**Plain Strain Module**” in “**Structural Mechanics Module**” of COMSOL 3.5a is selected to simulate wave propagation in non-piezoelectric solid materials. The piezoelectric materials need “**Piezo Plane Strain Module**” in **Piezoelectric Effects**. Using these modules, we only need to give values to c_{ijkl} and ρ for a particular solid (non-piezo) material or c_{ijkl} , e_{jkl} , ϵ_{ij} and ρ for a piezoelectric medium, no matter in transient analysis or in frequency analysis.

For fluid medium: in time domain and in frequency domain

In our simulation, no external force is applied to the fluidic domain, so $f = 0$, and Eq. (2.1.4) becomes:

$$\nabla^2 p - \frac{\rho_0}{\lambda'} \frac{\partial^2 p}{\partial t^2} = 0 \quad (3.1.3)$$

Using the Fourier transform this equation can be converted to:

$$\nabla^2 p + \frac{\rho_0}{\lambda'} \omega^2 p = 0 \quad (3.1.4)$$

“PDE Coefficient Form” in “Multiphysics” is selected to model wave motion in fluid medium. A variable p , pressure, is defined here. Since COMSOL has special required formalism for PDE in time domain as below:

$$e_a \frac{\partial^2 p}{\partial t^2} + d_a \frac{\partial p}{\partial t} + \nabla \cdot (-c \nabla p - \alpha p + \gamma) + a p + \beta \cdot \nabla p = f \quad (3.1.5)$$

According to Eq. (3.1.3), we can set e_a as density ρ (e.g., $e_a = 1000 \text{ kg/m}^3$ for water), c as bulk modulus λ' (e.g., $c = 2.2 \cdot 10^9 \text{ N/m}^2$ for water) and all the other coefficients including d_a , a , α , β , γ and f as zero, and then Eq. (3.1.5) is converted to Eq. (3.1.3).

In frequency domain, the formalism in COMSOL is as follows:

$$\nabla \cdot (-c \nabla p - \alpha p + \gamma) + a p + \beta \cdot \nabla p = f \quad (3.1.6)$$

According to Eq. (3.1.4), we can set a as $\rho \cdot \omega \cdot \omega$ (e.g., $a = 1000 \cdot \omega \cdot \omega$ for water), c as bulk modulus λ' (e.g., $c = 2.2 \cdot 10^9 \text{ N/m}^2$ for water) and all the other coefficients including α , β , γ and f as zero, and then Eq. (3.1.6) is converted to Eq. (3.1.4).

3.1.2 Sources of excitation

For piezoelectric medium: in time domain and in frequency domain

To generate ultrasonic waves with piezoelectric materials, a dynamic electric potential is applied to this active material. In transient analysis, a sine pulse is first defined in global expressions in COMSOL, with source = $\sin(2 \cdot \pi \cdot f \cdot t) \cdot (t < 1/f)$ and $f = 100 \text{ MHz}$ (here t is time in COMSOL, and its default unit is second). Then give ‘source’ to piezoelectric material as electric potential in electric boundary conditions. In stationary analysis, the amplitude and the phase of the sine pulse are directly applied to the piezoelectric material as electric potential in electric boundary conditions. And its frequency is defined in the setting of solver.

For solid medium: in time domain and in frequency domain

To generate ultrasonic waves with a solid (non-piezoelectric material), the sources can be loaded either as volume forces in the medium or surface forces (or displacements) on the boundaries, which correspond to load in domain settings or

load in boundary settings in the solid plain strain module.

For fluid medium: in time domain and in frequency domain

To generate ultrasonic waves in fluidic medium, the sources can be loaded either as volume forces in the medium or surface forces (or displacements) on the boundaries, which correspond to \mathbf{f} in domain settings or \mathbf{g} in Neumann boundary conditions in PDE module (or \mathbf{r} in Dirichlet boundary condition) according to COMSOL formalism, respectively.

3.1.3 Boundary conditions

3.1.3.1 Coupling boundary conditions

For solid/fluid coupling boundary condition

As mentioned above, PDE Coefficient Form is used to simulate wave motion in fluids. In PDE module, the formalism in COMSOL is as follows (for convenience, the formalisms in COMSOL are displayed here again as shown in Eq. 3.1.7 and Eq. 3.1.8):

$$e_a \frac{\partial^2 p}{\partial t^2} + d_a \frac{\partial p}{\partial t} + \nabla \cdot (-c \nabla p - \alpha p + \gamma) + \alpha p + \beta \cdot \nabla p = f, \text{ in } \Omega, \text{ (in time domain)} \quad (3.1.7)$$

or

$$\nabla \cdot (-c \nabla p - \alpha p + \gamma) + \alpha p + \beta \cdot \nabla p = f, \text{ in } \Omega, \text{ (in frequency domain)} \quad (3.1.8)$$

$$\mathbf{n} \cdot (c \nabla p) = g, \text{ on } \partial \Omega, \text{ (Neumann conditions)} \quad (3.1.9)$$

or

$$hp = r, \text{ on } \partial \Omega, \text{ (Dirichlet conditions)} \quad (3.1.10)$$

where, Ω is the computational domain; for the situation including several subdomains, it is the union of all subdomains; $\partial \Omega$ is the domain boundary; and \mathbf{n} is the outward unit normal vector on $\partial \Omega$.

Eq. (3.1.7) and Eq. (3.1.8) are the PDEs, which must be satisfied in Ω . Eq. (3.1.9), a generalized Neumann boundary condition, and Eq. (3.1.10), a Dirichlet boundary condition, are the boundary conditions that must be held on $\partial \Omega$.

As to set boundary conditions, choose for each boundary Neumann condition or Dirichlet condition according to the actual situation.

Since the relation between the pressure and the displacement field in fluid is given by $\mathbf{grad}(p) = \rho \cdot \omega^2 \cdot \mathbf{U} = -\rho \cdot (\partial^2 u / \partial t^2)$ [135], the mechanical boundary conditions at the solid/fluid interface can be expressed as

$$\begin{cases} \mathbf{n} \cdot \mathbf{T} = -p & \text{at the solid side} \\ \mathbf{n} \cdot (c \nabla p) = c \cdot \rho \cdot a_n & \text{at the fluid side} \end{cases} \quad (3.1.11)$$

where \mathbf{T} is stress tensor and \mathbf{n} is the interface outward unit normal vector on $\partial\Omega$ which is illustrated in Fig. 3.1.1. Moreover, p is the pressure at the fluid side and a_n is the normal particle acceleration at the solid side. For example, in time domain, $-a_n = utt \cdot \mathbf{nx_solid} + vtt \cdot \mathbf{ny_solid}$ (u, v are defined variables in solid module, which mean x displacement and y displacement, respectively; utt stands for $\partial^2 u / \partial t^2$ and vtt for $\partial^2 v / \partial t^2$ in COMSOL). Thus, Neumann conditions is used to couple fluid and solid, and set \mathbf{g} as $-c \cdot \rho \cdot (utt \cdot \mathbf{nx_solid} + vtt \cdot \mathbf{ny_solid})$ (e.g., $\mathbf{g} = -2.2 \cdot 10^{12} \cdot (utt \cdot \mathbf{nx_solid} + vtt \cdot \mathbf{ny_solid})$ for water). In frequency domain, the condition should be:

$$\mathbf{g} = c \cdot \rho \cdot \omega^2 \cdot (u \cdot \mathbf{nx_solid} + v \cdot \mathbf{ny_solid}).$$

At the solid side, set boundary force load as below (the formalisms are the same in time domain and in frequency domain):

$$\mathbf{F}_x = -p \cdot \mathbf{nx_solid},$$

$$\mathbf{F}_y = -p \cdot \mathbf{ny_solid}.$$

For solid/solid coupling boundary condition

Furthermore, the mechanical boundary conditions should be continuous at the solid/solid interface. In fact, in COMSOL, if the variables of displacement, u, v , have the same formalism to stand for the same meaning in different subdomains, continuous condition is default at their interface. We do not need to change anything at the solid/solid interface.

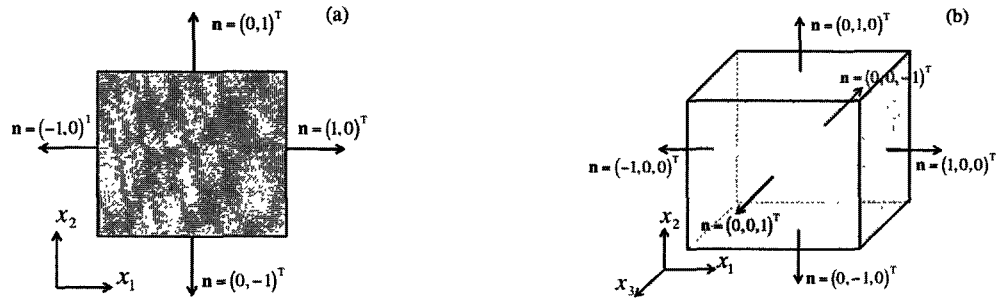


Fig. 3.1.1 Outward unit normal vector on $\partial\Omega$: (a) 2-D model; (b) 3-D model.

3.1.3.2 Symmetrical boundary conditions

The FEM calculation always takes a huge memory in COMSOL. To avoid out of memory problem and to reduce calculation time, symmetrical boundary conditions are sometimes applied. The calculated domain should be half (one axial symmetry) or quarter (two orthogonal axes symmetry) of the whole domain using this method. In solid modules, symmetrical boundary condition has already existed. However, for a fluid medium in PDE module, there is no existed symmetrical boundary condition. In fact, according to the indication of Neumann conditions, we can set $\mathbf{g} = 0$ on the desired boundary to obtain a symmetrical boundary condition. At this time, it manifests $\mathbf{n} \cdot (c\nabla p) = 0$. It means the gradient of the pressure is zero along normal direction of this side.

3.1.3.3 Absorbing boundary condition

Different from simulations in time domain, what is modeled in frequency domain is the continuous (or sine) wave distribution of the acoustic field. For this reason, it is not convenient to have snapshots of the acoustic field at any time point for the propagation process, and the total field hence appears as a summation of the incident wave and multiple reflections from all the boundaries before the fully attenuation of the waves, which will make the simulation results really complicated for analysis and even nonsense. So it is necessary to remove all the reflections from bulk boundaries. The most convenient solution is to add Absorbing Region (AR) all around the edges of the model to suppress any unwanted reflection. This will provide constructive results in frequency domain. Essentially, there are typically two kinds of AR, one is

Viscoelastic Absorbing Region (VAR) and the other is called Perfectly Matched Layer (PML).

A. Viscoelastic Absorbing Region

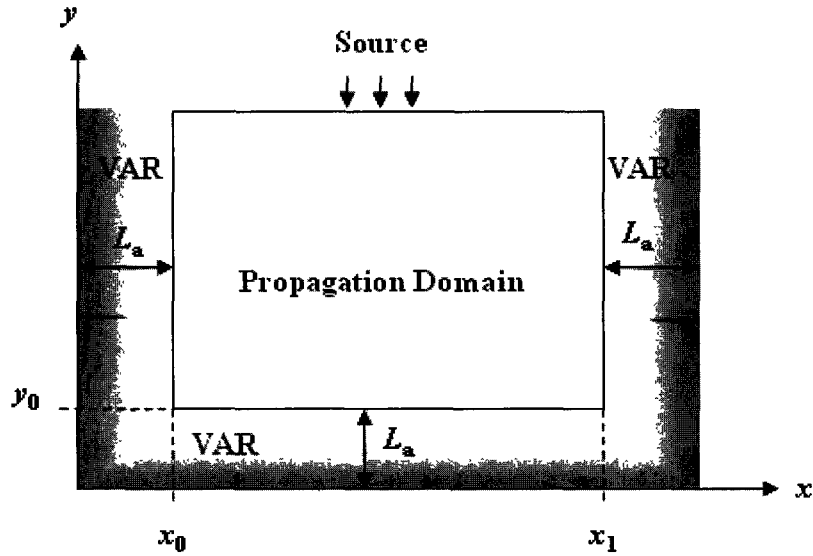


Figure 3.1.2: Settings of 2-D VAR

The visco-elasticity of materials is usually described by complex stiffness modulus, where the real and imaginary parts are related to the elastic and damping properties, respectively. The imaginary parts, which will subsequently appear in the damping term of displacement solutions, is directly linked to attenuations in the amplitudes of waves, so VAR is set by continuously increasing the imaginary parts of the complex modulus, in order to accelerative absorb the waves without causing reflections because of the discontinuity in material properties (acoustic impedance).

In this case, as shown in Fig. 3.1.2, for a 2-D model, if the length of VAR is set to be L_a , the AR will locate in the area $x < x_0$, $x > x_1$ and $y < y_0$, outside the Propagation Domain (PD). To attain the aim of minimizing the amplitudes of reflections to 0.1% of that of incident waves, the length of VAR can ultimately be reduced to 3 times of the maximum wavelength ($L_a \geq 3\lambda_{\max}$) of all the propagating modes after optimization^[136].

For a solid material with stiffness constants c_{ij} (c_{ij} is real), the c_{ij}^{AR} in VAR is

defined in COMSOL as follows:

$$c_{ij}^{AR} = c_{ij} + i * c_{ij} * A_0 * (A_1 + A_2 + A_3)$$

$$A_1 = \left(\frac{x_0 - x}{L_a} \right)^n * (x < x_0), \quad A_2 = \left(\frac{x - x_1}{L_a} \right)^n * (x_1 < x), \quad A_3 = \left(\frac{y_0 - y}{L_a} \right)^n * (y < y_0) \quad (3.1.12)$$

where, x is a variable, denoting the distance from a point in VAR to the interface between VAR and PD; and A_0, x_0, x_1, y_0, n are constants to be optimized.

In the same way, for a viscoelastic material with complex $c_{ij} = c'_{ij} + i c''_{ij}$, the c_{ij}^{AR} in VAR is defined as:

$$c_{ij}^{AR} = c_{ij} + i * c'_{ij} * A_0 * (A_1 + A_2 + A_3) \quad (3.1.13)$$

Here, A_0, A_1, A_2, A_3 are the same as in Eq. 3.1.12.

B. Perfectly Matched Layer

Similar to VAR, PML is also set all around the PD, and as indicated by its name, the main principle to set a PML is to keep the acoustic impedance in the AR always match with that of the PD at the aim of absorbing waves. To reveal the nature of the performance of PML, a simple example is cited.

For linear acoustics in fluid with mean density ρ_0 and speed of sound v_0 , the linear wave equation for acoustical pressure p with angular frequency ω is:

$$\nabla^2 p - k^2 p = 0, \quad k = \omega/v_0 \quad (3.1.13)$$

And the corresponding plane wave solution is

$$p = p_0 e^{i(\omega t - k \vec{r})} \quad (3.1.14)$$

where \vec{r} is the position vector along the direction of propagation.

For this medium, the acoustic impedance, also called as characteristic impedance is

$$Z_a = \rho_0 v_0 \quad (3.1.15)$$

For the simplest case, when a sound wave incident perpendicularly from PD medium 1 into AR medium 2, the reflection coefficient R , which is related to the acoustical impedances of the adjacent media, is defined as:

$$R = \frac{Z_{a2} - Z_{a1}}{Z_{a2} + Z_{a1}}, \quad Z_{a1} = \rho_1 v_1, \quad Z_{a2} = \rho_2 v_2 \quad (3.1.16)$$

If Z_{a1} is matched to Z_{a2} , $R = 0$, which means non-reflection.

On the other hand, we can set the density ρ^{AR} and wave velocity v^{AR} in AR to make the wave from the fluid fully attenuated by:

$$\rho^{AR} = \rho_0 (1 - i\sigma_0), \quad v^{AR} = \frac{v_0}{(1 - i\sigma_0)} \quad (3.1.17)$$

Rewrite the motion equation for a harmonic wave as:

$$\nabla^2 p - [k(1 - i\sigma_0)]^2 p = 0 \quad (3.1.18)$$

σ_0 , which can also be a function, is a constant here, related to damping ratio.

And the corresponding solution is

$$p = p_0 e^{i(\omega t - k\vec{r})} e^{-\sigma\vec{r}} \quad (3.1.19)$$

Here, $\sigma = \sigma_0 k$ is the damping coefficient, and the term $e^{-\sigma\vec{r}}$ leads to attenuation of wave during propagation.

In this way, the wave is “absorbed” in the AR and no reflection comes back to the PD.

C. Improved Absorbing Boundary Condition

A deeper insight indicates that in the aspects of absorbing, the nature of performance by changing material properties in VAR is quite similar to that of PML. VAR and PML have basic principles in common: one is “absorbing”, the other one is avoiding reflection, no matter by continuously changing the material properties or keeping the acoustic impedance matched. In VAR, an increasing imaginary part (standing for attenuation) is only added to each term of c_{ij} (however, the acoustic impedance changes in VAR, which will induce a small reflection to degrade the accuracy of results), and in PML, a constant imaginary part is only added to density ρ (in this case, instabilities are sometimes present in long simulations). Combining VAR and PML, an improved Absorbing Boundary Condition (ABS) is proposed in this thesis for both fluids and solids.

For isotropic materials ($C_{11} = 4 * C_{66}$), the phase velocities of longitudinal wave and transversal wave are defined as:

$$v_p = \sqrt{\frac{C_{11}}{\rho}}, \quad v_s = \sqrt{\frac{C_{66}}{\rho}}.$$

As stated in Eq.3-1, we can define in Absorbing Region (AR):

$\rho^{AR} = \rho_0 (1 + i\sigma)$ and $c_{ijkl}^{AR} = c_{ijkl} / (1 + i\sigma)$, $\sigma = A_0 * (A_1 + A_2 + A_3)$, A_0, A_1, A_2 and A_3 are the same as in Eq. (3.1.12).

Then $v^{AR} = v_0 / (1 + i\sigma)$, so the acoustic impedance in AR is matched to that in PD, $Z_a = \rho^{AR} v^{AR} = \rho_0 v_0$. The corresponding solution is $u = u_0 e^{i(\omega t - k\vec{r})} e^{-\sigma\vec{r}}$, the wave is attenuated increasingly in AR.

In the same way, in fluid there is only longitudinal wave defined as:

$$v_p = \sqrt{\frac{\lambda'}{\rho}}$$

As stated in section 3.1.1, after replacing the variables in Eq. 3.1.6, it would be:

$$\nabla \cdot (-\lambda' \nabla p) + \rho \omega^2 p = 0 \quad (3.1.20)$$

Here, in AR we define $\rho^{AR} = \rho_0 (1 - i\sigma)$ and $\lambda'^{AR} = \lambda'_0 / (1 - i\sigma)$, then the acoustic impedance in AR is matched to that in PD and the corresponding solution is $p = p_0 e^{i(\omega t - k\vec{r})} e^{-\sigma\vec{r}}$, the wave is attenuated increasingly in AR.

3.1.4 Simulation examples

Before we simulate the properties of high-frequency transducer arrays, the properties of transient wave propagation in different kinds of media are investigated at first.

3.1.4.1 Wave propagation in solids

Fig. 3.1.3 illustrates the model's geometry and dimensions. The propagation domain has a length of 4 mm and a height of 2 mm. A piston pressure source is applied to a part of the upside boundary. The source is a sine pulse, and it is expressed as source = $\sin(2 * \pi * f) * (t < 1/f)$, $f = 100e6$ in COMSOL 3.5a. In COMSOL, s is a curve parameter standing for a proportional factor. It is zero at the starting point of a curve

and is one at the end. In Fig. 3.1.3, the defined source is only applied in the centre part (with a length of 1 mm) of the top side of PD. So by calculation it can be expressed as $\text{source} \cdot (3/8 < s) \cdot (s < 5/8)$ which means the source is located from 3/8 of the top side to its 5/8. At $t = 15 \times 10^{-8}$ (unit in second), that is 15 wave periods, the acoustic fields in SiO_2 (isotropic solid) and in Si (anisotropic solid) are displayed in Fig. 3.1.4. Fig. 3.1.4a shows the acoustic field (expressed as total displacement) in isotropic SiO_2 , in which the compression wave, compression boundary wave, shear boundary wave, head wave and surface wave can be observed. Fig. 3.1.4b is the acoustic field in anisotropic Si, in which the Quasi (Q)-compression wave, Q-compression boundary wave, Q1-shear boundary wave, Q1-shear wave cusp, head wave and surface wave can be observed. It demonstrates the finite element method with COMSOL is reasonable.

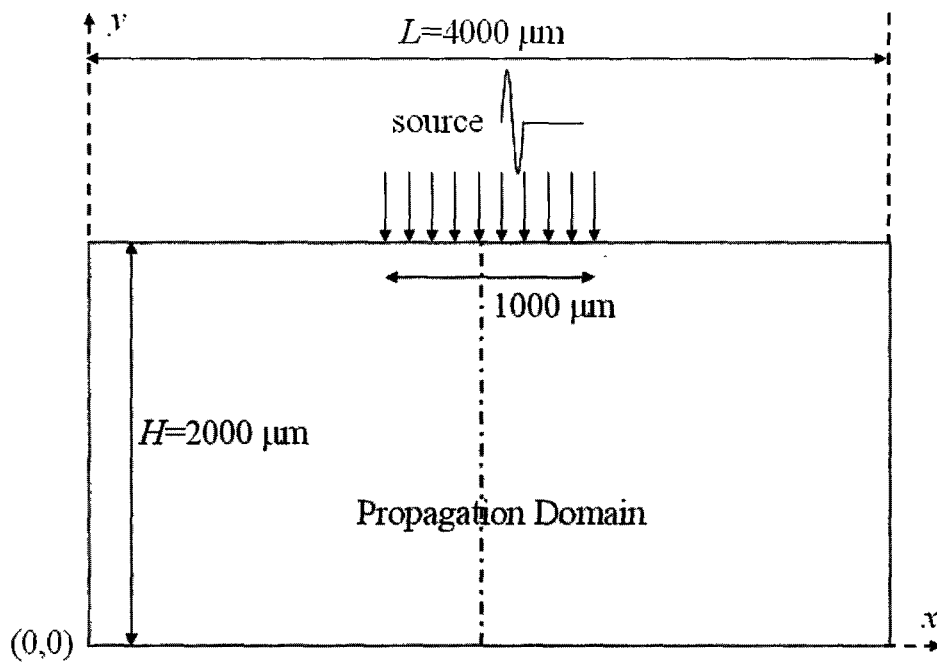


Figure 3.1.3: Geometry of the model (the dash-dot line can be used as a symmetrical boundary to save simulation time and memory)

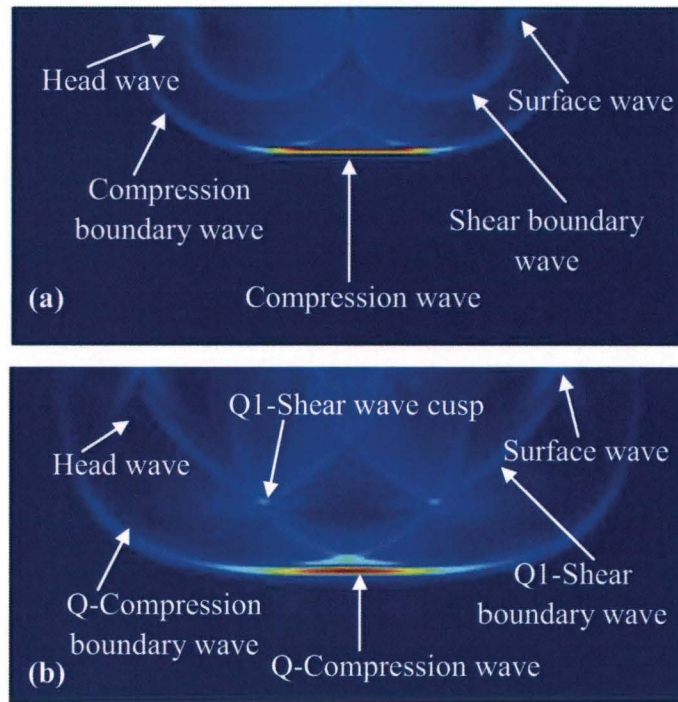


Figure 3.1.4: Wave propagation in piston pulse mode in (a) Isotropic solid (SiO₂) (b) Anisotropic solid (Si)

3.1.4.2 Simulation of wave propagation in fluids

For simulation of wave propagation in a fluid, such as water, PDE Coefficient Module is used in COMSOL. Similar to that in section 3.1.4.1, a sine pulse pressure is applied to a part of the top side in piston mode. As shown in Fig. 3.1.5, the transient acoustic field (expressed as pressure) shows there is no shear wave in water. The compression wave and compression boundary wave can be observed.

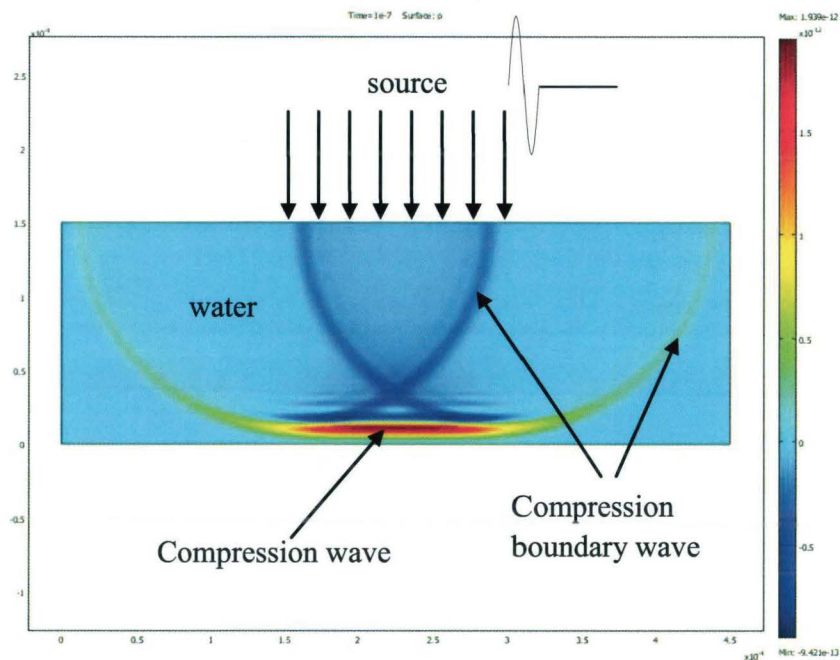


Figure 3.1.5: Transient wave propagation in water

3.1.4.3 Simulation of wave excitation with piezoelectric transducers

Piezoelectric materials are often used to generate ultrasound. The attention needs to be paid on the coupling between piezoelectric material and wave propagation domain. The displacement should be continuous at the interface of piezoelectric/non-piezoelectric solids. Fortunately, it is convenient to set this coupling boundary condition in COMSOL. Transient simulations always consume a lot of time and memory due to many time steps. Using symmetrical boundary condition is sometimes an efficient way to solve this problem for a symmetrical plane. For a symmetrical plane, we can choose 1/2 or 1/4 even 1/8 (in 3-D models) of the whole domain for modeling. The requirement for memory is increased exponentially other than linearly with the number of degrees of freedom ($A \cdot n^k$, here A is a constant, n is the number of degrees of freedom and $k > 1$). It means if we use half part of the domain to model, the required memory would be decreased to less than half of the previous requirement. Use the same signs to stand for the same variable in different domains (for example, u and v stand for x - and y -displacement, respectively, in all piezo and non-piezo solid domains), and it is considered to be continuous by default at their interface. Excited by one period of sine pulse voltage (whose frequency is 100

MHz), LiNbO_3 36°/Y-cut emits ultrasound, and the transient wave motion in anisotropic Si is displayed in Fig. 3.1.6. We can observe the compression wave, compression boundary wave, shear boundary wave, shear wave cusp, head wave and surface wave after 15 wave periods (15T, T = 0.01 μs) propagation. Here, **Piezo Plane Strain Module of Piezoelectric Effects** is employed for both LiNbO_3 and Si domains. For Si domain, “decoupled” is selected in physics sub-domain setting (in fact, the decoupled Piezo Plane Strain Module has the same effect as Plane Strain Module in Structural Mechanics Module). Symmetrical boundary conditions can be selected directly from these solid modules.

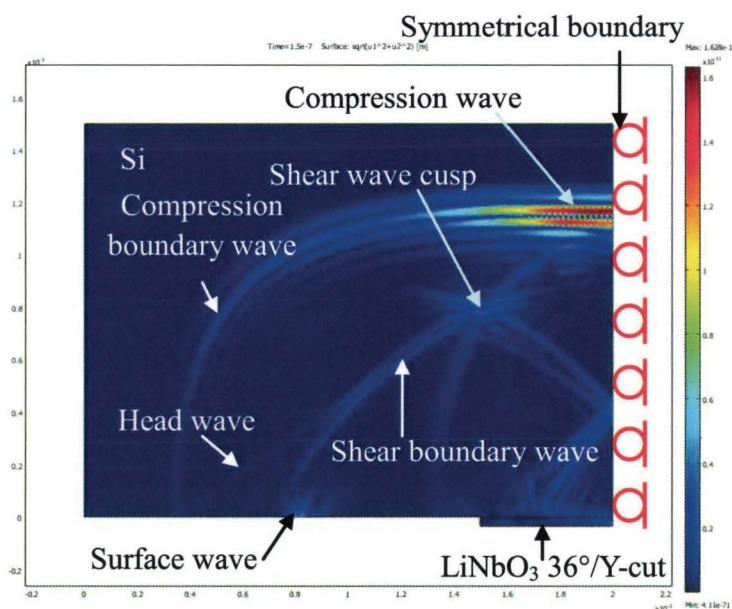


Figure 3.1.6: Wave propagation in anisotropic Si coupled with LiNbO_3 36°/Y-cut transducer excited by a sine pulse voltage

3.1.4.4 Wave steering excited by linear phased array sources

An ultrasonic phased array transducer is composed of a number of individual piezoelectric elements. Each element is driven by an electric pulse in the way to steer and focus a transmitting ultrasonic beam in an inspection medium. An image of the medium can be reconstructed from the received signal of the elements working in reflection mode.

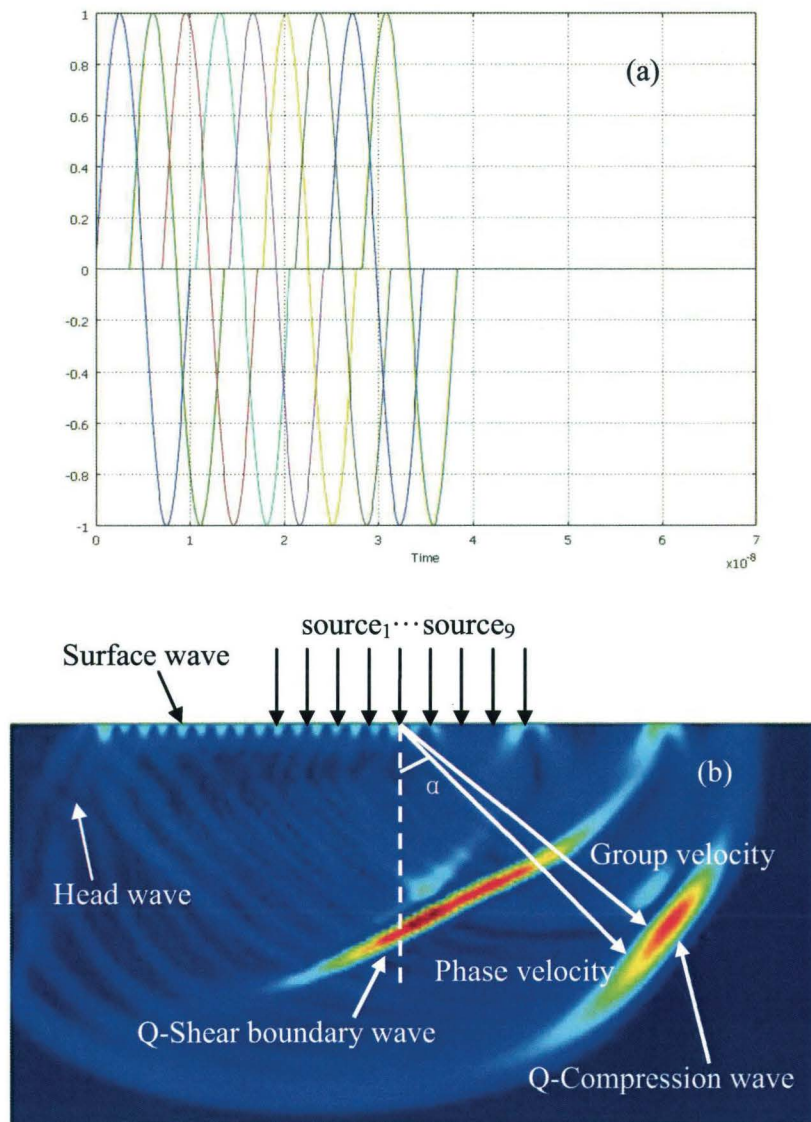


Figure 3.1.7: Steering of phased arrays in anisotropic Si (a) Nine excitation array sources in sine pulse mode and (b) Acoustic field steering by 45 degrees

The simulation procedure can also be used to study linear phased array by applying phase delayed electrical signals to consecutive elements. One can study the angular dependence of the beam pattern by steering the beam using simulation with phase-delayed excitation. To investigate the steering property of phased arrays in ideal conditions (in piston mode), nine sine sources in pulse mode are applied to the top side of anisotropic Si, and each pulse source (100 MHz) is illustrated in detail in Fig. 3.1.7a. About the calculation of phase delay, more information is given in Annex 1. Fig. 3.1.7b is the acoustic field after wave propagation for seven periods of time

($7T$, $T = 0.01 \mu\text{s}$). It is a typical steered beam pattern with a steering angle of 45° . The width of the main beam, the side lobe, and the focal distance all changed slightly as a function of the steering angle because the array has a finite size. In the defined array, steering angle is $\alpha = 45^\circ$, width of the element is $w = 38 \mu\text{m}$, kerf size is $4 \mu\text{m}$, and pitch is $p = 40 \mu\text{m}$, which is almost equalling to one-half of the wavelength in Si, so there is no grating lobes ^[137]. Group velocity and phase velocity can be distinguished from it. The beam pattern in Fig. 3.1.7b was calculated by using transient analysis in COMSOL at 100 MHz.

3.1.4.5 Scattering of coarse boundary (rough surface)

The transient analysis by FEM computation is adopted in real applications. To decrease the influence of reflection, the rough surface is applied in this work to scatter the waves propagating into the backing materials. However, the question is what degree of the roughness could efficiently scatter the waves. We investigate the roles of different rough degree at the surrounding coarse boundaries. Fig. 3.1.8 is the geometry of this model. Six dimensions ($d = 0\lambda, 0.1\lambda, 0.2\lambda, 0.25\lambda, 0.5\lambda, 1.0\lambda$, $\lambda = 84\mu\text{m}$ in Si at 100 MHz) of roughness are selected and compared in transient simulation in piston mode, where the acoustic field performances with rough dimensions $d = 0.1\lambda$ and $d = 1.0\lambda$ are displayed in Fig. 3.1.9. The source is the same as stated in section 3.1.4.1. Fig. 3.1.9a-d are obtained at $t = 4T$ ($T = 0.01 \mu\text{s}$ at 100 MHz), $t = 5T$, $t = 6T$, $t = 8T$, respectively. They show that the reflection wave keeps a regular wave front and the rough boundaries do not efficiently scatter the incident waves. Fig. 3.1.9e-h are also obtained at $t = 4T$, $t = 5T$, $t = 6T$, $t = 8T$, respectively. They show that the reflection wave does not keep a regular wave front and the rough boundaries efficiently scatter the incident waves. Fig. 3.1.10 illustrates quantitatively the total displacement at the right bottom point of this model at different times. They are obtained from six dimensions of roughness as stated above. They have totally the same scales in x- and y- coordinates. We can see from Fig. 3.1.10 that a compression wave is generated at the beginning. At $t = 5T$ a shear boundary wave arrives at this right bottom point. Around $t = 8T$ a reflectance of compression wave arrives

overlapped with a mixture of surface wave and head wave.

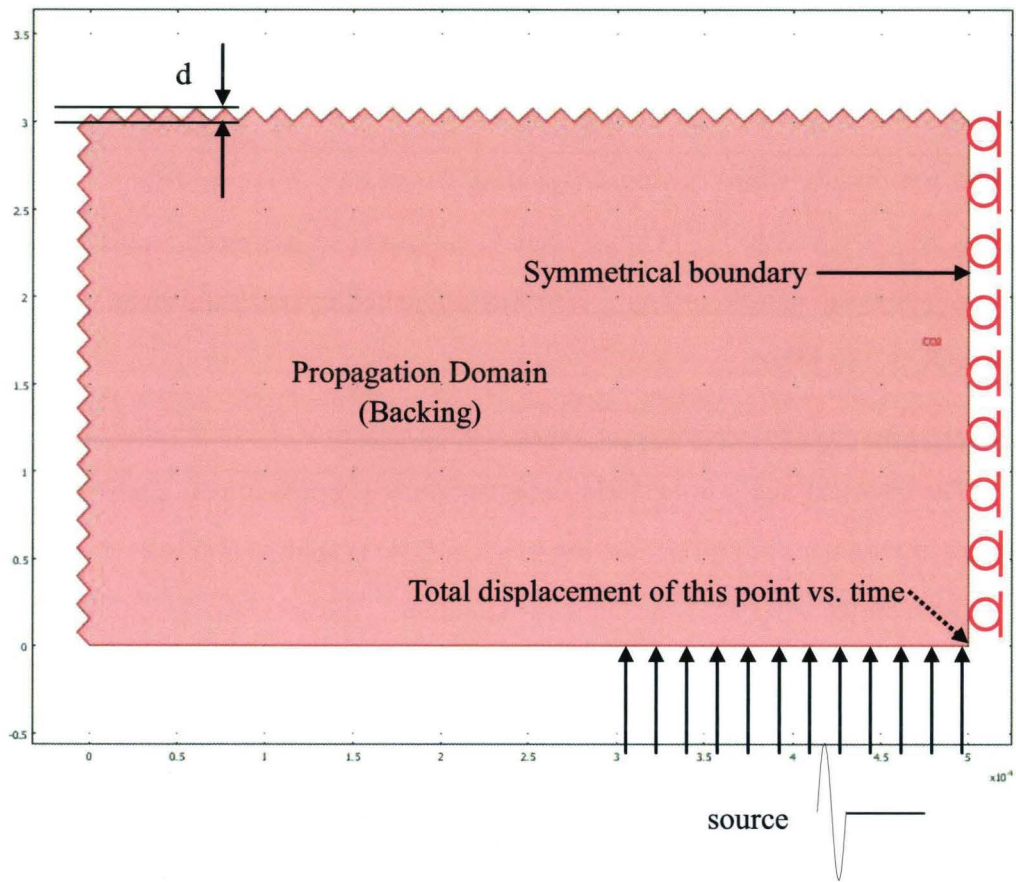


Figure 3.1.8: Geometry of the model

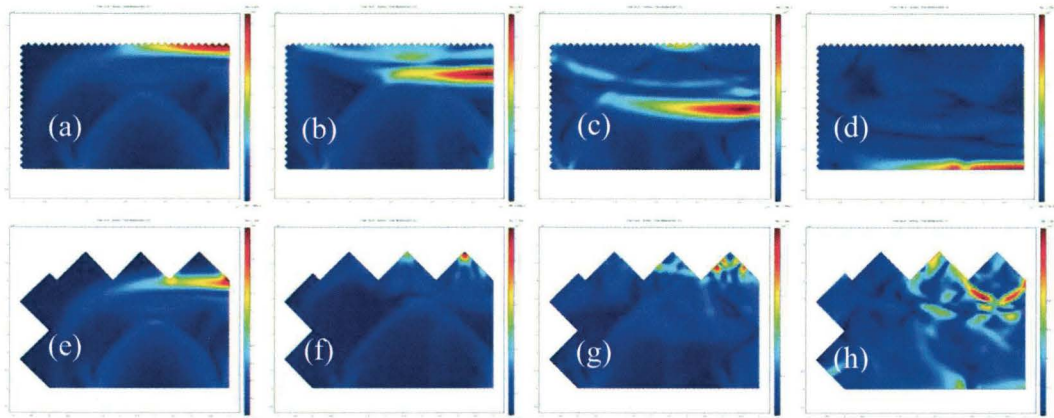


Figure 3.1.9: Transient acoustic field performances with rough dimensions $d = 0.1\lambda$: (a) $t = 4T$ (b) $t = 5T$ (c) $t = 6T$ (d) $t = 8T$ and $d = 1.0\lambda$: (e) $t = 4T$ (f) $t = 5T$ (g) $t = 6T$ (h) $t = 8T$

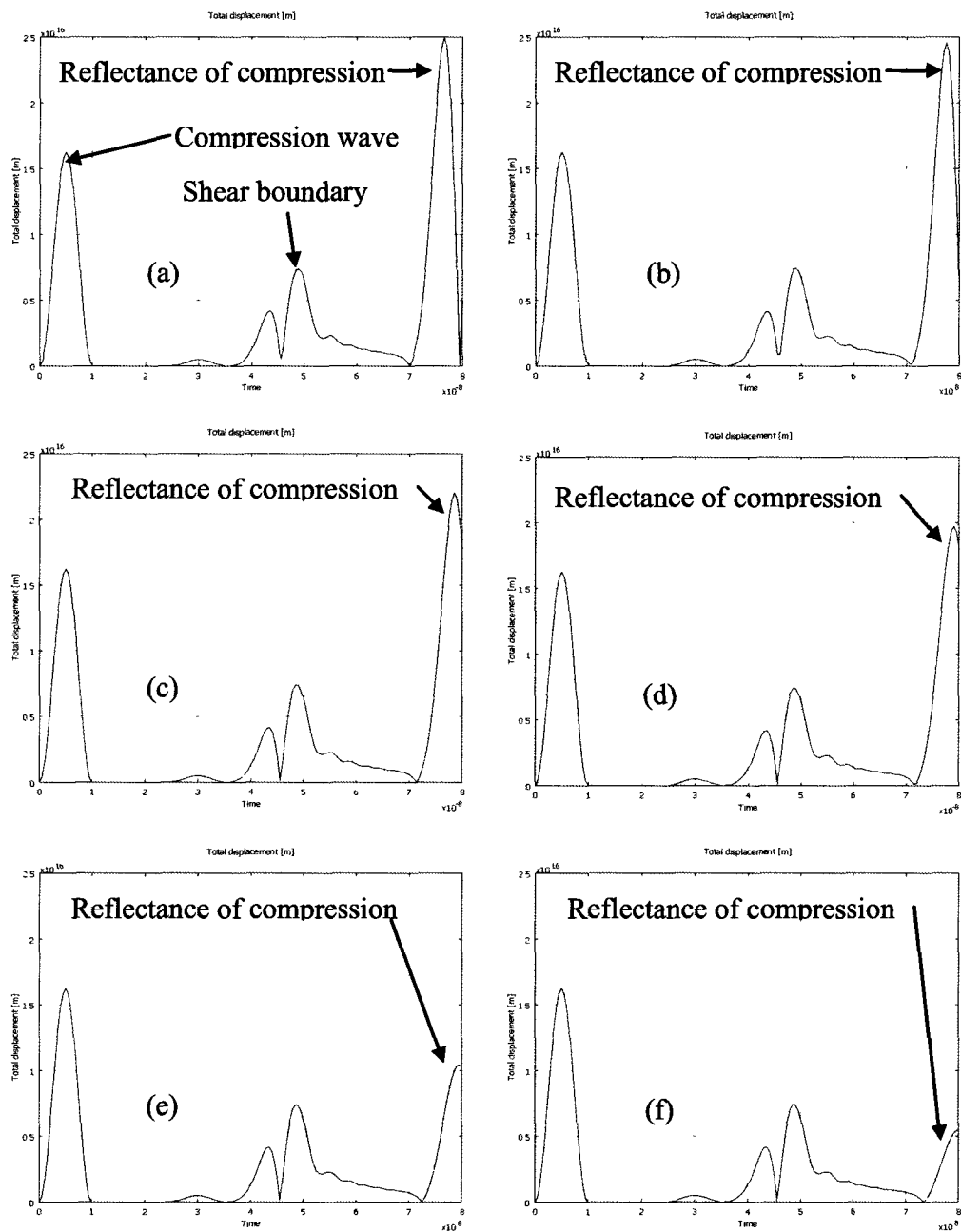


Figure 3.1.10: Total displacement at the right bottom point of this model (a) $d = 0\lambda$, (b) $d = 0.1\lambda$, (c) $d = 0.2\lambda$, (d) $d = 0.25\lambda$, (e) $d = 0.5\lambda$, (f) $d = 1.0\lambda$.

Fig. 3.1.10a shows when $d = 0\lambda$, that is a plane boundary, the reflectance (expressed as total displacement) is almost 60% high than the generated compression wave. Compared Figs. 3.1.10a-f, the reflectance decreases with an increase of roughness dimension. When $d = 1.0\lambda$, the reflectance decreases to 1/3 of the generated compression wave. Combining with Fig. 3.1.9h, it indicates most of the incident

waves are scattered by the coarse boundary. In conclusion, in order to decrease the noise from reflectance waves in backing, a rough surface whose dimension is around 1.0λ should be considered to scatter a majority of incident waves.

3.2 Simulation of buffered transducer arrays

Although LiNbO_3 has favorable electromechanical coupling efficiency and robust single crystal structures, the fabrication of high-frequency LiNbO_3 arrays based on conventional configuration is still a great difficulty for the thin film etching techniques. The traditional dicing technique becomes extremely difficult to perform when the material is so thin and delicate. So far there is no report on kerfed LiNbO_3 arrays in frequency higher than 100 MHz. Therefore, it is necessary to develop a novel structure to facilitate the process without affecting the performance of the array. An alternative configuration based on buffered focal silicon lens is put forward in this work as shown in Fig. 3.2.1. The insertion of silicon focal lens can facilitate volumetric imaging. The spatial resolution along x-axis can be controlled by the linear phased array. The spatial resolution along z-axis can be controlled by the silicon focal lens. Moreover, using silicon substrate makes it possible to integrate the arrays with IC (Integrated Circuit), which facilitates microminiaturization of electronics.

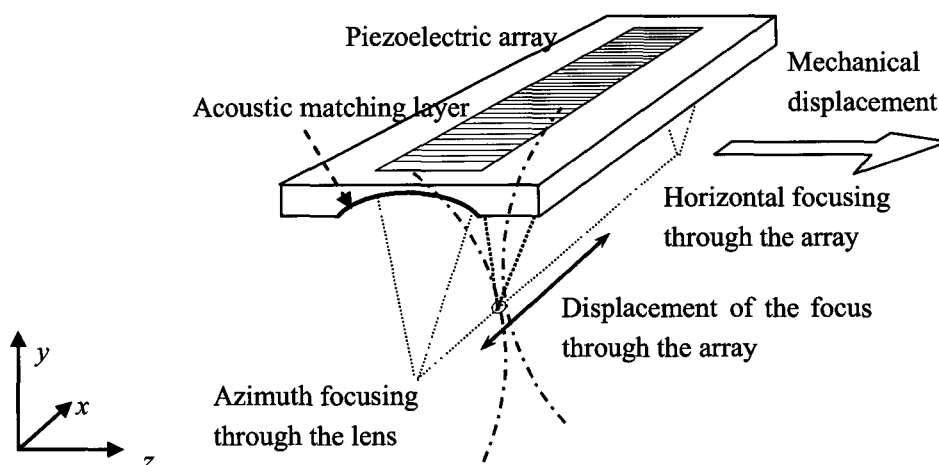


Figure 3.2.1: Schematic diagram of linear array on silicon lens for volumetric imaging

Here we use COMSOL, finite element software, to model and simulate the

properties of the arrays. 3-D simulation consumes too much memory and duration. Therefore, we simplify the 3-D model to a 2-D simulation in x - y plane to investigate the properties of the arrays, and a 2-D simulation in z - y plane to investigate the properties of single element (including piezoelectric materials, focal lens, and acoustic matching layer).

3.2.1 2-D simulation in x - y plane (simulation of array transducer with a buffer layer)

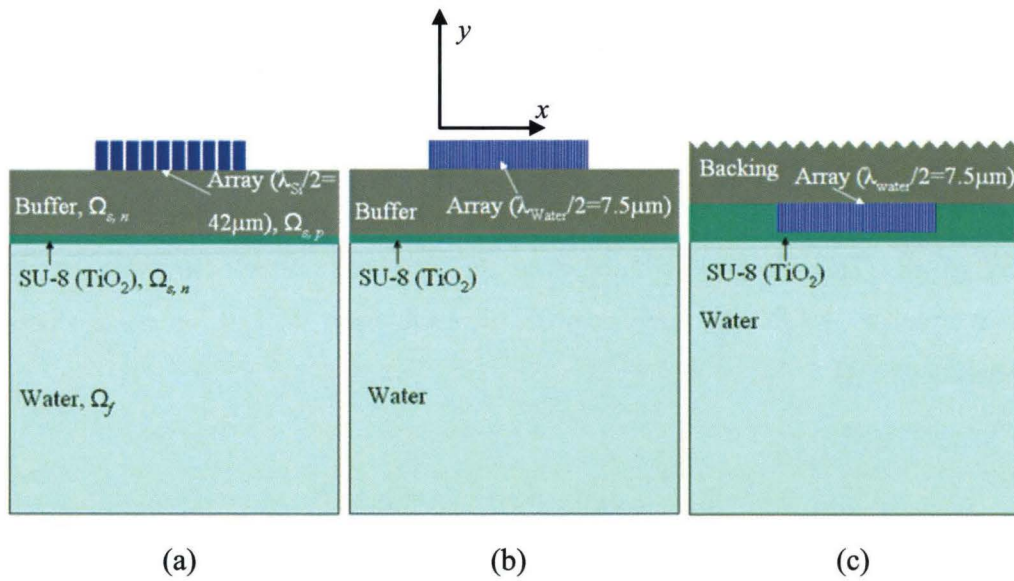


Figure 3.2.2: Structures of different arrays: (a) 10-element buffer, pitch is 42 μm ; (b) 49-element buffer, pitch is 7.5 μm ; (c) 49-element backing, pitch is 7.5 μm .

The traditional configuration of the array transducer is the backing-layer structure where the wave is emitted directly into water using mechanical matching and the backward propagating wave is scattered by the rough backing surface of the silicon substrate (see Fig. 3.2.2c). Ideally, the pitch (p) should be limited to half wavelength in water to avoid grating lobes ($p \leq 7.5 \mu\text{m}$, the wavelength in water is 15 μm at 100 MHz). As a result, the kerf width (d) should be smaller than 7.5 μm . For such kind of full-kerfed array, the kerf etching with high aspect ratio ($h/d > 33 \mu\text{m}/7.5 \mu\text{m}$) is required. But it is impossible to fabricate such small features in the piezoelectric arrays using state-of-the-art technologies. As stated later in Chapter 4, we have investigated that the smallest pitch of 42 μm could be obtained for a

full-kerfed single crystal LiNbO₃ array with a thickness (h) of 33 μm .

The goal of this work is to develop a full-kerfed linear array for volumetric imaging application with an acceptable resolution. Here, an alternative configuration based on a buffered silicon lense, as shown in Fig. 3.2.1, is put forward to avoid the difficulties in the high depth/width aspect ratio etching. A buffered silicon layer is placed between the piezoelectric array and a matching layer (SU-8 composite), which allows the wave to propagate in water through silicon and the matching layer. This results in a much smaller aspect ratio thanks to the much larger velocity of sound in silicon (At 100 MHz, the wavelength in Si (λ_{Si}) is 84 μm , then the pitch is half of this value, 42 μm).

Two linear array transducers, with different dimensions and the same buffered configuration, are designed at 100 MHz to investigate the influence of different pitch sizes. The properties of conventional backing configuration are also considered for comparison. The electrical impedance, the crosstalk effect, and the acoustic characteristics of LiNbO₃ transducer arrays have been studied by finite element modeling (FEM).

A. Model design

To investigate the influence of pitch size for this buffered configuration, another buffer-layer array of different dimensions ($p = 7.5 \mu\text{m}$) is also considered here which is shown in Fig. 3.2.2b. The widths of the element of Fig. 3.2.2a and Fig. 3.2.2b are 22 μm and 5.5 μm , respectively. To study the effect of buffer layer, a conventional structure (see Fig. 3.2.2c) is designed with the same array parameters as Fig. 3.2.2b but without Si buffer layer. Thus, to investigate the effect of the size of the pitch in buffered arrays, we can compare Fig. 3.2.2a and Fig. 3.2.2b (They have the same structure but different array configuration). To study the effect of buffer layer, we can compare Fig. 3.2.2b and Fig. 3.2.2c (They have the same array number and aperture but different structures).

In order to obtain higher sensitivity and broader bandwidth transduction, the thickness of the matching layer must be in quarter wavelength thick and the acoustic impedance is $Z_m = \sqrt{Z_f Z_s}$ for the buffer structure (or $Z_m = \sqrt{Z_f Z_{\text{piezo}}}$ for the backing structure). The matching material considered in this study is an SU-8-based

nano-composite (mixed with nano-powder of TiO_2), the acoustic impedance of which could be arbitrarily adjusted to meet the required values [¹³¹].

B. Focusing acoustic field

Numerical results for continuous wave beam focusing are given in Figs. 3.2.3a-c, where the pressure modulus represents the acoustic field in fluid and the total displacement represents the acoustic field in solids (buffer, backing, array elements, and matching layer). The array has an element number $N = 10$ (or $N = 49$), the width of the element $w = 22 \mu\text{m}$ (or $w = 5.5 \mu\text{m}$), and pitch distance $p_1 = 42 \mu\text{m}$ ($\lambda_{\text{Si}}/2$) (or $p_2 = 7.5 \mu\text{m}$ ($\lambda_{\text{water}}/2$)). All the elements are electrically driven by a sinusoidal signal (with amplitude of 1 volt and frequency of 100 MHz) with necessary phase delays for the beam focusing. The results indicate that the wave beam of the 10-element array is not as efficient as the other two 49-element arrays, but it shows an obvious effect of focusing. Moreover, the grating and side lobes are both slightly visible. In addition, the surface waves and focused compression waves are observed in the silicon buffer layer in Fig. 3.2.3 (a) and (b). Most of the compression waves are transmitted to water due to the employment of SU-8 (mixed with TiO_2) acoustic matching layer. Fig. 3.2.3c shows an ideal example; however, as stated above, it is impossible to arrive at this property using state-of-the-art technologies. To obtain the lateral resolution at the azimuth plane, the wave propagation is studied in time domain (transient analysis). Fig. 3.2.4 shows the steering acoustic field and axial pressure distribution in water (in pulse mode). Fig. 3.2.5 shows the focusing acoustic field in pulse mode. The lateral pressure distribution is quantitatively illustrated along the azimuth focalization plane in water for two buffer layer transducers. It shows that the lateral spatial resolutions are, respectively, $86 \mu\text{m}$ and $82 \mu\text{m}$ for the 10-element array and 49-element one. That is to say, the lateral spatial resolution is just increased by 4.65% when the pitch size decreases from $42 \mu\text{m}$ to $7.5 \mu\text{m}$. This indicates that the sizes of the pitch (between $7.5 \mu\text{m}$ and $42 \mu\text{m}$) almost have no influence on the resolutions in buffered arrays.

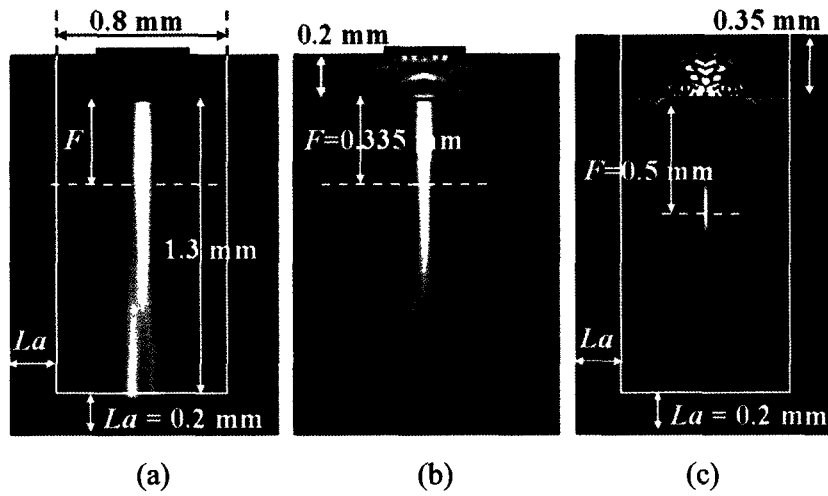


Figure 3.2.3: Focusing acoustic field (F is focal length) (a) 10-element buffer, pitch is $42\mu\text{m}$; (b) 49-element buffer, pitch is $7.5\mu\text{m}$; (c) 49-element backing, pitch is $7.5\mu\text{m}$.

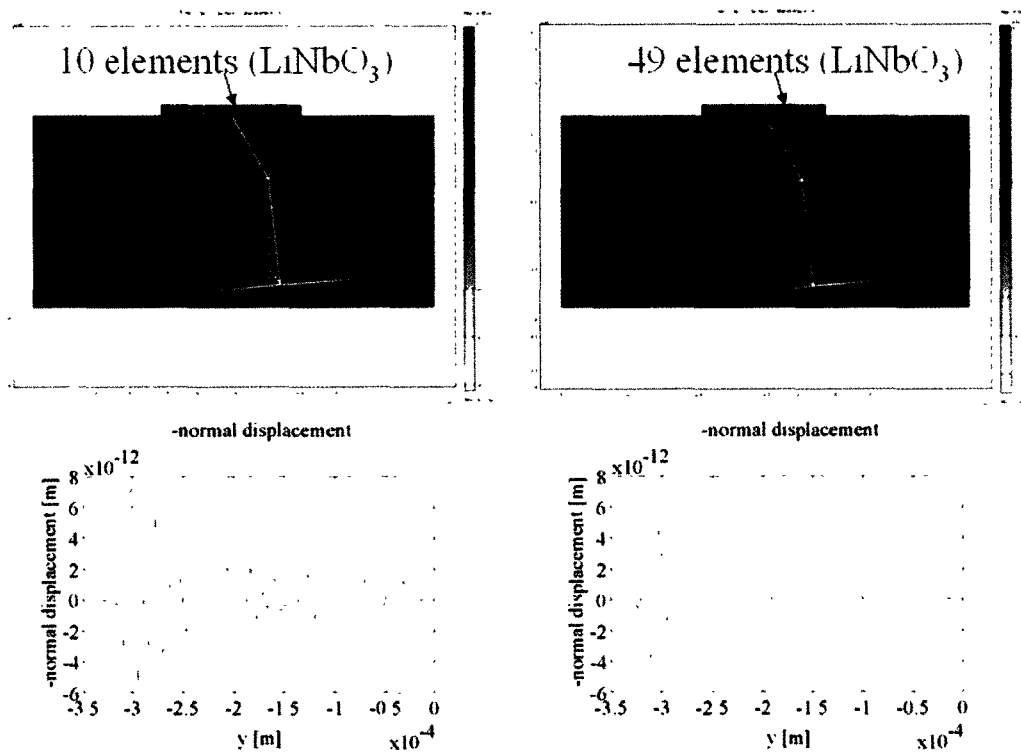


Figure 3.2.4: Steering acoustic field and axial pressure distribution in water (in pulse mode).

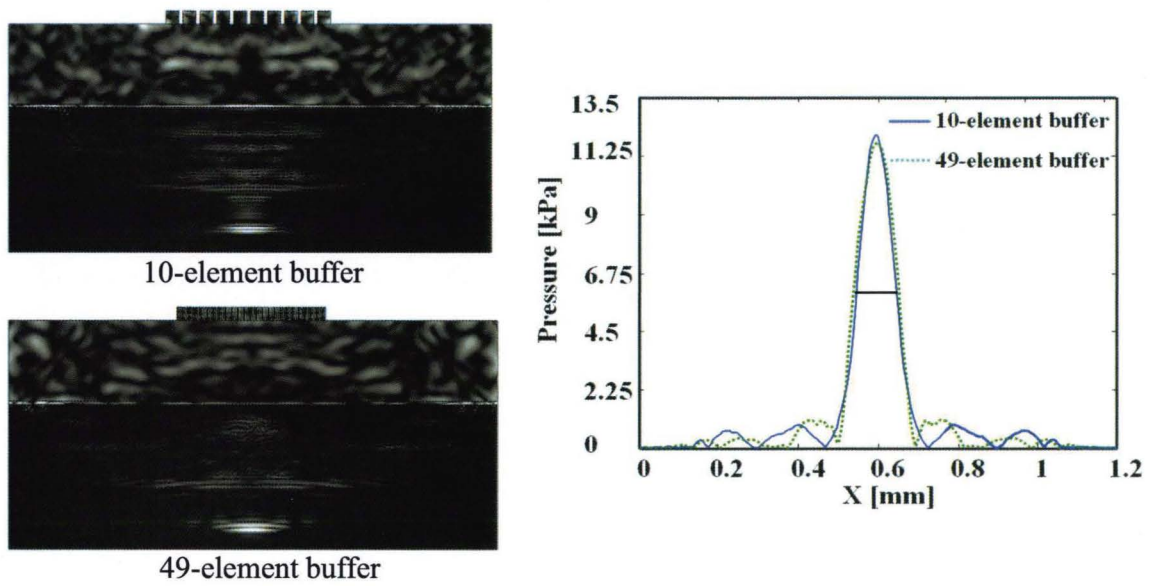


Figure 3.2.5: Focusing acoustic field and lateral pressure distribution in water (in pulse mode).

The phase delay correction has to be considered due to the insertion of silicon buffer. For instance, if the sound propagates only in the buffer, it will have a focus at the point of F' , as shown in Fig. 3.2.6. However, the sound will refract at the interface of buffer/SU-8/water, thus the actual focus should be located at the point F . The equation for the phase delay after correction is displayed in Fig. 3.2.6, where the phase delay due to the SU-8 layer is neglected because of its very thin thickness ($7.2 \mu\text{m}$).

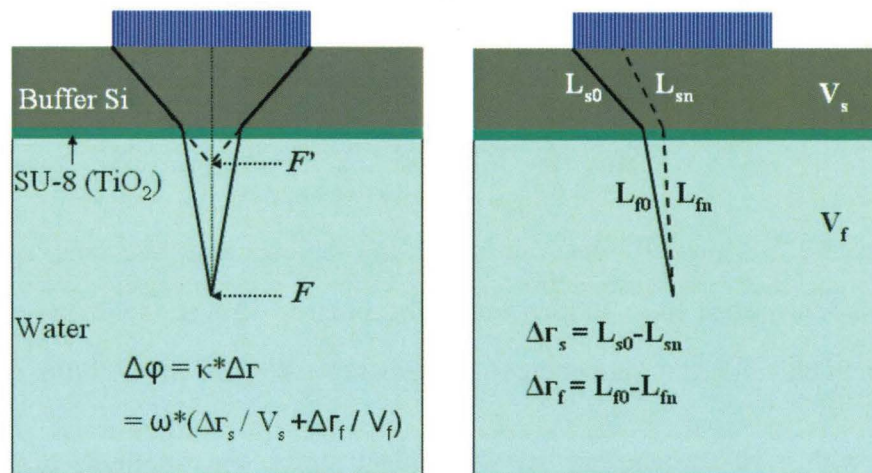


Figure 3.2.6: Principle of phase delay correction (F' is the fictitious focus in Si and F is the actual focus in fluid)

C. Crosstalk

Reducing the element crosstalk level is very important in array designs, especially for phased arrays, because the crosstalk between elements affects the directivity pattern and the sensitivity. Crosstalk has two sources: mechanical and electrical. Here we only analyse the mechanical crosstalk as the electrical crosstalk is often less than mechanical crosstalk^[138]. To simulate this phenomenon, the electrical boundaries were set in such a way that only the central element of the array ($n = 0$) is applied with 1 volt potential (V_{in}) while the other elements $n = -4 \dots, -1, 1 \dots 5$ for the 10-element structure (or $n = -24 \dots, -1, 1 \dots 24$ for the 49-element structure) are opened. The crosstalk is defined as the relative electrical response (V_n) at each element:

$$\text{Relative electric response} = 20\log|V_n/V_{in}|.$$

Because the dielectric properties are not activated in kerf filler (air), this measure only reflects the strength of mechanical coupling; the electric coupling was not included.

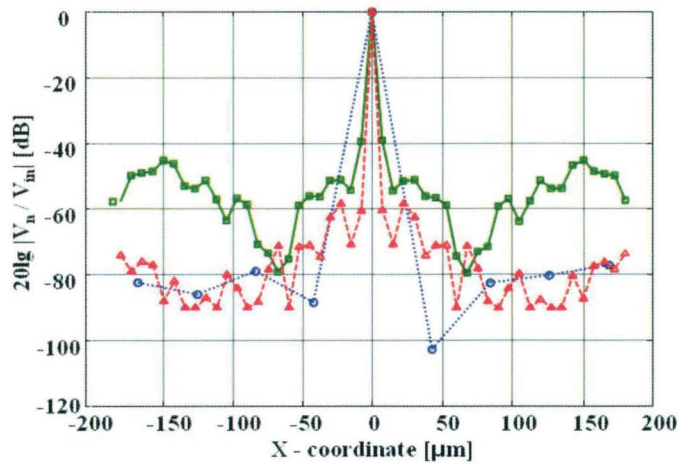


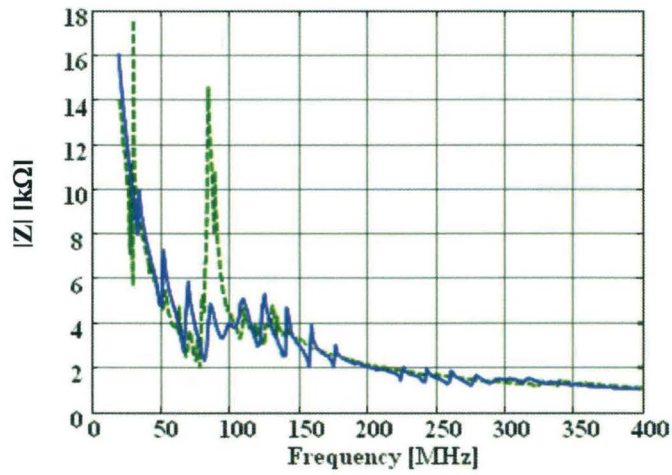
Figure 3.2.7: Crosstalk determined by the neighboring elements response (in amplitude): (dotted line) 10-element buffer, pitch = 42 μm ; (solid line) 49-element buffer, pitch = 7.5 μm ; (dashed line) 49-element backing, pitch = 7.5 μm .

With a 10-element and two 49-element arrays, the amplitude of the element response is plotted in Fig. 3.2.7, which shows a maximum crosstalk of less than -39 dB. The crosstalk of the 10-element array is clearly the smallest of less than -74 dB.

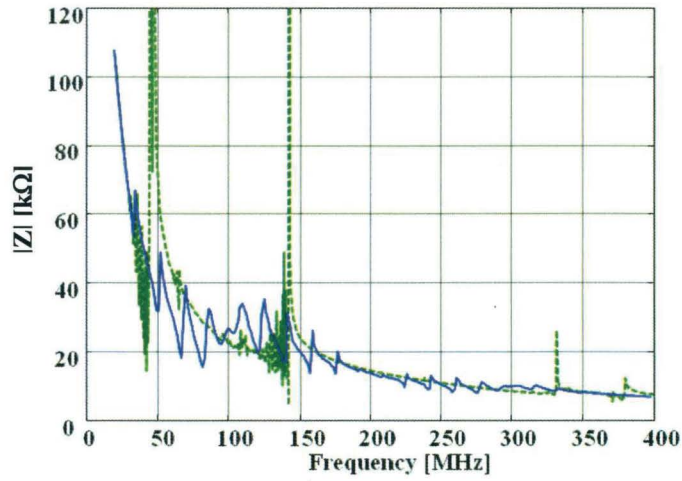
As a rule of thumb in transducer design, the crosstalk level for the nearest neighbour should be less than -30 dB in order to avoid superposing in ultrasonic imaging ^[139]; based on our calculations, the air kerf scheme is sufficient to satisfy this requirement.

D. Electrical impedance

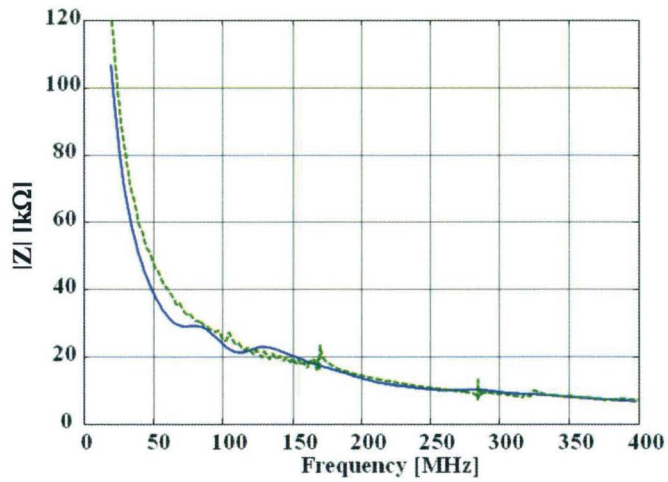
Electrical impedance is an important parameter that conditions the transducer matching to optimize the transducer bandwidth and sensibility. Many researchers use KLM model to calculate electrical impedance for single element ultrasonic transducer. However, KLM model is a one-dimensional model. When the width of the transducer is compatible to the thickness (for instance, in array element), KLM model would be no longer accurate. We use two methods, FEM (by COMSOL) and KLM, for comparison to calculate the electrical impedance in an array, respectively. Using COMSOL, this impedance can be obtained by integrating the current density on the surface of the element electrode (the other elements are electrically opened). The impedance magnitudes of the central element for the above considered 10-element buffer array by 2-D FEM (calculated using COMSOL3.5a) and 1-D KLM calculation are shown in Fig. 3.2.8a, and those for 49-element buffer structure are shown in Fig. 3.2.8b, for 49-element backing structure in Fig. 3.2.8c. These results indicate three points. First, the 2-D FEM results are generally consistent with the 1-D KLM simulations. Second, 2-D FEM results show some peaks below 150 MHz. We analyze that these great peaks are caused by the lateral mode ^[140,141] vibration which will occur when the width is compatible to the thickness. Third, the impedances are, respectively, about 4 k Ω , 26.4 k Ω and 24.2 k Ω at 100 MHz for each structure. The smaller element has greater impedance. These values mean that the electrical matching is necessary in future application of 100 MHz arrays.



(a)



(b)



(c)

Figure 3.2.8: Electrical impedances (in modulus) of the central element by FEM (dashed line) and KLM (solid line) calculations for (a) 10-element buffer, pitch is 42 μm ; (b) 49-element buffer, pitch is 7.5 μm ; (c) 49-element backing, pitch is 7.5 μm .

3.2.2 2-D simulation in z-y plane (simulation of single element transducer with a focal lens)

A. Model design

In z-y plane of Fig. 3.2.1, the basic model configuration consists of a single LiNbO₃ element along a flat boundary radiating into water through a silicon lens with an acoustic impedance matching layer of quarter-wavelength (see Fig. 3.2.9).

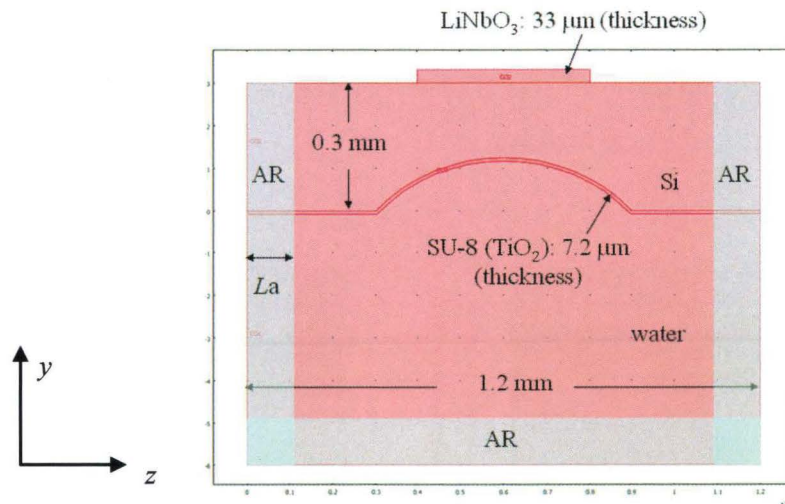


Figure 3.2.9: Geometry of the model, the radius of the lens is 420 μm.

B. FEM results

To design and fabricate high frequency transducers, the critical work is to select the suitable piezoelectric material. The imaging tests showed that sensitivity is the most important factor for transducers to obtain a high-quality image. Compared to other piezoelectric materials, the most valuable feature of LiNbO₃ crystal is that this material has high coupling capability, making it possible to build a device with high sensitivity and large bandwidth. Here, single crystal LiNbO₃ (36°/Y-cut) is chosen as the active piezoelectric material. It is reported in ^[142,143] that LiNbO₃ single crystal performs better than PZT ceramics, PVDF, and 1–3 PZT fibre composite to obtain a high-quality image. Thus, LiNbO₃ crystal 36°/Y-cut is just compared with ZnO. Their sinus wave responses are shown in Figs. 3.2.10 (a) and (b). Figs. 3.2.11 (a) and (b) illustrate their horizontal distributions of the absolute pressure in water. Compared with ZnO, the wave image derived by LiNbO₃ 36°/Y-cut element sees a greater pressure and the pressure at the focus is enhanced by 16.53%.

To investigate the influence of the acoustic impedance mismatching, a model

without matching layer is simulated, as shown in Fig. 3.2.10c and Fig. 3.2.11c. The enhancement of transmitted wave can be observed with acoustic impedance matching layer and is up to 314.7% compared to that without matching layer. Thus, it is necessary to insert an acoustic impedance matching layer to substantially increase the focal energy. Meanwhile, the stationary response of the LiNbO_3 without focal lens is illustrated in Fig. 3.2.10d, and Fig. 3.2.11d shows its horizontal distributions of the absolute pressure in water. Compared with the LiNbO_3 with focal lens (see Fig. 3.2.10a), it is clear that the wave disperses dramatically in water when not propagating through the focal lens. The energy is so weak at the penetration depth that it is of little use in medical imaging.

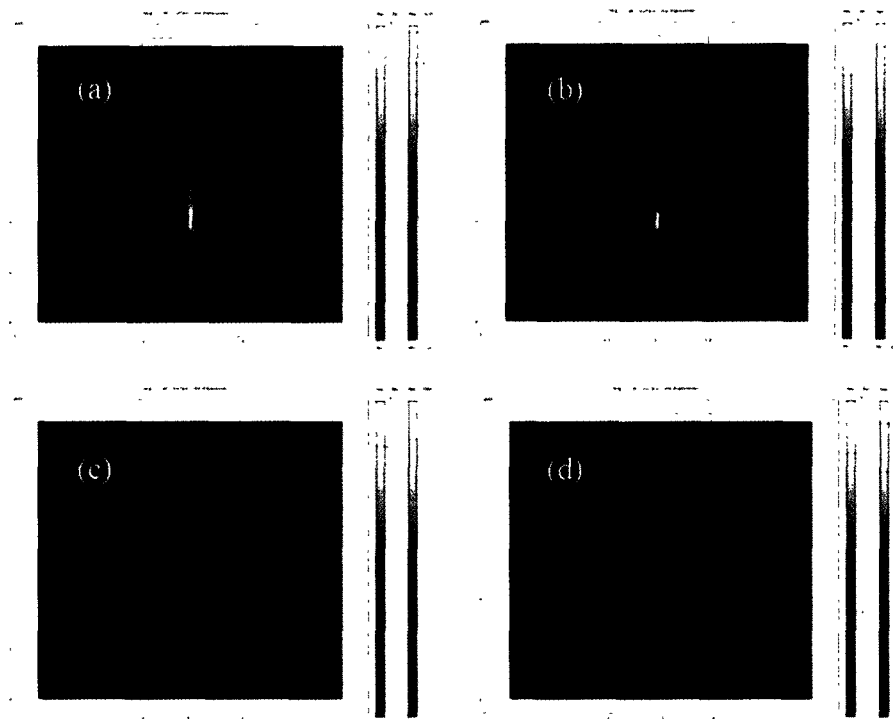


Figure 3.2.10: Stationary analysis of absolute pressure in water and total displacement in solid. (a) LiNbO_3 36° Y-cut with matching layer and focal lens; (b) ZnO with focal lens and matching layer; (c) LiNbO_3 with focal lens no matching layer; (d) LiNbO_3 with matching layer no focal lens

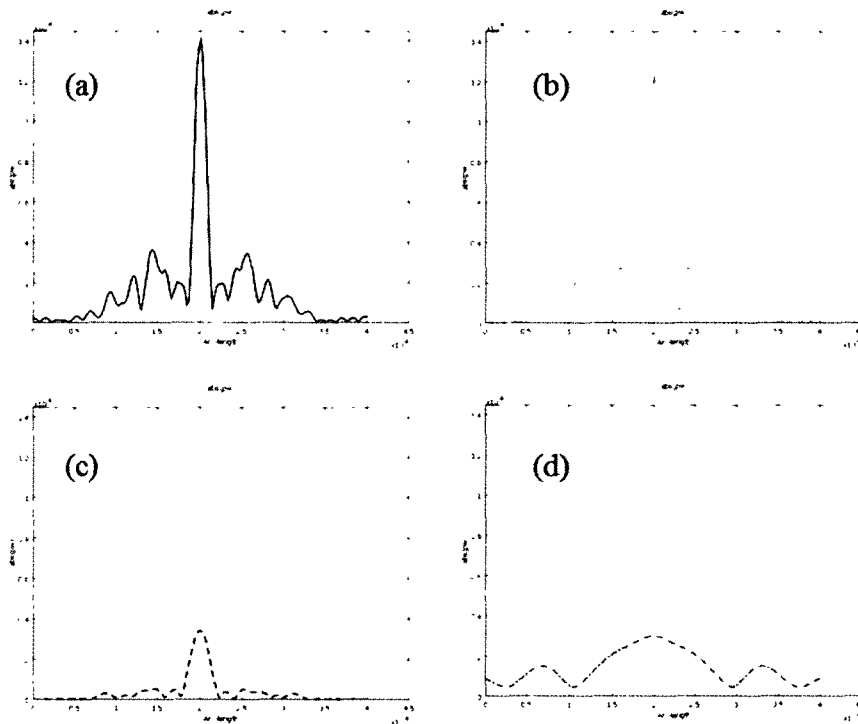


Figure 3.2.11: Continuous wave analysis of horizontal distribution of pressure amplitude in water: (a) LiNbO₃ with matching layer and focal lens; (b) ZnO with matching layer and focal lens; (c) LiNbO₃ with focal lens no matching layer; (d) LiNbO₃ with matching layer no focal lens.

Finally, the focal model with matching layer derived by LiNbO₃ is chosen based on the above results. Fig. 3.2.12 illustrates the impulsion response of the transducer at 100 MHz. A period of sine impulse voltage with amplitude of 1 volt is applied to the LiNbO₃ element. The images of (a)-(i) are obtained at the time of 1T (1T = 0.01 μs), 2T, 3T, 4T, 10T, 20T, 30T, 38T, 45T, respectively. Fig. 3.2.12 (a) to (b) show the energy radiated by the transducer is strong. Fig. 3.2.12 (c) to (h) obviously demonstrate that the lens attributes to the focusing of the waves and the focus point possessing the largest energy can be obtained at the time of 38T (Fig. 3.2.12 (h)). After converging the wave begins to disperse shown in Fig. 3.2.12 (i). Multi-reflected waves (reverberation by the buffer) do not disturb the desired signal significantly. In summary, the transducer performs well in wave emission and the reflected waves have little effect on the focusing wave.

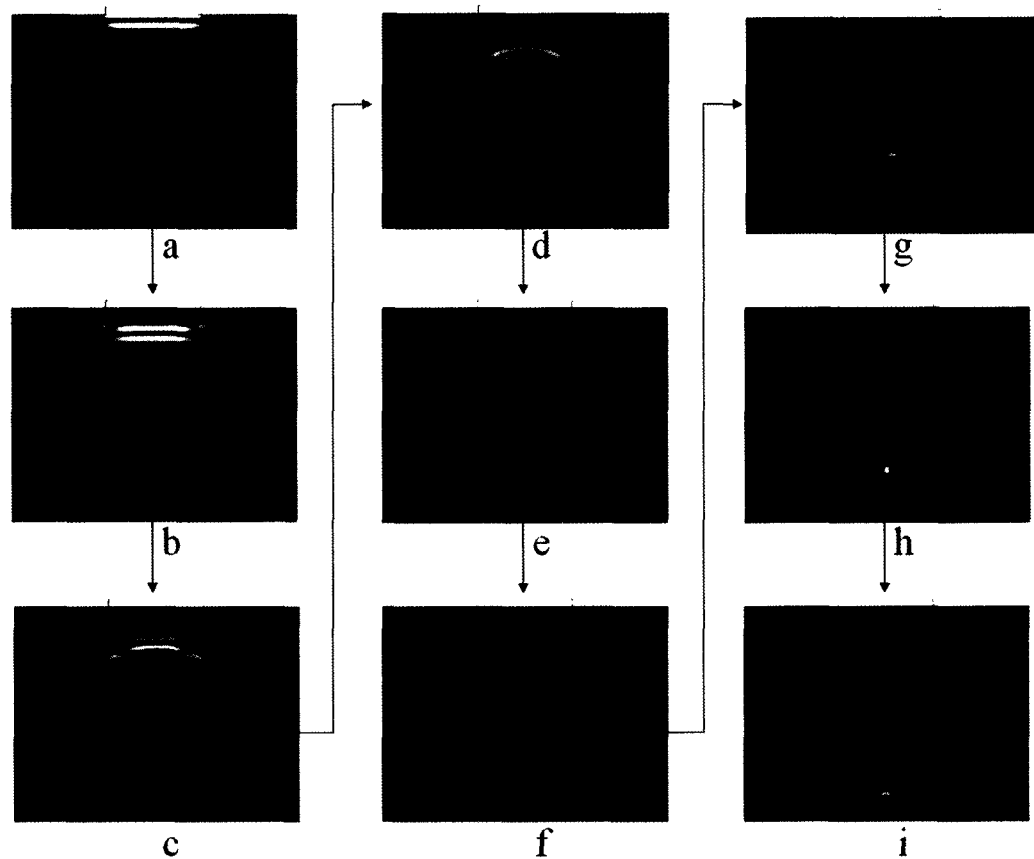


Figure 3.2.12: Snapshots of wave propagation with matching layer between Si and water, at (a) $t = 1T$, (b) $t = 2T$, (c) $t = 3T$, (d) $t = 4T$, (e) $t = 10T$, (f) $t = 20T$, (g) $t = 30T$, (h) $t = 38T$ and (i) $t = 45T$, respectively ($T = 0.01 \mu\text{s}$): pressure amplitude in water and total displacement in solid.

C. Conclusion

In conclusion, the above results show the wave derived by LiNbO_3 $36^\circ/\text{Y}$ -cut element sees a better directivity than that by ZnO and the energy at the focus is increased by 16.53%. The matching layer plays an important role in the enhancement of transmitted wave. The enhancement is up to 314.7% in pressure amplitude at the focal point. The focal lens attributes a lot to the directivity and the resolution. The numerical analysis indicates the transducer integrated with a focal silicon lens and mechanical matching layer is feasible for imaging application.

3.3 Summary

In this chapter, we use the finite element numerical simulations for the optimized design. We simulate the wave propagations in solids (including isotropic

and anisotropic solids) and in fluid. Then piezoelectric transducer is coupled with non-piezoelectric materials. Wave steering excited by linear phased array sources and wave scattering of coarse boundary (rough surface) are studied. And systematic simulations are carried out for a designed buffered transducer array. Several conclusions arrive based on these simulations.

Firstly, in order to decrease the noise from reflectance waves in backing, a rough surface whose dimension is around 1.0λ should be considered to scatter a majority of incident waves.

Secondly, 2-D FEM model is more accurate to calculate the electrical impedance for piezoelectric array elements than KLM model which is usually used in 1-D models.

Finally, comprehensive studies are made for the backing-layer and buffered-layer arrays. Generally, the backing one serves a higher sensitivity. Nevertheless, the buffered one has a less constraint on pitch size, and it brings possibilities in the fabrication.

Chapter 4: LiNbO₃-based array fabrication and characterization

Previous attempts to fabricate 100 MHz array were based on thin film (fabricated by deposition to form polycrystalline films) design ranging in thickness between 10 μm and 40 μm , which suffers from several drawbacks such as slow deposition rates, high levels of stress generated during processing which can lead to cracking of the film, and low efficiency in generating ultrasound. Far more important for the thin film design, though, is that how to realize the patterning of small-scale features within the array and to eliminate the crosstalk between different elements. As mentioned in Chapter 1, Yukio Ito's group has reported 100 MHz arrays using ZnO thin films^[62]. They fabricated a 32-element array on a sapphire focal lens with a pitch of 100 μm , in which the large pitch brought about a low resolution. K. Shung's group has developed a 120 MHz kerfless array using 12 μm thick PZT films^[67,68]. However, the crosstalk between the deferent elements resulted in a significant ringing because of the kerfless structure. In contrast, the single crystal design proposed here allows the sensitivity enhancement by using piezoelectric material with coupling coefficient that is higher than that of thin films. For example, the electromechanical coupling coefficient of single crystal LiNbO₃ is $k_t = 0.49$ when generating longitudinal waves, while those of thin films are $k_t = 0.27$ and 0.34 ^[68] for ZnO and PZT, respectively.

Sputtering or sol-gel technologies are often chosen when ZnO or PZT are the piezo-active materials in the development of high-frequency ultrasonic array transducer. In this chapter, we use single crystal LiNbO₃ 36°/Y-cut combined with bonding, lapping and dry etching techniques that simplify the manufacturing processes^[144]. (Note: the thickness of LiNbO₃ is around 30 μm for resonating at 100 MHz. There are almost no methods to obtain so thin films of single crystal other than bonding and lapping techniques.) However, the fabrication of high frequency LiNbO₃ arrays is still a challenge due to the limit of separating the array elements. Because, on one hand, the element size in a high-frequency array is too reduced for conventional

dicing technique. On the other hand, the element is too thick for thin film etching techniques, particularly when very high depth/width aspect ratio is required. There is no hitherto report on kerfed LiNbO_3 arrays in high frequency.

This part will provide more technical details for linear array design through FEM simulations (by COMSOL). To investigate their properties and get a desired array transducer, some important structural parameters and characteristics are calculated, including kerf filler, kerf depth, pitch size, acoustic field, and crosstalk.

This chapter also investigates the etching method for kerfs and then describes the fabrication and evaluation of above 100 MHz linear arrays made from single crystal LiNbO_3 . Moreover, the array is characterized using Network Analyzer. The measured electrical impedance and crosstalk are compared to the finite element method (FEM) simulation results.

4.1 Simulation of backing transducer arrays

4.1.1 Model design

Section 3.2 discusses in detail the comparison between backing array structure and buffered array structure. Backing array structure possesses higher sensitivity despite of more difficulties in array fabrication. Our objective in this part is to obtain a LiNbO_3 array of backing structure.

As shown in Fig. 4.1.1a, in the backing-layer structure, the wave is emitted directly into water after mechanical matching and the backward propagating wave is scattered by the rough back surface of the silicon substrate. The structural parameters in an array play a critical role in the performance of the transducers. These structural parameters include pitch size, kerf width, kerf depth and thickness of the transducer which are defined and illustrated in Fig. 4.1.1b.

There are overall three pieces of requirement for these parameters. Firstly, in the thickness mode, the thickness of the transducer should be half wavelength in the piezoelectric material. For example, one wavelength is $66 \mu\text{m}$ in LiNbO_3 at 100 MHz. To generate longitudinal waves in thickness resonant mode, the thickness of LiNbO_3 elements should be $33 \mu\text{m}$. Secondly, pitch should be limited to half wavelength in transmission medium, generally water. For example, one wavelength is $15 \mu\text{m}$ in water at 100 MHz. To avoid grating lobes, the pitch should be $7.5 \mu\text{m}$. Thirdly, element width should be as big as possible in the range of pitch. For example, to

maintain the efficiency of transmission, the element width should be close to $7.5\ \mu\text{m}$ at 100 MHz. Correspondingly, the kerf width should be as small as possible. Fig. 4.1.1a shows a simulated focusing field in water, obtained by finite element calculation using COMSOL. The array has 32 LiNbO_3 elements resonating at 100 MHz, whose thickness, pitch and kerf width are $33\ \mu\text{m}$, $7.5\ \mu\text{m}$ and $2.5\ \mu\text{m}$, respectively. These ideal structural parameters result in an excellent focusing performance.

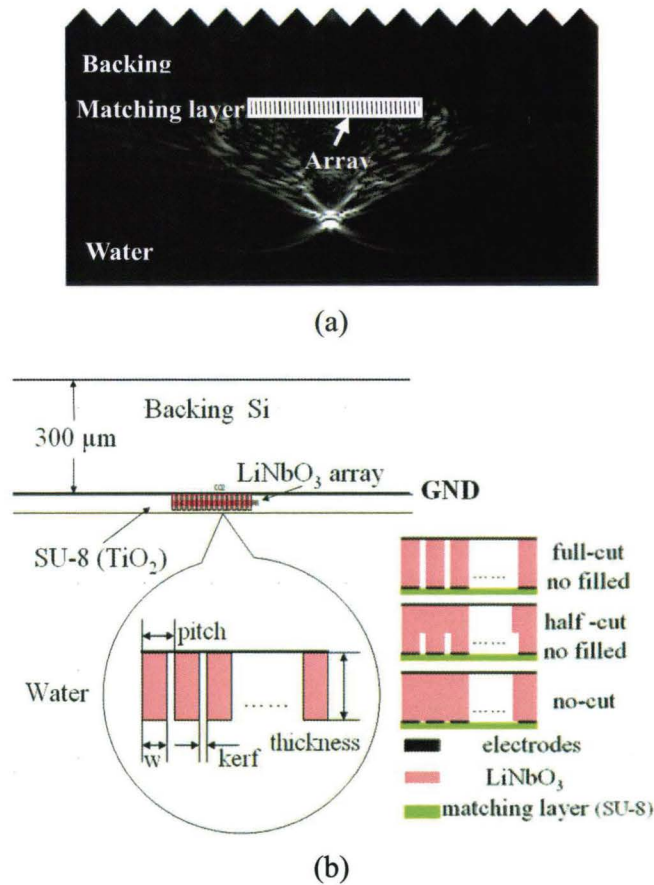


Figure 4.1.1: (a) Designed array structure and simulated focusing field in impulsion wave (b) Schematic cross-section for definitions of pitch, kerf width, element width and thickness of the transducer

However, the high depth/width aspect ratio is really a great challenge in etching piezoelectric materials to obtain kerfs. There is no hitherto report on fabricated arrays with so critical structural parameters in higher frequency of 80 MHz.

The backing-layer array model design is showed in Fig. 4.1.1b. Because the backing material reduces ringing resulting from reverberation of pulses and scatters

the ultrasonic energy, thus the bandwidth of ultrasonic transducer is widened. The backing material should be highly attenuating and is used to control the vibration of the transducer by absorbing the energy radiated from the back face of the piezoelectric material. Also, the material must have the same acoustic impedance as the crystal to prevent an echo from a crystal/damping interface from returning energy back to the crystal and creating reverberation noise. Here, silicon is chosen as the backing layer due to its acoustic impedance close to that of the piezoelectric elements, and the feasibility of combining the transducer array with integrated circuits. 36°/Y-cut single crystal LiNbO₃ was chosen as the active piezoelectric material for its favorable electro-mechanical efficiency and robust single crystal property.

The acoustic characteristics of some materials are displayed in Table 4.1.1. The SU-8-composite is mixed with nano-powder of TiO₂ to adjust its acoustic impedance (Z_a) to be $Z_{SU-8} = \sqrt{Z_{piezo} \cdot Z_{water}}$. Here, c_{11} is the first term of stiffness matrix, v_L is the longitudinal velocity, and ρ is the mass density. The following part is focused on the effect of pitch size, kerf filler and kerf depth on the array's performances. It is helpful to have a better understanding for the optimized design.

Table 4.1.1 Acoustic characteristics of some materials

Item	LiNbO ₃ ²	Si (buffer)	SU-8 ³ (matching)	SU-8 ⁴ (matching)	water
c_{11} (N/m ² ×10 ¹⁰)	20.3	16.56	1.966	1.566	—
B^1 (N/m ² ×10 ⁹)	—	—	—	—	2.2
v_L (m/s×10 ³)	6.57	8.43	2.886*		1.48
ρ (kg/m ³ ×10 ³)	4.7	2.33	2.36*	1.88*	1
Z (kg/m ² -s×10 ⁶)	30.88	19.64	6.81	5.43	1.48
¹ Bulk moduli of fluid ² 36°/Y-cut ³ TiO ₂ : 25 wt% for LiNbO ₃ and water					
⁴ TiO ₂ : 15 wt% for Si and water *Measured values					

4.1.2 Beam behaviour

a. Effect of pitch size on grating lobes (Acoustic field)

The directivity pattern depends greatly on pitch size in an array. The pitch size (p) should be limited to $\lambda/2$ in order to avoid grating lobes which will lead the array

transducer useless. However, the fabrication of arrays with small features remains a great challenge. A bigger pitch size has to be selected. To investigate more details of the effect of pitch size on grating lobes, the acoustic field in water is studied at different pitch sizes as shown in Fig. 4.1.2. The LiNbO₃ arrays are designed at 100 MHz. The wavelength in water, λ , is 15 μm for this frequency. All of the arrays are phased to focus at 500 μm in water. Comparing these figures, we can see when p is greater than 1.5λ , the grating lobes get close to the main lobe, which will lead the array transducer hardly useful. It can be concluded that the pitch size should be limited to smaller than 1.5λ . In addition, comparing Figs. 4.1.2 (d) and (e), it can be found when kerf width (k) increases while p keeps the same, sensitivity will decrease while directivity pattern keeps almost the same.

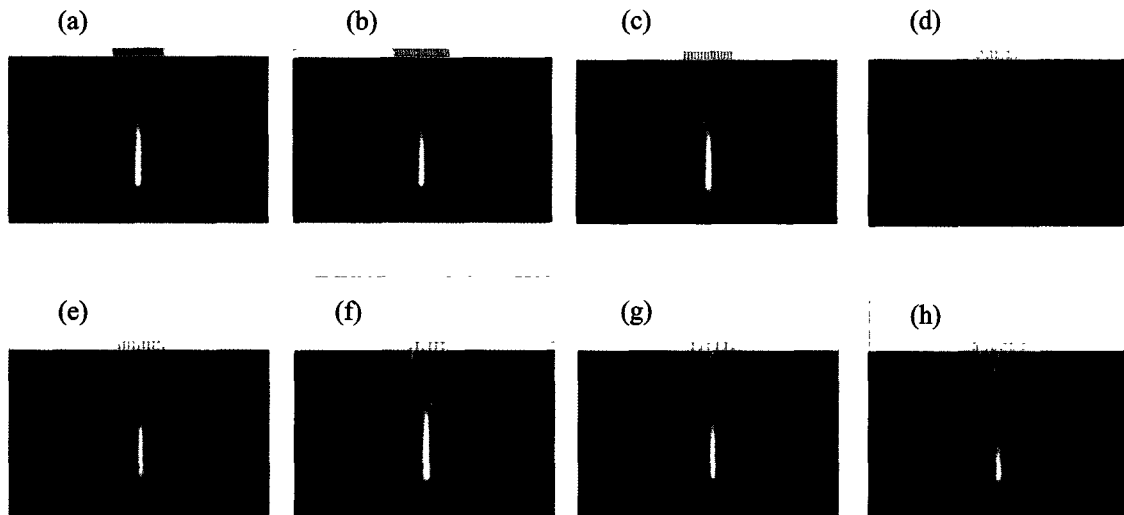


Figure 4.1.2: Acoustic fields with different pitch sizes: (a) $p = 0.5\lambda$, $k = 2 \mu\text{m}$; (b) $p = 0.75\lambda$, $k = 3 \mu\text{m}$; (c) $p = 1.0\lambda$, $k = 5 \mu\text{m}$; (d) $p = 1.5\lambda$, $k = 10 \mu\text{m}$; (e) $p = 1.5\lambda$, $k = 4.5 \mu\text{m}$; (f) $p = 2.0\lambda$, $k = 10 \mu\text{m}$; (g) $p = 2.5\lambda$, $k = 12.5 \mu\text{m}$; (h) $p = 2.8\lambda$, $k = 15 \mu\text{m}$. Here, $\lambda = 15 \mu\text{m}$, p is pitch size and k is kerf width.

b. Effect of kerf filler

Kerf fillers can affect the imaging resolution and sensitivity. FEM is used to simulate the acoustic fields to investigate this effect. The steering field and focusing field are illustrated in Fig. 4.1.3. Fig. 4.1.3 (1) is drove by ideal piston sources, and it is displayed here for reference. Fig. 4.1.3 (2) is from full-cut linear array filled with

SU-8 polymer, Fig. 4.1.3 (3) is from full-cut linear array without fillers. Comparing Fig. 4.1.3 (2) and Fig. 4.1.3 (3), we can see the no filled array has better beam performances than the filled array. Thus, in the following design, we try to fabricate no filled arrays.

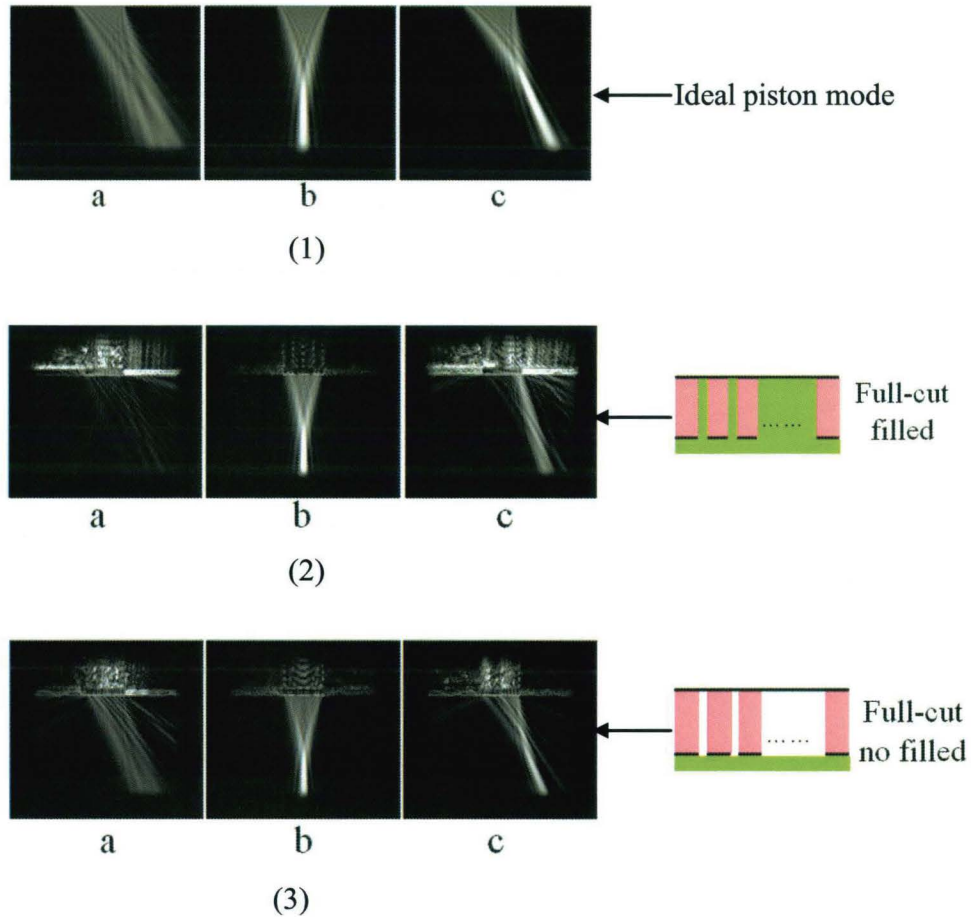


Figure 4.1.3: Acoustic field of steering 25° in a, focusing in b, and focusing and steering 25° in c for (1) linear array drove by ideal piston mode sources for reference; (2) full-cut linear array filled with SU-8 polymer; (3) full-cut linear array filled with air (in other words, without fillers).

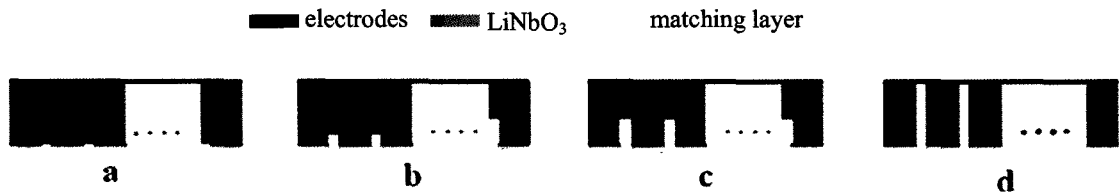
c. Effect of kerf depth

The fabrication of piezoelectric transducers is really a great challenge due to the small features in an array (to obtain kerfs with very high depth/width aspect ratio). To investigate the influence of kerf depth on the transducer's properties, such as beam performances and crosstalk, finite elemental numerical method is employed and an appropriate model is established in COMSOL3.5a. In the simulation, 32 elements are

used as the active aperture. The critical dimensions of the arrays are: $p = 7.5 \mu\text{m}$, $w = 5 \mu\text{m}$, $h = 33 \mu\text{m}$. The location of the focal point is determined by the phase delays and the width of the active aperture. By varying the phase delays, the radiation beams can be focused or steered/focused to different points in the image. This process of dynamic focusing can dramatically improve the quality of the ultrasonic images over a fixed-focusing system.

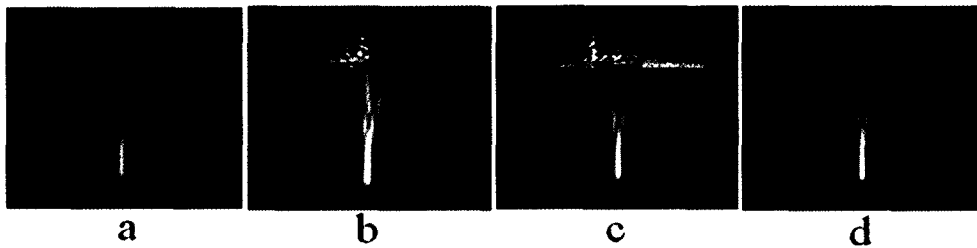
As shown in Fig. 4.1.4-1, four values of kerf depth are investigated. They are, respectively, $0 \mu\text{m}$ (seeing Fig. 4.1.4-1a), $5 \mu\text{m}$ (seeing Fig. 4.1.4-1b), $16 \mu\text{m}$ (seeing Fig. 4.1.4-1c), and $33 \mu\text{m}$ (seeing Fig. 4.1.4-1d). Fig. 4.1.4-2 and Fig. 4.1.4-3 show the continuous wave beam steering and focusing. The results in Fig. 4.1.4-2 and Fig. 4.1.4-3 demonstrate that, with dynamic focusing delays, the array could be well focused at the predicted distance and direction. And radiation grating lobes appear at approximately 50° in Fig. 4.1.4-2a. These severe undesired lobes will degrade imaging resolution significantly because they will induce false or superposing images during ultrasonic imaging. The undesired lobes in $5\text{-}\mu\text{m}$ -cut array are not as severe as in no-cut array, but the focusing result is still bad compared to that of the ideal full-cut array. Fortunately, the half-cut array performs almost the same as the full-cut one in focusing (seeing Fig. 4.1.4-2c-d). Moreover, three points can be concluded according to the steering/focusing results in Fig. 4.1.4-3. Firstly, the no-cut and $5\text{-}\mu\text{m}$ -cut arrays have severe grating lobes (seeing Fig. 4.1.4-3a-b). These severe undesired lobes are compatible to the main lobe, which indicated that these arrays are useless in phased array imaging. Secondly, there is almost no grating lobe for the half-cut array as shown in Fig. 4.1.4-3c, and slight grating lobe are visible for the full-cut array as shown in Fig. 4.1.4-3d. These slightly undesired lobes are much weaker than the main lobe, thus it would not greatly affect the imaging resolution. This indicates that these arrays are acceptable in ultrasonic imaging. Thirdly, comparing the main lobes in Fig. 4.1.4-3c and Fig. 4.1.4-3d, it can be seen that the resolution of the full-cut array is higher than the half-cut one. In order to investigate more detailed information, the lateral pressure distribution along focusing plane in radiation medium is summarized in Fig. 4.1.5 quantitatively for these arrays with different kerf depth. Generally, it shows the kerf depth plays a greater role in beam steering/focusing than in focusing. The curve of half-cut array is generally close to that of the full-cut one in both cases of focusing and steering/focusing. As demonstrated in Fig. 4.1.5b, the Full-Width-at-Half-Depth (FWHD) is $55 \mu\text{m}$ for the half-cut array, and is $42 \mu\text{m}$ for

the full-cut one. The curves of the 5- μm -cut array in two cases are both very close to those of the no-cut one. The big peaks other than the main lobe are up to one third of the main peak in pressure amplitude, which results in no use of these arrays in ultrasonic imaging using steering/focusing. In conclusion, all of these results indicate that compared with the ideal full-cut array, the half-cut one can serve a satisfactory beam performance, while the no-cut and 5- μm -cut ones are not acceptable.

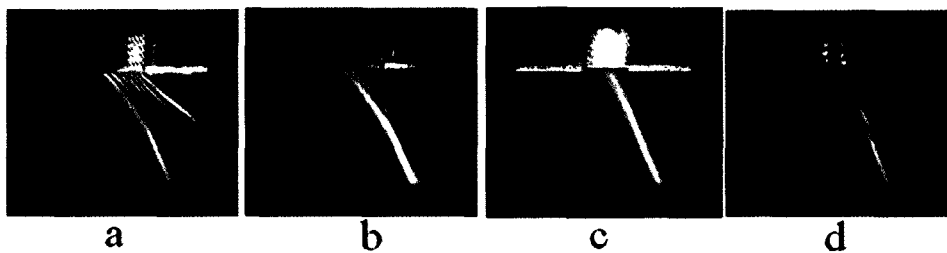


(1) Arrays with different cut depth:

(a) No-cut array (b) 5 μm -cut array (c) Half-cut array and (d) Full-cut array.

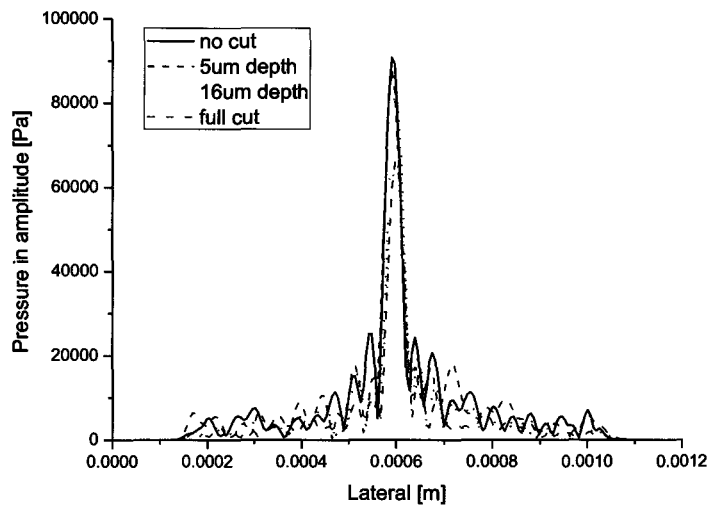


(2) Focusing (Focal distance = 500 μm)

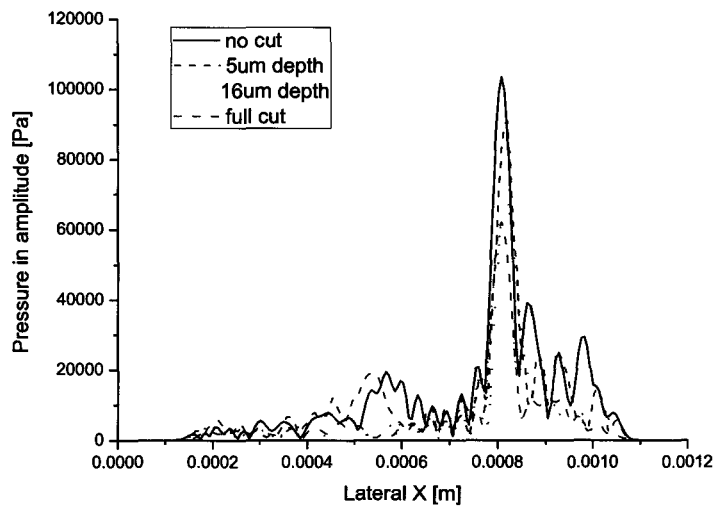


(3) Steering ($\theta = 25^\circ$) and focusing (Focal distance = 500 μm)

Figure 4.1.4: Simulated radiation field of the phased arrays



(a) Focusing (Focal distance = 500 μm)



(b) Steering ($\theta = 25^\circ$) and focusing (Focal distance = 500 μm)

Figure 4.1.5: Lateral pressure distribution for arrays with different kerf depth: 0 μm cut, 5 μm cut, 16 μm cut, and 33 μm cut

Crosstalk is another important characteristic influencing the imaging quality. In order to investigate the relationship between crosstalk and kerf depth, FEM simulation is carried out. The electrical boundaries are set that only the central array element ($n = 0$) is excited with 1 volt sine potential (V_{in}) while the other elements are opened. As explained previously, the crosstalk is then defined as the electrical response (V_n) at each element. Fig. 4.1.6 shows relation between the crosstalk (in amplitude) of

adjacent element and the kerf depth of the arrays. It shows that the crosstalk has a linear correlation with the kerf depth. Based on the linear relation, it can be seen that the crosstalk is lower than -20 dB when the kerf depth is larger than 13 μm . The crosstalk value of -20 dB is usually acceptable in ultrasonic imaging. In this 32-element half-cut array, the crosstalk of each element is calculated and is presented in Fig. 4.1.7. It shows that the crosstalk is lower than -20 dB. For comparison, as shown in Fig. 4.1.7, the 32-element arrays of 5 μm kerf depth and 33 μm kerf depth are also characterized by crosstalk on each element. The crosstalk values of 3- μm -cut array are too high to be accepted. And the values of the full-cut array are all lower than -28 dB, which is promising. But the full-cut array is not possible to be obtained using state-of-the-art technologies. Although half-cut array has greater crosstalk than the full-cut one, it possesses less lateral modes when generating longitudinal waves. In conclusion, it demonstrates that the half-cut array is a promising candidate, which can favor a lot for the micromachining process due to the much lower aspect ratio compared to the full-cut one.

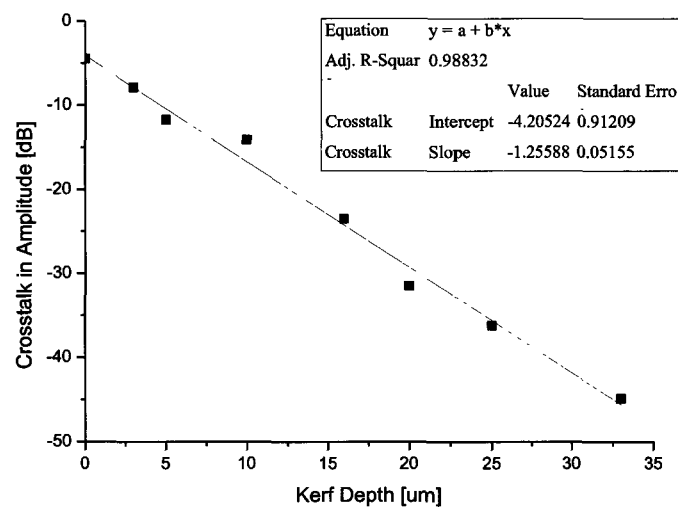


Figure 4.1.6: Simulated crosstalk (in amplitude) for adjacent element in arrays with different kerf depth

In summary, the effect of kerf depths is investigated by finite element analysis including focusing/steering acoustic fields and crosstalk. Half-cut array is demonstrated to be a promising candidate for micromachining due to much smaller depth/width aspect ratio and acceptable transducer performances.

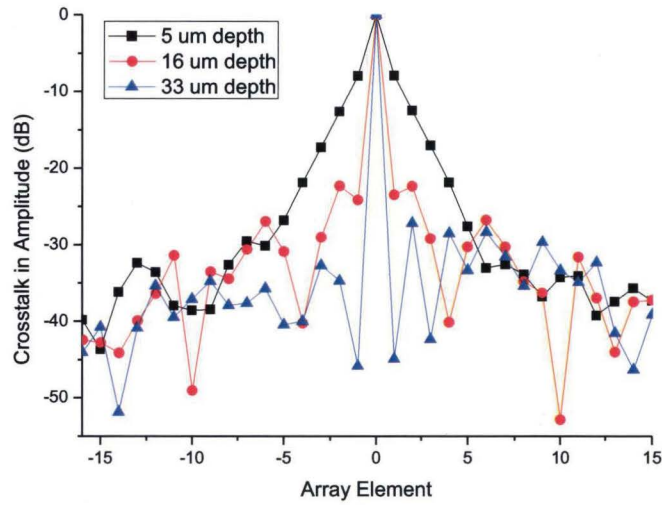


Figure 4.1.7: Crosstalk determined by the neighboring elements response (in amplitude) in 3 arrays of different kerf depth.

4.2 Investigation of etching LiNbO₃ 36°/Y-cut arrays

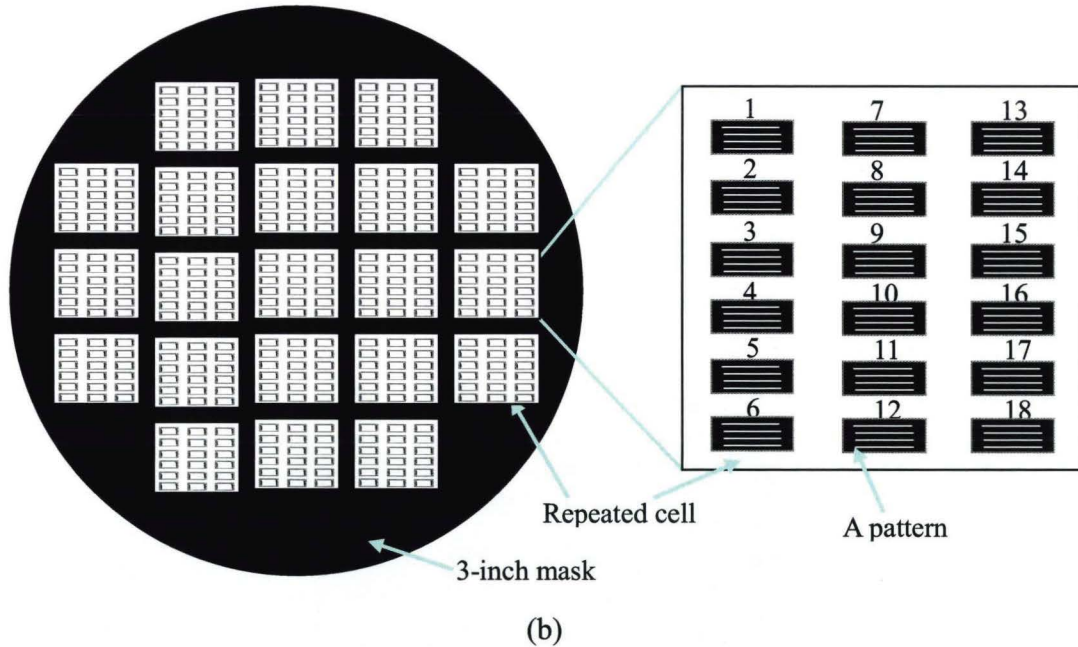


Figure 4.2.1: Schematic top view of 18 different patterns in a 3-inch quartz mask.

In order to investigate the limit in the fabrication of high-frequency arrays, 18 patterns are designed in a cell which is repeated on a 3-inch mask as shown in Fig.

4.2.1. Patterns 1 to 6 have a same pitch size of 7.5 μm but different element widths. Patterns 7 to 12 have a pitch size between 10 to 15 μm and different element widths. Patterns 13 to 18 have a same pitch size of 42 μm but different element widths. Their detailed dimensions are shown in Table 4.2.1.

Table 4.2.1 Detailed dimensions of patterns 1-18 on the mask

Pattern Index	μm		Pattern Index	μm		Pattern Index	μm	
	pitch	kerf		pitch	kerf		pitch	kerf
1	7.5	3.5	7	15	5	13	42	15
2		3	8		4	14		10
3		2.5	9		3	15		8
4		2	10		2	16		5
5		1.5	11	13	3	17		4
6		1	12	10	3	18		3

To make a kerfed array, we have investigated two methods to etch single crystal LiNbO_3 . They are focused ion beam (FIB) and inductively coupled plasma (ICP) reactive ion etching (RIE).

4.2.1 Focusing Ion Beam (FIB)

Wet etch and dry etching methods are widely used in shaping LiNbO_3 crystals [145,146]. In the wet etching process, HF/HNO_3 mixture is usually chosen as the etchant. But it results in a rough bottom in the single crystals as shown in Fig. 4.2.2 [147].



Figure 4.2.2: SEM image of LiNbO_3 pattern etched by HF and HNO_3 acids in a 1 : 2 ratio, where the HF was a 48% solution and the nitric acid was a 78% solution [147].

Dry etching is a more controllable process and has the advantage of being highly anisotropic [148]. We tried a dry etching method here to obtain kerfs in LiNbO₃ array. It is Focusing Ion Beam (FIB) method.

Fig. 4.2.3 shows etching images using FIB method. The FIB equipment in our lab is an FEI STRATA DB 235 and it uses gallium ion sources. In a Gallium Liquid-Metal Ion Source (LMIS), gallium metal is placed in contact with a tungsten needle and heated. Gallium wets the tungsten, and a huge electric field (greater than 10⁸ V/cm) causes ionization and field emission of the gallium atoms. Source ions are then accelerated to an energy of 5-50 keV (kiloelectronvolts), and focused onto the sample by electrostatic lenses. LMIS produced high current density ion beams with very small energy spread. The modern FIB can deliver tens of nanoamperes of current to a sample, or can image the sample with a spot size on the order of a few nanometers.

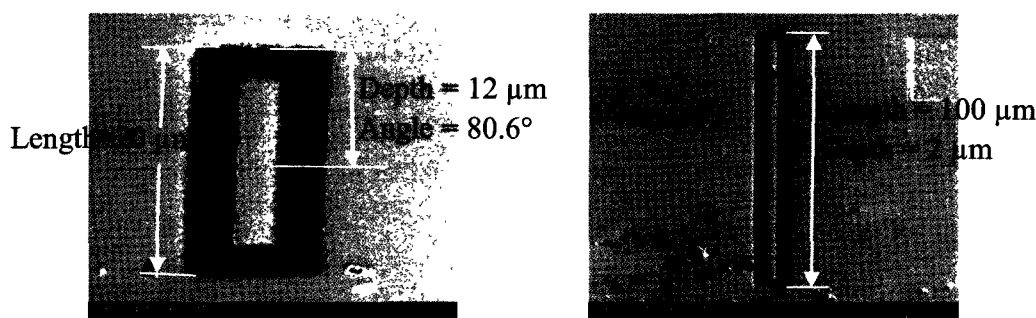


Figure 4.2.3: Etching images using focusing ion beam (FIB) method

In Fig. 4.2.3, the left one shows the kerf in LiNbO₃ is 2 μm wide, 20 μm long and 12 μm deep. The sidewall angle is 80.6°. It means that aspect ratio as high as 6:1 can be obtained in the etched kerfs. It is estimated that, for a full-kerfed array, a pitch of 0.7 wavelengths can be obtained in single crystal LiNbO₃.

This process in the left image took 10 minutes. The FIB cost is 60 euros per hour. The kerf (2 μm wide, 100 μm long and 2 μm deep) in the right image also took 10 minutes to be etched. However, in the high-frequency (about 100MHz) array fabrication, the kerf between elements should be about 1000 μm long and 30 μm deep. It will take about 1500 minutes for etching just one element. No mention to 128

elements, the cost for only one element would be as high as 1500 euros. Therefore, we abandon this method in our array fabrication. Nevertheless, this method provides a possibility to fabricate a much desired array.

4.2.2 Inductively Coupled Plasma (ICP) Reactive Ion Etching (RIE)

We also investigated other feasibilities other than FIB method to fabricate high-frequency array elements. It is inductively coupled plasma (ICP) reactive ion etching (RIE).

As far as ICP RIE is concerned, I like to introduce its operating principle.

Firstly, Reactive Ion Etching (RIE) is an etching technology used in microfabrication. It uses plasma to chemically react with the materials deposited on wafers or the wafer itself. The plasma is generated under low pressure (vacuum) by an electromagnetic field. High-energy ions from the plasma attack the wafer surface and react with it to produce gas. The gas products can be taken away by a pump. Thus the surface materials are removed or, in other words, etched.

Secondly, Inductively Coupled Plasma (ICP) is a type of plasma source in which the energy is supplied by electric currents which are produced by electromagnetic induction, that is, by time-varying magnetic fields ^[149]. There are two types of ICP geometries: planar and cylindrical. In planar geometry, the electrode is a coil of flat metal wound like a spiral. In cylindrical geometry, it is like a helical spring. The cylindrical coil can generate higher density of plasma. When a time-varying electric current is passed through the coil, it creates a time-varying magnetic field around it, which in turn induces azimuthal electric currents in the rarefied gas, leading to the formation of plasma. Argon is one example of a commonly-used rarefied gas. ICP has two benefits: (1) ICP discharges are of relatively high electron density, on the order of 10^{15} cm^{-3} . As a result, ICP discharges have wide applications where high-density plasma is needed. (2) ICP discharges are relatively free of contamination because the electrodes are completely outside the reaction chamber.

ICP RIE has demonstrated its potential in batch fabrication of deep anisotropic microstructures in silicon and enabled high-aspect-ratio (more than 100:1) deep

silicon etching, which produced great impact on MEMS device fabrication. More recently, high speed directional etching using ICP plasma has been extended to materials other than silicon. Non conventional materials like LiNbO₃ can be etched using various fluorine- and fluorocarbon-based chemistries. However, in contrast to well-studied silicon or silicon dioxide etching, many problems exist in RIE etching of non conventional materials. Because crystalline metal oxide films tend to be chemically very inert, LiNbO₃ is difficult to structure, in particular with high resolution and reasonably fast etch rate. It has been dry etched using chemically reactive gases such as CHF₃, CF₄ and SF₆ [150,151,152]. In this work, the ICP RIE process for etching LiNbO₃ is carried out in Femto-St institute, Besancon. For deep microstructures in LiNbO₃, CHF₃ was not available on the DRIE (deep RIE, which uses ICP RIE system) machine. In addition, the previous trials showed that using CF₄/He plasma instead of an SF₆/He allowed the etching speed to be multiplied by a factor 5 (0.5 μm/min instead of 0.1 μm/min), and the etched profile to be improved by over 13° (75° instead of 62°). Thus we used CF₄/He gas mixture in our experimental fabrication. The fabrication process is illustrated in Fig. 4.2.4.

As shown in Fig. 4.2.4, electroplated nickel (Ni, 6 μm thick) was used as mask material. The Ni patterns are obtained by lift-off process. Prior to the electroplating of the Ni layer, a 100 nm of Cr/Ni adhesion/seed layer was deposited by sputtering onto the clean substrate (see Fig. 4.2.4a). A positive 12 μm thick AZ9260 photoresist was patterned by contact photolithography (the principle of photolithography is introduced in the following part) using a standard process (see Fig. 4.2.4b). For the electroplated mask, a 6 μm thick layer was electroplated in the photoresist stencil using a typical Watts bath based on Ni sulfamate (lower stress than Ni sulfate) at a current density of 1.5 A/dm² and a bath temperature of 50°C (see Fig. 4.2.4c). At the end of the process the photoresist was removed by acetone and the plating layer by RIE (see Fig. 4.2.4d).

The deep plasma etching (see Fig. 4.2.4e) is carried out using a multiplex AOE reactor of STS with an ICP RF (radio frequency) generator (using planar coil) of 3 kW and a RIE generator of 1.5 kW. The maximum size of the wafer is 6 inches, and the gas available includes CF₄ and He. The temperature of the substrate holder can be

varied between 20 and 80°C. The samples were bonded to Si carriers with a thermal grease to cool the sample. Selectivity and etch rate were estimated from Scanning Electron Microscope (SEM) images normalized against profile measurements of the same feature.

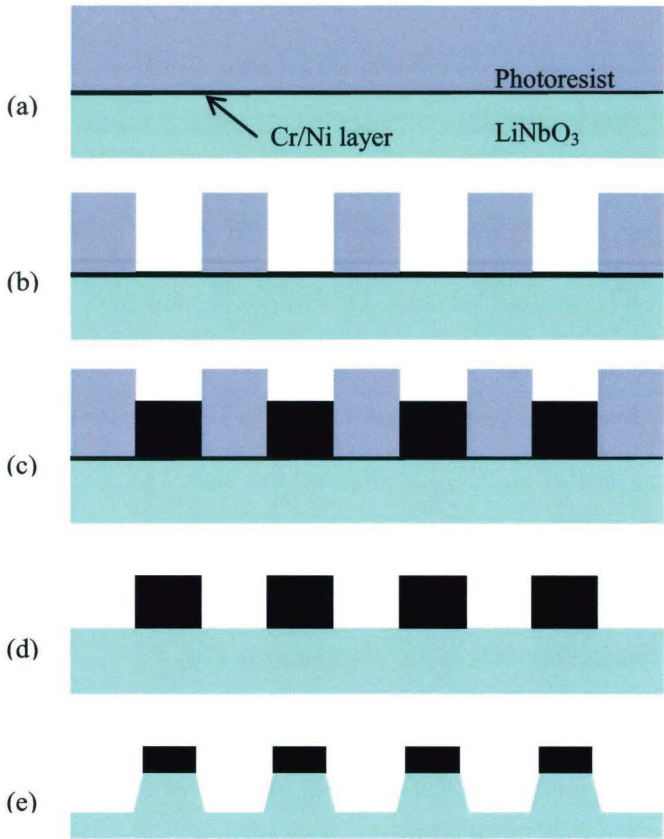


Figure 4.2.4: Fabrication process of LiNbO₃ arrays

The selectivity ratio and profile angle, determining the performance of the transducer arrays, are the most important parameters in dry etching of LiNbO₃ film. To explore the limitation of the high aspect ratio ICP LiNbO₃ deep etching, several patterns with a fixed pitch of 42 μm are designed, varying the kerf widths according to the different d/w ratios (w: kerf width; d: kerf depth). Fig. 4.2.5 shows the etching results for different aspect ratios under optimized process parameters. The insets are the SEM images of the different etching profiles. The desired etching profile is square shaped; however, as illustrated in Fig. 4.2.5, a tapered profile develops in the transducer array.

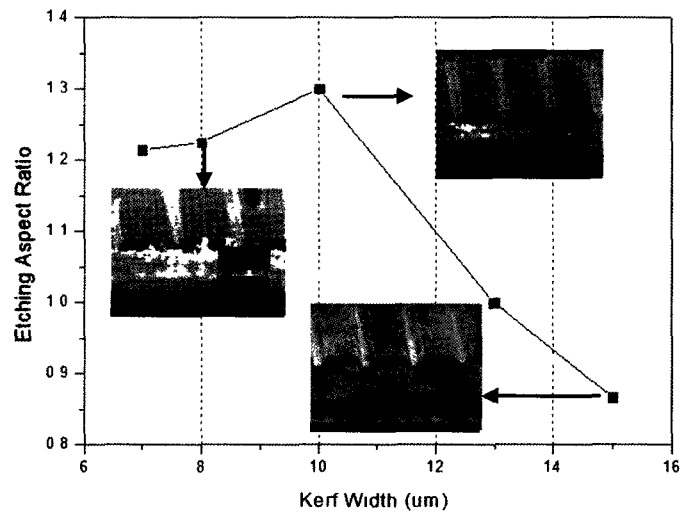


Figure 4.2.5: Etching aspect ratio as a function of the kerf width.

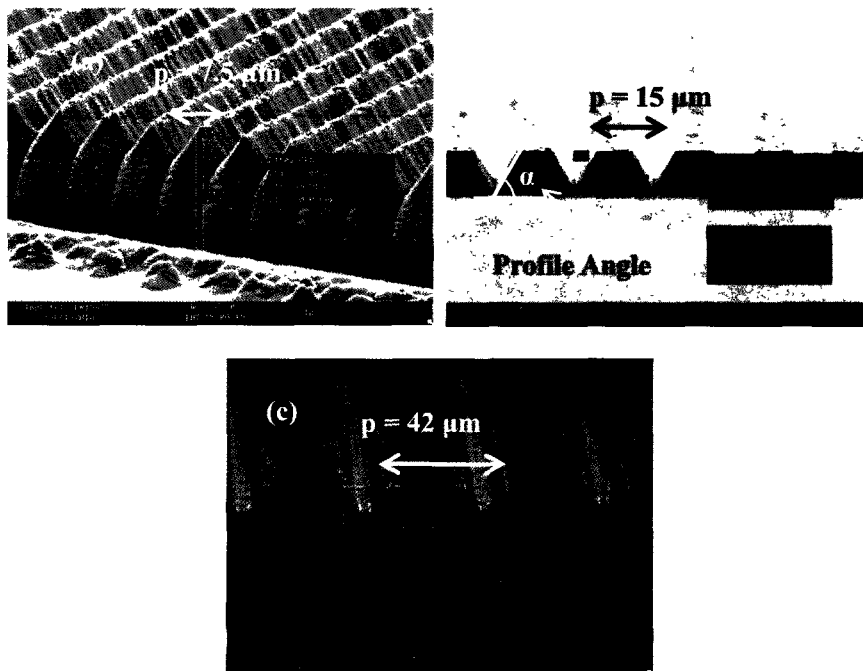


Figure 4.2.6: Etched patterns with different pitch sizes and kerf widths: (a) pitch = 7.5 μm ; (b) pitch = 15 μm ; and (c) pitch = 42 μm ; the profile angle is $\alpha = 67^\circ$

Keeping the kerf depth at 14 μm , shown in Fig. 4.2.5, the aspect ratio of etching profile increases with the kerf width decreasing till it stops by forming a V-shaped groove, and the positive tapered profile angle ranges between about 62° and 80° . If the mask selectivity does not limit the process in terms of achievable depth, the aspect ratio is limited to values around 1.3 by the profile angle. The aspect ratio of the large kerf ($\geq 10 \mu\text{m}$) etching is up to 1.3, while for the smaller kerf it decreases gradually.

As the aspect ratio reduces to about 1^[153], it has been suggested that the etching rate begins to be limited by transport of etch gases into the kerf and etch products out of the kerf. For closely spaced structures, this would result in profile angles less than 60°, which is unacceptable for fabricating high-frequency arrays. Therefore, it is hard to get a large etching depth (tens of micrometers), in particular for fine structures.

It is evident that a great range of aspect ratios are obtainable. It is, however, also interesting to calculate the minimum element pitch that can be obtained with ICP etching technique. Fig. 4.2.6 presents the SEM image of the realized array without matching layers. The results show that all kerfs are grooved in a V-shape. The width of the etched kerf is a function of its depth because of the crystalline structure of LiNbO₃. For a 100 MHz array, the thickness of LiNbO₃ elements should be 33 μm, and the width of the element should be wider than the kerf width to enable the transducer to work effectively. As illustrated in Fig. 4.2.6a, the top part of each element was removed due to lateral etching. This tapered structures resulted in no use for generating waves. The array with a pitch of 42 μm seems excellent in the structure with 16-μm kerf depth and a 75° profile angle as shown in Fig. 4.2.6c, but the large pitch will lead to a low resolution for imaging. The array in Fig. 4.2.6b with depth of 8.5 μm shows an acceptable etched profile. The profile angle is illustrated in Fig. 4.2.6b. According to the etching results, it is impossible to achieve a fine structure with the pitch less than 20 μm under the optimal process conditions. Thus, it can be predicted that the smallest pitch could be obtained at about 25 μm (about 1.6 λ, λ is 15 μm--the corresponding wavelength in water at 100 MHz) by the ICP RIE method.

4.3 Fabrication of LiNbO₃ 36°/Y-cut transducer array on silicon

4.3.1 Process flow

Based on the above discussion, we choose ICP RIE method to etch single crystal LiNbO₃. Fig. 4.3.1 illustrates the fabrication flow of the array transducer. As shown in

Fig. 4.3.1a, a layer of chromium (Cr)/indium (In) was first deposited by evaporation technique to the surface of backing substrate which is a silicon wafer (2 mm thick) and to the back side of LiNbO₃ 36°/Y-cut wafer (about 300 μm thick). The thickness of Cr layer is around 10 nm, and In layer is around several hundred of nanometers to one micrometer. The LiNbO₃ was then bonded on backing material, and then precisely thinned by lapping to a desired thickness (16 μm). The bonding process is carried out in an oven at 170°C. Thanks to the key advantages (including low melting point, ability to creep and remove stress as dissimilar materials cool, and reduced warpage) of indium, a high quality of bonding is given.

During the lapping process, micro-scaled diamond particles are introduced. As shown in Fig. 4.3.2, a mechanical thickness measurement gauge was used to measure the thickness of LiNbO₃ layer during this step. After top electrodes patterning, as stated in part 4.2.2, the array was obtained by ICP RIE etching with CF₄/He gas mixture, using electroplated Ni (6 μm thick) as mask material (see Fig. 4.2.4b). More details about the etching process can be found in part 4.2.2. Then the active elements (piezoelectric elements: *p*) should be covered with a mechanical matching layer (here SU-8 based material is chosen, more information can be found in ^[131] about the potentialities and fabrication process of SU-8 nanocomposites) which permits an efficient electro-mechanical conversion into the radiation fluid (*f*). The method of adding matching layer is illustrated in Figs. 4.3.1 (c) and (d).

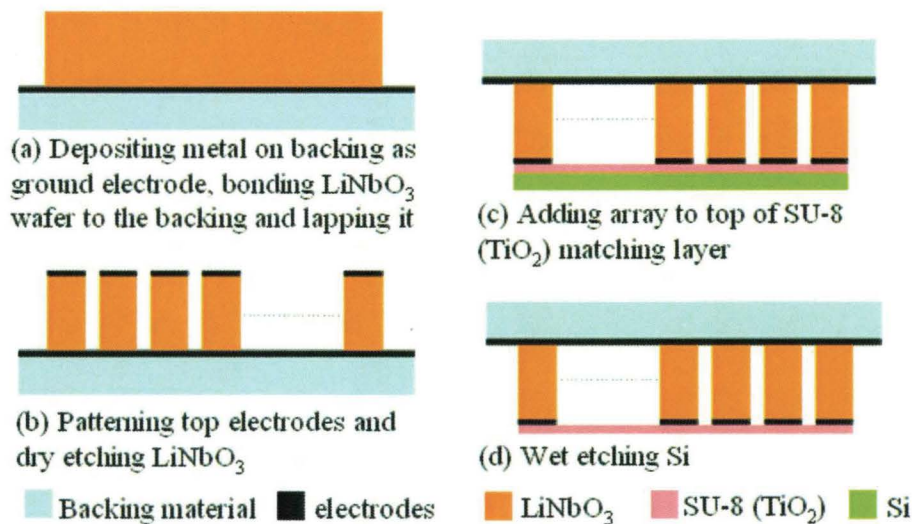


Figure 4.3.1: Fabrication flow of the array transducer

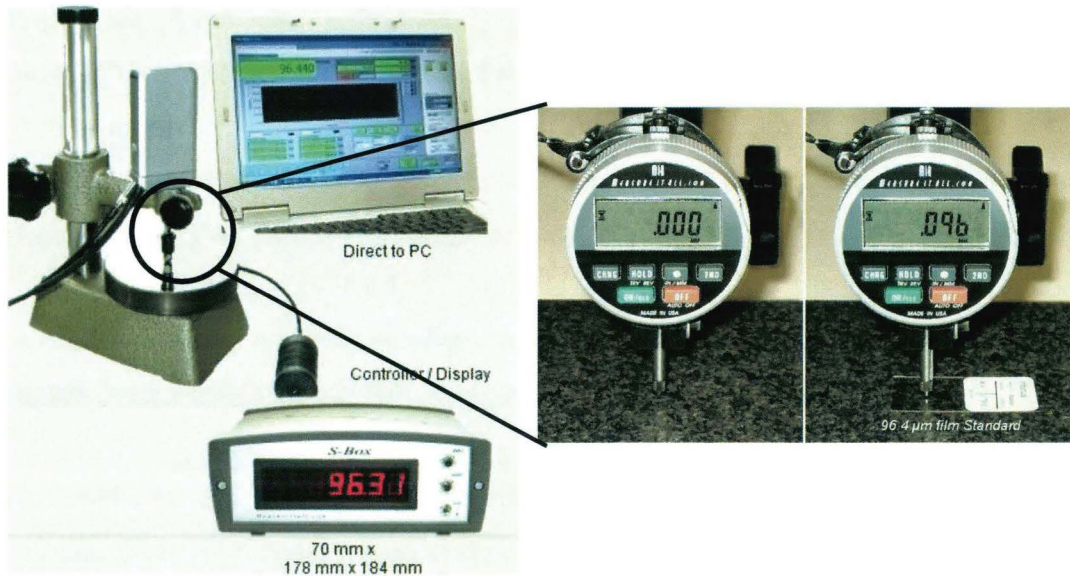


Figure 4.3.2: Thickness measurement gauge used to test the thickness of LiNbO_3 layer

4.3.2 Fabricated array transducers

Different size combinations of array pitches and kerf widths were patterned on the same mask as shown in Fig. 4.3.3.

Fig. 4.3.3 presents the optical microscope images of the realized arrays. Fig. 4.3.4 presents the SEM images of the realized arrays without matching layers. The results show that the etched kerf depth is a function of the kerf width. Because of LiNbO_3 crystal structure, all kerfs were obtained in V grooves with a 75° vertical angle. Thus, for a 200 MHz array, the thickness of LiNbO_3 elements should be $16 \mu\text{m}$, the kerf depth should be $8 \mu\text{m}$ for the half-cut array, and correspondingly, the kerf width is up to $4.2 \mu\text{m}$. The width of the element should be larger than the kerf width to maintain an efficient emission, so the smallest pitch that could be obtained is $10 \mu\text{m}$ (that is 1.3λ , λ is the corresponding wavelength in water at 200 MHz, $7.5 \mu\text{m}$) by the ICP RIE method.

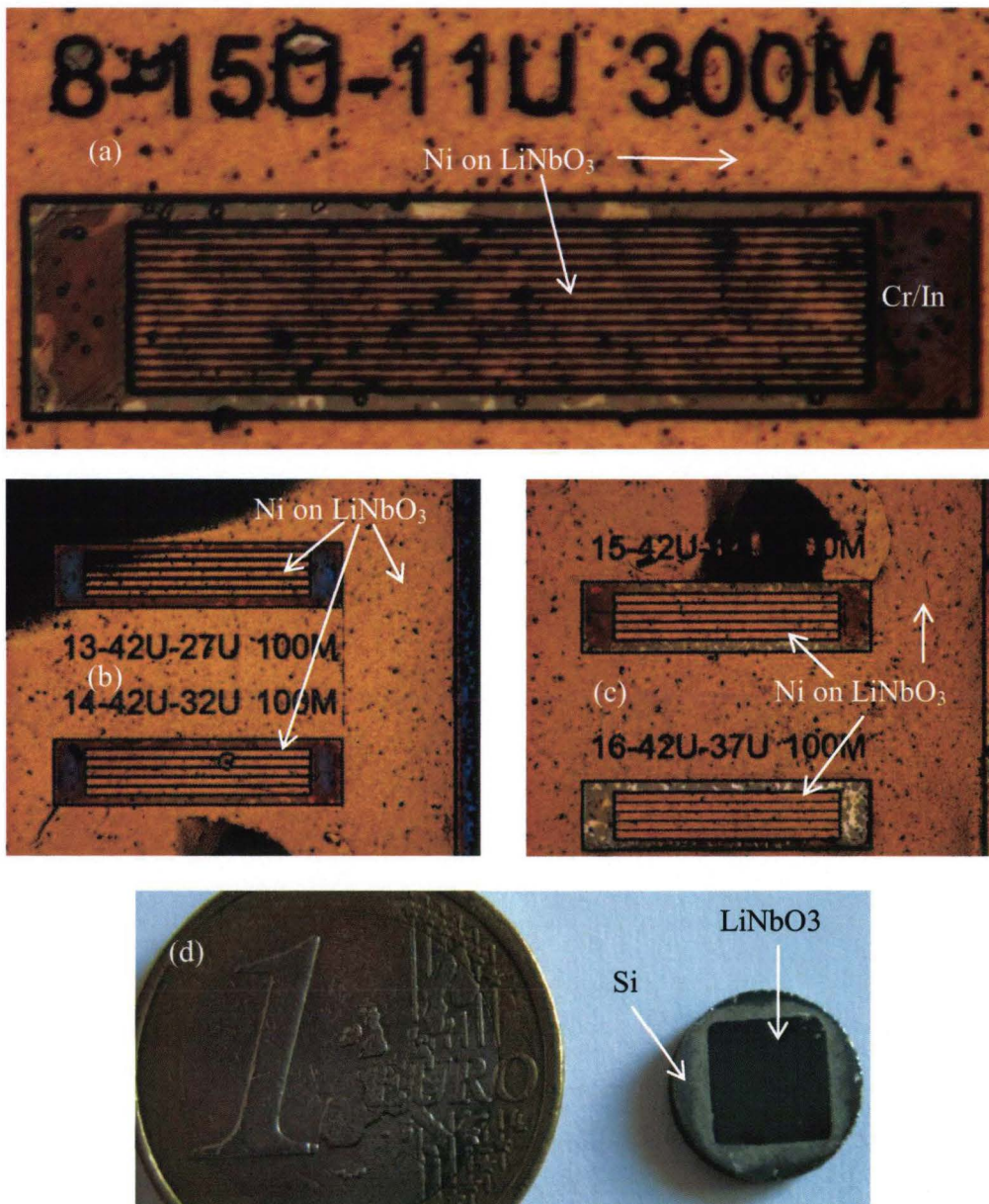


Figure 4.3.3: Optical microscope images of the realized LiNbO₃ arrays (with a thickness of 16 μm) etched by ICP: (a) pitch = 15 μm, kerf = 4 μm for pattern 8 (b) pitch = 42 μm, kerf = 15 μm for pattern 13 and kerf = 15 μm for pattern 14 (c) pitch = 42 μm, kerf = 7 μm for pattern 15 and kerf = 5 μm for pattern 16 (d) fabricated sample compared with a piece of one euro.

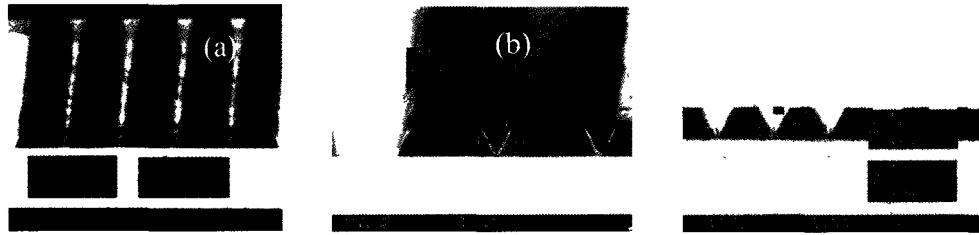


Figure 4.3.4: SEM images of LiNbO₃ arrays (with a thickness of 16 μm) etched by ICP: (a) pitch = 42 μm, kerf = 20 μm; (b) pitch = 42 μm, kerf = 14 μm; (c) pitch = 15 μm, kerf = 7 μm; all have about 75° kerf angle.

4.3.3 Discussion of fabricated patterns

Table 4.3.1 summarizes the 18 patterns of LiNbO₃ arrays fabricated by ICP RIE. In conclusion, only patterns 8, 13, 14, 15, 16 are obtained. The thickness of LiNbO₃ is 16 μm. And the arrays were partly kerfed due to the limit of the single crystal structure.

Table 4.3.1 Fabricated patterns of LiNbO₃ arrays by ICP RIE

Pattern Index	μm		Pattern Index	μm		Pattern Index	μm		
	pitch	kerf		pitch	kerf		pitch	kerf	
1	7.5 (F)	3.5	7 (F)	15	5	13 (S)	42	15	
2		3	8 (S)		4	14 (S)		10	
3		2.5	9 (F)		3	15 (S)		8	
4		2	10 (F)		2	16 (S)		5	
5		1.5	11 (F)		13	3		17 (F)	4
6		1	12 (F)		10	3		18 (F)	3

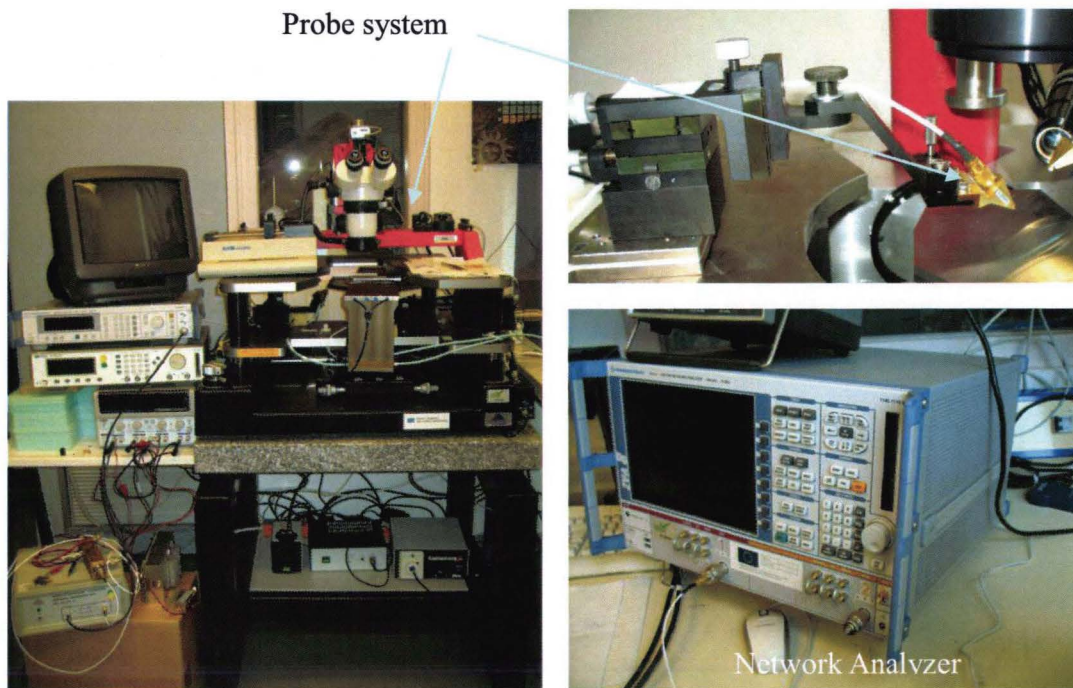
F: Failed

S: Successful

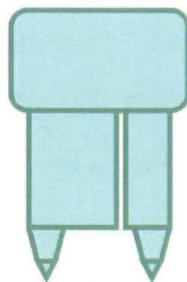
4.4 Characterization of LiNbO₃ 36°/Y-cut transducer array

4.4.1 Measurement method

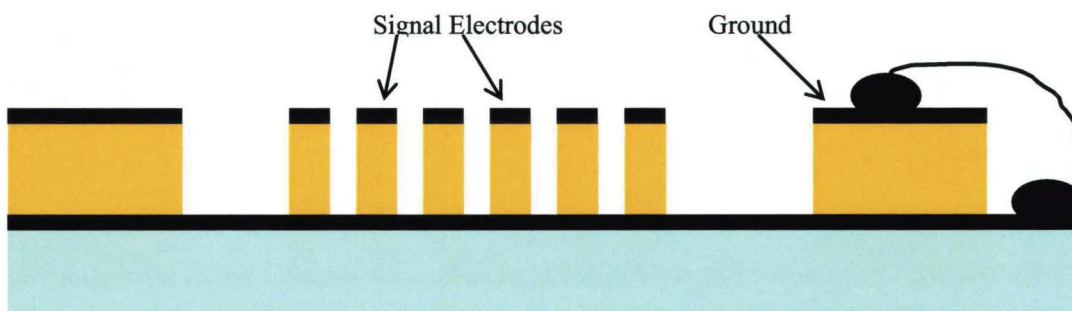
We use the following system, as shown in Fig. 4.4.1a, to characterize our devices.



(a)



(b)



(c)

Figure 4.4.1: (a) Measurement system including Network Analyzer and micro-probe system (b) Schematic top view of micro-probes (c) Schematic cross-section of detailed ground connection.

The system constitutes of a Rhode and Scharwtz Vector Network Analyzer (VNA) and a Karl Suss micro-probe system. For our high-frequency measurement, the network analyzer benefits a wide bandwidth (300 kHz ~ 8 GHz). And the double side micro-probe system is from Cascade Microtech, Inc. which is a worldwide leader in the precision electrical measurement and test of advanced semiconductor devices—integrated circuits (ICs), chips, circuit boards, modules, MEMS, 3D TSV, LED devices and more. We obtain the electrical impedance and crosstalk of our devices through measuring the S_{11} and S_{21} scattering parameters of the two-port device by this network analyzer with the micro-probe system. There is a calibration before the measurements. The calibration of the network analyzer of the measurement workbench is achieved to obtain the S_{ij} parameters in the plane of the probes. So the compensation of the cables and probes impedances is achieved using standard ‘Short circuit’, ‘Opened Circuit’, ‘through line’ and ‘50 Ohms load’ on a calibrated sample used as reference.

Attention needs to be paid on the micro-probes. As shown in Fig. 4.4.1b, a pair of micro-probes is in the same plane. Thus, if a voltage is applied to the array element, the ground and the signal electrode should be in the same plane. In our experiment, we used gold wire bonding to solve this problem. The detailed connection scheme is illustrated in Fig. 4.4.1c.

4.4.2 Measured results

Finally, the transducer arrays with the pitch of 42 μm and 15 μm are obtained, respectively.

To compare the measured electrical impedance with the simulation results, a 5-element array is realized as shown in Fig. 4.3.4a. The element width is 24 μm . Fig. 4.4.2 presents the impedance magnitudes of the central element for the 5-element array. The solid line is the measured result obtained from S_{11} parameter by Network Analyzer, which is consistent to the 2-D FEM (from COMSOL) simulation result (dashed line). It shows that the impedance magnitude is around 1 k Ω at the resonant frequency of 230 MHz. Moreover, the measured S_{21} scattering parameters are also

Pour des raisons indépendantes de notre volonté, il nous est impossible de reproduire cette page car celle-ci n'étant pas présente dans l'original qui nous a été transmis.

Pour des raisons indépendantes de notre volonté, il nous est impossible de reproduire cette page car celle-ci n'étant pas présente dans l'original qui nous a été transmis.

Chapter 5: ZnO-based array fabrication and characterization

Thin-film zinc oxide (ZnO) single element transducers have been widely used for acoustic microscopy applications in the frequency range of 100 MHz to 1 GHz [154,155,156,157]. Beyond 100 MHz ultrasonic arrays have not been developed. Unlike high-frequency single-element transducers, as explained previously, one of the major challenges in developing high-frequency ultrasonic transducer arrays is the patterning of small-scale features within the arrays. For example, ZnO linear arrays designed for 300 MHz operation should have array elements with maximum a pitch of 7.5 μm (1.5λ) and a kerf width of 3 μm , whose thickness should be 8 μm for the desired resonant frequency. A number of researchers have focused their efforts on the fabrication methods of high-frequency arrays [62,158,159,160], and several different approaches are being taken, such as dice-and-fill method, Interdigital pair bonding (IPB) and laser micromachining. In general, all of these fabrication methods are somewhat empirical, have low efficiency, and have correspondingly high fabrication costs.

To realize ZnO-based arrays, the development of ZnO etching techniques with high etching rates, high selectivity over mask materials, highly anisotropic etch profiles, and smooth side-walls is essential. However, systematic studies of ZnO etching processes have not been hitherto extensively performed. Several research groups investigated the behaviors of thin-film ZnO using dry and wet etching processes [161,162,163,164,165,166,167] and severe lateral undercutting (see Fig. 5.1), however, is produced by various wet-chemical etchants (the hitherto smallest ratio of lateral etching to vertical etching is 0.82 obtained in [168]). As shown in Fig. 5.1, a is lateral etching and b is vertical etching. The ratio of lateral etching to vertical etching is then defined as a/b .

On the other hand, detailed information about etching process for thick-film ZnO is lacking. Thick-film ZnO arrays were only reported by Yukio Ito with 100- μm -wide pitch and 10- μm -wide V-grooved kerfs [62]. Here, “thick” is a relative word to the film thinner than 1 μm .

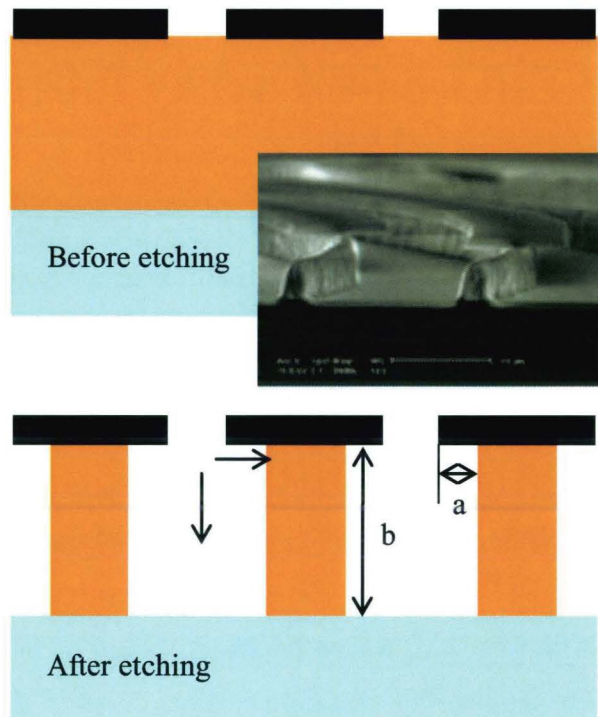


Figure 5.1: Schematic diagram of lateral undercutting: a is lateral etching, b is vertical etching. Inset is an SEM image to present the severe lateral undercut in wet etching of ZnO films ^[169]

This chapter investigates two methods to obtain ZnO-based ultrasonic phased arrays. The first one is wet etching ZnO thick films to fabricate high-frequency arrays. The second one is using a novel approach where the silicon substrate is etched to replace etching ZnO.

5.1 Fabrication of ZnO-based transducer array using wet etching method

In this work, we present a controllable wet etching method for 3- μm -wide kerf in 8- μm -thick-film ZnO to fabricate a novel device of high-frequency c-axis ZnO-based linear array transducers. This method makes it possible to define the lateral element dimension and position with the resolution offered by photolithography techniques. On the other hand, the characteristics of the transducer are measured and compared to the theoretical predictions obtained by Finite Element Method (FEM by COMSOL).

5.1.1 Geometry design

Fig. 5.1.1 describes the schematic geometry of ultrasonic transducer array based on wet etching of thick ZnO films. The array consists of a thick-film ZnO sandwiched between two metal electrodes, the bottom one deposited on a silicon wafer whose other face is not polished to scatter the backward transmitted waves. A $\lambda/4$ -thick matching layer (here, as stated in Chapter 4, SU-8 doped with TiO_2 is considered) is applied to the front of the array to make sure a greater transmittance.

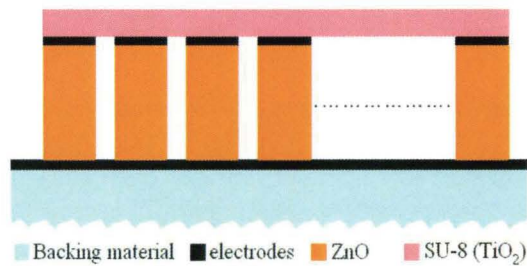
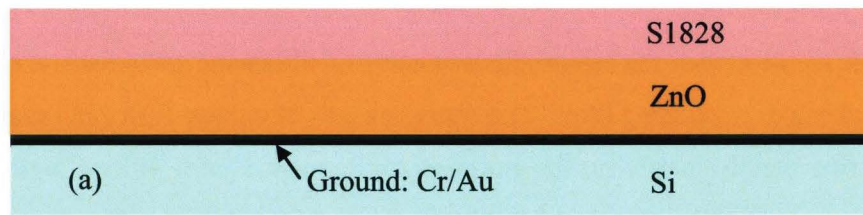


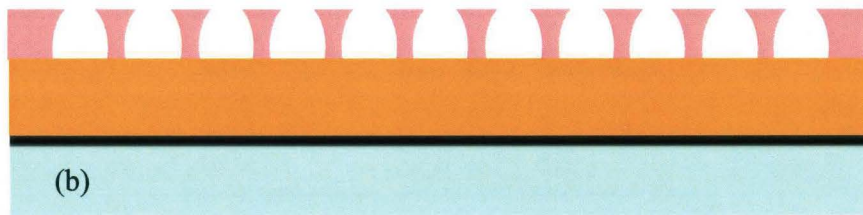
Figure 5.1.1: Schematic geometry of air kerfed ultrasonic transducer array based on wet etching of ZnO films

5.1.2 Fabrication of thick-film ZnO transducer arrays

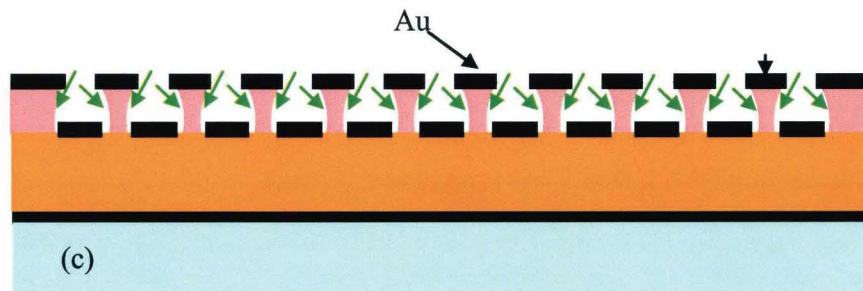
For our fabrication of high-frequency array transducer, the process flow is illustrated in Fig. 5.1.2. As shown in Fig. 5.1.2a, after a bottom layer of Cr/Au (100 Å/1000 Å) is deposited on the front of a one-face-polished silicon wafer, a 8- μm -thick ZnO film is deposited to the sample by RF-magnetron sputtering for 10 hours at 120 W and room temperature with $\text{Ar}:\text{O}_2 = 8:1$ (whose flow is 40 sccm to 5 sccm) and total gas pressure of 0.02 mbar. Then a 4- μm -thick positive photoresist, S1828, is patterned on its surface as sacrificial mask (see Fig. 5.1.2b). Evaporation process is used to deposit a second thin-film Cr/Au (100 Å/1000 Å) on the front of the sample. Remover PG is used to lift-off the photoresist for 3 hours at 70°C to get top electrode patterns (see Fig. 5.1.2c). At last, ZnO films are wet etched (see Fig. 5.1.2d) by 10 wt% ammonium chloride (NH_4Cl) solution for 2.5 hours at 20°C (etching rate is around 60 nm/min).



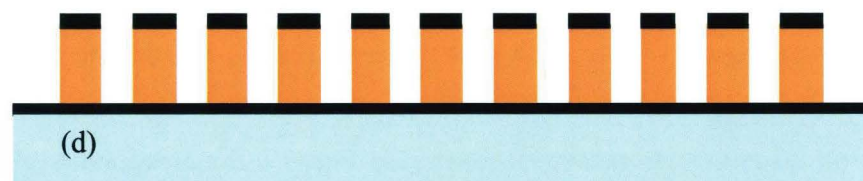
(a) Depositing Cr/Au as ground layer, sputtering ZnO and then spin-coating positive photoresist S1828



(b) Patterning S1828 through lithography process



(c) Depositing Au through evaporation process to obtain an anisotropic deposition



(d) Lift-off S1828 and then wet etching ZnO films

Figure 5.1.2: Schematic process flow for fabricating thick-film ZnO transducer arrays

During the fabrication, evaporation process is chosen to deposit Au films. Our evaporation system is MECA 2000. The evaporation process determines an anisotropic growth of thin films. This anisotropic deposition is essential in lift-off process. Otherwise, if using an isotropic deposition technique, the photoresist patterns are totally covered with metal and correspondingly cannot be removed.

In addition, the sputtering process is chosen to deposit ZnO films. The equipment

of our ZnO sputtering system is a Coating System E306A from Edwards, Inc. Fig. 5.1.3 shows the X-ray diffraction (XRD) pattern of ZnO sample ^[170]. As shown in Fig. 5.1.3, there is platinum (Pt) on the X-ray pattern because there is some under ZnO serving as bottom electrode. A peak is present at $2\theta = 34.39^\circ$ corresponding to (002) plane of pure ZnO. This plane indicates a strong texture along the c-axis.

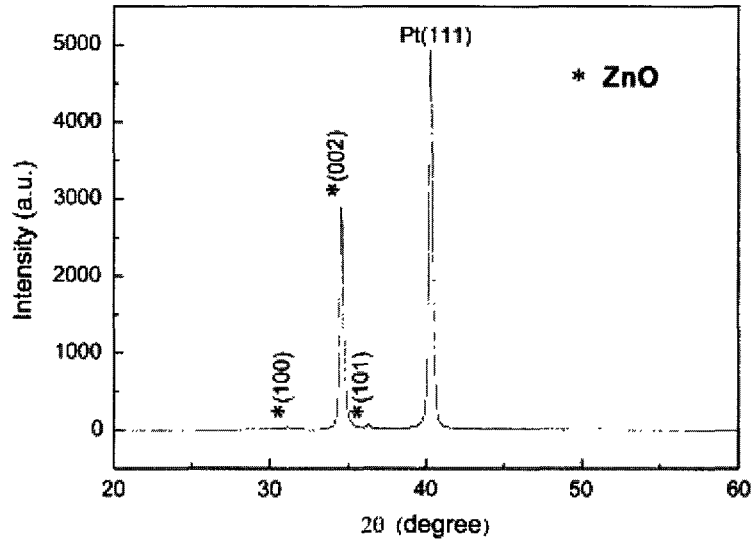


Figure 5.1.3: X-ray diffraction (XRD) pattern of ZnO ^[170]

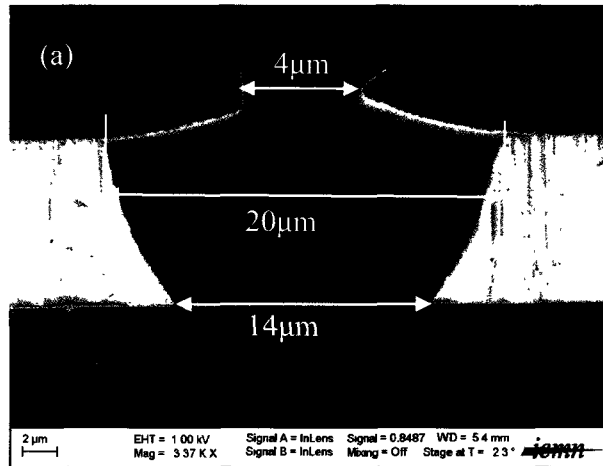
After the process flow in Fig. 5.1.2, the fabricated ZnO arrays are obtained. Fig. 5.1.4 shows that the ZnO thick films have a good c-axis growth orientation in which robust longitudinal waves can be generated. Table 5.1.1 compares the critical parameters during wet etching experiments. When etched by different chemical solutions, the kerf trench would present quite different structures. Fig. 5.1.4a shows a cross-section of a 4- μm -wide kerf in 8- μm -thick ZnO films, which is obtained by isotropic etching using HCl solution (concentration: 0.5 wt%) for 8 min. It results in a severe lateral etching and a V-sloped profile. Fig. 5.1.4b is a 7- μm -wide kerf in 8- μm -thick ZnO films, which is obtained by over etching in NH_4Cl solution (concentration: 10 wt%) for 2.5 hours and has an opposite-V-sloped profile. Fig. 5.1.4c illustrates a thick-film ZnO array with a pitch of 13 μm and a kerf width of 4 μm , whose detailed kerf is shown in Fig. 5.1.4d.

Fig. 5.1.4e illustrates two thick-film ZnO arrays with a pitch of 7.5 μm and a kerf width of 3 μm /4.5 μm . They are obtained by anisotropic etching using NH_4Cl solution (concentration: 10 wt%) for 2.5 hours. The only difference between figures (b) and (d) is the aspect ratio. Fig. 5.1.4b has a 7- μm -wide kerf between top electrodes and Fig.

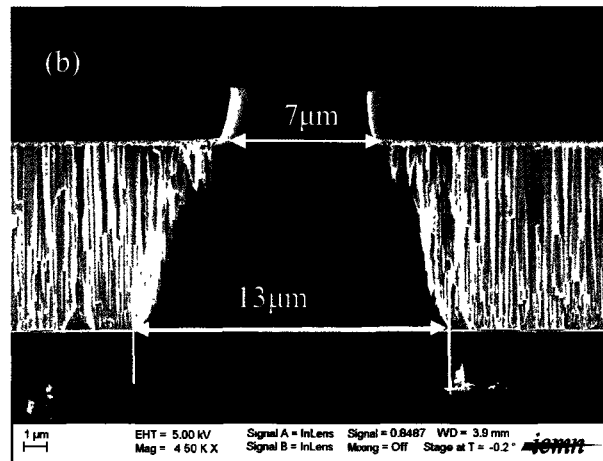
5.1.4d has a 4- μm -wide kerf. They are both 8- μm thick and are both obtained by 2.5 hours etching using 10 wt% NH_4Cl solution at 20°C. It indicates that the bigger kerf width results in a higher etching rate. So the trench with a bigger kerf width will be over etched when the thinner trench is exactly etched in the same conditions.

The comparison of Fig. 5.1.4 (a) and (d) indicates that a high concentration of H^+ will produce an isotropic etching and in contrast, a very low concentration of H^+ will generate anisotropic etching to produce a very vertical profile ^[171]. Thus, to acquire a very vertical profile of kerf trench in c-axis ZnO films as shown in Fig. 5.1.4d, attention should be paid to two critical aspects: First, the choice of the suitable solution which has very low concentration of H^+ , such as 10 wt% NH_4Cl aqueous solution, because the low concentration of H^+ will give a slow etching rate that enables definition of small ZnO features without severe lateral undercut; Second, the precise control of the duration to avoid over etching as well as non-sufficient etching.

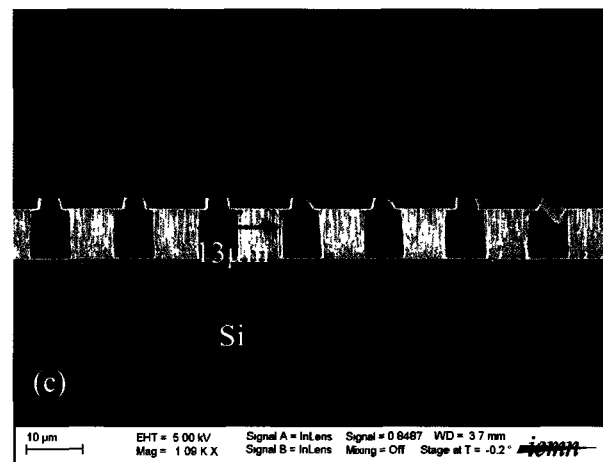
The lateral etching can be observed in Fig. 5.1.4d, and the ratio of lateral etching to vertical etching is about 0.25 which is much smaller than the result reported in ^[172], which results in a possibility to obtain a pitch of a λ ($\lambda = c/f$, where c is speed of sound in water and $c = 1480$ m/s). For example, linear arrays designed for 300 MHz operation should have ZnO array elements with a thickness of 8 μm corresponding to a kerf width of 3 μm (1 μm is kerf of top electrode and 2 μm of which is caused by lateral etching). To get a pitch of a λ (5 μm at 300 MHz), the element width should be $w = 2$ μm . In comparison, the 80 MHz thick-film-based transducer presented by Zhou and Shung ^[173] has a pitch of 36 μm , equivalent to a pitch of 2.0 λ . A 24 MHz PZT arrays on silicon substrates can get a limit pitch of 75 μm ($p = 2.5 \lambda$) by the new method proposed by Pedersen ^[174]. Typical values of resonant frequency and pitch obtained with the fabrication method mentioned earlier are 30 MHz and 100 μm ($p = 2.0 \lambda$) by direct dicing ^[175], 30 MHz and 74 μm ($p = 1.5 \lambda$) by laser ablation of PZT ^[176], 50 MHz and 40 μm ($p = 1.4 \lambda$) by interdigital pair bonding ^[177] and 100 MHz and 100 μm ($p = 6.7 \lambda$) by wet etching 10- μm -thick ZnO films using HCl/HNO_3 solution ^[90].



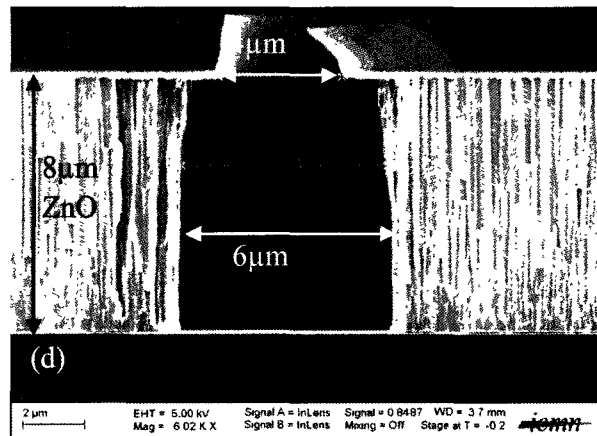
(a) A 4- μm -wide kerf obtained by isotropic etching using HCl solution (concentration: 0.5 wt%)



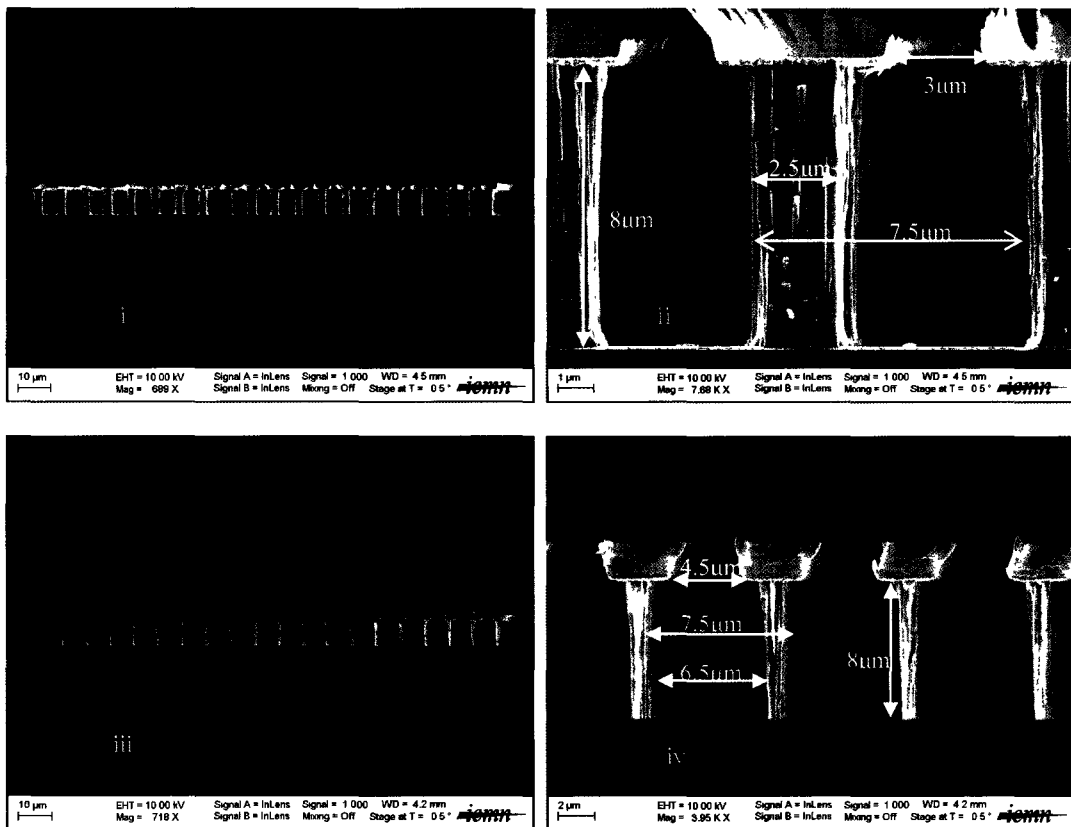
(b) A 7- μm -wide kerf obtained by over etching using NH_4Cl solution (concentration: 10 wt%)



(c) An array with a pitch of 13 μm and a kerf width of 6 μm by anisotropic etching using NH_4Cl solution (concentration: 10 wt%)



(d) Detail of a 6- μm -wide kerf shown in (c)



(e) Arrays with a pitch of 7.5 μm and a kerf width of 3 μm (i and ii)/4.5 μm (iii and iv) by anisotropic etching using NH_4Cl solution (concentration: 10 wt%)

Figure 5.1.4: SEM images of cross-sections for 8- μm -thick-film ZnO arrays

Table 5.1.1 Critical parameters in wet etching experiments

Solution	Concentration	Etching time	Kerf between top electrodes	Lateral etching	Vertical etching rate	Profile
HCl	0.5 wt%	8 min	4 μm	16 μm	1 $\mu\text{m}/\text{min}$	V-sloped
NH ₄ Cl	10 wt%	2.5 h	7 μm	6 μm	—	Opposite-V-sloped
NH ₄ Cl	10 wt%	2.5 h	4 μm	2 μm	53nm/min	vertical

5.1.3 Discussion of fabricated patterns

Table 5.1.2 summarizes the 18 patterns of ZnO arrays fabricated by wet etching method. In conclusion, 14 patterns are obtained whose kerfs were bigger than 2 μm . And they are totally kerfed thanks to novel properties of wet etching using NH₄Cl. Pattern 4-6 and Pattern 10 failed because we failed to obtain the small features of 1 μm , 1.5 μm and 2 μm in lithography. Future studies will include the improvement of lithography to achieve all of the 18 patterns.

Table 5.1.2 Fabricated patterns of LiNbO₃ arrays by ICP RIE

Pattern Index	μm		Pattern Index	μm		Pattern Index	μm		
	pitch	kerf		pitch	kerf		pitch	kerf	
1 (S)	7.5	3.5	7 (S)	15	5	13	42 (S)	15	
2 (S)		3	8 (S)		4	14		10	
3 (S)		2.5	9 (S)		3	15		8	
4 (F)		2	10 (F)		2	16		5	
5 (F)		1.5	11 (S)		13	3		17	4
6 (F)		1	12 (S)		10	3		18	3

F: Failed

S: Successful

5.1.4 Characterization of thick-film ZnO transducer arrays

The Finite Element Method (FEM) with COMSOL software is employed for simulation. The characteristics of the concerning materials are summarized in Table 5.1.3. Attention should be paid to SU-8-based matching layer. It is an isotropic material,

so the acoustic impedance Z is ρv_L and the first term of the stiffness matrix c_{11} is ρv_L^2 .

Table 5.1.3 Acoustic characteristics of some materials

Item	ZnO*	Si	SU-8 ^{2*}	Water
c_{11} (N/m ² ×10 ¹⁰)	20.97	16.56	2.06	—
B^1 (N/m ² ×10 ⁹)	—	—	—	2.2
v_L (m/s×10 ³)	6.08	8.43	2.88	1.48
ρ (kg/m ³ ×10 ³)	5.676	2.33	2.48	1
Z (kg/m ² -s×10 ⁶)	34.5	19.64	7.15	1.48

¹Bulk modulus of fluid ²Doped with nanocomposites of TiO₂: 30 wt% for ZnO and water

*Measured values for fabricated films

The array transducer's bandwidth and electrical matching have a tight relationship with the electrical impedance (Z) of the array elements. This impedance can be obtained by integrating the current density on the surface of the element electrode. Fig. 5.1.5 shows the real and imaginary parts of Z of the central element for 15-element array in Fig. 5.1.4c by 2-D (2-Dimensional) FEM calculation (dotted line). The solid lines are the measured results for real and imaginary parts of Z obtained from S_{11} parameter by Network Analyzer, which are consistent to the FEM simulation results. It shows the real part of Z is around 200 Ω at 300 MHz. In order to obtain a great wave generation, the electrical impedance should be matched to 50 Ω , which will be taken into account in future works. In addition, a great peak can be observed in real part and imaginary part around 80 MHz. It is produced by lateral-mode resonance. In fact, this phenomenon will appear when the width of the element is compatible to its height. Finally, the measured results present some peaks which are caused by resonance of Si backing. For the simulation results, the resonance of backing is eliminated using absorbing boundary conditions, so there is no such kind of peaks.

With a 15-element array, the measured scattering parameters S_{21} are consistent with calculated crosstalk results, showing a maximum magnitude of -53 dB in air (seeing Fig. 5.1.6) at 300 MHz. Here, the S_{11} and S_{21} scattering parameters of the two-port device are measured by Rhode and Schwartz Virtual Network Analyzer (VNA) with a Karl Suss prober system.

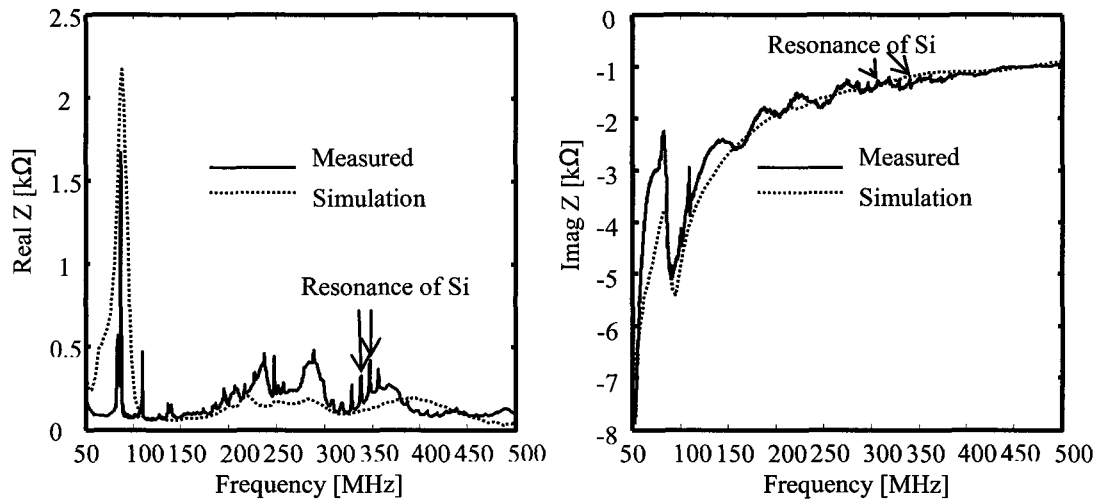


Figure 5.1.5: Measured and simulated electrical impedances of central element in a 15-element ZnO array.

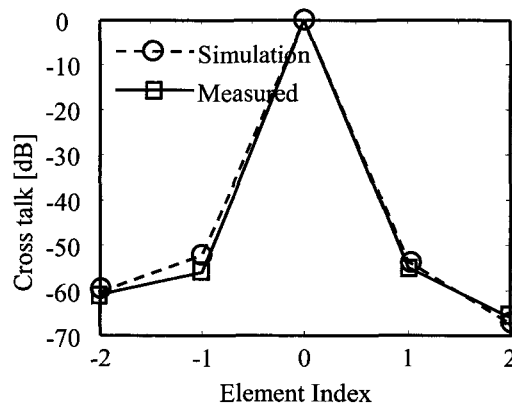


Figure 5.1.6: Measured and simulated crosstalk of adjacent (1, -1) and second adjacent (2, -2) elements in ZnO array.

This novel wet-chemical etching method provides the possibility to acquire a pitch of a λ at 300 MHz. Its behavior in acoustic field plays an important role in determinations of transducer's properties. Fig. 5.1.7 illustrates the simulated acoustic field performances of focusing and steering by 32-element arrays with a pitch of a λ (here λ is 5 μm , the wavelength in water at 300 MHz) and a kerf width of 3 μm . It shows that although the ratio of element width to thickness is 0.25 (2 $\mu\text{m}/8 \mu\text{m}$), much smaller than the minimum aspect ratio of 0.6^[178] required to separate the thickness mode from the higher frequency lateral modes, its field performance is acceptable for

scanning scope of $\pm 25^\circ$, because the first grating lobe stays out of this angular scope and would not affect the imaging resolution.

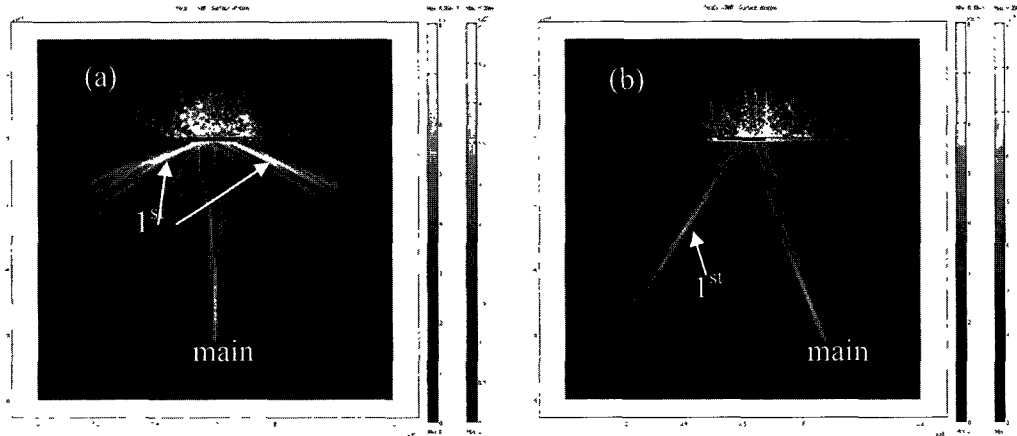


Figure 5.1.7: Acoustic field in water by 32-element array with a pitch of a λ at 300 MHz for: (a) Beam focusing at 500 μm (b) Beam focusing and steering 25 degrees at 500 μm . Here, “main” stands for main lobe and “1st” for 1st grating lobe.

5.1.5 Summary

A novel wet etching method with very small lateral undercut is presented to fabricate thick-film ZnO-based ultrasound transducer arrays. The wet-chemical etchant is NH_4Cl aqueous solution with a concentration of 10 wt% and the etching rate is 60 nm/min at 20°C. The duration should be controlled precisely to avoid over etching as well as non-sufficient etching. This technique results in a possibility to obtain a pitch of a λ at 300 MHz. A 13- μm -pitch ZnO array is achieved due to a small ratio (0.25) of lateral etching to vertical etching. This ratio of small lateral etching from NH_4Cl aqueous solution is studied and discussed for the first time. Finite element method is employed to calculate electrical impedance, crosstalk and focusing/steering acoustic field performances of the transducer. The characteristics of the transducer are measured and compared to the theoretical predictions. Future work will include fabrication of acoustic matching layer, measurement of pulse-echo response and investigation of decreasing electrical impedance of the array elements.

5.2 A novel method for fabrication of piezoelectric transducer arrays on Si substrate

For high-frequency phased arrays, effective etching techniques and processes are required to produce vertical and smooth surfaces with high etching rates in ZnO films. Wet etch process does not satisfy the requirements of small-scale feature size due to the property of isotropy, producing a large undercut beneath the photoresist or metal etch mask ^[169]. Dry etching process for ZnO thin film is necessary for advanced device fabrication due to its anisotropic etching property. Reactive ion etching (RIE) using inductively coupled plasma (ICP) RIE system has demonstrated its potential in batch fabrication of deep anisotropic microstructures in silicon and enabled high-aspect-ratio deep silicon etching, which produced great impact on MEMS device fabrication. However, in contrast to well-studied silicon or silicon dioxide etching, many problems exist in RIE etching of non conventional materials related to the chemical composition of materials which leads to low etch rate and low etch selectivity (to etch mask) and limits the formation of high aspect ratio microstructures. Dry etching has been used in the fabrication process of ZnO-based devices ^[179]. Plasma-induced damage causes critical errors in piezoelectronic device action. Moreover, in such a dry etching, a metal layer must often be used as an etch mask, because photoresist is decomposed under the influence of the plasma, producing carbon residues. When a metal layer is used on top of ZnO as an etch mask, it should be removed after etching ZnO and it cannot be used as electrode because the plasma would degrade electrical properties of the metal layer ^[169]. But it is difficult to remove the metal layer after the ZnO delineation, because most metal etchants attack ZnO. To solve those problems, a novel method to fabricate ultrasonic transducer array is proposed in this work. It is a mask-free and self-aligned approach.

5.2.1 Fabrication of thick-film ZnO transducer arrays

Silicon micromachining technology is employed due to the following advantages: potentially low cost due to the batch processing nature, possibility of

integrating transducers and circuits on a single chip, and size miniaturization ^[180]. In this fabrication, etching piezoelectric material is replaced by etching silicon substrate. The array consists of a thick-film ZnO array sandwiched between two metal electrodes, the bottom one sputtered on a pre-etched silicon wafer whose other face is not polished to scatter the backward transmitted waves.

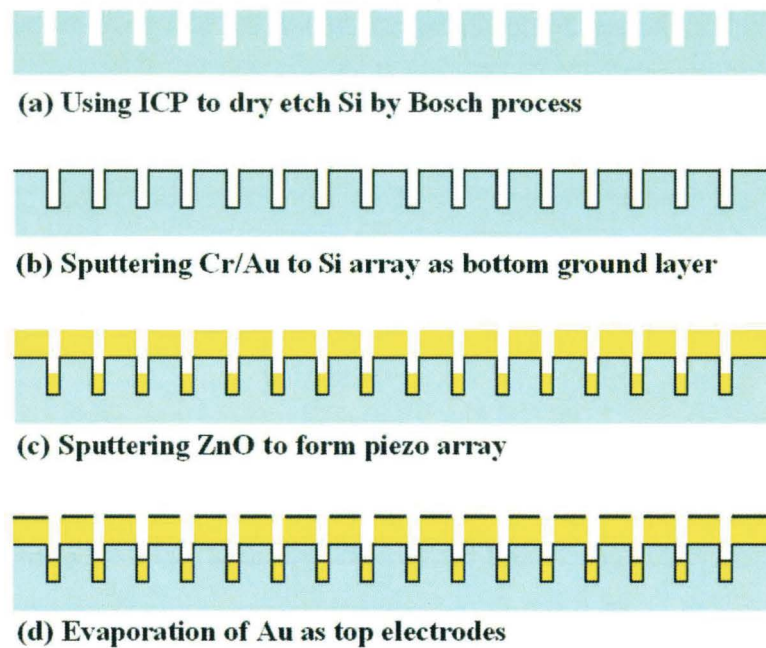
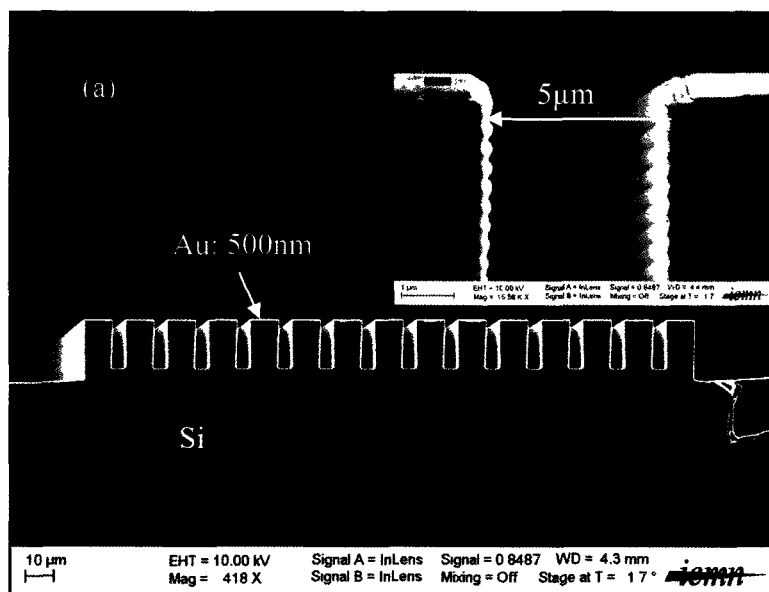


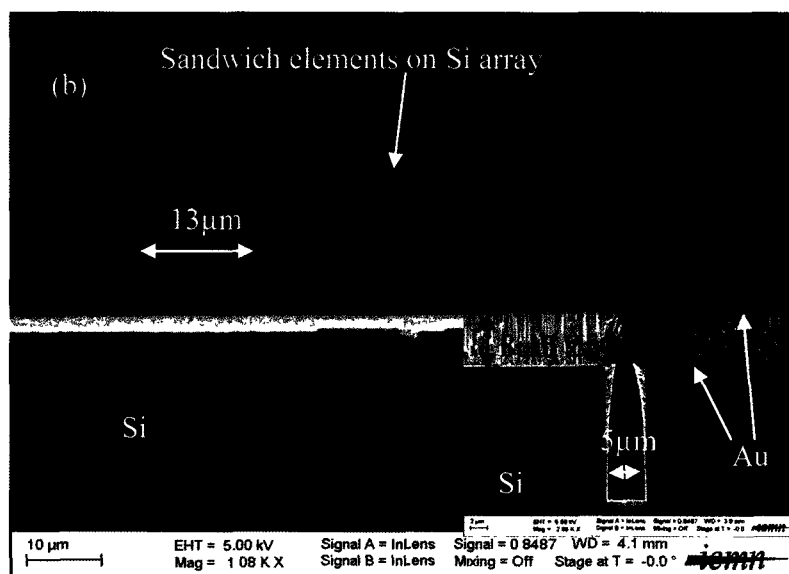
Figure 5.2.1: Schematic process flow for fabricating thick-film ZnO array transducer: (a) Bosch process is used to obtain a vertical sidewall during the ICP etching process; (b) Sputtering process is used to obtain a continuous ground layer due to the isotropic deposition of the sputtering process; (c) A mature sputtering process is used to grow ZnO films; (d) Evaporation process is used to obtain separate top electrodes due to the anisotropic deposition during evaporation process.

The schematic process flow is illustrated in Fig. 5.2.1. A 4- μm -thick negative photoresist, AZnLOF2070, is first patterned on silicon wafer as hard mask. STS (Surface Technology Systems) equipment is used to deep etch silicon (seeing Fig. 5.2.1a). As explained previously, it combines two etching techniques: ICP (Inductively Coupled Plasma) and RIE (Reactive Ion Etching). Particularly, a specific technique is used with this appliance: the “Bosch” process. This process is

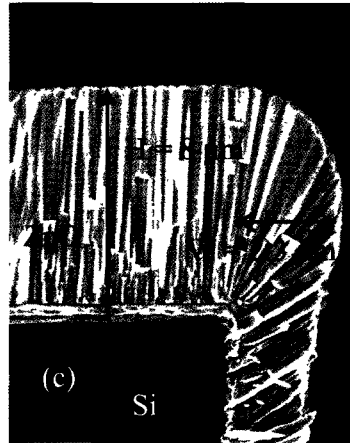
based on the alternation of a passivation step (C_4F_8) and an etching step (SF_6). This method allows obtaining very straight and deep profiles. The Bosch process is performed for 4.5 min at $10^\circ C$ (a Bosch cycle includes 3 s etching by SF_6 and 2s passivation by C_4F_8).



(a) Etched silicon array with bottom ground layer embedded with amplified kerf view in top-right corner: a continuous ground layer of Au is obtained due to the isotropic growth during sputtering deposition process



(b) Front view of ZnO film on silicon array with top electrodes embedded with a cross-section view of ZnO sandwich elements on etched Si array



(c) Detail of cross-section for ZnO growth property: H is vertical growth, W is lateral growth

Figure 5.2.2: SEM images of fabricated arrays

After etching silicon and sputtering 500 nm gold film as bottom ground layer (see Fig. 5.2.1b), a 8- μm -thick ZnO film is attached to the front of samples by RF-magnetron sputtering for 10 hours at 120 W and room temperature with Ar:O₂ = 8:1 (whose flow is 40 sccm to 5 sccm) and total gas pressure of 0.02 mbar (see Fig. 5.2.1c). Then Cr/Au (100 Å/2000 Å) is evaporated on the surface to form top electrodes and the surrounding ground layer (see Fig. 5.2.1d and Fig. 5.2.2b).

The embedded view in Fig. 5.2.2a shows that the ground layer of gold is continuous on the whole surface of silicon substrate. The embedded view in Fig. 5.2.2b shows the ZnO thick films have a good c-axis growth orientation in which robust longitudinal waves can be generated. However, because of the angle constraint of ZnO film lateral growth in the kerfs (detailed information is illustrated in Fig. 5.2.2c, a lateral growth of ZnO suffers from the isotropic deposition of the sputtering process. The lateral growth results in a relatively large pitch in an array), the film thickness has a limit of 1.6 times of the kerf width in silicon array, which results in no possibilities to obtain a pitch a λ ($\lambda = c/f$, where c is speed of sound in water and $c = 1480$ m/s). As shown in Fig. 5.2.2c, the ratio of vertical to lateral growth is $H/W = 8 \mu\text{m}/2.3 \mu\text{m} = 3.48$. In fact, the minimum pitch that can be obtained is around 2.0λ . For example, linear arrays designed for 300 MHz operation should have ZnO array elements with a thickness of 8 μm corresponding to a kerf width of $d = 5 \mu\text{m}$. To get good acoustic field

performances, the width of the element, w , should be bigger than d , so the pitch should be at least $10 \mu\text{m}$ (that is about 2.0λ , $\lambda = 5 \mu\text{m}$ in water at 300 MHz).

5.2.2 Discussion of fabricated patterns

Table 5.2.1 summarizes the 18 patterns of ZnO arrays fabricated by this novel method. In conclusion, only Pattern 7 and Patterns 13-16 are obtained. Their kerfs are not thinner than $5 \mu\text{m}$. And they are totally kerfed because their elements are separated from each other. To obtain more patterns, investigations of smaller lateral growth need to be considered when sputtering ZnO.

Table 5.2.1 Fabricated patterns of ZnO arrays by etching Si method

Pattern Index	μm		Pattern Index	μm		Pattern Index	μm		
	pitch	kerf		pitch	kerf		pitch	kerf	
1	7.5 (F)	3.5	7 (S)	15	5	13 (S)	42	15	
2		3	8 (F)		4	14 (S)		10	
3		2.5	9 (F)		3	15 (S)		8	
4		2	10 (F)		2	16 (S)		5	
5		1.5	11 (F)		13	3		17 (F)	4
6		1	12 (F)		10	3		18 (F)	3

F: Failed

S: Successful

5.2.3 Characterization of thick-film ZnO transducer arrays

Finite element method is applied to analyze the performance of the transducer arrays. The characteristics of the concerning materials are summarized in Table 5.1.3. This novel method provides the possibility to acquire a pitch of 2.0λ . Its behavior in acoustic field plays an important role in determinations of transducer's properties. The grating lobes and side lobes in acoustic field indicate a false image or a superimposing image during ultrasound imaging. Fig. 5.2.3 illustrate the simulated acoustic field performances of focusing and steering by 32-element arrays with a pitch of 2.0λ (here λ , the wavelength in water at 300 MHz is $5 \mu\text{m}$) and a kerf width of $4 \mu\text{m}$. It shows that the

array with a pitch of 2.0λ is impossible to apply in steering scanning. For steering application, it is necessary to investigate a method to obtain a pitch smaller than a λ . Thus, reducing lateral growth of ZnO is necessary to obtain a smaller pitch. An improved method will be investigated in the following part 5.2.4.

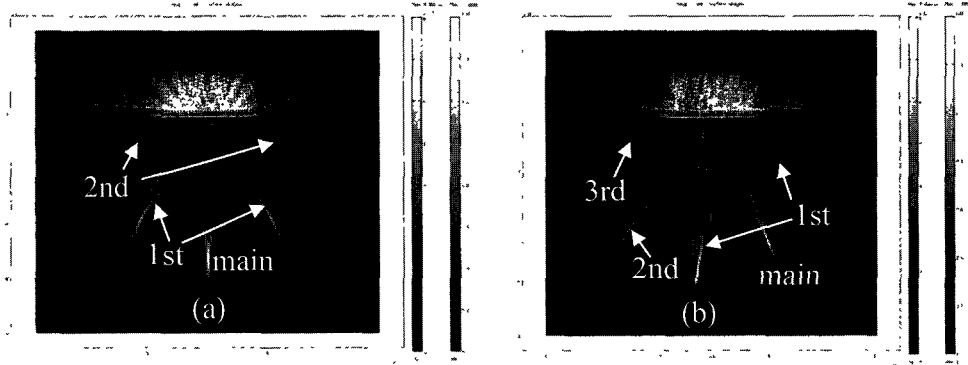


Figure 5.2.3: Acoustic field in water by 32-element array with a pitch of 2.0λ for: (a) Beam focusing at $500 \mu\text{m}$; (b) Beam focusing and steering 25 degrees at $500 \mu\text{m}$. Here, “main” stands for main lobe, “1st” for first grating lobe and “2nd” for second grating lobe.

Fig. 5.2.4 shows the real and imaginary parts of impedance of the central element for 15-element array in Fig. 5.2.2b by 2-D (2-Dimensional) FEM calculation (dotted line). The solid line is the measured results obtained from S_{11} parameter measured by Network Analyzer, which is consistent to the FEM simulation result. It shows the real part of Z is around 200Ω at 300 MHz . In order to obtain an efficient wave generation, the electrical impedance should be matched to 50Ω , which will be taken into account in future works. In addition, the measured results present some peaks which are caused by resonance of Si backing. For the simulation results, the resonance of backing is eliminated using absorbing boundary conditions, so there is no such kind of peaks.

With a 15-element array, the measured scattering parameters S_{21} are consistent with calculated results, showing an adjacent crosstalk of -47 dB in air at the resonating frequency. The S_{11} and S_{21} scattering parameters of the two-port device are measured by Rhode and Schwartz Virtual Network Analyzer (VNA) with a Karl Suss prober system.

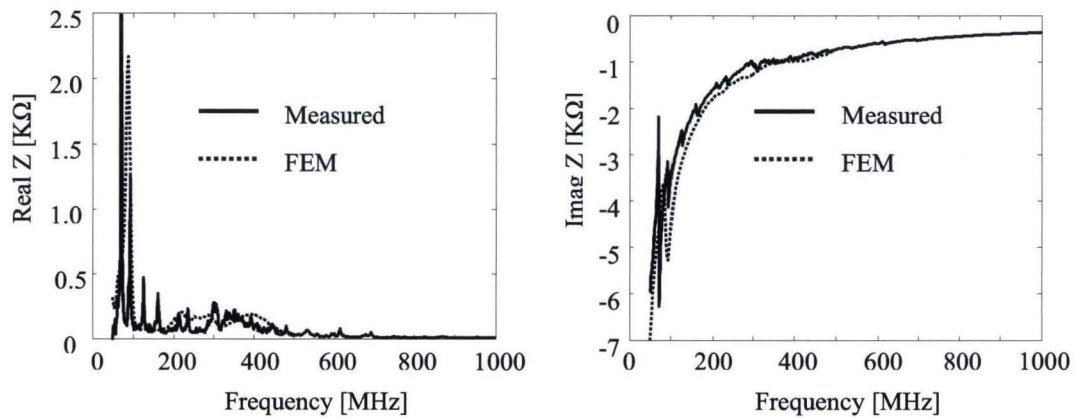


Figure 5.2.4: Measured and simulated electrical impedances of ZnO element.

5.2.4 Improvement of sputtering process with rotation 90°

In the above statement, we presented a novel method using silicon micromachining integrated with deposition of piezoelectric thick films to fabricate high-frequency ZnO-based linear array transducers. This integration makes it efficient to define the features in an array instead of etching ZnO films. However, the lateral growth of ZnO films is obvious (vertical to lateral growth is about 8 μm to 2.3 μm) and this degrades the realization of kerfs with high aspect ratio. In this work, we investigate a novel method to solve this problem of severe lateral growth.

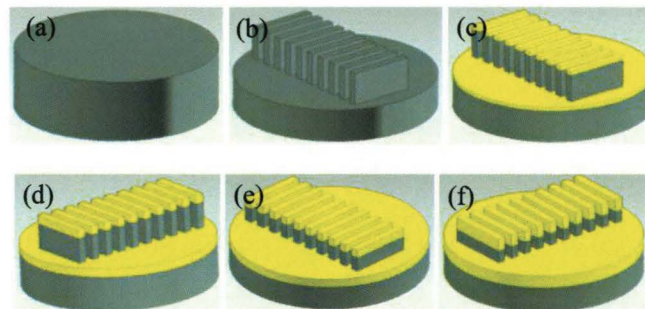
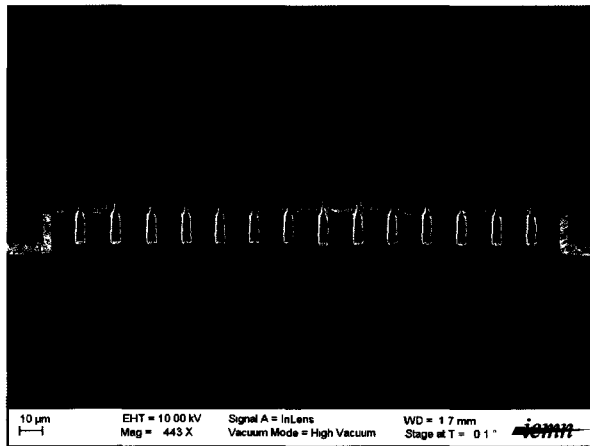
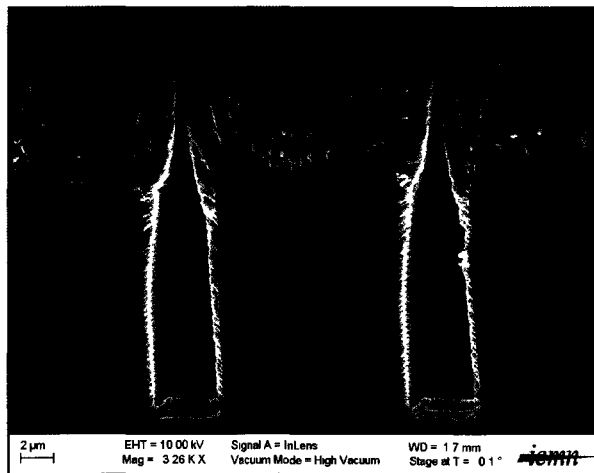


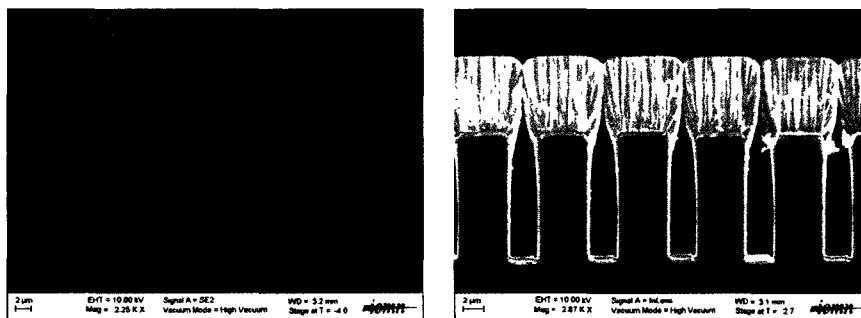
Figure 5.2.5: An improved 4-step deposition method of ZnO films: (a) Original Si substrate; (b) Etching Si using STS machine and Botch process; (c) Sputtering Au/Cr (500 nm/10 nm) and depositing ZnO for three hours at Angle 0°; (d) Depositing ZnO for three hours at Angle 90°; (e) Depositing ZnO for three hours at Angle 180°; (f) Depositing ZnO for three hours at Angle 270°.



(a) 15-element ZnO array with a pitch of 15 μm



(b) amplified detailed kerfs in the array of (a), and the pitch is 15 μm , thickness is 8 μm , kerf is 4 μm



(c) 20-element ZnO array with a pitch of 7.5 μm

Figure 5.2.6: SEM images of sandwich ZnO arrays deposited by 4 steps with 90° rotations for each step.

Previously, we used just one step to sputter ZnO films and the total duration time was 12 hours to obtain a thickness of 8 μm . However, the lateral growth of ZnO films

would continue because there is no change of orientation during RF sputtering process. Here we divide the sputtering process into four steps. Each step contains ZnO deposition for 3 hours. And the device is rotated by 90° between each step as shown in Fig. 5.2.5. Thus the total deposition time is 12 hours, the same as before. After the four steps are completed, the SEM images of sandwiched ZnO arrays are illustrated in Fig. 5.2.6. Fig. 5.2.6a is a 15-element ZnO array with a pitch of 15 μm. Its amplified detailed kerfs are shown in Fig. 5.2.6b. We can see that the elements are separated although the lateral growth is not avoided. The vertical to lateral growth is about 8 μm to 1.9 μm ($8/1.9 = 4.21$). When the pitch of the array is decreased to 7.5 μm and the kerf width is decreased to 2.5 μm, the elements are connected to their neighbors, as shown in Fig. 5.2.6c, and this array is useless. Nevertheless, the ratio of vertical to lateral growth is improved by 21% (from 8/2.3 to 8/1.9).

5.2.5 Discussion of fabricated patterns using rotation method

Table 5.2.2 Fabricated patterns of ZnO arrays by rotation method

Pattern Index	μm		Pattern Index	μm		Pattern Index	μm		
	pitch	kerf		pitch	kerf		pitch	kerf	
1	7.5 (F)	3.5	7 (S)	15	5	13 (S)	42	15	
2		3	8 (S)		4	14 (S)		10	
3		2.5	9 (F)		3	15 (S)		8	
4		2	10 (F)		2	16 (S)		5	
5		1.5	11 (F)		13	3		17 (S)	4
6		1	12 (F)		10	3		18 (F)	3

F: Failed

S: Successful

Table 5.2.2 summarizes the 18 patterns of ZnO arrays fabricated by rotation method. In conclusion, Patterns 7-8 and Patterns 13-17 are obtained. And they are totally kerfed because their elements are separated from each other. Compared Table 5.2.1 and Table 5.2.2, we can conclude that Pattern 8 and Pattern 17 are obtained due to the adoption of rotation method. It indicates that the lateral growth decreases by

21%. The electrical characterization and measurement of the improved array will be included in future studies.

Using this approach, the minimum pitch that can be obtained is around 1.6λ . For example, linear arrays designed for 300 MHz operation should have ZnO array elements with a thickness of $8 \mu\text{m}$ corresponding to a kerf width of $d = 4 \mu\text{m}$. To get good acoustic field performances, the width of the element, w , should be bigger than d , so the pitch should be at least $8 \mu\text{m}$ (that is about 1.6λ , $\lambda = 5 \mu\text{m}$ in water at 300 MHz).

5.2.6 Summary

We propose a novel method using silicon micromachining integrated with deposition of piezoelectric thick films to fabricate high-frequency ZnO-based linear array transducers. Piezoelectric elements are formed by sputtering thick-film ZnO onto etched features of a silicon substrate so that the difficult etching process for ZnO films is avoided by etching silicon. This integration makes it simple and efficient to define the features in an array instead of etching ZnO films. Finite element method is employed to simulate the wave propagation in water based on this new transducer configuration. A $13\text{-}\mu\text{m}$ -pitch ZnO sandwich array is achieved with a thickness of $8 \mu\text{m}$ for 300 MHz. The characteristics of the transducer are measured and compared to the theoretical predictions (finite element results) including electrical impedance and crosstalk.

On the other hand, the lateral growth of ZnO films is studied. A 4-step method with rotation 90° between each step of sputtering is investigated. The lateral growth of ZnO has been decreased by 21%.

Future work will include investigation of avoiding ZnO lateral growth to obtain smaller pitch (using ionized metal plasma sputtering technique to deposit ZnO films) and decreasing electrical impedance of the array elements to achieve electrical matching. Because of the high equivalent impedance of the array elements, broadband electrical matching is difficult using conventional microcoaxial cables matching. A potential solution is to combine the transducer array with an integrated circuit (IC).

Conclusions and prospects

The objective of this thesis focuses on the development of kerfed array transducers with a central frequency of above 100 MHz. Two aspects are mainly investigated. The first one is the finite element numerical simulations for the optimized design. The second one is the fabrication using different experimental processes based on micro electromechanical system (MEMS) technologies.

In the section of numerical studies, finite element method is used to obtain a comprehensive understanding of high frequency array transducers. In piezoelectric backing array transducers, the effects of pitch size, kerf filler and kerf depth on the acoustic field, electrical impedance and crosstalk are investigated. And systematic simulations are carried out for a designed buffered transducer array.

In the section of experimental fabrication and characterization, MEMS based technologies are applied to obtain high-frequency array elements. In conclusion, three approaches are investigated. Firstly, 36°/Y-cut single crystal LiNbO₃ have been patterned by means of ICP RIE micromachining to create ultrasonic arrays resonating in the frequency range of 100-200 MHz. For a 200 MHz half-kerfed LiNbO₃ array, the smallest pitch could be obtained to 10 μm depending on this ICP RIE technology. Secondly, a novel wet etching method with very small lateral undercut is presented to fabricate thick-film ZnO-based ultrasound transducer arrays. The wet-chemical etchant is NH₄Cl aqueous solution with a concentration of 10 wt% and the etching rate is 60 nm/min at 20°C. The duration should be controlled precisely to avoid over etching as well as non-sufficient etching. This technique results in a possibility to obtain a pitch of a λ at 300 MHz. Thirdly, we propose a mask-free and self-aligned method using silicon micromachining integrated with deposition of piezoelectric thick films to fabricate high-frequency ZnO-based linear array transducers. This integration makes it simple and efficient to define the features in an array instead of etching ZnO films. A 13-μm-pitch ZnO sandwich array is achieved with a thickness of 8 μm for

300 MHz. On the other hand, the lateral growth of ZnO films is studied. A 4-step method with rotation 90° between each step of sputtering is investigated. The lateral growth of ZnO has been decreased by 21% by using the improved approach.

Future works will include investigation of avoiding ZnO lateral growth to obtain smaller pitch and decreasing electrical impedance of the array elements to achieve electrical matching. Because of the high equivalent impedance of the array elements, broadband electrical matching is difficult using conventional microcoaxial cables matching. A potential solution is to combine the transducer array with an integrated circuit (IC). Further investigation will also include the fabrication of electronic interconnection to test the small arrays. Furthermore, we will fabricate the acoustic matching layer and measure the pulse-echo response of the transducers.

Annex 1: Calculation of phase delay

An ultrasound beam was focused or steered in the azimuth plane by supplying each array element with appropriate time-delayed signals. In calculation of time delay (or phase delay), the most important thing is to find out the wave path difference Δr . Then the time delay and phase delay can be given as:

$$\Delta t = \Delta r / v$$

$$\Delta \phi = \omega * \Delta t = \omega * \Delta r / v$$

where v is speed of wave, ω is angular frequency.

In the following part, we will introduce the calculation of Δr .

a. Steer without buffer

Fig. A.1.1 is the sketch of wave path difference in a linear phased array (the element number is N) steered by an angle of θ . It can be seen that $\Delta r_n = d n \sin \theta$.

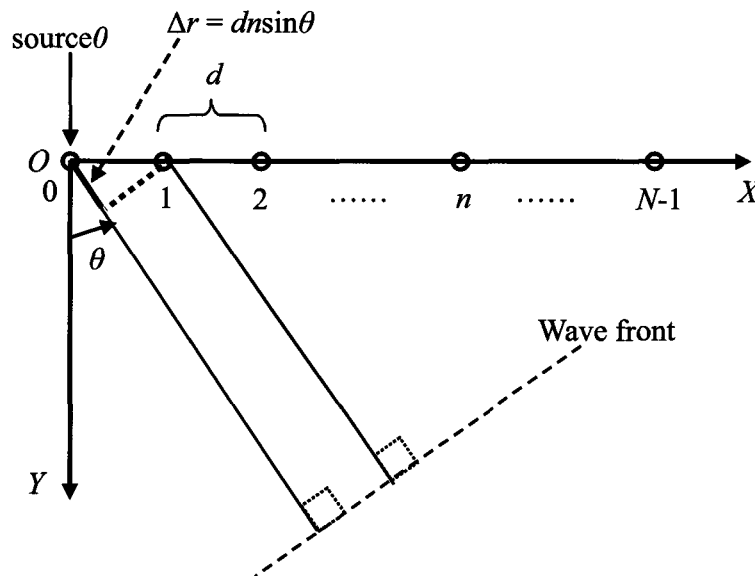


Figure A.1.1: Sketch of wave path difference in steering an angle of θ

b. Focus without buffer

Fig. A.1.2 is the sketch of wave path difference in a linear phased array (the element number is $2N+1$) focusing at a distance of F . It can be seen that $\Delta r_n =$

$$\sqrt{F^2 + (Nd)^2} - \sqrt{F^2 + [(N-n)d]^2} .$$

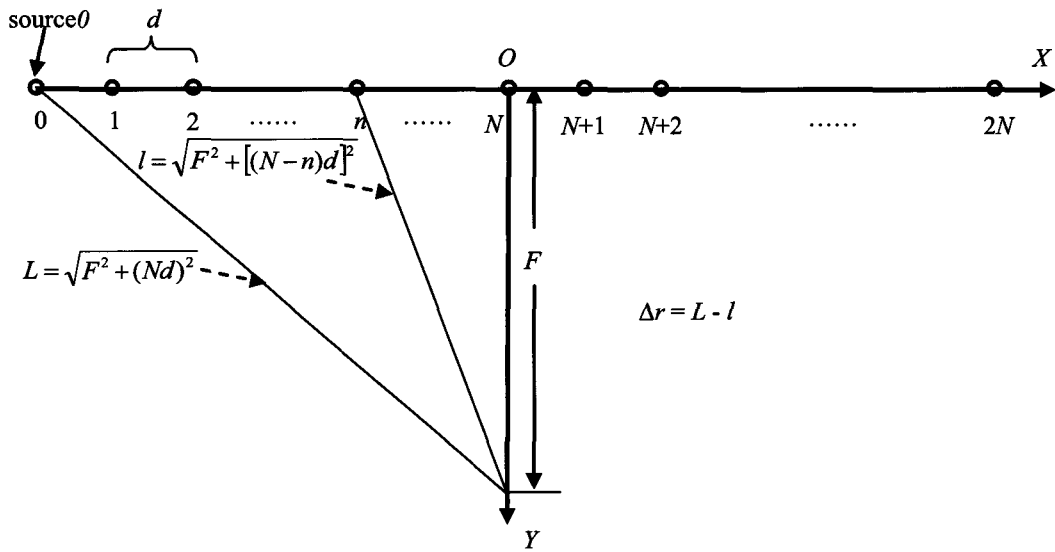


Figure A.1.2: Sketch of wave path difference in focusing at distance of F

c. Focus and steer without buffer

Fig. A.1.3 is the sketch of wave path difference in a linear phased array (the element number is $2N+1$) steered by an angle of θ and focusing at a distance of F . It can be seen that $\Delta r_n = F - \sqrt{F^2 + (nd)^2 - 2Fnd \cos(90^\circ - \theta)}$.

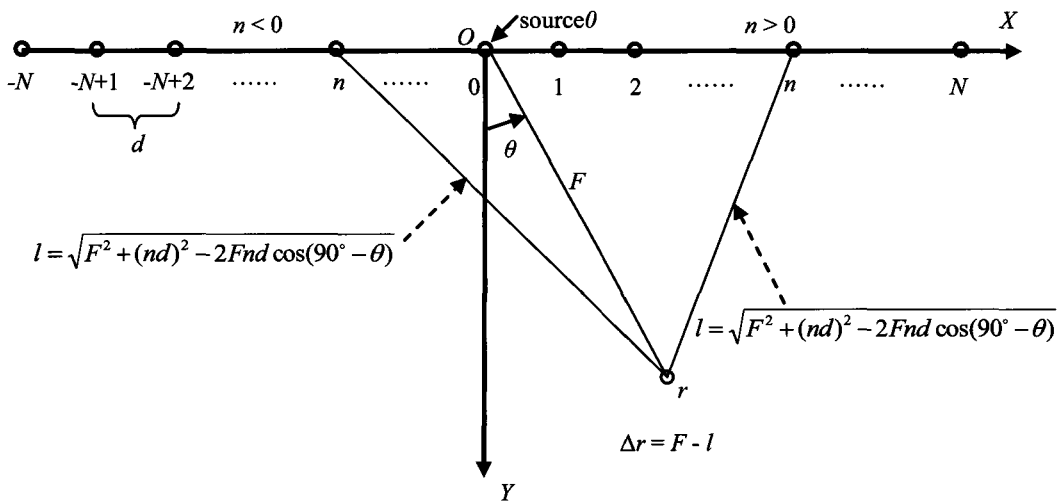


Figure A.1.3: Sketch of wave path difference in steering an angle of θ and focusing at distance of F

d. Focus with buffer

Fig. A.1.4 is the sketch of wave path difference in a buffered linear phased array (the element number is $2N + 1$) focusing at a distance of K . The thickness of the buffer

is d . It can be seen that Δr_n consists of two parts, Δr_b in buffer and Δr_w in water. Then the time delay can be given as:

$$\Delta t_n = (d - l_b) / v_1 + (K - l_w) / v_2$$

where v_1 and v_2 are, respectively, the longitudinal wave speeds in buffer and water. In order to get l_b and l_w , the following calculation needs to be considered.

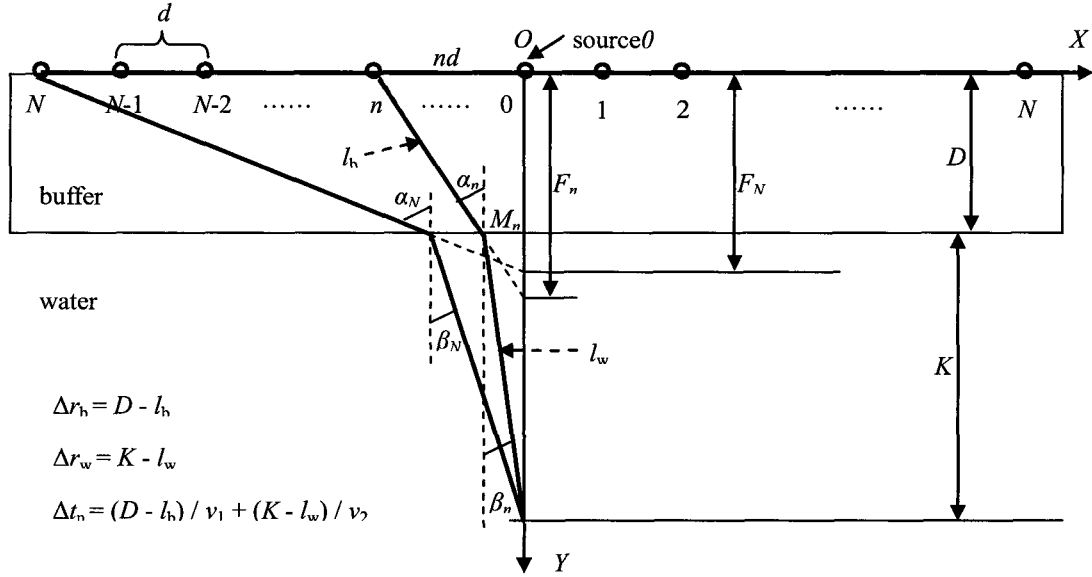


Figure A.1.4: Sketch of wave path difference for a buffered linear array in focusing at distance of K

As shown in Fig. A.1.4, the refraction at the interface between buffer layer and water was taken into account in calculating the time delays. When the ultrasound beam excited at each array element is propagating through the buffer and approaches the edge of the buffer at an angle α , its transmission into water will be at an angle β . According to Snell's law, we have:

$$\frac{\sin \alpha_n}{\sin \beta_n} = \frac{v_1}{v_2} \quad (\text{A-1})$$

Here,

$$\sin \alpha_n = \frac{nd}{\sqrt{(nd)^2 + F_n^2}} \quad (\text{A-2})$$

$$\sin \beta_n = \frac{M_n}{\sqrt{M_n^2 + K^2}} \quad (\text{A-3})$$

From Figure A-4, we can get the relation between M_n and F_n :

$$\frac{M_n}{nd} = \frac{F_n - D}{F_n} \longrightarrow M_n = \frac{F_n - D}{F_n} \cdot nd \quad (\text{A-4})$$

According to (A-1)-(A-4), we can get the equation about F_n :

$$\frac{v_1^2}{v_2^2} = \frac{(nd)^2}{(nd)^2 + F_n^2} \cdot \left[1 + \frac{K^2 \cdot F_n^2}{(F_n - D)^2 \cdot (nd)^2} \right] \quad (\text{A-5})$$

Substituting v_1 , v_2 , K , d and n with constants, we can get the value of F_n .

Then the actual wave paths l_b and l_w can be given as:

$$l_b = \frac{D}{F_n} \cdot \sqrt{(nd)^2 + F_n^2}$$

$$l_w = \sqrt{K^2 + \left(\frac{F_n - D}{F_n} \cdot nd \right)^2}$$

At last, the time delay is given:

$$\Delta t_n = \Delta r_b / v_1 + \Delta r_w / v_2 = (D - l_b) / v_1 + (K - l_w) / v_2 \quad (\text{A-6})$$

Furthermore, the delay between array elements was introduced symmetrically so that the wave would propagate perpendicularly to the array.

Annex 2.1: Parameters of the used materials

Table A.2.1.1 Elastic constants and mass density of concerning materials for high frequency ultrasonic transducer elaboration ^[181]

Group	Material	Class	Elastic constants (10^{10} N/m ²)							Density (kg/m ³)
			c_{11}	c_{12}	c_{13}	c_{33}	c_{44}	c_{14}	c_{66}	
Isotropic	Fused Silica-SiO ₂		7.85	1.61						2203
	Au	m3m	19.25	16.30			4.24			19300
	Si	m3m	16.56	6.39			7.95			2329
Hexagonal	PZT-4	trans. iso	13.9	7.8	7.4	11.5	2.56			7500
	ZnO	6mm	20.97	12.11	10.51	21.09	4.25			5676
Tetragonal	In	4/mmm	4.53	4.0	4.15	4.51	0.651		1.21	7280
Trigonal	Al ₂ O ₃	$\bar{3}m$	49.7	16.3	11.1	49.8	14.7	-2.35		3986
	LiNbO ₃	3m	20.3	5.3	7.5	24.5	6.0	0.9		4700
	LiTaO ₃	3m	23.3	4.7	8.0	27.5	9.4	-1.1		7450
	α -quartz/cry. SiO ₂	32	8.67	0.70	1.19	10.72	5.79	-1.79		2648

Table A.2.1.2 Stiffness piezoelectric constants and permittivity for some common used piezoelectric materials [214]

Group	Material	Class	Piezoelectric constants matrix e_{ij} (C/m ²)	Permittivity ϵ_{ij}^S (10 ⁻¹¹ F/m)
Hexagonal	ZnO	6mm	$\begin{bmatrix} 0 & 0 & 0 & 0 & -0.59 & 0 \\ 0 & 0 & 0 & -0.59 & 0 & 0 \\ -0.61 & -0.61 & 1.14 & 0 & 0 & 0 \end{bmatrix}$	$\begin{bmatrix} 7.38 & 0 & 0 \\ 0 & 7.38 & 0 \\ 0 & 0 & 7.83 \end{bmatrix}$
	PZT-4	6mm	$\begin{bmatrix} 0 & 0 & 0 & 0 & 12.7 & 0 \\ 0 & 0 & 0 & 12.7 & 0 & 0 \\ -5.2 & -5.2 & 15.1 & 0 & 0 & 0 \end{bmatrix}$	$\begin{bmatrix} 650 & 0 & 0 \\ 0 & 650 & 0 \\ 0 & 0 & 560 \end{bmatrix}$
Trigonal	LiNbO ₃	3m	$\begin{bmatrix} 0 & 0 & 0 & 0 & 3.7 & -2.5 \\ -2.5 & 2.5 & 0 & 3.7 & 0 & 0 \\ 0.2 & 0.2 & 1.3 & 0 & 0 & 0 \end{bmatrix}$	$\begin{bmatrix} 38.9 & 0 & 0 \\ 0 & 38.9 & 0 \\ 0 & 0 & 25.7 \end{bmatrix}$
	LiTaO ₃	3m	$\begin{bmatrix} 0 & 0 & 0 & 0 & 2.6 & -1.6 \\ -1.6 & 1.6 & 0 & 2.6 & 0 & 0 \\ 0 & 0 & 1.9 & 0 & 0 & 0 \end{bmatrix}$	$\begin{bmatrix} 36.3 & 0 & 0 \\ 0 & 36.3 & 0 \\ 0 & 0 & 38.1 \end{bmatrix}$
	α -Quartz crystal-Si O ₂	32	$\begin{bmatrix} 0.171 & -0.171 & 0 & -0.0406 & 0 & 0 \\ 0 & 0 & 0 & 0 & -0.0406 & -0.171 \\ 0 & 0 & 0 & 0 & 0 & 0 \end{bmatrix}$	$\begin{bmatrix} 3.92 & 0 & 0 \\ 0 & 3.92 & 0 \\ 0 & 0 & 4.1 \end{bmatrix}$

Table A.2.1.3 Material constants for piezoelectric ultrasonic transducer simulation

Material	ρ kg/m ³	c_{33}^E GPa	e_{33} C/m ²	ϵ_{33}^S 10 ⁻¹¹ F /m	$k_t = \frac{e_{33}}{\sqrt{c_{33}^D \epsilon_{33}^S}}$ ¹	$v_P = \sqrt{c_{33}^D / \rho}$ m/s	$\lambda / 2$ ² μm	$Z_A = \rho v_P$ ³ MRayl
ZnO	5676	210.9	1.14	7.83	0.270	6331	31.7	35.93
LiNbO ₃ (Y-cut/36°)	4700	193.2	4.51	34.34	0.485	7340	36.7	34.50
PZT-4	7500	115.0	15.1	560	0.511	4557	22.8	34.18
Si (Baking /Buffered)	2329	165.6				8432	42.2	19.64
In (Bonding)	7280	45.1				2489	12.4	18.12
Au (Electrode)	19300	192.5				3158	15.8	60.95
Water (Trans. medium)	1000	2.25				1500	15.0	1.50

¹ $c_{33}^D = c_{33}^E + e_{33}^2 / \epsilon_{33}^S$; ² at 100 MHz; ³ acoustic characteristic impedance

Annex 2.2: Material tensor transformations

Though a physical phenomenon or a physical property, in Newton's mechanics, is independent of the reference system, their description can have different forms under different coordinate systems. Many physical properties exhibiting anisotropy with the use of tensor are direction dependant. As an example, the elastic constant tensor c_{ijkl} (or its matrix representation c_{IJ}) describing material elasticity, needs to be defined by fixing a certain symmetry orientation with respect to the used coordinate axes (usually coincide with the symmetry or the principle axes of the material). The elements of this tensor will take different values if the material structure or the coordinate axes are differently orientated.

Generally, under the orthogonal Cartesian x-y-z coordinates system (or 3-dimensional Euclidean space), to change the orientation between two arbitrary directions (or to re-orientate a rigid body) require three axial rotation operations, (while to coincide an axis to a given direction or to re-orientate a plane, only two rotations are needed).

The coordinates transform from the initial ones [x, y, z] to the new ones [x', y', z'] can be carried out by a matrix transform of the coordinates in the general form

$$\begin{bmatrix} x' \\ y' \\ z' \end{bmatrix} = \begin{bmatrix} a_{11} & a_{12} & a_{13} \\ a_{21} & a_{22} & a_{23} \\ a_{31} & a_{32} & a_{33} \end{bmatrix} \cdot \begin{bmatrix} x \\ y \\ z \end{bmatrix} \quad (\text{A.2.2.1})$$

and the counter-clockwise rotation transform of α , β , γ around respectively x, y, z axis is performed by using their direction cosine matrix

$$a_x^\alpha = \begin{bmatrix} 1 & 0 & 0 \\ 0 & \cos \alpha & \sin \alpha \\ 0 & -\sin \alpha & \cos \alpha \end{bmatrix} \quad (\text{A.2.2.2})$$

$$a_y^\beta = \begin{bmatrix} \cos \beta & 0 & \sin \beta \\ 0 & 1 & 0 \\ -\sin \beta & 0 & \cos \beta \end{bmatrix} \quad (\text{A.2.2.3})$$

$$a_z^\gamma = \begin{bmatrix} \cos \gamma & \sin \gamma & 0 \\ -\sin \gamma & \cos \gamma & 0 \\ 0 & 0 & 1 \end{bmatrix} \quad (\text{A.2.2.4})$$

If we consider the rotation order in x, y, z and the rotation direction (clockwise or counter-clockwise), there are twelve possibilities (or conventions) to fulfill an arbitrary orientation operation, in which the most commonly used is known as the Euler angles rotations (Figure A.2.2.1):

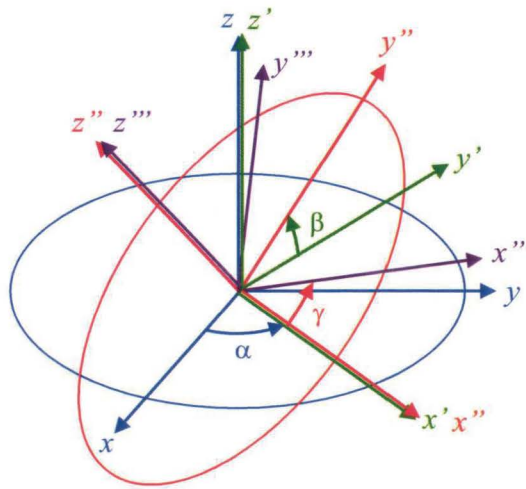


Figure A.2.2.1: Three rotations of Euler angles

First rotation: a counter-clockwise rotation of α around z with

$$a_z^\alpha = \begin{bmatrix} \cos \alpha & \sin \alpha & 0 \\ -\sin \alpha & \cos \alpha & 0 \\ 0 & 0 & 1 \end{bmatrix}$$

Second rotation: a counter-clockwise rotation of β around x' with

$$a_{x'}^\beta = \begin{bmatrix} 1 & 0 & 0 \\ 0 & \cos \beta & \sin \beta \\ 0 & -\sin \beta & \cos \beta \end{bmatrix}$$

Third rotation: a counter-clockwise rotation of γ around z''

$$a_{z''}^\gamma = \begin{bmatrix} \cos \gamma & \sin \gamma & 0 \\ -\sin \gamma & \cos \gamma & 0 \\ 0 & 0 & 1 \end{bmatrix}$$

The final transform matrix is obtained by the product of the three individual rotation

matrices

$$a = a_z^\alpha a_x^\beta a_z^\gamma, \quad (\text{A.2.2.5})$$

Usually, a specific angle rotation does not have to follow the Euler angles convention. Any twelve transform step or order can be applied.

Based on the above coordinates transform with axes rotation matrix a , we can consider the tensor transformation.

To get the transform of the elastic constant tensor c_{ijkl} , begin with the basic relation of Hooke's law of $T_{ij} = c_{ijkl} S_{kl}$ and first transform respectively the second rank stress tensor T_y and strain tensor S_{kl} into the new system.

For stress tensor T_{ij}

$$T'_{ij} = a_{ik} a_{jl} T_{kl} \quad (\text{A.2.2.6})$$

where a_{ik} and a_{jl} are the elements of the rotation matrix a . The detailed form of Eq.

(A.2.2.6) can be developed

$$\begin{aligned} T'_{11} &= a_{1k} a_{1l} T_{kl} = a_{11}^2 T_{11} + 2a_{11} a_{12} T_{12} + 2a_{11} a_{13} T_{13} + a_{12}^2 T_{22} + 2a_{12} a_{13} T_{23} + a_{13}^2 T_{33} \\ T'_{22} &= a_{2k} a_{2l} T_{kl} = a_{21}^2 T_{11} + 2a_{21} a_{22} T_{12} + 2a_{21} a_{23} T_{13} + a_{22}^2 T_{22} + 2a_{22} a_{23} T_{23} + a_{23}^2 T_{33} \\ T'_{33} &= a_{3k} a_{3l} T_{kl} = a_{31}^2 T_{11} + 2a_{31} a_{32} T_{12} + 2a_{31} a_{33} T_{13} + a_{32}^2 T_{22} + 2a_{32} a_{33} T_{23} + a_{33}^2 T_{33} \\ T'_{23} &= T'_{32} = a_{2k} a_{3l} T_{kl} = a_{21} a_{31} T_{11} + (a_{21} a_{32} + a_{22} a_{31}) T_{12} + (a_{21} a_{33} + a_{23} a_{31}) T_{13} \\ &\quad + a_{22} a_{32} T_{22} + (a_{22} a_{33} + a_{23} a_{32}) T_{23} + a_{23} a_{33} T_{33} \\ T'_{13} &= T'_{31} = a_{1k} a_{3l} T_{kl} = a_{11} a_{31} T_{11} + (a_{11} a_{32} + a_{12} a_{31}) T_{12} + (a_{11} a_{33} + a_{13} a_{31}) T_{13} \\ &\quad + a_{12} a_{32} T_{22} + (a_{12} a_{33} + a_{13} a_{32}) T_{23} + a_{13} a_{33} T_{33} \\ T'_{12} &= T'_{21} = a_{1k} a_{2l} T_{kl} = a_{11} a_{21} T_{11} + (a_{11} a_{22} + a_{12} a_{21}) T_{12} + (a_{11} a_{23} + a_{13} a_{21}) T_{13} \\ &\quad + a_{12} a_{22} T_{22} + (a_{12} a_{23} + a_{13} a_{22}) T_{23} + a_{13} a_{23} T_{33} \end{aligned} \quad (\text{A.2.2.7})$$

Using the matrix form of the tensor, i.e.

$$T' = \begin{bmatrix} T'_1 \\ T'_2 \\ T'_3 \\ T'_4 \\ T'_5 \\ T'_6 \end{bmatrix} = \begin{bmatrix} T'_{11} \\ T'_{22} \\ T'_{33} \\ T'_{23} = T'_{32} \\ T'_{13} = T'_{31} \\ T'_{12} = T'_{21} \end{bmatrix} = M \begin{bmatrix} T_1 \\ T_2 \\ T_3 \\ T_4 \\ T_5 \\ T_6 \end{bmatrix} = MT \quad (\text{A.2.2.8})$$

with

$$M = \begin{bmatrix} a_{11}^2 & a_{12}^2 & a_{13}^2 & 2a_{12}a_{13} & 2a_{11}a_{13} & 2a_{11}a_{12} \\ a_{21}^2 & a_{22}^2 & a_{23}^2 & 2a_{22}a_{23} & 2a_{21}a_{23} & 2a_{21}a_{22} \\ a_{31}^2 & a_{32}^2 & a_{33}^2 & 2a_{32}a_{33} & 2a_{31}a_{33} & 2a_{31}a_{32} \\ a_{21}a_{31} & a_{22}a_{32} & a_{23}a_{33} & a_{22}a_{33} + a_{23}a_{32} & a_{21}a_{33} + a_{23}a_{31} & a_{21}a_{32} + a_{22}a_{31} \\ a_{11}a_{31} & a_{12}a_{32} & a_{13}a_{33} & a_{12}a_{33} + a_{13}a_{32} & a_{11}a_{33} + a_{13}a_{31} & a_{11}a_{32} + a_{12}a_{31} \\ a_{11}a_{21} & a_{12}a_{22} & a_{13}a_{23} & a_{12}a_{23} + a_{13}a_{22} & a_{11}a_{23} + a_{13}a_{21} & a_{11}a_{22} + a_{12}a_{21} \end{bmatrix} \quad (\text{A.2.2.9})$$

Similar procedure may be used to determine the strain tensor transform from

$$S'_{ij} = a_{ik}a_{jl}S_{kl} \quad (\text{A.2.2.10})$$

But it's much easier to use the energy conception for its determination. Knowing that the mechanical energy density $W = T_{ij}S_{kl}$ is a scalar quantity and it's an invariant

under different coordinates $W = W' = T'_{ij}S'_{kl} = T'_{ij}S'_{kl}$. In matrix form, there is

$$\begin{aligned} W &= T^T S = (M^{-1}T)^T S = T'^T (M^{-1})^T S \\ W' &= T'^T S' \end{aligned} \quad (\text{A.2.2.11})$$

where the superscript T means the matrix transpose.

$$\text{Hence} \quad (M^{-1})^T S = S' \quad \text{and} \quad S = M^T S' \quad (\text{A.2.2.12})$$

From the relations (A.2.2.8), (A.2.2.12) and the Hooke's law

$$T' = M^T T = M^T M c_{IJ} S = M^T M c_{IJ} M^T S' = c'_{IJ} S' \quad (\text{A.2.2.13})$$

Therefore, the elastic constant matrix transform is

$$c'_{IJ} = M \cdot c_{IJ} \cdot M^T \quad (\text{A.2.2.14})$$

The transform for the piezoelectric constant tensor or matrix may be carried out in the similar way. Take its definition in the matrix form

$$D = e_{ij} S \quad (\text{A.2.2.15})$$

The coordinate transform of D and S in their matrix form are

$$D' = aD \quad \text{and} \quad S = M^T S' \quad (\text{A.2.2.16})$$

$$\text{Then} \quad D' = a \cdot e_{ij} S = a \cdot e_{ij} M^T S' = e'_{ij} S' \quad (\text{A.2.2.17})$$

$$\text{Therefore} \quad e'_{ij} = a \cdot e_{ij} \cdot M^T \quad (\text{A.2.2.18})$$

The permittivity constant transform $\epsilon'_{ij} = a_{ij} a_{kl} \epsilon_{kl}$ can also be obtained,

from $D = \varepsilon_{kl} E$, $D' = aD$ and $E' = aE$, by

$$\varepsilon'_{ij} = a \varepsilon_{kl} a^T \quad (\text{A.2.2.19})$$

in which $a^T = a^{-1}$ has been used and a^{-1} is the reciprocal direction cosine matrix.

Annex 2.3: Multiple quarter wavelength mechanical matching

The recursive formulas for the determination of the acoustic impedances in a multilayer matching system are listed in Table A.2.3.1, where Z_I , Z_T are respectively the acoustic impedance of the incident and the transmitting medium, Z_i^N that of the i -th layer in the N matching layers system that is determined from the impedances of the incident, transmitting medium and those of the $N-1$ matching layers system.

Table A.2.3.1 Recursive formulae for the calculation of the acoustic impedances in a multilayer matching system

Matching layer number	Chebyshev's formulas	DeSilets' formulas	Souquet's formulas
1	$Z_1^1 = \sqrt{Z_I Z_T}$	$Z_1^1 = \sqrt[3]{Z_I (Z_T)^2}$	$Z_1^1 = \sqrt[3]{2Z_I (Z_T)^2}$
2	$Z_1^2 = \sqrt{Z_I Z_1^1}$, $Z_2^2 = \sqrt{Z_1^1 Z_T}$	$Z_1^2 = \sqrt[3]{Z_I (Z_1^1)^2}$, $Z_2^2 = \sqrt[3]{Z_1^1 (Z_T)^2}$	$Z_1^2 = \sqrt[3]{2Z_I (Z_1^1)^2}$, $Z_2^2 = \sqrt[3]{2Z_1^1 (Z_T)^2}$
... *	...
N	$Z_i^N = \sqrt{Z_{i-1}^{N-1} Z_i^{N-1}}$	$Z_i^N = \sqrt[3]{Z_{i-1}^{N-1} (Z_i^{N-1})^2}$	$Z_i^N = \sqrt[3]{2Z_{i-1}^{N-1} (Z_i^{N-1})^2}$
	$i = 1, \dots, N, \quad Z_0^{N-1} = Z_I, \quad Z_N^{N-1} = Z_T$		

* improved DeSilets' formulas [182 , 183]: two quarter layers matching $Z_1^2 = \sqrt[3]{Z_I^4 Z_T^3}$; $Z_2^2 = \sqrt[3]{Z_I Z_T^6}$ and three quarter layers matching $Z_1^3 = \sqrt[5]{Z_I^{11} Z_T^4}$; $Z_2^3 = \sqrt[5]{Z_I^5 Z_T^{10}}$; $Z_3^3 = \sqrt[5]{Z_I Z_T^{14}}$

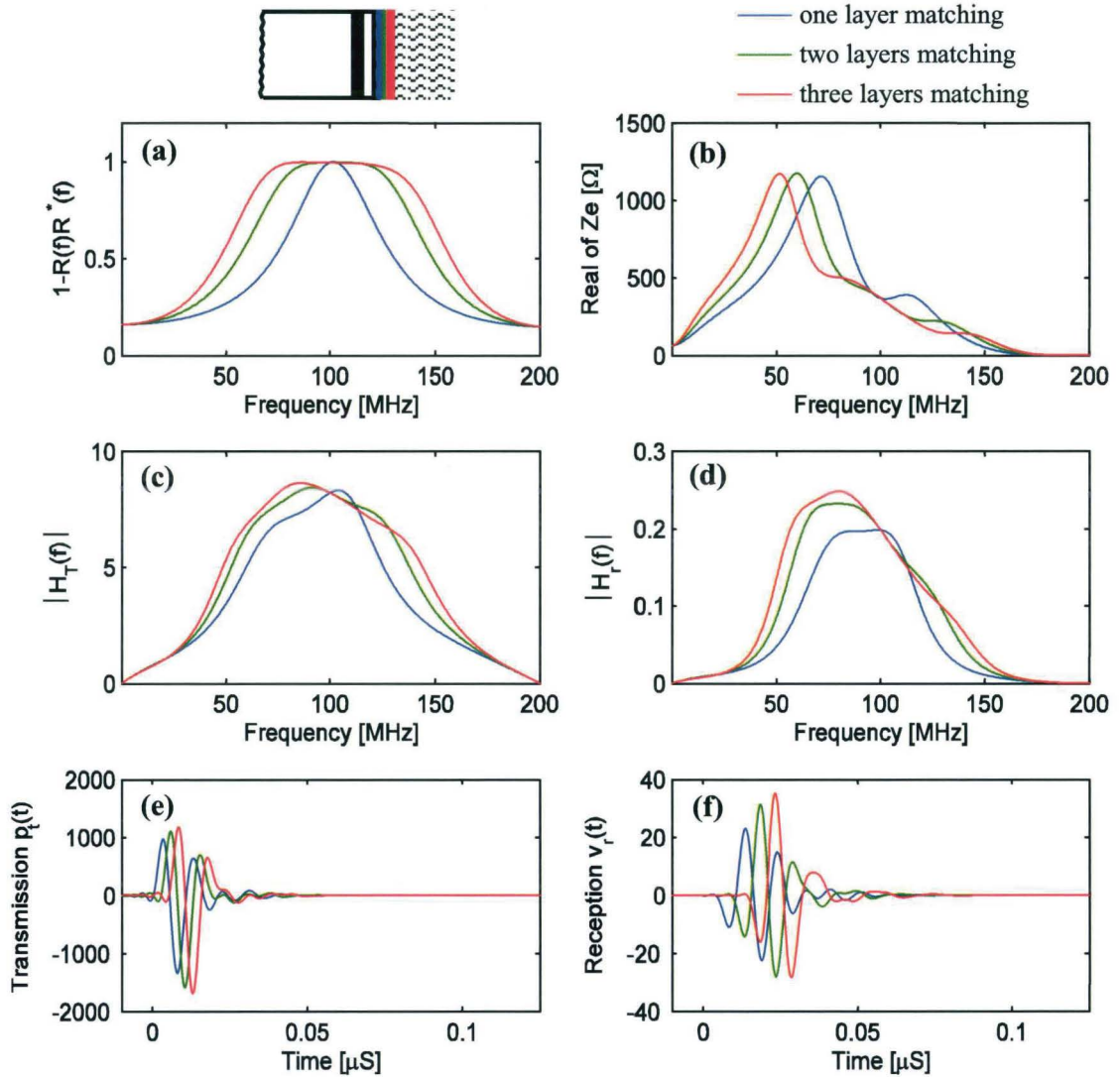


Figure A.2.3.1 Multi-layer (quarter wavelength) matching for LiNbO₃ transducer ($Z_p = 34.5MPa$) of 100 MHz free resonant frequency with water front load ($Z_T = 1.5MPa$) using Chebyshev's formulas.

Figure A.2.3.1 is the calculated results obtained using Chebyshev's formula for LiNbO₃ transducer matching with one, two and three quarter-wavelength matching layers. With the increasing of the layer number, both the transfer functions gain and the bandwidth are further improved (see Figure A.2.3.1 (c) and (d)). The pulse amplitude in the corresponding impulsion response is also progressively increased with an extra time delay (in Figure A.2.3.1 (e) and (f)).

Figure A.2.3.2 shows the results for two layers matching of LiNbO₃ transducer

using differently derived formulas of Chebyshev, DeSilets, modified DeSilets and Souquet. The differences in the transducer performance in terms of their sensibility and bandwidth are not significant (Figure A.2.3.2 (c) and (d)), nor in their impulsion response (Figure A.2.3.2 (e) and (f)).

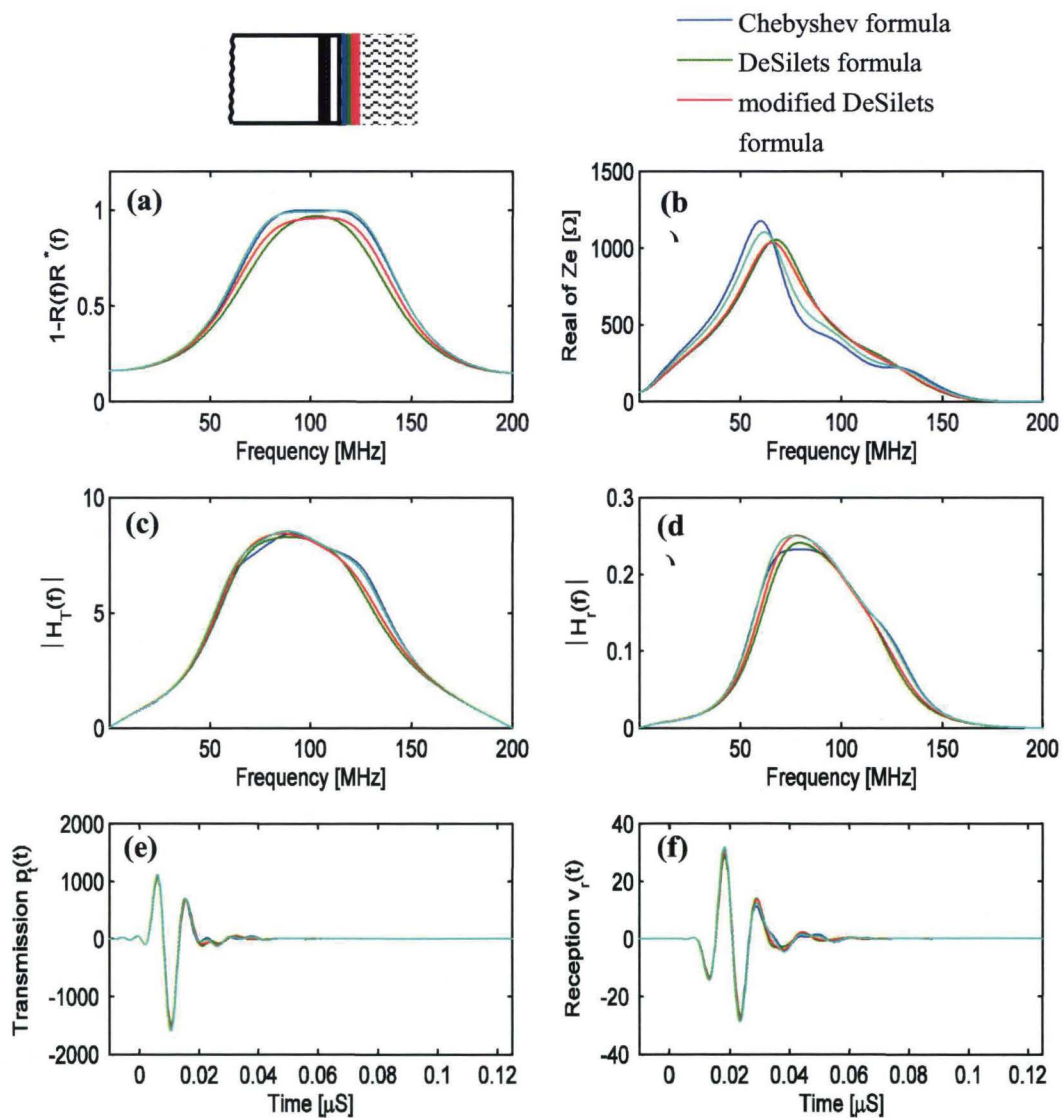


Figure A.2.3.2 Two-layer matching (quarter wavelength) for LiNbO_3 transducer ($Z_p = 34.5 \text{ MPa}$) of 100 MHz free resonant frequency with water front load ($Z_T = 1.5 \text{ MPa}$) using different formulas of Chebyshev, DeSilets and Souquet.

References

- [1] Dr. Joseph Woo, Ashort *history of the development of ultrasound in Obsterics and Gynecology*, Obsterics ultrasound, available at: <http://www.ob-ultrasound.net>
- [2] Barry B. Goldberg, M. D., *Obsteric US Imaging: The Past 40Years, Radiology*, available at: <http://radiology.rsnajns.org/cgi/reprint/215/3/622.pdf>
- [3] R. F. Browne, M. Jeffers, T. McDermott, R. Grainger, D. Mulving, R. G. Gibney, and W. C. Torreggiani, "Intra-operative ultrasoundguided needle localization for impalpable testicular lesions," *Clin.Radiol.*, vol. 58, pp. 566–569, Jul. 2003.
- [4] D. Stephens, et al., "The acoustic lens design and in vivo use of a multifunctional catheter combining intracardiac ultrasound imaging and electrophysiology sensing," *IEEE Trans. Ultrason. Ferroelectr. Freq. Control*, vol. 55, no. 3, pp. 602–618, Mar. 2008.
- [5] P. Wilcox, C. Holmes, and B. Drinkwater, "Advanced reflector characterization with ultrasonic phased arrays in nde applications," *IEEE Trans. Ultrason. Ferroelectr. Freq. Control*, vol. 54, no. 8, pp. 1541–1550, Aug. 2007.
- [6] J. McGarrity, G. Hayward, and D. Powell, "A facet ensemble approach for evaluation of array performance in ultrasonic nde," *IEEE Trans. Ultrason. Ferroelectr. Freq. Control*, vol. 41, no. 1, pp. 19–25, Jan. 1994.
- [7] Novelline, Robert (1997). *Squire's Fundamentals of Radiology* (5th ed.). Harvard University Press. pp. 34–35. ISBN 0674833392.
- [8] Savord B, Solomon R. Fully sampled matrix transducer for real time 3D ultrasonic imaging. IEEE Ultrasonics Symposium; 2003. pp. 945–953.
- [9] Austeng A, Holm S. Sparse 2-D arrays for 3-D phased array imaging – experimental validation. *IEEE Trans Ultras, Ferro, and Freq Control*. 2002;49:1087–1093.
- [10] Light ED, Davidsen RE, Fiering JO, Hruschka TA, Smith SW. Progress in two-dimensional arrays for real-time volumetric imaging. *Ultrasonic Imaging*. 1998;20:1–15.
- [11] Oralkan O, Ergun AS, Cheng CH, Johnson JA, Karaman M, Lee TH, Khuri-Yakub BT. Volumetric Ultrasound Imaging Using 2-D CMUT Arrays. *IEEE Trans Ultras, Ferro, and Freq Control*. 2003;50:1581–1594.
- [12] Ira O. Wygant, Xuefeng Zhuang, David T. Yeh, *Student*, Omer Oralkan, A. Sanli Ergun, Mustafa Karaman, and Butrus T. Khuri-Yakub, "Integration of 2D CMUT Arrays with Front-End Electronics for Volumetric Ultrasound Imaging," *IEEE Trans Ultras, Ferro, and Freq Control.*, 55, pp. 327–342, 2008.
- [13] D. Turnbull and F. Foster, "Fabrication and characterization of transducer elements in two-dimensional arrays for medical ultrasound imaging," *IEEE Trans. Ultrason., Ferroelect., Freq. Contr.*, vol. 39, no. 4, pp. 464–475, 1992.
- [14] Jesse T. Yen, Chi Hyung Seo, Samer I. Awad, and Jong S. Jeong, "A Dual-Layer Transducer Array for 3-D Rectilinear Imaging," *IEEE Trans. Ultrason., Ferroelect., Freq. Contr.*, vol. 56, no. 1, pp. 204–212, 2009.
- [15] Saijo Laboratory, available at:
<http://www.ecei.tohoku.ac.jp/imaging/highfrequency-e.html>

- [16] G. R. Lockwood, D. H. Turnbull, D. A. Christopher and F. S. Foster, "Beyond 30MHz Applications of high-frequency ultrasound imaging", *IEEE Eng. Med. Biol.*, 15 (6), pp. 60-71, (1996)
- [17] C.J. Pavlin and F. S. Foster, *Ultrasound microscopy of the eye*, New York: Springer-Verlag, 1995.
- [18] D. H. Turnbull, B. G. Starkoski, K. A. Harasiewicz, J. L. Semple, L. From, A. K. Gupta, D. N. Sauder, and F. S. Foster, "A 40–100 MHz B-scan ultrasound backscatter microscope for skin imaging," *Ultrasound Med. Biol.*, 21 (1), pp. 79–88, (1995).
- [19] Y. Saijo and A. F. W. van der Steen, *Vascular ultrasound*, Tokyo: Springer, 2003.
- [20] F. S. Foster, et al., "A new ultrasound instrument for *in vivo* microimaging of mice," *Ultrasound Med. Biol.*, 28 (9), pp. 1165–1172, (2002).
- [21] A. Briggs, *Advances in acoustic microscopy*. New York and London: Plenum Press, 1995.
- [22] H. Vettters, E. Matthaei, A. Schulz and P. Mayr, "Scanning Acoustic Microprobe Analysis for Testing Solid State Materials", *Materials Science and Engineering*, A122, pp. 9-14, (1989).
- [23] F. Dunn, *Ultrasonic tissue characterization*, New York: Springer-Verlag, 1996.
- [24] S. Schenkl, E. C. Weiss, F. Stracke, D. Sauer, M. Stark, I. Riemann, R. M. Lemor, K. König, "In-vivo observation of cells with a combined high-resolution multiphoton–acoustic scanning microscope", *Microscopy Research and Technique*, 70(5), pp. 476–480, (2007).
- [25] J. Bereiter-Hahn, I. Karl, H. Luers, M. Voth, "Mechanical basis of cell shape: Investigations with the scanning acoustic microscope", *Cell Biochem. Biol.* 23, pp. 337–348 (1995).
- [26] J. Zoller, K. Brandle, J. Bereiter-Hahn, "Cellular motility *in vitro* as revealed by scanning acoustic microscopy depends on cell-cell contacts", *Cell Tissue Res.* 290, pp. 43–50, (1997).
- [27] Y. Saijo, M. Tanaka, H. Okawai, F. Dunn, "The ultrasonic properties of gastric-cancer tissues obtained with a scanning acoustic microscope system", *Ultrasound Med Biol* 17, pp. 709–714, (1991).
- [28] G. J. Czarnota, M. C. Kolios, J. W. Hunt, M. D. Sherar "Ultrasound imaging of apoptosis. DNA-damage effects visualized." *Methods Mol Biol* 203, pp. 257-77, (2002).
- [29] B. T. Khuri-Yakub, S. Akamine, B. Hadimioglu, H. Yamada, C. F. Quate, "Near-field acoustic microscopy", *SPIE Scanning Microscopy Instrumentation*, 1556, pp. 30-39, Gordon S. Kino; Ed. 1991.
- [30] I. Ladabaum, X. Jin, H.T. Soh, A. Atalar, B.T. Khuri-Yakub, "Surface micromachined capacitive ultrasonic transducers, *IEEE Trans. Ultrason. Ferroelectr. Freq. Control* 45 (3), 678–690, (1998).
- [31] F. Akasheh, T. Myers, J.D. Fraser, S. Bose, A. Bandyopadhyay, "Developments of pMUTs", *Sens. Actuators A* 111, 275–287, (2004).
- [32] J.-Y. Lu, "Experimental study of high frame rate imaging with limited diffraction beams", *IEEE Trans. Ultrason. Ferroelectr. Freq. Control.*, 45, pp. 84–97, (1998).
- [33] A. Sarti, C. Corsi, E. Mazzini and C. Lamberti, "Maximum likelihood segmentation of ultrasound images with Rayleigh distribution", *IEEE Trans. Ultrason. Ferroelectr.*

- Freq. Control.*, 52, pp. 947–60, (2005).
- [34] J. M. Cannata et al, “Self-focused ZnO transducers for ultrasonic biomicroscopy”, *J. Appl Phys.* 103 (8), art. 084109, 2008.
- [35] Guo-Hua Feng et al, “Fabrication of MEMS ZnO dome-shaped-diaphragm transducers for high-frequency ultrasonic imaging”, *J. Micromech. Microeng.* 15, pp 586-590, 2005.
- [36] J.-H. Mo et al, “Crosstalk reduction with a micro-machined diaphragm structure for integrated ultrasound transducer arrays”, *IEEE Transactions on Ultrasonics, Ferroelectrics and Frequency Control*, Vol 39, (1) pp 48-52, 1992.
- [37] H. H. Kim, J. M. Cannata, and K. K. Shung, “20 MHz-40 MHz dual element transducers for high frequency harmonic imaging”, *IEEE Trans. Ultrason., Ferroelect., Freq. Contr.*, vol. 55, pp. 2683–2691, 2008.
- [38] K. T. Son and C. C. Lee, “Input impedance matching of acoustic transducers operating at off-resonant frequencies”, *IEEE Trans. Ultrason., Ferroelect., Freq. Contr.*, vol. 57, pp. 2784–2794, 2010.
- [39] J. A. Jensen, “Simulation of advanced ultrasound systems using Field II”, *IEEE International Symposium on Biomedical imaging from nano to macro*, (2004) Arlington, Virginia.
- [40] L. Satyanarayan, C. Sridhar, and K. Balasubramaniam, “Simulation of ultrasonic phased array technique for imaging and sizing of defects using longitudinal waves”, *International Journal of Pressure Vessels and Piping*, vol. 84, pp. 716–729, 2007.
- [41] G. S. Kino, in *Acoustic Waves*. Newyork: Printice Hall, 1987.
- [42] Wenkang Qi and Wenwu Cao, “Finite element study on 1-D array transducer design”, *IEEE Trans. Ultrason., Ferroelect., Freq. Contr.*, vol. 47, pp. 949–955, 2000.
- [43] Lethiecq M., Feuillard G., Ratsimandresy L., Nguyen-Dinh A., Pardo L., Ricote J., Andersen B., and Millar C., “Miniature high frequency array transducers based on new fine grain ceramics,” *Proc. 1994 IEEE Ultrasonics Symposium*, pp. 1009–1013, 1994.
- [44] Nguyen-Dinh A., Ratsimandresy L., Mauchamp P., Dufait R., Flesch A., and Lethiecq M., “High frequency piezo-composite transducer array designed for ultrasound scanning applications,” *Proc. IEEE Ultrasonics Symposium*, pp. 943–947, 1996.
- [45] J. M. Cannata, Q. F. Zhou, and K. K. Shung, “Development of a High Frequency (35 MHz) Linear Ultrasonic Array using 2-2 Composite Elements,” *Proc. IEEE Ultrasonics Symposium*, pp. 894–897, 2004.
- [46] R. Liu, K. A. Harasiewicz, and F. S. Foster, “Interdigital pair bonding for high frequency (20–50) ultrasonic composite transducers,” *IEEE Trans. Ultrason., Ferroelect., Freq. Contr.*, vol. 48, pp. 299–306, 2001.
- [47] J. W. Sliwa, Jr., S. Ayter, and J. P. Mohr, III, “Method for making piezoelectric composite,” U.S. Patent 5 239 736, 1993.
- [48] Jianhua Yin, Marc Lukacs, Kasia Harasiewicz, Stuart Foster, “Ultra-Fine Piezoelectric Composites For High Frequency Ultrasonic Transducers,” *IEEE International Ultrasonics, Ferroelectrics and Frequency Control Joint 50th Anniversary Conference*, pp 1962-1965, 2004.
- [49] J. Yin, M. Lukacs, K. A. Harasiewicz, and F. S. Foster, “Design and fabrication of

- ultrafine piezoelectric composites,” *Ultrason. Imag.*, vol. 26, pp. 203–216, 2005.
- [50] J.M. F. S. Foster, C. J. Pavlin, G. R. Lockwood, L. K. Ruyn, K. A. Harasiewicz, L. Berude, and A. M. Rauth, “Principles and applications of ultrasound backscatter microscopy,” *IEEE Trans. Ultrason. Ferroelect. Freq. Contr.*, vol. 40, pp. 608-616, 1993.
- [51] F. S. Foster, C. J. Pavlin, K. A. Harasiewicz, D. A. Christopher and D. H. Turnbull, “Advances in ultrasound biomicroscopy, ” *Ultrasound in Med.&Biol.*, vol. 26, pp.1-27, 2000.
- [52] J. M. Cannata, J. A. Williams, Q. F. Zhou, T. A. Ritter and K. K. Shung, “Development of a 35-MHz piezo-composite ultrasound array for medical imaging,” *IEEE Trans. Ultrason. Ferroelect. Freq. Contr.*, vol. 53, pp.224-236, 2006.
- [53] Q. F. Zhou , D. Wu , F. T. Djuth , C. G. Liu and K. K. Shung, “High-frequency Piezoelectric PZT Film Micromachined Ultrasonic Transducers,” *Proc. IEEE Ultrasonics Symposium*, pp. 1057–1060, 2007.
- [54] J. J. Bernstein, S. L. Finberg, K. Houston, L. C. Niles, H. D. Chen, L. E. Cross, K. K. Li, and K. Udayakumar, “Micromachined high frequency ferroelectric sonar transducers,” *IEEE Trans. Ultrason. Ferroelectr. Freq. Control*, vol. 44, no. 5, pp. 960–969, Sep. 1997.
- [55] G. Pang, M. Sayer, G. R. Lockwood, and M. Watt, “Fabrication of PZT sol gel composite ultrasonic transducers using batch fabrication micromolding,” *IEEE Trans. Ultrason. Ferroelectr. Freq. Control*, vol. 53, no. 9, pp. 1679–1684, Sep. 2006.
- [56] I. Ladabaum, B. T. Khuri-Yakub, and D. Spoliansky, “Micromachined ultrasonic transducers: 11.4 MHz transmission in air and more,” *Appl. Phys. Lett.*, vol. 68, no. 12, pp. 7–9, 1996.
- [57] F. Dauchy and R. A. Dorey, “Thickness mode high frequency MEMS piezoelectric micro ultrasound transducers,” *J. Electroceram.*, vol. 19, no. 4, pp. 383–386, 2007.
- [58] C. G. Liu, D. W. Wu, Q. F. Zhou, F. T. Djuth, K. K. Shung, “High-Frequency (50-100MHz) Medical Ultrasound Transducer Arrays Produced by Micromachining Bulk PZT Materials,” *Proc. IEEE Ultrasonics Symposium*, pp. 690–693, 2008.
- [59] K. Kushida, Y. Ito, H. Takeuchi, H. Kanda and K. Sugawara. 100 MHz band ultrasonic array transducers utilizing epitaxially grown ZnO films, *Ultrasonics Int. 91 Con. Proc.*, 379-382 (1991).
- [60] Y. Ito, K. Kushida, H. Kanda, H. Takeuchi, K. Sugawara and H. Onozato. Thin-film ZnO ultrasonic transducer arrays for operation at 100 MHz, *Ferroelectrics*, **134**, 325-330 (1992).
- [61] Y. Ito, K. Kushida, K. Sugawara and H. Takeuchi. High-frequency ultrasonic transducer arrays using ZnO thin films, *IEEE Ultrasonics Symposium*, 1117-1125 (1993).
- [62] Y. Ito, K. Kushida, K. Sugawara and H. Takeuchi. A 100-MHz ultrasonic transducer array using ZnO thin films, *IEEE Transactions on Ultrasonics, Ferroelectrics, and Frequency Control*, **42**, 316-324 (1995).
- [63] C. E. Morton and G. R. Lockwood, “Evaluation of kerfless linear arrays,” *Proc. IEEE Ultrasonics Symp.*, 2002, pp. 1257–1260.
- [64] C. E. M. Demore, J. A. Brown, and G. R. Lockwood, “Investigation of cross talk in

- kerfless annular arrays for high-frequency imaging,” *IEEE Trans. Ultrason. Ferroelectr. Freq. Control*, vol. 53, no. 5, pp. 1046–1056, May 2006.
- [65] X. Zhu and E. S. Kim. Microfluidic motion generation with acoustic waves, *Sensors and Actuators A*, **66**, 355-360 (1998).
- [66] Toshiki Takayasu, Marie Nakazawa, Kentaro Nakamura and Sadayuki Ueha, “A 100-MHz 32-Array Transducer Using Lithographically-Made Electrodes and Vapor-Deposited Polyurea Film,” *Proc. IEEE Ultrasonics Symp.*, 2008, pp. 1773–1776.
- [67] D. W. Wu, Q. Zhou, B. P. Zhu and K. K. Shung. High-frequency (> 100 MHz) PZT thick film transducers and kerfless arrays, *IEEE Ultrasonics Symposium*, 1-2 (2008).
- [68] D. W. Wu, Q. Zhou and K. K. Shung. Very high frequency (beyond 100 MHz) PZT kerfless linear arrays, *IEEE Transactions on Ultrasonics, Ferroelectrics, and Frequency Control*, **25**, 2304-2310 (2009).
- [69] Q. F. Zhou, K. K. Shung, Q. Zhang, and F. T. Djuth, “High frequency piezoelectric micromachined ultrasonic transducers for imaging applications,” in *Proc. SPIE*, vol. 6223, Orlando, FL, Apr. 19–20, 2006.
- [70] Q. F. Zhou, J. M. Cannata, R. J. Meyer, D. J. Van Tol, W. J. Hughes, K. K. Shung, and S. Trolier-McKinstry, “Fabrication and characterization of micro tonpizl high frequency transducer derived by PZT thick films,” *IEEE Trans. Ultrason. Ferroelectr. Freq. Control*, vol. 52, no. 3, pp. 350–357, 2005.
- [71] F. Akasheh, T. Myers, J.D. Fraser, S. Bose, A. Bandyopadhyay, Development of piezoelectric micromachined ultrasonic transducers, *Sens. Actuators A*, 111 (2004) 275–287.
- [72] P.C. Eccardt, K. Neiderer, Micromachined ultrasonic transducers with improved coupling factors from a CMOS compatible process, *Ultrasonics*, 38 (2000) 774–780.
- [73] S.C. Ko, Y.C. Kim, S.S. Lee, S.H. Choi, S.R. Kim, Micromachined piezoelectric membrane acoustic device, *Sens. Actuators A*, 103 (2004) 130–134.
- [74] K. Yamashida, H. Katata, M. Okuyama, H. Miyoshi, G. Kato, S. Aoyagi, Y. Suzuki, Arrayed ultrasonic microsensors with high directivity for inairuse using PZT thin film on silicon diaphragms, *Sens. Actuators A*, 97–98 (2002) 302–307.
- [75] K. Yamashida, L. Chansomphou, H. Murakami, M. Okuyama, Ultrasonic micro array sensors using piezoelectric thin films and resonant frequency tuning, *Sens. Actuators A*, 114 (2–3) (2004) 147–153.
- [76] A. Goldstein, R.L. Powis, Medical ultrasonic diagnostics, in: R.N Thurston, A.D. Pierce (Eds.), *Ultrasonic Instruments and Devices I*, in: E. Papadakis (volume ed.), *Physical Acoustics*, vol. XXIII, Academic Press, New York, 1999, pp. 43–191.
- [77] I. Ladabaum, X. Jin, H.T. Soh, A. Atalar, B.T. Khuri-Yakub, Surface micromachined capacitive ultrasonic transducers, *IEEE Trans. Ultrason. Ferroelectr. Freq. Contr.*, 45 (3) (1998) 678.
- [78] Firas Akasheh, Todd Myers, John D. Fraser, Susmita Bose, Amit Bandyopadhyay, “Development of piezoelectric micromachined ultrasonic transducers,” *Sensors and Actuators A*, 111 (2004) 275–287.
- [79] Zhihong Wang, Weiguang Zhu, Jianmin Miao, Hong Zhu, Chen Chao, Ooi Kiang Tan, Micromachined thick film piezoelectric ultrasonic transducer array, *Sensors and Actuators A*, 130–131 (2006) 485–490.

- [80] P. Osbond, C.M. Beck, C.J. Brierley, M.R. Cox, S.P. Marsh, N.M. Shorrocks, The influence of ZnO and electrode thickness on the performance of thin film bulk acoustic wave resonators, *Proceedings of the IEEE Ultrasonics Symposium*, 1999, pp. 911–914.
- [81] P.C. Eccardt, K. Neiderer, Micromachined ultrasonic transducers with improved coupling factors from a CMOS compatible process, *Ultrasonics*, 38 (2000) 744.
- [82] H. Zhang, G. D. Song, D. C. Li, Z. J. Guan, S. J. Jin, “Design of capacitive microfabricated ultrasonic transducer,” *J. of Tianjin University*, 41, (2008), pp. 17-20.
- [83] A. Ergun, H. Yongli, C. Cheng, O. Oralkan, J. Johnson, H. Jagannathan, U. Demirci, G. Yaralioglu, M. Karaman, and B. Khuri-Yakub, “Broadband capacitive micromachined ultrasonic transducers ranging from 10 kHz to 60 MHz for imaging arrays and more,” *Proc. IEEE Ultrason. Symp.*, 2002, pp. 1039–1043.
- [84] Marc Lukacs and F. Stuart Foster, Performance and Characterization of New Micromachined High-Frequency Linear Arrays, *IEEE Trans. Ultrason. Ferroelectr. Freq. Contr.*, 53 (10) (2006) 1719-1729.
- [85] J.F. Gelly et al., Comparison of piezoelectric (thickness mode) and MEMS transducers, *Proc. of IEEE Ultrasonics Symposium*, Hawaii, October 6–9, 2003.
- [86] Y. Huang et al., A solution to the charging problems in capacitive micromachined ultrasonic transducers (CMUTs), *IEEE Transactions on UFFC*, 52 (4) (2005) 578–580.
- [87] P.C. Eccardt, K. Neiderer, Micromachined ultrasonic transducers with improved coupling factors from a CMOS compatible process, *Ultrasonics*, 38 (2000) 744.
- [88] Yongli Huang, Xuefeng Zhuang, Edward O. Haeggstrom, A. Sanli Ergun, Ching-Hsiang Cheng, Butrus T. Khuri-Yakub, Capacitive micromachined ultrasonic transducers (CMUTs) with isolation posts, *Ultrasonics*, 48 (2008) 74–81.
- [89] Joule, James (1842), *Sturgeon's Annals of Electricity* 8: 219.
- [90] Y. L. Huang, S. Jose, Micro-electro-mechanical transducers, US patent, No. US20080197751A1 (2008).
- [91] Marc Lukacs, Michael Sayer, Geoff Lockwood and Stuart Foste, Laser Micromachined High Frequency Ultrasonic Arrays, *Proc. IEEE Ultrason. Symp.*, 1999, pp. 1209–1212.
- [92] R. Farlow, W. Galbraith, M. Knowles and G. Hayward, Micromachining of a Piezocomposite Transducer Using a Copper Vapour Laser, *IEEE Trans. Ultrason. Ferroelectr. Freq. Contr.*, 48 (3) (2001) 639-640.
- [93] K. K. Shung, “High Frequency Ultrasonic Imaging”, *J. Med Ultrasound*, 17(1) pp. 25–30, 2009.
- [94] X. Zhu and E. S. Kim “Microfluidic Motion Generation with Loosely-Focused Acoustic Waves”, *Transducer'97*, pp. 837-838, 1997.
- [95] K. Yokosawa et al, “Intra-Corporeal Imaging and Differentiation of Living Tissue with an Ultra-High-Frequency Ultrasound Probe”, *Ultrasound in Med. & Biol.* 26(4), pp. 503–507, 2000
- [96] B. A. Auld, *Acoustic Fields and Waves in Solids*, 2nd ed. Krieger, Malabar, FL, 1990.
- [97] Joel F. Rosenbaum, *Bulk acoustic wave Theory and devices*, Artech House, Boston-London, 1988.
- [98] Copyright 1984-2007 The MathWorks, Inc. Version 7.5.0.338 (R2007b)

- [99] K. K. Wong, (Editor), *Properties of Lithium Niobate*, (Emis Datareviews Series, 28), INSPEC, The Institution of Engineering and Technology, London, UK, 2002.
- [100] C. Jagadish, S. Pearton, *Zinc oxide bulk, thin films and structures*, Elsevier Ltd, 2006.
- [101] APC International Ltd. *Piezoelectric Ceramics: Principles and Applications*, APC International, Ltd. 2002
- [102] F. Duval, *PZT thick films for high frequency transducers*, Cranfield University, 2003
- [103] W.P. Mason, *Electromechanical Transducers and Wave Filters*, D. Van Nostrand, New York, 1942; 2nd ed. Princeton, NJ, Van Nostrand-Reinhold, 1948.
- [104] W.P. Mason, *Physical Acoustics and the Properties of Solids*, D. Van Nostrand Co., Princeton, NJ, 1958.
- [105] W. P. Mason, Use of piezoelectric crystals and mechanical resonators in filters and oscillators, in "Physical Acoustics" (W. P. Mason, ed.) Vol. IA, Chapter 5. Academic Press, New York, 1964.
- [106] R. Krimholtz, D.A. Leedom, G.L. Matthaei, "New Equivalent Circuit for Elementary Piezoelectric Transducers", *Electron. Lett.* 6, pp. 398-399, 1970.
- [107] D. Leedom, R. Krimholtz, and G. . Matthaei, *IEEE Trans. Sonics Ultrason.* SU-18, 128, 1971.
- [108] M. Redwood, "Experiments with the electrical analogue of a piezoelectric transducer", *J. Acoust. Soc. Am.* 36 (10) 1872-1880, 1964.
- [109] F.S. Foster, L.K. Ryan, D.H. Turnbull, "Characterization of Lead Zirconate Titanate ceramics for use in miniature high frequency (20-80 MHz) transducers, *IEEE Trans on Ultrasonics, Ferroelectrics and Frequency Control*, 38, pp. 446-453, 1991.
- [110] Q. Zhang, P.A. Lewin, P.E. Bloomfield, "PVDF Transducers- A Performance Comparison of Single-Layer and Multilayer Structures", *IEEE Trans on Ultrasonics, Ferroelectrics and Frequency Control*, 44, pp.1148-1156, 1997.
- [111] S. Sherrit, S. P. Leary, B. P. Dolgin and Y. Bar-Cohen, "Comparison of the Mason and KLM equivalent circuits for piezoelectric resonators in the thickness mode", in: *IEEE Proceeding of the Ultrasonic Symposium*, 1999.
- [112] M. Castillo, P. Acevedo, E. Moreno, "KLM model for lossy piezoelectric transducers", *Ultrasonics*, 41(8), 671-679, 2003.
- [113] R. E. Collin, *Proc. IRE* 43, 179, 1955.
- [114] G. S. Kino, *Acoustic Waves: Device, Imaging and Analog Signal Proceeding*, Prentice-Hall Inc., Englewood Cliffs, New Jersey, 1987.
- [115] G. Kossof, "The effects of backing and matching on the performance of piezoelectric ceramic transducers", *IEEE Transactions on Sonics and Ultrasonics*, SU-13 (1), 20-30, 1966
- [116] J. H. Goll, B. A. Auld, "Multilayer impedance matching schemes for broadbanding of water loaded piezoelectric transducers and high Q electric resonators", *IEEE Trans. Sonics Ultrason.* SU-22 (1), 52, 1975.
- [117] C. S. Desilets, J. D. Fraser, and G. S. Kino. "The design of efficient broad-band piezoelectric transducers", *IEEE Transactions on Sonics and Ultrasonics* SU-25 (3), 115-125, 1978.
- [118] J. H. Goll, "The design of broad-band fluid-loaded ultrasonic transducers", *IEEE Trans. Sonics Ultrason.* SU-26 (6), 385, 1979.
- [119] J. Souquet, P. Defranould, J. Desbois, "Design of low-loss wideband ultrasonic transducers for noninvasive medical application", *IEEE Trans. Sonics Ultrason.*

- SU-26 (2), 75-81, 1979.
- [120] T. Gudra, K. J. Opielinski, "Influence of acoustic impedance of multilayer acoustic systems on the transfer function of ultrasonic airborne transducers", *Ultrasonics* 40, pp 457–463, 2002.
 - [121] K.J. Opielinski, T. Gudra, "Influence of the thickness of multilayer matching systems on the transfer function of ultrasonic airborne transducer", *Ultrasonics* 40, pp 465–469, 2002.
 - [122] S. Thiagarajan, R.W. Martin, A. Proctor, I. Jayawadena, F. Silverstein, "Dual layer matching (20 MHz) piezoelectric transducers with glass and parylene", *IEEE Transactions on Ultrasonics, Ferroelectrics, and Frequency Control* 44 (5), 1172–1174, 1997.
 - [123] T. Inoue, M. Ohta, S. Takahashi, "Design of ultrasonic transducers with multiple acoustic matching layers for medical application", *IEEE Transactions on Ultrasonics, Ferroelectrics and Frequency Control*, 34 (1), pp. 8–16, 1987.
 - [124] S. Sato, H. Katsura, and K. Kobayashi, "Experimental Investigation of Phased Array Using Tapered Matching Layers", *Proc. IEEE Ultrason. Symp.* 2, p. 1235, 2002.
 - [125] N. Felix, L. Ratsimandresy, and R. Dufait, "High Bandwidth, High Density Arrays for Advanced Ultrasound Imaging", *Proc.-IEEE Ultrason. Symp.* 2, p. 1123, 2001.
 - [126] Venkataramani, V. Subramaniam, "Matching layer having gradient in impedance for ultrasound transducers", *J. Acoust. Soc. Am.* 119 (2), p. 698, 2006.
 - [127] S. Saffar, A. Abdullah, "Determination of acoustic impedances of multi matching layers for narrowband ultrasonic airborne transducers at frequencies <2.5 MHz – Application of a genetic algorithm", *Ultrasonics*, article in press, 2011.
 - [128] K. K. Shung and M. Zipparo, "Ultrasonic transducers and arrays," *IEEE Eng. Med. Biol.* 6, pp. 20–30, 1996.
 - [129] Q. F. Zhou, J. H. Cha, Y. Huang, R. Zhang, W. Cao, J. M. Cannata, K. K. Shung, "Nanocomposite matching layers for high frequency ultrasound transducer," *IEEE Ultrasonics Symposium*, pp. 2365-2368, 2006.
 - [130] Q. F. Zhou, J. H. Cha, Y. Huang, R. Zhang, W. Cao, K. K. Shung, "Alumina/epoxy nanocomposite matching layers for high-frequency ultrasound transducer application", *IEEE Trans Ultrason Ferroelectr Freq Control.* 56 (1), 213-219, 2009.
 - [131] S. Wang et al, "SU-8-Based nanocomposites for acoustical matching layer", *IEEE Trans. Ultrason. Ferroelect. Freq. Contr.*, 56 (7), pp.1483-1489, 2009.
 - [132] F. Tiefensee, C. Becker-Willinger, G. Heppe, P. Herbeck-Engel, A. Jakob, "Nanocomposite cerium oxide polymer matching layers with adjustable acoustic impedance between 4MRayl and 7 MRayl", *Ultrasonics*, 50, 363-366, 2010.
 - [133] Wenkang Qi and Wenwu Cao, Finite element study on 1-D array transducer design, *IEEE Trans on Ultrasonics, Ferroelectrics and Frequency Control*, 47, pp. 949-955, 2000.
 - [134] G. S. Kino, *Acoustic Waves*, Newyork : Prentice Hall, 1987.
 - [135] Bernard Hosten and Christine Biateau, Finite element simulation of the generation and detection by air-coupled transducers of guided waves in viscoelastic and anisotropic materials, *J. Acoust. Soc. Am.* 123(4), pp.1963-1971, 2008.
 - [136] Weina Ke, 3D simulations of air-coupled generation and reception of guided waves-Application to defect detection in composite material structures, Ph.D. thesis, France, 2009.

- [137] W. Friedrich, H. Kaarmann, and R. Lerch, Finite element modelling of acoustic radiation from piezoelectric phased array antennas, *Proc. IEEE Ultrason. Symp.*, 1990, pp. 763–767.
- [138] R. Lerch, Simulation of piezoelectric devices by two- and three-dimensional finite element methods, *IEEE Trans on Ultrasonics, Ferroelectrics and Frequency Control*, **37**, pp. 233-246, 1990.
- [139] Wenkang Qi and Wenwu Cao, Finite element study on 1-D array transducer design, *IEEE Trans on Ultrasonics, Ferroelectrics and Frequency Control*, **47**, pp. 949-955, 2000.
- [140] Marc Lukacs, Stuart Foster, Laser micromachined high frequency ultrasonic arrays, *IEEE Ultrasonics Symposium*, pp. 1209-1212 (1999).
- [141] G. Kino, C. Desilets, Design of slotted transducer arrays with matched backings, *Ultrasonics Imaging*, **1**, pp. 189-209 (1979).
- [142] J. Z. Zhao and C. H. F. Alves. Performance of 50 MHz transducers incorporating fiber composite, PVDF, PbTiO₃ and LiNbO₃, *IEEE Ultrasonics Symposium*, pp. 1185-1190 (1999).
- [143] D. A. Knapik. A 100-200 MHz ultrasound biomicroscope, *IEEE Transactions on Ultrasonics, Ferroelectrics, and Frequency Control*, **47**, 1540-1549 (2000).
- [144] M. Lippert, C. Bruneel and F. Bruneel, “High Frequency Ultrasonic Transducers with Near Optimal Efficiency”, *Rev. Sci. Instrum.*, Vol. 69 (12), pp. 4160-4165, 1998.
- [145] 2J. G. Scott, A. J. Boyland, S. Mailas, C. Grivas, O. Vagner, S. Lagoutte, and W. Eason, *Appl. Surf. Sci.* **230**, 138 (2004).
- [146] 3N. Mitsugi, H. Nagata, K. Shima, and M. Tamai, *J. Vac. Sci. Technol. A* **16**, 2245 (1998).
- [147] Ian E. Barry, Graeme W. Ross, Peter G.R. Smith, Robert W. Eason, Gary Cook, Microstructuring of lithium niobate using differential etch-rate between inverted and non-inverted ferroelectric domains, *Materials Letters*, **37** (1998) 246–254.
- [148] 4D. M. Manos and D. L. Flamm, *Plasma Etching: An Introduction Academic*, New York, (1989), p. 476.
- [149] A. Montaser and D. W. Golightly, eds. *Inductively Coupled Plasmas in Analytical Atomic Spectrometry*, VCH Publishers, Inc., New York, 1992.
- [150] Tamura M. and Yoshikado S. “Etching characteristics of LiNbO₃ crystal by fluorine gas plasma reactive ion etching”, *Surface and Coatings Technology* 169-170 (2003) pp. 203-207. pp. 216 – 220.
- [151] Yang W. S., Lee H.-Y., Kim W. K., and Yoon D. H. “Asymmetry ridge structure fabrication and reactive ion etching” *Optical Materials* **27** (2005) pp. 1642 – 1646.
- [152] Samuel Queste, Gwenn Ulliac, Jean-Claude Jeannot and Chantal Khan Malek, DRIE of non-conventional materials: first results, *Multi-Material Micro Manufacture*, S. Dimov and W. Menz (Eds.), 2008 Cardiff University, Cardiff, UK. Published by Whittles Publishing Ltd.
- [153] S. Benchabane, L. Robert, J. Y. Rauch, A. Khelif, and V. Laude, “Highly selective electroplated nickel mask for lithium niobate dry etching”, *J. Appl. Phys.* (**105**), 094109 (2009).
- [154] R. A. Lemons and C. F. Quate 1974 Acoustic Microscopy-Scanning Version *Appl. Phys. Lett.* **4** 163-165.
- [155] K. Yamada, H. Shimizu, and M. Minakata 1986 Planer Structure Focusing Lens for Operation at 200 MHz and its Application to the Reflection-Mode Acoustic Microscope *IEEE Trans. Ultrason. Symp.* 745-748.
- [156] J. Kushibiki, and N. Chubachi 1985 Material Characterization by Line-Focus-Beam

- Acoustic Microscope *IEEE Trans. Ultrason., Ferroelect., Freq. Contr.* **32** 189-212.
- [157] B. T. Khuri-Yakub 1993 Scanning Acoustic Microscopy *Ultraso.* **31** 361-372.
- [158] C. G. Liu, D. W. Wu, Q. F. Zhou, F. T. Djuth, and K. K. Shung 2008 High-Frequency (50-100 MHz) Medical Ultrasound Transducer Arrays Produced by Micromachining Bulk PZT Materials *IEEE Trans. Ultrason. Symp.* 690-693.
- [159] T. Pedersen, T. Zawada, K. Hansen, and R. Lou-Moeller 2010 Fabrication of High-Frequency pMUT Arrays on Silicon Substrates *IEEE Trans. Ultrason., Ferroelect., Freq. Contr.* **57** 1470-1477.
- [160] M. Lukacs, M. Sayer, G. Lockwood, and S. Foster 1999 Laser Micromachined High Frequency Ultrasonic Arrays *IEEE Trans. Ultrason. Symp.* 1209-1212.
- [161] Han-Ki Kim, et al. 2004 Inductively-coupled-plasma reactive ion etching of ZnO using BCl₃-based plasmas and effect of the plasma treatment on Ti/Au ohmic contacts to ZnO *Thin Solid Films* **447-448** 90-94.
- [162] R. Chen, X. M. Bian, et al. 2008 Research on Property and Wet Etch of ZnO Films Growth by Radio-Frequency Magnetron Sputtering <http://scholar.ilib.cn/A-会议记录ID~7036642.html>
- [163] S. Humad, et al. 2003 High Frequency Micromechanical Piezo-on Silicon Block Resonators http://pmans.ese.upenn.edu/Papers/Piazza_iedm2003.pdf
- [164] L. Yan, J. Wu, and W. C. Tang 2005 A 1.14 GHz Piezoelectrically Transduced Disk Resonator http://ieeexplore.ieee.org/xpl/freeabs_all.jsp?arnumber=1453902
- [165] J. C. Sun, et al. 2007 Realization of controllable etching for ZnO film by NH₄Cl aqueous solution and its influence on optical and electrical properties *Applied Surface Science* **253** 5161-5165.
- [166] D. G.Yoo, et al. 2008 Fabrication of the ZnO Thin Films Using Wet-Chemical Etching Processes on Application for Organic Light Emitting Diode (OLED) Devices *Surface & Coatings Technology* **202** 5476-5479.
- [167] B. H.Seo, et al. 2008 Study on the Wet Etch Behavior of a Zinc-Oxide in Acid Solutions *Journal of the Korean Physical Society* **53** 402-405.
- [168] T. Wu, et al. 2003 The compatibility of ZnO piezoelectric film with micromachining process *Sensors and Actuators A* **104** 61-67.
- [169] J. W. Kwon, et al. 2005 Fine ZnO patterning with controlled sidewall-etch front slope, *J. MicroElectro Mechanical Systems* **14** (3) 603-609.
- [170] T. Gryba, J. Carlier, S. X. Wang et al. One port contour-mode ZnO piezoelectric MEMS resonator, *Microelectron. Eng.* (2011), doi:10.1016/j.mee.2011.04.062
- [171] S. Humad, et al. 2003 High Frequency Micromechanical Piezo-on Silicon Block Resonators http://pmans.ese.upenn.edu/Papers/Piazza_iedm2003.pdf
- [172] T. Wu, et al. 2003 The compatibility of ZnO piezoelectric film with micromachining process *Sensors and Actuators A* **104** 61-67.
- [173] D. W. Wu, Q. F. Zhou, K. K. Shung, C. G. Liu, and F. T. Djuth 2008 High-Frequency Piezoelectric PZT films micromachined Ultrasonic Arrays *IEEE Trans. Ultrason. Symp.* 1222-1225.
- [174] T. Pedersen, T. Zawada, K. Hansen, and R. Lou-Moeller 2010 Fabrication of High-Frequency pMUT Arrays on Silicon Substrates *IEEE Trans. Ultrason., Ferroelect., Freq. Contr.* **57** 1470-1477.
- [175] S. Michau, P. Mauchamp, and R. Dufait 2004 Piezocomposite 30 MHz Linear Arrays for Medical Imaging: Design challenges and Performances Evaluation of a 128 elements Arrays *IEEE Trans. Ultrason. Symp* 898-901.
- [176] M. Lukacs, F. S. Foster, et al. 2006 Performances and Characterizations of New Micromachined High-Frequency Linear Arrays *IEEE Trans. Ultrason., Ferroelect.,*

- Freq. Contr.* **53** 1719-1729.
- [177] R. Liu, K. A. Harasiewicz, and F. S. Foster 2001 Interdigital Pair Bonding for High Frequency (20-50 MHz) Ultrasonic Composite Transducers *IEEE Trans. Ultrason., Ferroelect., Freq. Contr.* **48** 299-306.
 - [178] G. Kino and C. Deslets 1979 Design of slotted transducer arrays with matched backings *Ultrasonic Imaging* **1** 189-209.
 - [179] H. Kim, et al., Inductively-coupled-plasma reactive ion etching of ZnO using BCl₃-based plasmas and effect of the plasma treatment on Ti/Au ohmic contacts to ZnO, *Thin Solid Films*, 447-448 (2000), pp. 90-94.
 - [180] Cheol-Hyun Han and Eun Sok Kim, Micromachined piezoelectric ultrasonic transducers based on parylene diaphragm in silicon substrate, *IEEE Ultrasonics Symposium*, 919-923 (2000).
 - [181] Daniel Royer and Eugène Dieulesaint, *Ondes élastiques dans les solides*, Tome 1, Maisson, Paris, 1996.
 - [182] J. M. Cannata, "High frequency (>20 MHz) ultrasonic arrays for medical imaging applications," Ph.D. thesis, The Pennsylvania State University, 2004.
 - [183] M.-S. Choi, "Improvement of the design method using the KLM model for optimizing thickness-mode piezoelectric transducers", *Journal of the Korean Physical Society*, Vol. 45 (6), pp 1517-1522, 2004.

Réseaux de transducteurs haute fréquence (100-300 MHz) à déphasage réalisés à partir des technologies MEMS

Les réseaux de transducteurs ultrasonores haute fréquence à déphasage sont des candidats intéressants pour l'imagerie haute résolution en temps réel. De nombreuses difficultés interviennent lors du développement de réseaux avec une fréquence d'émission supérieure à 100 MHz: déphasage en haute fréquence, adaptation électrique, adaptation mécanique et fabrication des réseaux de transducteurs haute fréquence qui joue un rôle critique pour le développement de ces systèmes. Cette thèse porte notamment sur deux aspects spécifiques: la modélisation numérique par élément fini et la fabrication basée sur les microtechnologies et les MEMS.

Dans la partie consacrée aux simulations numériques, un modèle commercial basé sur les éléments finis, COMSOL 3.5a, est utilisé. Pour les réseaux de transducteurs piézoélectriques sur absorbeur en face arrière, l'influence du pas spatial, de la profondeur de séparation des transducteurs, de l'isolation mécanique de ces transducteurs sur le champ acoustique ont été étudiés ainsi que l'impédance électrique et le couplage. Ces simulations ont également été réalisées pour des réseaux de transducteur sur ligne à retard de propagation

Dans la partie consacrée aux réalisations expérimentales et à leur caractérisation, des réseaux ont été obtenus grâce aux technologies dédiées aux MEMS à partir de monocristaux de LiNbO₃ gravés par les technologies plasma et de ZnO déposé en couche mince. Ces réseaux de transducteur ont ensuite été caractérisés à l'analyseur de réseaux et les mesures électriques des impédances et des couplages ont permis de montrer la cohérence avec les prédictions théoriques.

Mots clés: Réseaux de transducteurs ultrasonores à déphasage, MEMS, simulation Eléments finis, Transducteur piézoélectrique haute fréquence

MEMS-based High-Frequency(100-300MHz) Ultrasonic Linear Phased Arrays

High-frequency ultrasonic phased array transducer is a desired candidate in real-time and high resolution imaging. Many difficulties will arise in the development of array imaging systems with an operating frequency of above 100 MHz: high-frequency phase-delay system, electrical matching problem, mechanical matching problem, and fabrication of high-frequency array transducers which play a critical role in ultrasonic phased array imaging systems. This dissertation focuses on mainly two aspects: the finite element numerical simulations in the optimized design and the fabrication using micro electromechanical system (MEMS) technologies.

In the section of numerical studies, a commercial finite element tool, COMSOL3.5a, is employed. In piezoelectric backing array transducers, the effects of pitch size, kerf filler and kerf depth on the acoustic field, electrical impedance and crosstalk are investigated. Systematic simulations are carried out for a designed buffered transducer array.

In the section of experimental fabrication and characterization, MEMS based technologies are applied to obtain high-frequency array elements. Single crystal LiNbO₃ arrays are made using ICP RIE technique. Two kinds of ZnO arrays are kerfed using wet chemical etching technique and micromachining silicon substrate, respectively. All of these arrays are characterized by Network Analyzer. The measured electrical impedance and crosstalk are consistent with the theoretical predictions.

Keywords: Ultrasonic phased array; High-frequency; MEMS; FEM simulation; Piezoelectric